FOSSIL ENERGY

DOE/BC/14899-34
(DE96001214)

A STUDY OF STEAM INJECTION IN FRACTURED MEDIA

SUPRI TR 101

By
Meliha Deniz Sumnu Dindoruk
Khalid Aziz
William Brigham
Louis Castanier

February 1996

Performed Under Contract No. DE-FG22-93BC14899

Stanford University
Stanford, California

Bartlesville Project Office
U. S. DEPARTMENT OF ENERGY
Bartlesville, Oklahoma

DOE/BC/14899-34
Distribution Category UC-122

A Study of Steam Injection in Fractured Media

SUPRI TR101

By
Meliha Deniz Sumnu Dindoruk
Khalid Aziz
William Brigham
Louis Castanier

February 1996

Work Performed Under Contract No. DE-FG22-93BC14899

Prepared for
U.S. Department of Energy
Assistant Secretary for Fossil Energy

Thomas Reid, Project Manager
Bartlesville Project Office
P.O. Box 1398
Bartlesville, OK 74005

Prepared by
Stanford University
088 Green Earth Sciences
Stanford, CA 94305-2220

Abstract

Steam injection is the most widely used thermal recovery technique for unfractured reservoirs containing heavy oil. There have been numerous studies on theoretical and experimental aspects of steam injection for such systems.

Fractured reservoirs contain a large fraction of the world supply of oil, and field tests indicate that steam injection is feasible for such reservoirs. Unfortunately there has been little laboratory work done on steam injection in such systems. The experimental system in this work was designed to understand the mechanisms involved in the transfer of fluids and heat between matrix rocks and fractures under steam injection.

Fine grid simulations, where both the fracture and the matrix systems were represented by grids, were used to study the effects of certain flow parameters. Among the fluid flow properties investigated, water-oil capillary pressure of the matrix and gas-oil capillary pressure of the fracture were found to have the strongest effect on oil recovery. Matrix gas-oil capillary pressure and fracture water-oil capillary pressure had little effect. Matrix and fracture relative permeabilities also had little effect on recovery.

Experimental design involved the use of both simulations and analytical heat transfer models. Steady state and transient heat transfer models were used to calculate heat losses to determine insulation thickness. Simulations were also used to determine thermocouple locations, maximum expected pressure in the system and injection rates.

Two phase, continuous steam drive experiments were performed on systems containing water, at differing rates, injection temperatures and back pressures. Saturation distributions, temperature distributions and heat fluxes were measured. The saturations were measured in-situ, both in the fractures and the consolidated rock matrix, by a CT scanner. The results indicated that steam does not enter the matrix, and prefers to flow in the fracture. The matrix is heated by conduction. Cyclic steam injection experiments showed the same results; steam saturation did not develop in the matrix.

Numerical simulations were used to model both continuous and cyclic steam injection experiments. To model experimental heat losses, heat loss models in the simulator had to be adjusted, based on analytical models. The results from the solution using a variable temperature inner boundary condition, and a convective outer boundary condition, showed good agreement with the experiments and heat transfer coefficients were incorporated into the simulator. After this adjustment, the results from the simulations agreed well with the experiments. Complete matches were made to the heat losses, temperatures and saturations.

Same numerical simulator was used to simulate a case with no external heat losses from the fracture-matrix system. This mimics the process in the field. No steam saturation developed in the matrix. However, when pressure cycling was simulated with no heat losses, matrix steam saturation did develop. This justifies the application of cyclic steam injection in fractured reservoirs, and pinpoints the need to modify any future laboratory work to minimize heat losses from the fractures.

Finally, simulation runs were performed for the laboratory system with oil present. The results were similar to the steam-water experiments. Steam only flowed in the fracture. Oil recovery was found to be mainly due to water imbibition, and conduction was the dominant heat transfer mechanism. When cyclic steam injection was simulated with no external heat losses, steam saturation did develop in the matrix; however, the oil recovery was similar to the case with no cycling, showing that water imbibition was the dominant recovery mechanism.

Contents

List of Tables

List of Figures

Chapter 1

Introduction

Fractured reservoirs are estimated to contain 25-30% of the world supply of oil. Many of these reservoirs contain heavy oil or tar that can only be recovered by a thermal recovery technique. For viscous crudes and tars, steam is by far the most widely used and the most successful technique. Field test results indicate that steam injection has good potential for fractured reservoirs. Fractures can also be created artificially during steam injection into reservoirs containing viscous crudes and tars. Physical processes taking place during steam injection should be understood thoroughly, and reliable models should be developed, for effective and economic recovery of oil from fractured systems.

Most of the theoretical and experimental work done on fractured reservoirs has been on isothermal processes. The numerical models developed for thermal processes are generally extensions of models for isothermal processes. The developed models have generally not been validated against experimental data. The limited experimental studies lack detailed measurements, especially temperature and saturation distributions in the fracture and matrix.

This work aims at understanding the physical processes in fractured systems by providing good experimental data.

Chapter 2 summarizes the previous work related to different aspects of steam injection in fractured systems, including field cases, theoretical and numerical studies, and experimental work. Previous CT applications on core characterization and flow

experiments are also reviewed.

Chapter 3, discusses fine grid simulations used to study the sensitivities of some flow parameters. These include capillary pressures in the matrix and fracture, and relative permeabilities.

Chapter 4 discusses fine grid simulations used to design the experimental model, and to determine some operating parameters such as injection rate and pressure. Expected heat losses from the model are determined by analytical heat transfer models, to help determine the necessary insulation thickness.

The experimental apparatus is described in Chapter 5. It gives details of the core holder, and fluid injection and production systems. It also describes the temperature, heat flux and pressure measurement system, together with data acquisition.

Chapter 6 discusses the measurement of certain core properties such as porosity and permeability using various methods. The procedure to measure porosity by CT scanner measurements is also described in this chapter.

The procedures used in the experiments are given in Chapter 7. The results are described for runs at different operating conditions, varying steam injection rate, injection temperature and back pressure. Techniques followed to process the CT images and reduce artifacts are also given in this chapter.

Chapter 8 gives a detailed analysis of experimental results. The analysis involves both analytical and numerical models. Different heat loss models in the simulator are reviewed. Analytical models, together with the simulations, helped in modeling heat losses. We also present history matches of saturations, temperatures and heat losses.

Cyclic steam injection in fractured systems is discussed in Chapter 9. We show both experimental and simulation results compared with the results from a case with no heat losses.

The analysis is extended to a system with oil present in Chapter 10. The calibrated simulator is used to investigate the physical mechanisms taking place during steam injection with oil present. The simulations are done for both conventional steam drive and cyclic steam injection.

The final chapter of the dissertation is Chapter 11, which gives conclusions obtained from this work and recommendations for further studies.

Appendix A lists the equipment used in the experiments with the addresses of the manufacturers. The listing of the data acquisition software used in the experiments is given in Appendix B, along with a short explanation of its use. The problems due to the inversion of Stehfest Algorithm are discussed in Appendix C.

Chapter 2

Literature Review

This chapter contains a literature review on the various aspects of steam injection in fractured systems. The chapter is organized in four sections. The first section describes field applications of steam injection in fractured systems. The second section summarizes previous theoretical and numerical work on steam injection in these systems. The third section gives a summary of the limited experimental work done previously, and finally, the use of CT scanners is discussed for both core characterization and fluid saturation measurements.

2.1 Field Applications

The interest in steam injection for fractured systems started almost a decade ago, since steam injection is the most feasible recovery technique for heavy oils and tars. Dillabough and Prats [25] described the design of a pilot to test a new recovery process for the crude bitumen in the Peace River tar accumulation in Western Canada. The recovery process was developed by scaled laboratory experiments and field tests. It involves a period of conventional steam drive, followed by pressurization and blowdown cycles, to achieve the optimal recovery of the crude bitumen. This process was chosen, instead of conventional steam drive, since steam tended to channel through a high mobility water zone which acted like a fracture. This process was found to be

successful based on results of the laboratory experiments and field tests. We investigated a similar type of process in the laboratory and by numerical simulation in this work, as described in Chapter 9.

Sahuquet and Ferrier [71] described a steam-drive pilot in Lacq Superieur field in the Southwest of France. The reservoir was a highly fractured carbonate and contained oil of 20° API. The best recovery technique was selected by analyzing the results from laboratory experiments done with core samples from the field. Among the three different recovery techniques studied: water, hot water and steam injection; steam injection proved to be the most successful. They reported a recovery of 68% of OOIP with steam injection, compared to a 13% recovery with natural imbibition, and a 9.5% additional recovery with hot water drive. Since their aim was to decide on the technique giving the most recovery, they did not report any temperature or saturation measurements, or even whether any measurements were made. However, they mentioned that at the end of the experiment the entire model was at the steam temperature.

Their pilot design, based on the experimental results, was successful; and the heat transfer was efficient, without early heat breakthrough. They believed that heat conduction smoothed the temperature profile between the fracture and the matrix. The results from the pilot were interpreted by a thermal stream-tube model. This pilot proved that steam injection can be an effective recovery technique for a highly fractured system and the pilot was extended fieldwide.

Britton et al. [10] developed a new in-situ steamflood method they called the FAST process (Fracture Assisted Steamflood Technology), and tested the method in a South Texas tar sand deposit containing a viscous tar of -2° API. The first phase of the process consisted of horizontally fracturing the production wells and stimulating them with high pressure steam. The horizontal fracture extended from the injection well to the producers, and steam was injected at high rates and pressures to hold the fracture open and to preheat the formation (fracture preheat phase). During the second phase, the injection rates and pressures were reduced to promote matrix steam injection and displacement of the liquid tar to the producing wells (matrix steam injection phase). In the final stage, the produced water was mixed with fresh

water and recycled through the reservoir (heat scavenging phase). The results of the pilot showed that horizontal fractures were efficient in mobilizing the tar. The post pilot core analysis indicated an average recovery efficiency of more than 50%. This pilot was interesting and different from the others in the sense that fractures artificially created a flow path for steam so that conduction heating could mobilize the viscous tar.

Stang and Soni [80] described a second FAST process pilot test in Saner Ranch, Maverick County, Texas. The reservoir contained tar ranging from -2 to 3° API gravity. The pilot test showed that a major portion of the reservoir can be heated in a reasonable time with the help of the horizontal fracture created artificially. Recovery was 40-45% of the OOIP. The performance of the pilot was numerically modeled. The objective was to develop a technique to predict flood performance of future potential applications, and to help understand the dominant flow mechanisms in the process. The fracture was modeled by assigning individual blocks to it. A match was obtained for the tar production, and temperatures and pressures. Modeling studies showed that flow through the horizontal fracture was the most important factor affecting the performance.

Closmann and Smith [15] reported an interesting study on analysis of the temperature measurements taken above and below a horizontal fracture in Athabasca tar sands. These field measurements were used to estimate the thermal properties of the formation and also provided information on the possible changes in the heat and fluid flow paths. The temperatures measured below the fracture plane were modeled using the one-dimensional heat conduction equation. To model the thermocouple temperatures above the fracture, a moving heat source solution was used successfully. Numerical simulations were also used to model the vertically rising steam zone. Simulation results were in fair agreement to the measured data. This study was important since it validated both the numerical simulation and the analytical models using field data.

Duerksen et al. [28] described a cyclic steam injection pilot in Cold Lake. Steam had to be injected above fracturing pressure to achieve the required injection rate. A fracture system was created from northeast to southwest. The recovery was 6.3% of

the OOIP. They used a fractured reservoir simulator to study cyclic and steam drive responses. The fracture system was modeled as an extended wellbore. They did not mention how they handled the fracture as a wellbore. Field observations and predicted values for oil production and steam-oil ratio (SOR) showed qualitative agreement in the early cycles for some of the wells. Differences were more significant in the later cycles with predicted oil production being much lower than actual production. This was due to a change in the fracture orientation, which occurred in the field but was not considered in the numerical model.

The initiation of a steam pilot in Vallecupa oil field in Italy was described by Chierici et al. [14]. The reservoir is a fractured carbonate, and the oil has an API gravity ranging between 16-26° API. The paper talks about the reservoir studies done, drilling and testing of the pilot wells, the characteristics of the surface facilities and the startup phase of the pilot. To evaluate the efficiency of the steam injection process in this field, hot-water flooding tests were performed on laboratory cores at various temperatures. The experiments were quite simple since their aim was to see how the residual oil saturation would change with hot water injection. They observed that residual oil saturation decreased with increasing temperature. They did not report any monitoring of temperatures or saturations in their core floods. The reduction in oil saturation was sufficient to conclude that steam injection would be a successful recovery technique for this field.

Couderc et al. [20] studied a steam pilot in Emeraude field in offshore Congo on the West African coast. The reservoir is very heterogeneous with siltstones and fractured compact limestones. The oil has a viscosity of 100 cp at reservoir conditions. The purpose of the steamflood was to circulate steam in fractured limestone beds, and with the help of vaporization, thermal expansion and oil viscosity reduction, to expel the oil from the siltstones. Some hot-water and steamflood experiments were conducted in the laboratory. These experiments were done in homogeneous siltstone cores instead of fractured cores. They were used to determine the amount of oil that could be expelled from the siltstone by thermal expansion and vaporization. Steamflooding was also done on the same type of core, and the recovery reached 84.5% of OOIP.

Based on the promising experimental results, two steamdrive five spots were started for a field pilot test. After three years of steam injection, the recovery rate was good. Numerical simulations were used to interpret the results from the pilot.

Reis [69] studied the induced fracturing in two heavy oil reservoirs in California due to cyclic steam injection. The first reservoir was shallow and consisted of unconsolidated sandy conglomerate. The fractures formed, due to steaming, were complex with multiple fractures opening and closing over a period of days. No model could be developed for this operation.

The second reservoir was deeper and was consolidated. Two vertical fractures were opened in this reservoir and stayed open. A simple linear one-dimensional heat conduction model was developed and the measured field data were successfully matched. The model assumed that the fracture instantly heated to the steam temperature and remained there. The heat transferred from the fracture to the matrix was modeled as a finite width, isothermal band along the fracture at steam temperature. The width of the band determined the distance the thermal energy moved in the matrix by condensed steam. The matrix away from the fracture was heated by conduction and the width of the band served as a history matching parameter. This study was important in the sense that it showed that heat conduction was the crucial mechanism for heating the matrix, and field measurements confirmed this. The temperatures measured by a thermocouple in an observation well matched well with the temperatures calculated from the conduction heat transfer model.

Hartemink et al. [38] used reservoir simulations to investigate the design and future interpretation of a steam pilot in Quarn Alam field in Oman. The objective was to test the steam-enhanced gas-oil gravity drainage of the heavy oil remaining in the fractured carbonate reservoir. The locations of the injectors and observation wells were chosen by using the results of the simulation study.

During the last decade, there have been several applications of steam injection in systems with both induced and natural fractures, and most of the applications were successful or promising. However, numerical studies, and especially experimental studies, are scarce. In fact, most of the decisions for these pilots were made by looking at the results of simple conventional laboratory tests on mostly homogeneous cores

and with few measurements. Numerical and theoretical studies on steam injection in fractured systems will be described in the next section.

2.2 Theoretical and Numerical Studies

Interest in modeling heat and fluid transfer in formations having high permeability streaks or fractures started in 1960's with the use of thermal recovery methods for heavy oils and bitumens. Thomas [82] presented a mathematical model for conduction heating of a formation with limited permeability. He assumed that heat is introduced by a noncondensable gas through a horizontal fracture. Heat transfer from the fracture was assumed to be by vertical conduction, and heat transfer by convection was neglected. Thomas [82] presented an example calculation for this process in an oil shale. Based on the distance moved by the isotherm, the volume of rock heated and the oil recovered were estimated. An example calculation was presented, but because of the lack of experimental data, the model was not validated.

Lesser et al. [54] formulated a similar model to represent the conduction heating of a rock with no permeability. A hot condensing gas was introduced through a horizontal fracture. The model consisted of one heat equation for the matrix, and heat and fluid flow equations for the fracture. Temperature histories were obtained by finite difference solutions for both fracture and matrix. The model was applied to heating of oil shale. They investigated heating rate effects of shale thermal diffusivity, fluid pressure in the fracture, and fracture spacing. A higher injection pressure resulted in a slower heating rate. Doubling the thermal diffusivity of the formation resulted in a more rapid rise in the formation temperature. Decreasing the fracture spacing caused an improvement in the heating rate. Again in this study, an application of the model was shown for the oil shale heating by steam injection, but no temperature data were available to compare with the model.

Abdus Satter [2] developed a model for conduction heating of reservoirs by steam injection. The model is different from Thomas' method, since the steam injection process is also considered after the steam breaks through to the producers. Equations are given to determine the temperature distribution in the reservoir after steam

injection has stopped. He investigated the effects of parameters such as injection rate, temperature, pay thickness and well spacing. An example calculation based on arbitrary data was given to show the application of the model. His model also was not verified against measured data.

All of the models described above only considered conduction in the formation, convection was neglected. Wheeler [89] developed three analytical solutions to model the heat transfer from the fractures to the matrix, by taking into account the effects of both conduction and convection in the reservoir, and heat loss to the overburden. The validity of the model was demonstrated by matching the numerical solution developed by Lesser et al. [54]. Applications of these solutions were presented to determine the fracture orientation from field temperature measurements.

Another analytical model that describes the conductive heat transfer from a fracture to the reservoir was developed by Satman [75]. He also assumed equally spaced horizontal fractures. Only the conductive heat flow from the fracture to the matrix was considered, and there was no heat loss from the matrix to the surrounding media, which restricted the application of this model in systems where heat losses are significant. As a practical application of this model, he showed the amount of heat that can be extracted from a geothermal reservoir as a result of reinjection. The validity of the model was tested against temperature distributions measured in an observation well during a reinjection field test. No examples were given on the applicability of this model for steam injection in fractured oil reservoirs.

van Wunnik and Wit [83] developed a more detailed analytical model to study the improvement of gravity drainage by steam injection in a fractured reservoir containing heavy oil. Models were developed for the mixing of the steam and the hydrocarbon gas, the temperature distribution in the caprock and the reservoir, and oil production by thermal expansion and gravity drainage. The models were applied to the Qarn Alam reservoir in Oman, which is a densely fractured chalk formation containing a moderately heavy oil. The results from the models showed that this reservoir can be a good one for steam injection.

Recently, Pooladi-Darvish et al. [65] studied steam injection into a single block of a naturally fractured reservoir, and analytical solutions were given for heat flow

and non-isothermal gravity drainage from the block. They neglected convection and assumed that heat conduction is the only heat transfer mechanism from the fracture to the matrix. The analytical solutions were compared to numerical solutions. No experimental measurements were available to support the validity of their model.

The work described above involved mostly analytical models, for the heat transfer from a fracture to surrounding matrix blocks, or the behavior of a single matrix block. Field scale modeling of fractured reservoirs undergoing steam injection evolved with the development of dual porosity and dual permeability models.

Geshelin et al. [34] presented a unique numerical study on the transport of injected and reservoir water through fractures induced during steam stimulation of tar sands and heavy oil deposits. Fractures created during the stimulation process acted as channels through which injected fluids flowed. The heat was assumed to be transferred from the fracture to the matrix by convection and conduction. The rate of fluid transfer from the fracture to the surrounding block was a function of the shape factor and the pressure difference between the fracture and the surrounding block. The shape factor was estimated by assuming a single narrow fracture instead of the double porosity assumption. The fracture model developed was incorporated into a conventional thermal simulator. Several steam stimulation runs were performed to analyze the behavior of the model. The model was not validated with any measured data.

Pruess and Narasimhan [66] presented a multiple interacting continua model (MINC), to simulate the heat and two-phase flow of steam and water in multidimensional fractured porous media. The flow domain was partitioned to computational volume elements by assuming thermodynamic equilibrium in each element. Transient flow of fluid and heat between the matrix and the fractures was treated numerically. The model was verified by comparing it with the analytical solution given by Warren and Root [87]. The model was applied to different problems in geothermal reservoir engineering, such as, flow to a well penetrating a fractured reservoir with low matrix permeability, boiling depletion of a fractured geothermal reservoir, and production and injection in a fractured geothermal five-spot pattern.

Lee and Tan [53] developed a multiple porosity/permeability thermal simulator for

fractured oil reservoirs. The simulator was different from the dual porosity simulators, for it allowed the linking of any pair of grid cells for the transfer of mass and energy. The matrix domain can thus be divided into two or more domains and linked to each other as well as to the fracture domain to define imbibition, drainage and heat transfer mechanisms. The heat transfer between the fracture and matrix was determined by an interporosity heat transfer coefficient which includes a shape factor and the thermal conductivity. The simulator was validated against simple isothermal analytical radial models.

After validation, the recovery mechanisms were simulated for steam-assisted gravity drainage of a dual-porosity, dual permeability heavy oil reservoir. This example was a fictitious field case to observe model behavior. The results showed that oil moved from the matrix to the fracture, by the interporosity transfer coefficients, as a result of thermal expansion and steam drive.

Chen et al. [13] developed a three-dimensional three-phase compositional simulator for steam injection in fractured systems. The matrix blocks were represented by cylinders, and, to represent the transient behavior in the matrix, it was divided into several matrix cells in the r-z directions. This was done to minimize the cost of discretization of the matrix. Matrix/matrix flow was not permitted between adjacent grids. The fluid and energy flow between the matrix and the fracture were described by an expression defining the cell dimensions used in the division of the matrix into several cells, and the potential difference between the matrix and the fracture. No comparisons with measured data were given. The simulator was used in an example case to investigate the sensitivity of oil recovery prediction to the discretization of the matrix block, the size of the matrix blocks and the capillary pressures. The results showed that matrix block should be discretized both radially and vertically to properly model the fluid and energy transfer between the matrix and the fractures. Matrix block size affected the oil recovery, and the rate of heat transfer between the matrix and the fracture was important in oil recovery.

Pruess and Wu [67] handled matrix-fracture flow by an analytical approach in their simulator which used the MINC formulation. The method combined a finite difference description of global flow in the fracture with an analytical representation

of interporosity flow by means of trial functions for fluid pressures and temperatures in the matrix blocks. These trial functions contained parameters which were calculated using simple mass and energy balances for each time step based on the matrix block shapes and dimensions. The method used was an extension of the technique developed by Vinsome and Westerveld [85] and it was validated against exact analytical solutions for fluid and heat exchange from individual matrix blocks.

A unique approach to modeling of heat and mass transfer in fractured systems is that of Mukhopadhyay and Sahimi [59]. They developed two and three dimensional fractal and non-fractal networks of interconnected fractures, as models of a fractured geothermal field, and studied two-phase flow and heat transfer in such systems. The reservoir was modeled as a set of interconnected fractures through which fluids flow. The fluids in the fracture do not flow into the matrix and the communication is only through heat transfer. No validation of the model was presented. Only the application of the model to a fictitious geothermal problem was given.

The studies described so far were mostly about different ways of modeling the processes in steam injection in fractured systems, both analytically and numerically. The applications of simulation and different analytical models to various aspects of steam injection processes in fractured oil reservoirs will be summarized next.

The applicability of steamflooding for carbonate reservoirs was summarized by Nolan et al. [60]. Carbonate reservoirs are generally very heterogeneous and the bulk of the matrix permeabilities are very low with fractures providing most of the conductivity for fluid flow. Heat conduction from the fluids moving in the high permeability channels heats the matrix and helps the oil to be expelled from the matrix. They conducted a series of laboratory experiments to compare the oil produced by this conductive heating mechanism. However, in the experiments they used homogeneous sandstone cores instead of the fractured carbonate cores. They justified their use of sandstone instead of carbonate by stating that the relative permeabilities are similar. No justification was given for using homogeneous cores instead of fractured ones. They also used a numerical simulator to analyze the sensitivity of certain parameters for steamflooding. A physical model, consisting of a homogeneous sandpack, was used to verify some of the heat scavenging results obtained from simulations. The

production data, and the temperature and pressure histories of the experiments, were in qualitative agreement with simulations. Both experiments and simulations showed that heat scavenging by pressure drawdown can improve the steamflood performance, for production continued even after steam injection was terminated.

Abad and Hensley [1] used a single-phase thermal simulator to investigate the applicability of steam flooding in differing reservoir geometries such as dipping and fractured reservoirs. They used a single porosity simulator, and a fracture was simulated with high permeability grid blocks. The physical properties used were those of fluid saturated California sandstones. Since the simulator was single phase, total heat and fluid production were calculated without quantifying the individual phases. The injected fluid and the reservoir fluid were distinguished by defining their physical properties such as density, viscosity and heat properties. The results of the simulations showed that fractures improved the sweep efficiency, however, most of the injected heat was produced through the fractures, so heat utilization was lower when the reservoir was fractured. Up to 80% of the injected heat could be produced through the fractures.

Lin [56] developed a fracture propagation model for cyclic steam stimulation by modifying a conventional thermal simulator. Fracture propagation kinematics, and heat transfer between the fracture and the reservoir, were included in the model. The model was validated by comparing the results to the results obtained from a different fracture simulator. The reservoir description and the fluid properties of a typical fictitious heavy oil reservoir were used for sensitivity studies, and simulations were done to investigate the effects of certain operating parameters. Two different simulation studies were conducted, a single well stimulation process and a four well pattern, to study fracture characteristics. The results indicated that in a single-well stimulation, a lag time existed between the beginning of injection and the reopening of the fracture and the recovery efficiency increased with the steam slug size and the steam injection rate. The four well pattern simulation showed that well interactions greatly affected the process mechanisms such as fracture propagation.

Briggs [6] described a simulator developed to predict the performance of cyclic steam injection for fractured carbonate reservoirs containing heavy oil. The model

used a simplified approach by combining analytical and numerical techniques. It assumed a system consisting of cubic matrix blocks surrounded by fractures. Flow of steam and condensate was in the fractures only, as is the case for double porosity models, and the heat transfer to the rock matrix was only by conduction. The temperature of the matrix blocks and the heat lost to the surrounding formation were obtained by an approximate solution to the heat conduction equation. The exchange of fluids between matrix and fracture were due to thermal expansion and countercurrent imbibition. The simulator was used to match a field case, but the results were not reported. Several sensitivity studies were done with the simulator. Small matrix blocks and high matrix permeabilities both showed faster recovery. A higher matrix porosity caused lower recovery, and larger fracture porosity increased the recovery. Steam soak times did not affect the recovery. Higher injection rates showed better recoveries. Performance improved with larger steam slugs. Steam pressures did not affect the recovery.

Jensen et al. [46] developed a numerical model to analyze their experimental results, and also to investigate the recovery mechanisms and to perform sensitivity studies. The model was a two-dimensional, three-phase, single porosity, thermal simulator. The fracture was modeled by using a fine high permeability layer. It extended along the length of the core and 8 grid blocks were used in the flow direction. However, the grids adjacent to the fracture were coarse, and they did not report any of the effects of grid size in their simulation studies. They presented different history matching cases for waterflooding and steamflooding in homogeneous and fractured cores. They only matched the average oil saturations, and did not match the temperature or steam saturation distributions. They also performed sensitivity studies on some parameters. Higher rates gave higher recoveries for steam injection. More oil was also recovered with a higher system pressure. The effect of fracture aperture was not found to be significant. Matrix permeability was found to be an important parameter affecting the rate of oil release from the matrix. The effect of oil-water capillary pressure on recovery was positive, due to capillary imbibition. The effect of fracture capillary pressure was not investigated, even though it can be an important parameter affecting recovery from fractured systems.

Oballa et al. [62] outlined different fractured reservoir models for their applicability to thermal recovery. They investigated how the type of fractured media model used affected the predicted results. Different dual porosity formulations, like MINC and vertical refinement models, and the dual permeability formulations, were implemented in a thermal simulator. They compared the results from these models with published data. Several cases were simulated. The effects of different fracture and matrix properties were investigated. Fracture permeability did not affect the results. Fracture water-oil capillary pressure decreased water imbibition. Gas-oil capillary pressure in the fracture increased gas flow to the matrix and increased oil recovery. These results were similar to what we observed by fine grid simulations that will be described in Chapter 3. Matrix permeability strongly affected the oil recovery. For a matrix with low permeability, depletion is slower and conductive heat transfer is more important. Matrix thermal properties were not found to significantly affect recovery. Water-oil capillary pressure of the matrix was the important parameter affecting water imbibition into the matrix, and increasing recovery. Heat conduction played an important part in the recovery process according to the simulation results.

None of the mentioned theoretical and numerical work on steam injection in fractured systems reported good experimental data to validate the models or to help understand the flow mechanisms. Unfortunately, not much experimental work has been done on steam injection in fractured systems. These are described in the next section.

2.3 Experimental Work

Dreher and Kenyon [27] flooded fractured carbonate disks with hot water and steam. They performed a series of flooding experiments at different temperatures and monitored the oil recovery. The only temperatures measured were at the inlet and outlet ports. They did not measure temperatures either in the core or in the fracture. The results showed that oil recovery increased with temperature. They then used simulations to model the process. However, they did not attempt to model and analyze their

experiments, but rather simulated a typical fractured carbonate reservoir and analyzed the results. The simulations showed that the matrix could be heated efficiently by conduction of heat from the fracture to the matrix. The effect of grid refinement in the matrix was also investigated, and the oil recovery was found to depend on the matrix grid block sizes. Steam injection rates and carbon dioxide generation also affected oil recovery.

Reis [68] summarized the recovery mechanisms for steam injection in fractured reservoirs. The most important recovery mechanism was identified as differential thermal expansion between the oil and the pores. Gas generation due to carbonate dissolution at high temperatures, and capillary imbibition were also important. Other mechanisms, like gravity drainage, solution gas drive, and distillation, were thought to be less important. He conducted very limited laboratory experiments on outcrop samples from different rocks of the Monterey formation in California, and on Berea sandstone. The amounts of oil expelled from these samples were measured at different temperatures. The samples were solid, not fractured, and only the amount of oil expelled was measured. The tests were not core floods but were conducted in a water filled autoclave kept at constant temperature. Oil recovery averaged 50% higher from the high temperature tests than from low temperature tests.

Jensen [45] studied steam flooding in fractured reservoirs both experimentally and numerically. He used fractured and solid Berea sandstone and carbonates from a Texas aquifer and from the Madison formation in Wyoming. Corefloods were performed by waterflooding followed by steam injection. Temperatures were only measured at the inlet and the outlet. He also mentioned that a thermocouple was located in the core, but its measurements were not reported. The average saturations were measured, both from production data and by weighing the sample. He investigated several parameters such as injection rate, fracture aperture, fracture orientation, and the type of oil used. The experiments showed that the recovery was due to water imbibition, decrease in oil viscosity and thermal swelling of fluids. Water imbibition was not a significant recovery mechanism for the carbonates since they were more oil wet. Gravity drainage and thermal expansion were important for these cores. He used a single porosity thermal simulator to history match the experiments. The fractures

were simulated by a fine single layer of high permeability grid blocks. He simulated both the waterflooding and steamflooding experiments for both fractured and solid cores. He only matched the average oil saturation in the core as a function of fluid injected, since there were not enough measurements on factors such as temperature in the fracture and matrix, and heat losses, for example.

Briggs et al. [7] presented some results from laboratory and simulation studies for steam injection into fractured carbonates containing heavy oil. The purpose of the work was to identify the recovery mechanisms. Their experimental work was mechanistic in nature. They used plugs cut from an outcrop of Permian Basin dolomite and live oil in experiments mimicking cyclic steam injection. They heated the core holder to a high temperature and monitored the oil recovery due to thermal expansion. Then brine was flowed to simulate countercurrent imbibition. The outlet end of the core holder was opened to the atmosphere, and depletion production was measured. The sequence ended with a hot water and steam flood. The test sequence was repeated at a higher temperature. The results indicated that imbibition played an important part in increasing the recovery, and that thermal expansion contributed little to the recovery. Since the aim of the experiments was to identify the relative importance of several mechanisms on the recovery, no temperature measurements were taken. No attempt was made to simulate their high temperature experiments, but their imbibition tests were simulated.

The experimental studies summarized above were quite limited and the measurements were mainly production data. Temperature measurements were not made and the heat losses were not monitored. Average saturations were calculated by material balance, so only average values could be obtained. It is obvious that good experimental data such as temperature and saturation measurements both in the fracture and matrix were needed to understand the processes taking place during steam injection in fractured systems.

Since CT measurements are an important part of this work, the next section of the literature review summarizes briefly the use of CT scanning as a tool for both core analysis and saturation measurements in the laboratory.

2.4 Computerized Tomography (CT) Applications

Computerized Tomography (CT) has been widely used as a core analysis and characterization tool. Bergosh et al. [5] discussed the application of a CT scanner as a fracture detection tool and also for quantifying fracture width and spacing, geometry, tortuosity, interconnectedness and drilling mud invasion. Honarpour et al. [40] characterized the reservoir rock by comparing X-ray attenuation values for different minerals resident in different cores.

Hunt et al. [44] conducted a detailed study comparing the advantages and disadvantages of various CT scanners. They discussed the application of CT scanners to quantify porosity and mineralogy. The correlation between CT data and permeability was also given. They also presented some artifact reduction techniques, and ways to handle beam hardening.

Kantzas et al. [49] quantitatively determined reservoir rock properties such as porosity, density and mineralogy. They developed density maps for the cores used, but did not report any of the porosity maps calculated. Instead, they reported the average porosities calculated from the CT numbers. There was good agreement between the average porosity and density values measured by the CT scanner and the values from conventional core analysis techniques.

Johns [47] measured the fracture aperture in a granite core by a second generation scanner. He developed a correlation between the CT numbers and the fracture aperture by calibrating the CT scanner for apertures between 0.075 and 3.875 mm. He then used the correlation to estimate the change of the fracture aperture along the fracture plane in a naturally fractured granite. His work was important, since he was able to estimate the aperture using only a second generation scanner with relatively large pixel sizes.

Peters and Afzal [63] developed a procedure to use CT measurements to characterize the heterogeneities in cores to be used in laboratory core floods. They used a sandpack in their experiments. In addition to the calculation of porosities and development of porosity maps; using streamtube calculations, they developed a technique to estimate permeabilities from CT measurements during a coreflood.

The use of a CT scanner to monitor fluid saturations in porous media will be discussed next by summarizing several studies done on this aspect. Quantitative measurement of fluid saturation by a CT scanner is more difficult than core characterization.

Cromwell et al. [21] studied the differences in CT numbers for Danian chalk and Berea sandstone when saturated with different fluids. They performed a set of displacement experiments using an iodine solution to displace mineral oil. They scanned the cores cross-sectionally and axially with a first generation CT scanner. They studied the saturation differences only qualitatively.

Wang et al. [86] used a second generation CT scanner to measure oil saturation distributions during immiscible flooding of Berea sandstone cores. The displacing fluid was potassium iodide solution. They plotted oil saturation maps calculated from the CT numbers as a function of time and location. However, they did not mention the procedure used to calculate two phase saturations.

Hove et al. [43] studied immiscible and miscible displacements in some North Sea sandstone plugs using a CT scanner. Images were taken in the direction of flow instead of perpendicular to the flow. The images were compared qualitatively, and no direct saturation calculations were made.

Wellington and Vinegar [88] used CT scanning to study the effect of foam for mobility control during carbon dioxide injection. They performed three phase displacement experiments with oil, water and gas and they also compared their CT images with the results calculated from a miscible simulator. The agreement was excellent. Even though they outlined a way to calculate three phase saturations by dual energy scanning for the first time, they did not report any quantitative saturation calculations.

The procedure to determine three phase saturations by CT scanners were outlined again in more detail in another paper by Vinegar and Wellington [84]. They discussed the choice of energy levels for dual energy scanning, and types of dopants. They used aluminum core holders since they are less dense than steel and cause fewer artifacts and problems during scanning. They applied the procedure that they proposed to a three-phase tertiary miscible carbon dioxide displacements in a Berea sandstone.

Withjack and Akervoll [90] constructed a rectangular core holder to study three-dimensional miscible displacement in a five-spot model. The porous medium consisted of glass beads, and displacement of oil by solvent flooding was monitored by CT scanning. The displacement was observed visually by three-dimensional image reconstructions. The images showed that viscous fingering was more significant in three-dimensional displacements than in two-dimensional displacements. Secondary fingers formed in the overriding tongue.

Chatzis et al. [11], using a CT scanner, qualitatively monitored the saturations during nitrogen injection in a Berea core saturated with oil and brine. They calculated the average CT numbers at different times for each slice as a function of position along the core.

CT scanners are not used widely in high temperature experiments due to the restrictions on core holder material. Sedgwick and Miles-Dixon [76] used a CT scanner to measure high temperature relative permeabilities of bitumen and water in a sandpack. They used an aluminum core holder. The bitumen and water saturations were calculated by averaging the pixel data for the whole cross-section. This work is important since it is the first high temperature application of CT measurements.

Demiral et al. [23] used CT imaging for steam and steam-foam displacements in a three-dimensional sand pack. They reported the presence of artifacts even though they used an aluminum core holder and internal Teflon to isolate the porous medium from the core holder. They did not calculate steam saturations, but they reported comparisons for different displacement processes using raw CT data. Sharma [78] extended this work by conducting steam injection experiments in the presence of oil. He calculated the three-phase saturations by using the CT numbers at two energy levels. However, he mentioned that the aluminum core holder caused problems in the saturation measurements due to its high density.

MacAllister et al. [57] conducted a study on relative permeability measurements by a CT scanner. Oil/water and gas/water relative permeabilities were determined for a Baker dolomite core. All of the saturations were determined by a CT scanner.

Peters and Gharbi [64] conducted a series of corefloods on a sandpack by displacing mineral oil by a brine solution containing barium chloride. Saturation distributions

measured by the scanner were qualitatively matched with numerical simulations. Average water saturations compared well with simulations. After history matching, the numerical model was used to scale the results of laboratory corefloods to other systems.

Quadeer et al. [9] used a CT scanner to analyze the errors introduced when relative permeabilities are calculated by using conventional techniques. They performed two-phase oil-water imbibition and drainage experiments and measured the saturation distributions with time using the CT scanner.

In none of these previous CT applications, a fractured system was used, nor were saturations in the fracture and the matrix measured during steam injection. Such measurements require accurate artifact free measurements, which were not possible with the conventional metal core holders used in the previous high temperature work. We have designed and built a unique core holder, from a high temperature plastic, that allows us to quantify saturations in both fracture and the matrix under steam injection conditions.

This literature review shows that there is a need for experimental work on steam injection in fractured systems. Detailed saturation and temperature measurements should be done for both matrix and fracture so that previously developed numerical and analytical models can be validated and better ones can be developed. Furthermore more work is needed on the isolation of recovery mechanisms for steam injection in fractured systems.

This work provides experimental data for steam injection in fractured systems. Accurate and detailed experimental measurements were made possible by using fine grid simulations and analytical calculations in the experimental design. The experimental results were used to calibrate a numerical simulator. Further, the calibrated simulator was used to study and isolate the recovery mechanisms for both cyclic and continuous steam injection.

Chapter 3

Fine Grid Simulations

Before designing and building the experimental apparatus, fine grid simulations were used to study the effects of certain flow parameters and to determine the experimental design parameters. Simulations performed can be classified into two categories:

- Simulations for sensitivity studies of certain rock-fluid properties, such as water-oil and gas-oil capillary pressures of matrix and fracture systems, and their relative permeabilities.
- Simulations for the determination of experimental design parameters.

Sensitivity studies done for the rock-fluid properties will be discussed in this chapter. Simulations for the experimental design parameters will be described in Chapter 4.

3.1 Sensitivity of Rock-Fluid Properties

A commercial thermal simulator (Computer Modeling Group's STARS [17]) was used for these simulations. The parameters used in the simulations are given in Table 3.1. The physical properties of the core used in the simulations were the properties of the Boise sandstone used. A cross-sectional (x-z) grid system was used. Figure 3.1 is a schematic representation of the grid system. The fracture is represented with fine grids having a high permeability and unit porosity. Fracture permeability was

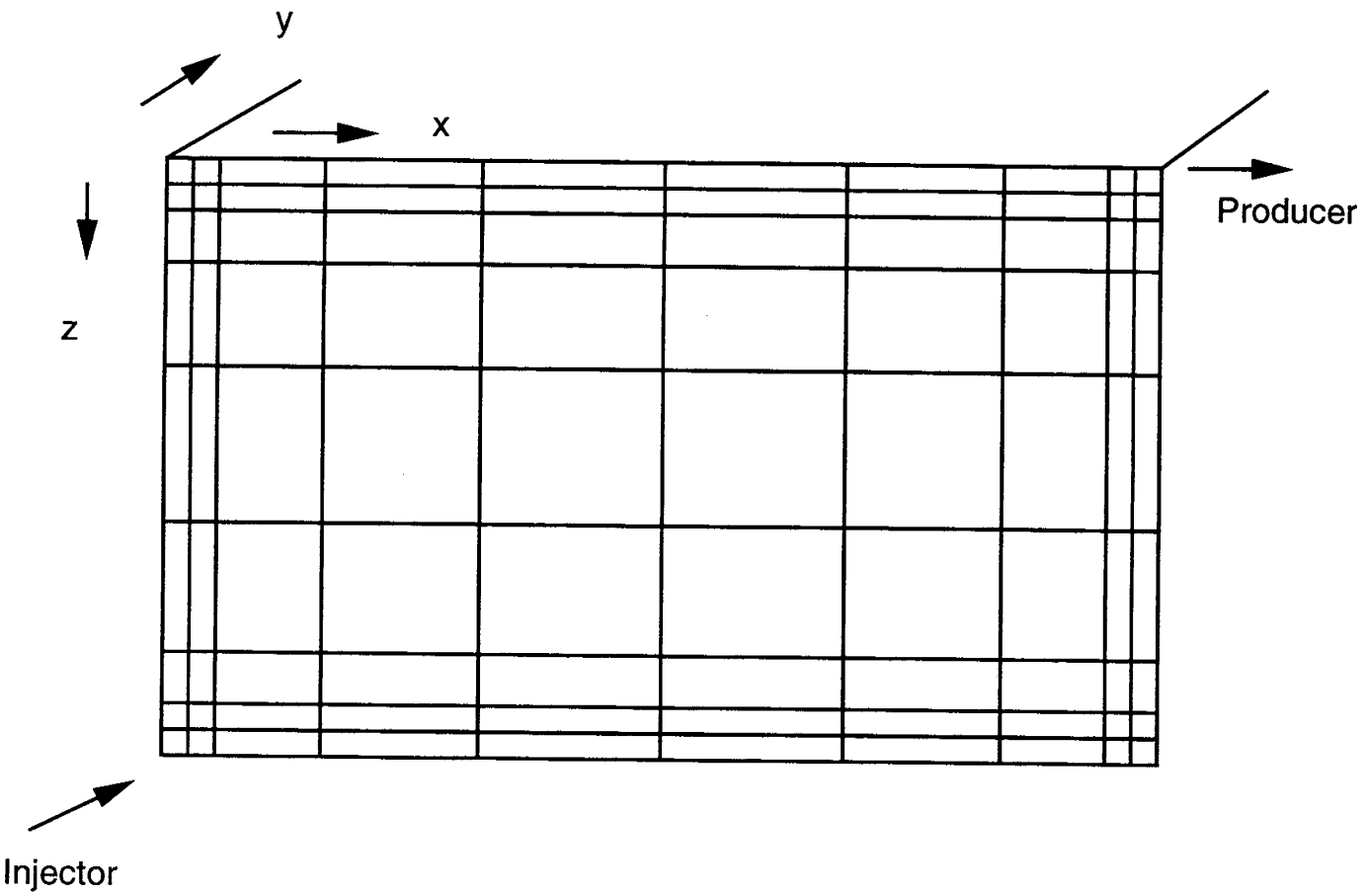

Figure 3.1: Schematic of fine grid system used in the simulations.

Table 3.1: Fine Grid Simulation Parameters

Matrix porosity, %	30
Matrix x-dir. permeability, md	900
Matrix y-dir. permeability, md	1400
Matrix z-dir. permeability, md	1400
Fracture permeability, md	84.4×10^6
Initial reservoir pressure, psia	25
Initial reservoir temperature, deg K	297
Initial oil saturation (matrix), fraction	0.8
Initial oil saturation (fracture), fraction	1.0
Steam injection rate (water eq.), cm^3/min	1.0
Production pressure, psia	20

calculated by using the equation given by Amyx et al. [3].

$$k = 8.44 \times 10^6 h^2 \tag{3.1}$$

where,

k = permeability, Darcys
h = width of the fracture, cm

The sizes of the grid blocks decrease as fracture is approached. Before starting the fine grid simulations, a sensitivity study was made on the effect of the number of grid blocks used in the simulation. The results justified the use of a $10 \times 1 \times 12$ grid system (Fig. 3.2). The grid system is two-dimensional with fractures surrounding the matrix on all four sides. The injector and producer are located parallel to the z-axis. The injector is completed at the bottommost layer and the producer is completed at the

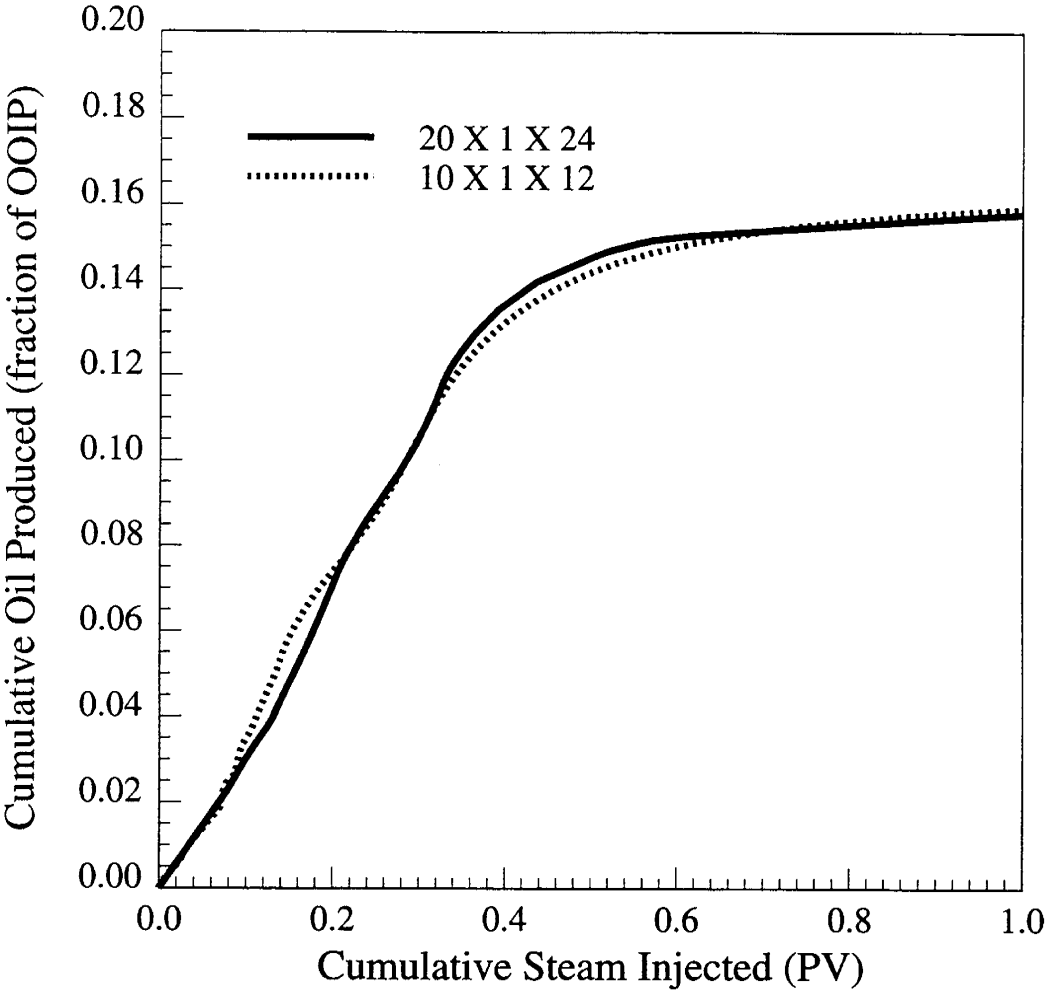

Figure 3.2: Grid size sensitivity.

topmost layer. They are located at the corners of the model in the vertical fractures. Initially the fractures are 100% saturated with oil, and the matrix has saturations of 80% oil and 20% water.

Three-dimensional simulations were also run to compare the results with the cross-sectional simulations. The grid system used was similar to the 2-D fine grid simulations, but the number of grid blocks in the y-direction was taken as three instead of one. Completion locations for the wells were same as the two-dimensional simulations. Figure 3.3 shows the comparison of three dimensional and two dimensional simulations in terms of cumulative oil produced as a function of cumulative steam injected. Saturation distributions (oil, steam and water) and oil recoveries were in close agreement, which justified the use of a two dimensional cross-sectional grid system for all subsequent sensitivity studies.

Sensitivity studies were done on the following flow parameters:

- Water-oil capillary pressure curve in matrix and in fracture.
- Gas-oil capillary pressure curve in matrix and in fracture.
- Oil-water and liquid-gas relative permeability curves in matrix and in fracture.

3.1.1 Effect of Capillary Pressure in Matrix

In the base-case simulation, water-oil and gas-oil capillary pressures of matrix and fracture were set to zero. Matrix capillary pressure curves in the study by Oballa et al. [61] were used in the sensitivity studies and are shown in Fig. 3.4.

When the water-oil capillary pressure of the matrix is set to zero, oil recovery is due to gravity only. However, when capillary pressure is greater than zero, condensed steam imbibes into the matrix and helps displace oil from the matrix. This effect significantly increases the oil recovery (Fig. 3.5).

Water and oil saturation maps at different times show the movement of water into the matrix and displacement of oil (Figs. 3.6, 3.7, 3.8 and 3.9). Note the scales of the x and z axes. Grid block numbers are used instead of the real dimensions in centimeters (20×10 cm). Visually, these maps tend to give the wrong impression about the sizes

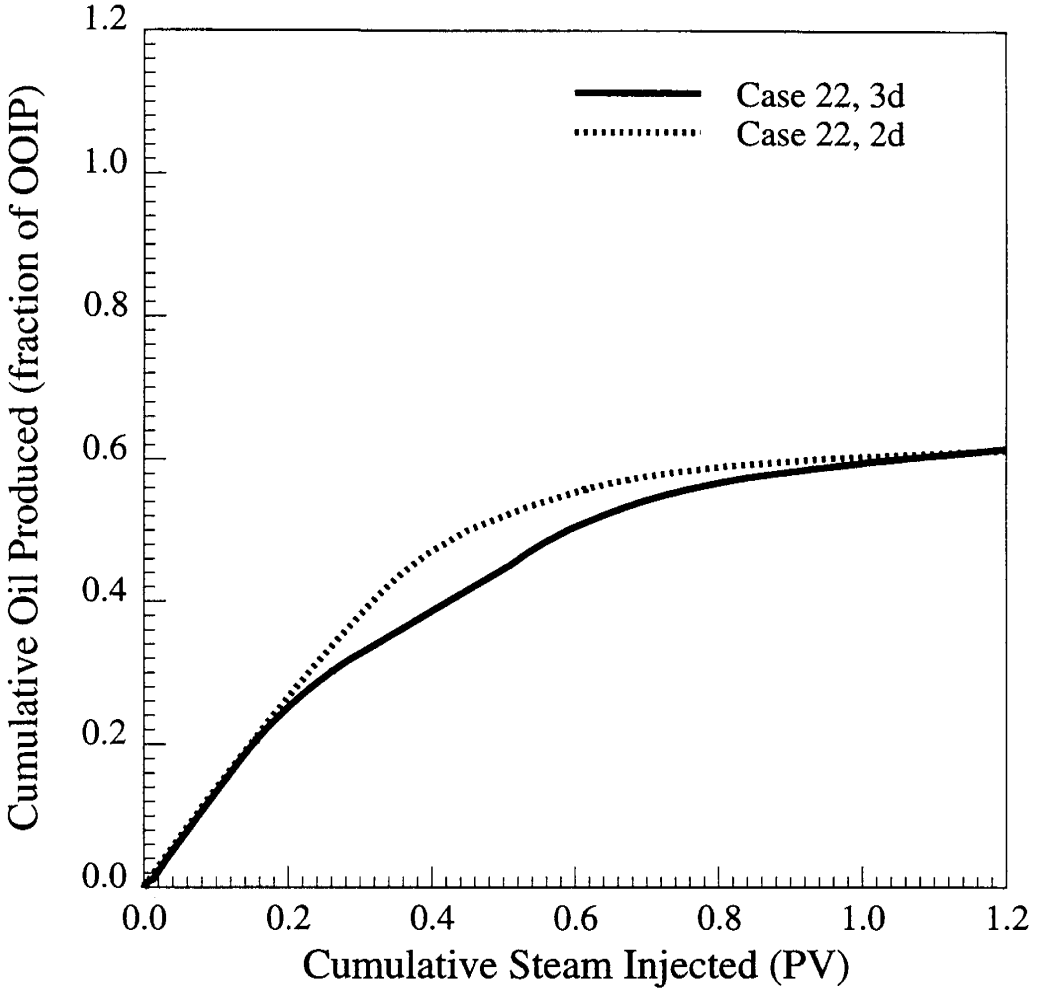

Figure 3.3: Effect of three dimensionality on the results.

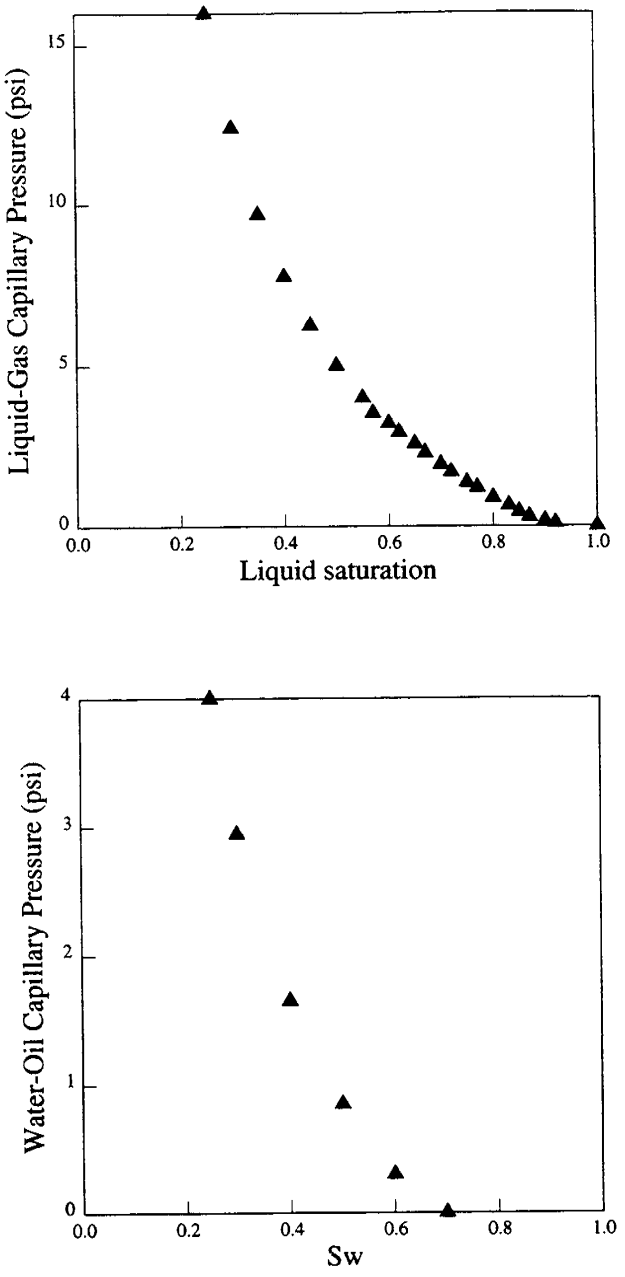

Figure 3.4: Matrix capillary pressure curves. Top: Oil-gas capillary pressure. Bottom: Water-oil capillary pressure.

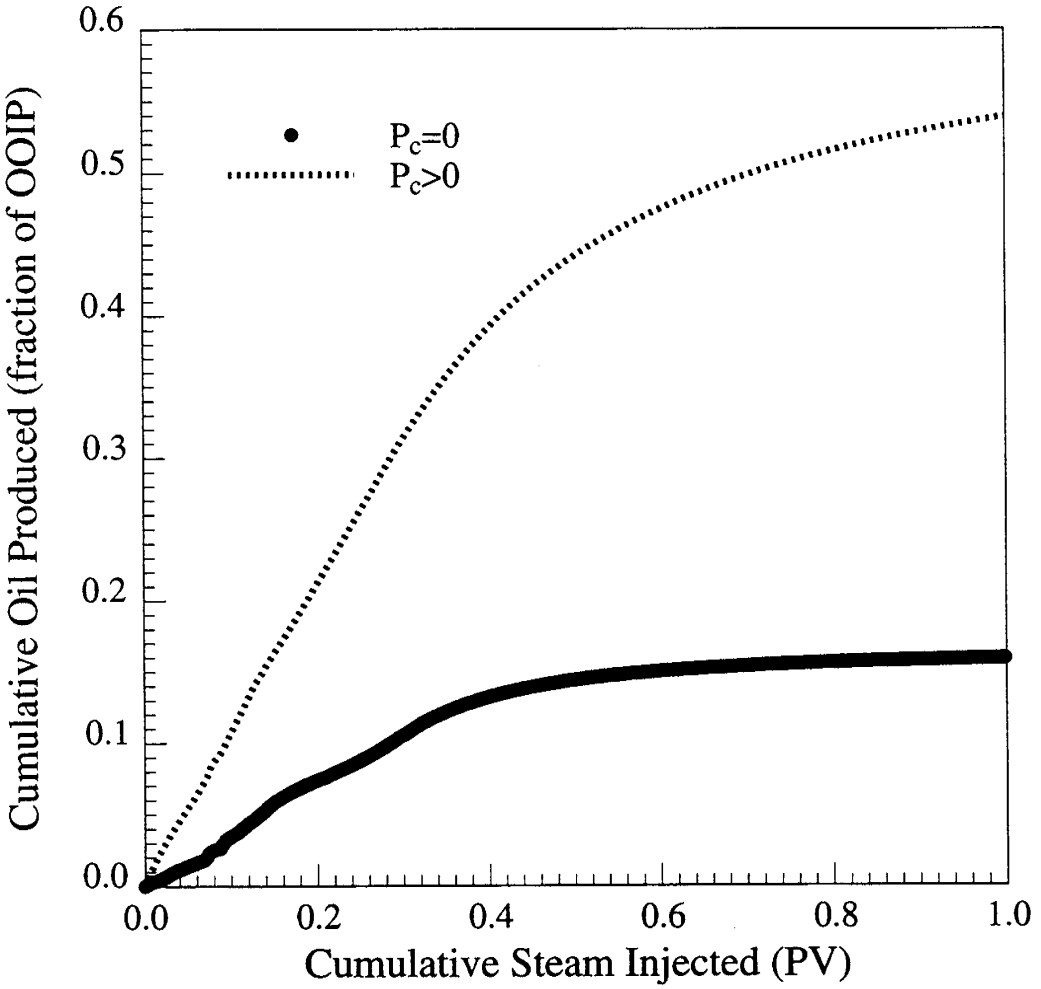

Figure 3.5: Effect of water-oil capillary pressure of matrix on oil recovery.

of the zones in and near the fracture. However, this method of presentation was found to be the best possible way of showing the changes at and near the fractures within the limitations of the plotting software. All further saturation and temperature map scales will be in terms of grid block numbers rather than the real dimensions.

At 0.3 pore volumes of steam injected, water saturation in the matrix started to increase as shown by the darker color in the matrix in Fig. 3.6b. The water saturation in the matrix is between 0.4 and 0.6 when water-oil capillary pressure is greater than zero. On the other hand, when there is no capillary pressure, the matrix water saturation stays at its initial value ($S_w = 0.2$). This is because there is no force causing water imbibition into the matrix. Oil saturation maps show a similar behavior (Fig. 3.7a and 3.7b). Oil saturation in the matrix decreases with time due to water imbibition displacing the oil. When capillary pressure is zero, only a very small amount of oil has been displaced from the matrix, the oil saturation in the matrix is virtually unchanged, and only the oil in the fracture is displaced. Steam saturation maps are not shown here due to their similar behavior for both cases. Steam only flows in the fracture, and goes immediately to the top fracture due to gravity. It is the condensed water from the steam that moves into the matrix to displace oil.

At a later time, 1.3 PV of steam injected, oil saturation in the matrix is reduced and water saturation is increased more for the nonzero capillary pressure case (Figs. 3.8b and 3.9b). Again there is little change in the matrix oil saturation when capillary pressure is zero, as can be seen in Fig. 3.8a. Only the oil in the fracture has been displaced.

These simulations showed that water-oil capillary pressure of the matrix has a positive effect on oil recovery, and water imbibition due to condensed steam can be an important recovery mechanism for steam injection into fractured systems.

By contrast, gas-oil capillary pressure of the matrix has no effect on oil recovery (Fig. 3.10). Steam only moves in the fracture, and the condensed steam does not imbibe into the matrix. Figures 3.11a and 3.11b show the water saturation maps at 1.3 PV of steam injected. Water saturations are the same for either zero or nonzero gas-oil capillary pressure. They both stay at the initial water saturation, confirming there was no imbibition into the matrix. Thus oil recovery is only by gravity from

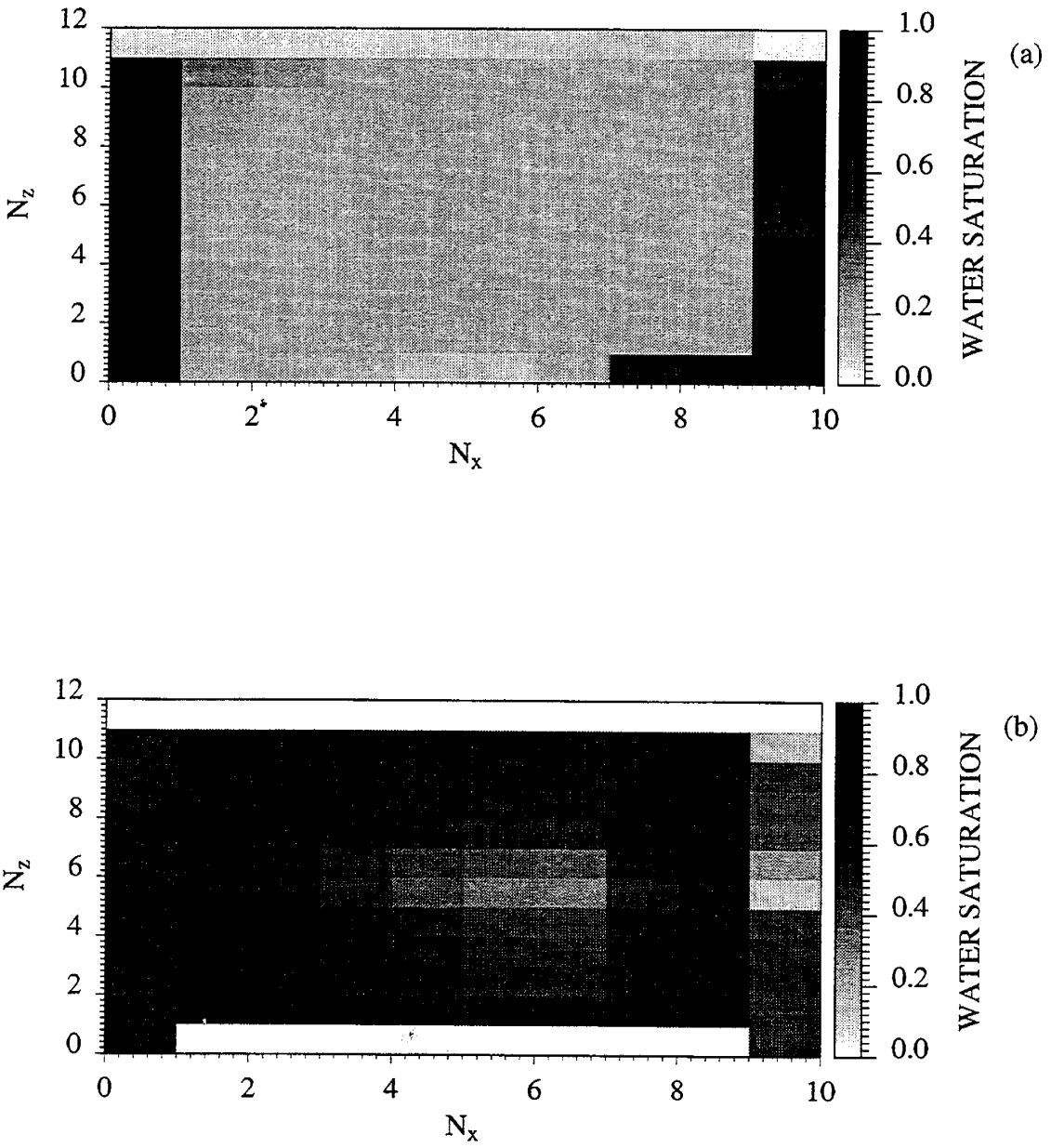

Figure 3.6: Water saturation maps at 0.3 PV steam injected. (a) Zero matrix water-oil capillary pressure. (b) Finite matrix water-oil capillary pressure.

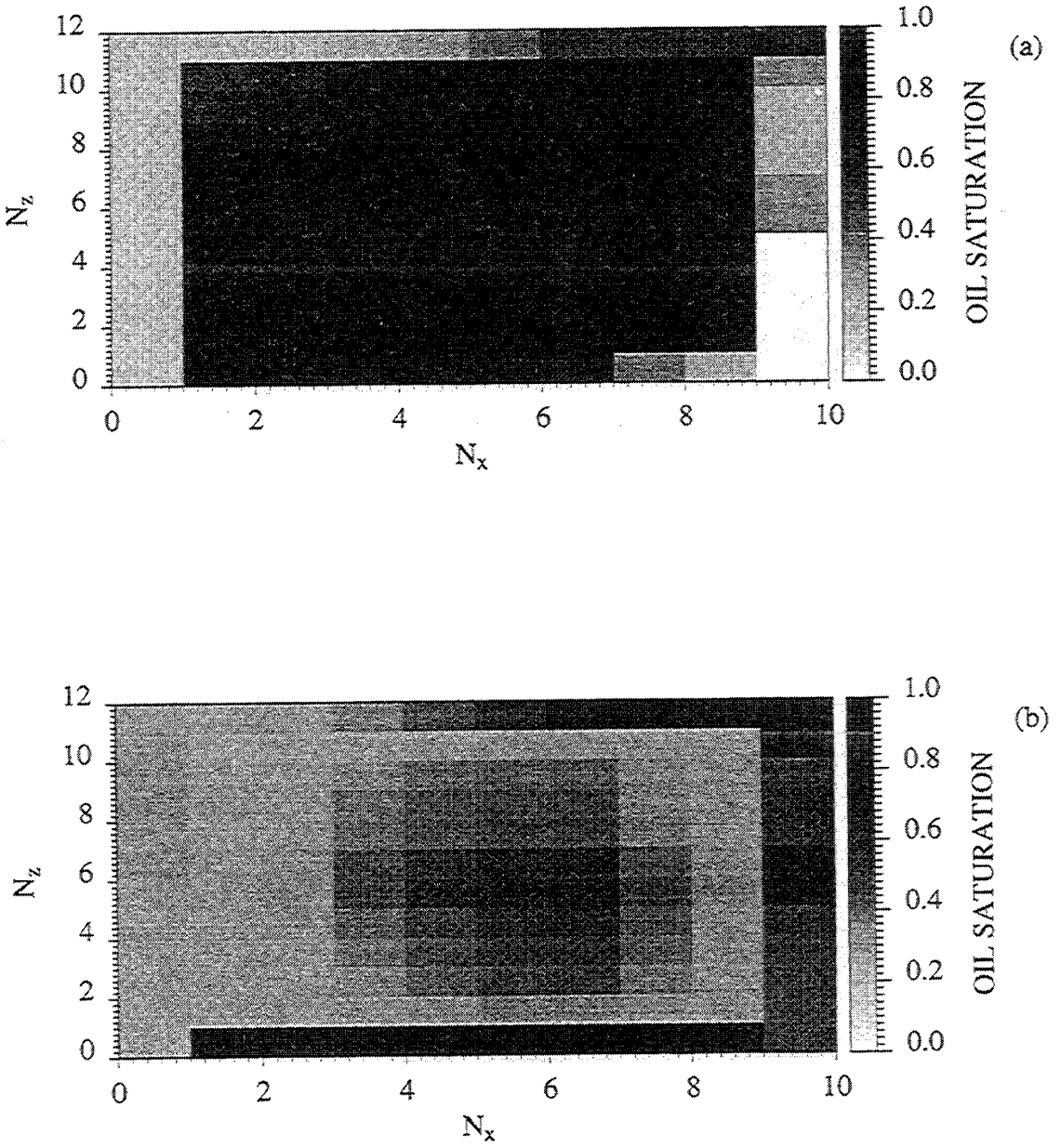

Figure 3.7: Oil saturation maps at 0.3 PV steam injected. (a) Zero matrix water-oil capillary pressure. (b) Finite matrix water-oil capillary pressure.

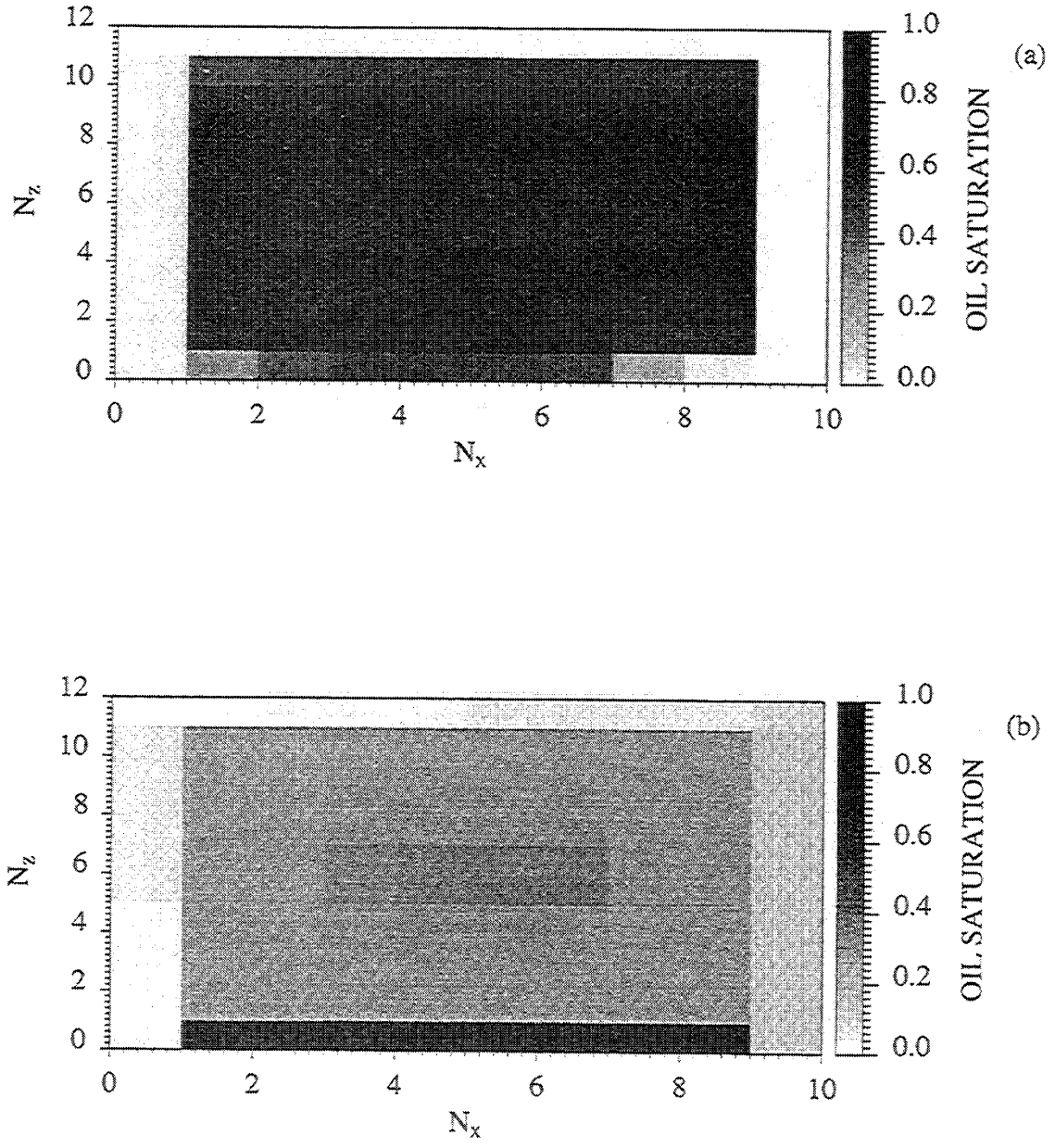

Figure 3.8: Oil saturation maps at 1.3 PV steam injected. (a) Zero matrix water-oil capillary pressure. (b) Finite matrix water-oil capillary pressure.

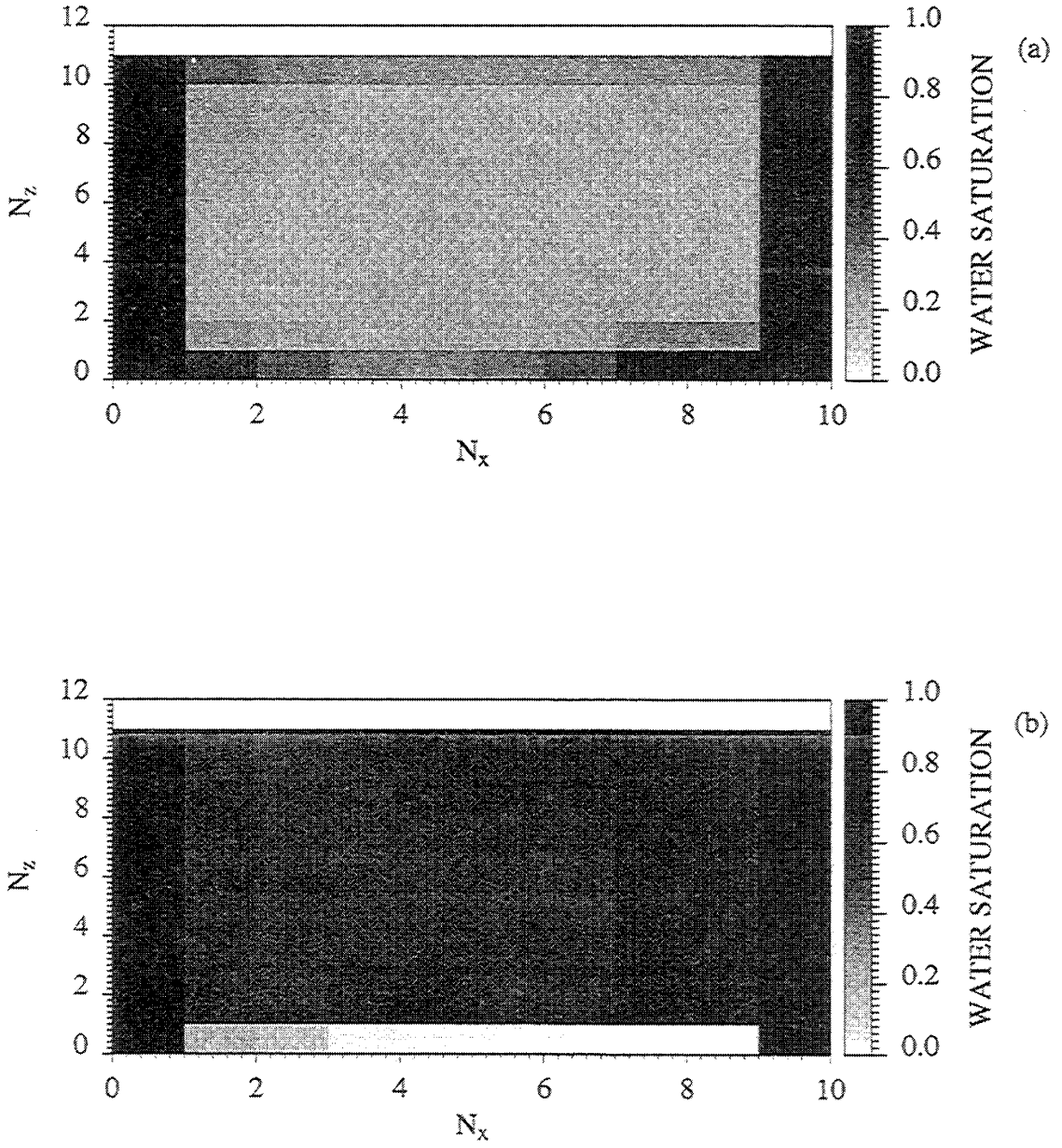

Figure 3.9: Water saturation maps at 1.3 PV steam injected. (a) Zero matrix water-oil capillary pressure. (b) Finite matrix water-oil capillary pressure.

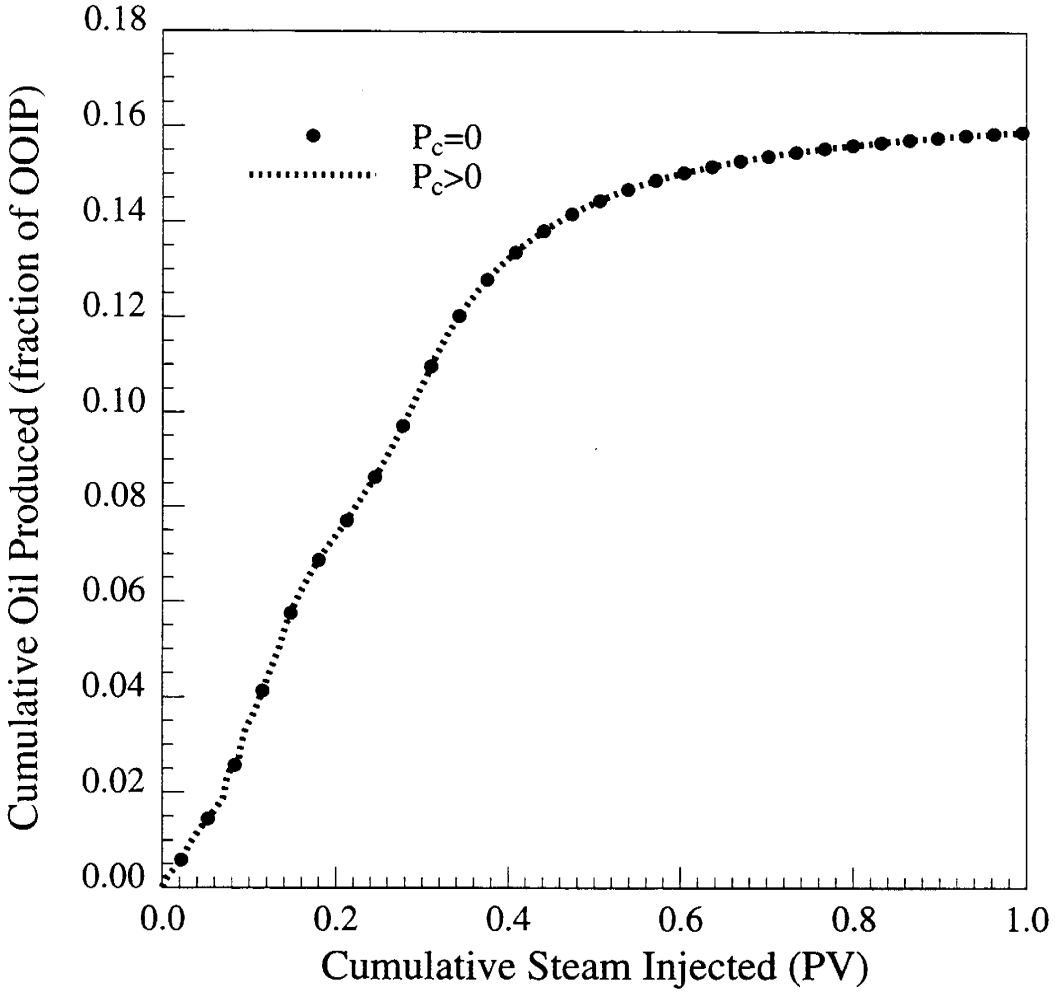

Figure 3.10: Effect on oil recovery of matrix gas-oil capillary pressure.

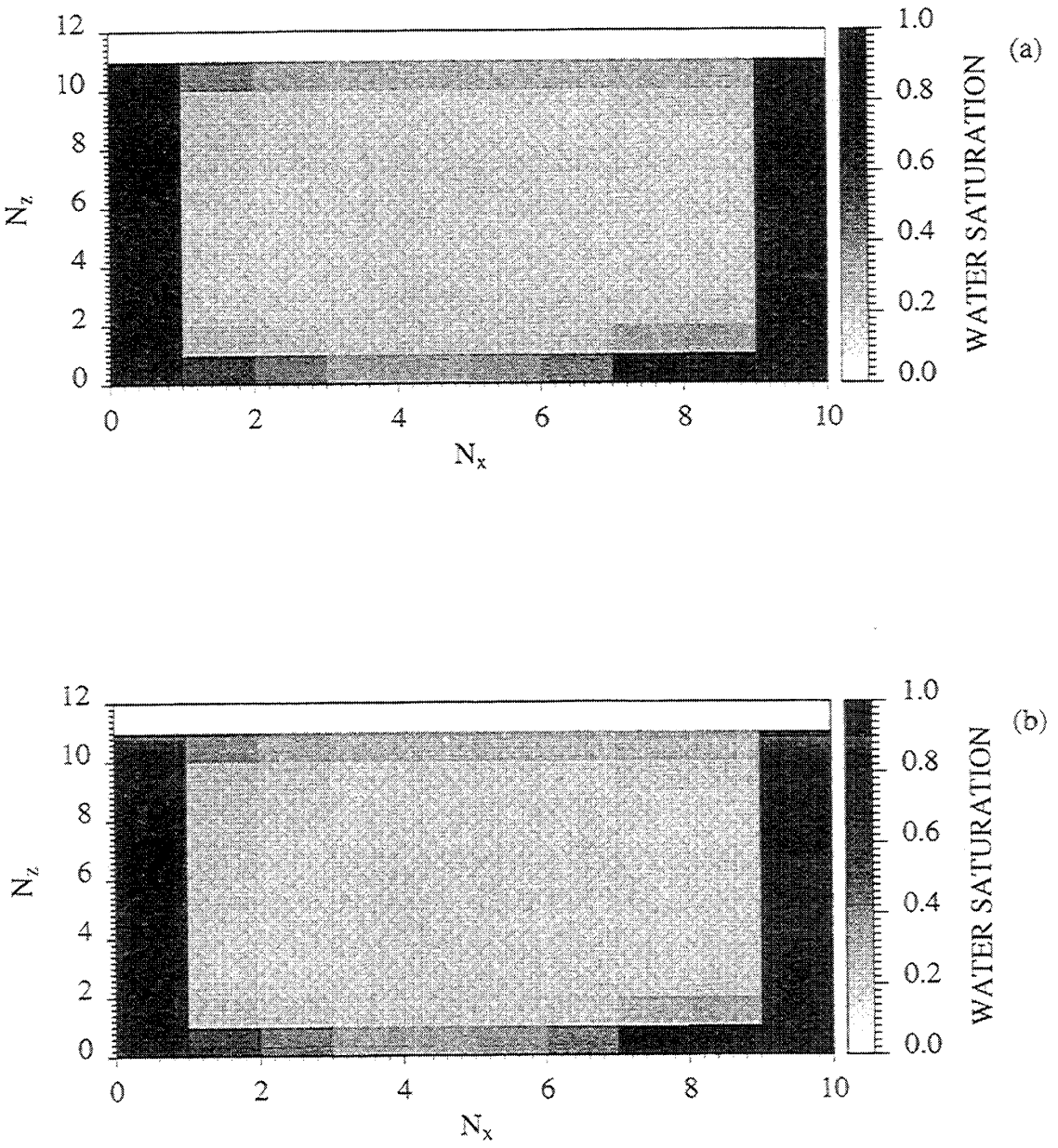

Figure 3.11: Water saturation maps at 1.3 PV steam injected. (a) Zero matrix gas-oil capillary pressure. (b) Finite matrix gas-oil capillary pressure.

the fractures.

3.1.2 Effect of Capillary Pressure in Fracture

The existence or absence of capillary pressure in the fracture is a controversial subject. In most fractured reservoir simulations, capillary pressure of the fracture were set to zero [50, 13, 12, 51]. Several authors however, claim that fracture capillary pressure should not be zero [32, 33, 41, 52].

In the base-case simulations, water-oil and gas-oil capillary pressures of the fracture are set to zero. Capillary pressure curves for the fracture used in the sensitivity studies are given in Fig. 3.12. For these sets of runs, matrix capillary pressures were set to zero.

Water-oil capillary pressure in the fracture decreased the oil recovery due to the decrease in water imbibition into the matrix (Fig. 3.13). The calculated recovery is, in fact, less than that for zero capillary pressure. When fracture capillary pressure is greater than zero, there was no change in water saturation either in the matrix or the fracture (Fig. 3.14b). Only steam flows in the fracture. Since there is a high mobility difference between steam and oil, oil in the fracture cannot be displaced, as shown in Fig. 3.15b. Oil saturation remains constant except along the top fracture, where the oil has been displaced. On the other hand, when capillary pressure is zero, condensed water flows in the fracture and displaces oil, as seen in Fig. 3.15a.
Gas-oil capillary pressure in the fracture has a positive effect on recovery (Fig. 3.16). There is a crossover between the two recovery curves, since some time must pass to heat the matrix by steam and thus mobilize the oil.

Figures 3.17a and 3.17b show the steam saturation maps at 0.5 PV of steam injected for zero and nonzero fracture gas-oil capillary pressures. When capillary pressure is zero, steam only moves in the fracture. There is no steam in the matrix. On the other hand, when gas-oil capillary pressure is greater than zero, steam moves into the matrix. The increased steam saturation in the matrix causes a decrease in the viscosity of oil, making the oil mobile and causing a significant increase in oil recovery. The oil saturation map in Fig. 3.18b shows the decrease in oil saturation.

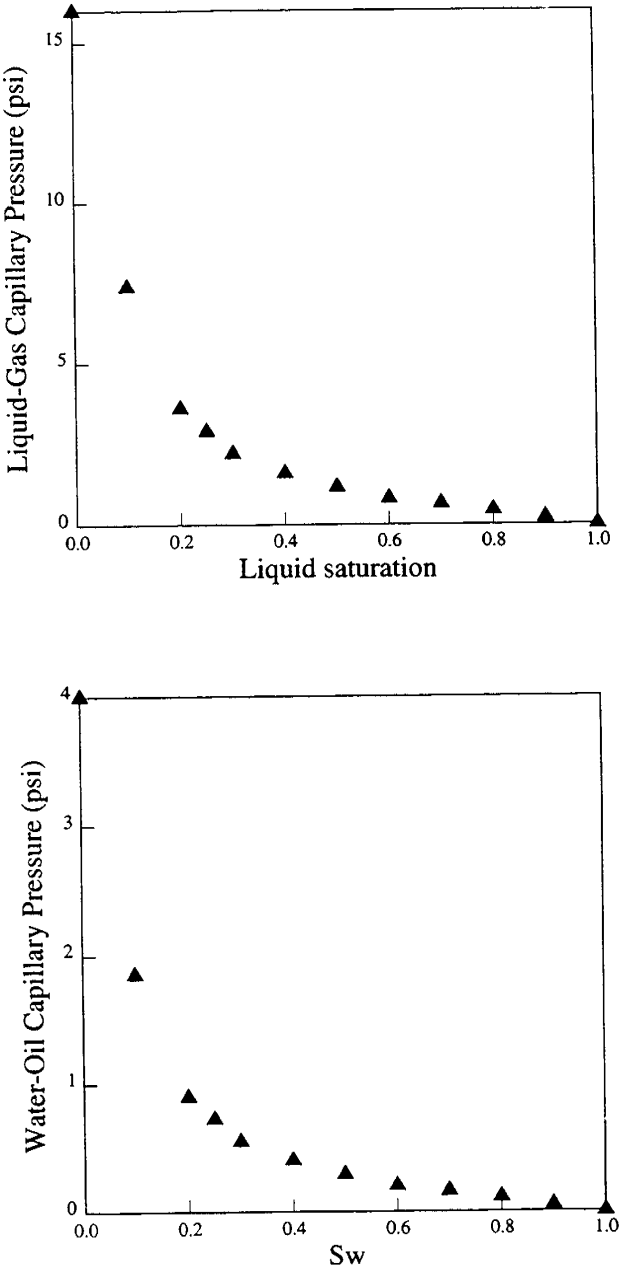

Figure 3.12: Capillary pressure curves for fracture. Top: Gas-liquid capillary pressure. Bottom: Water-oil capillary pressure.

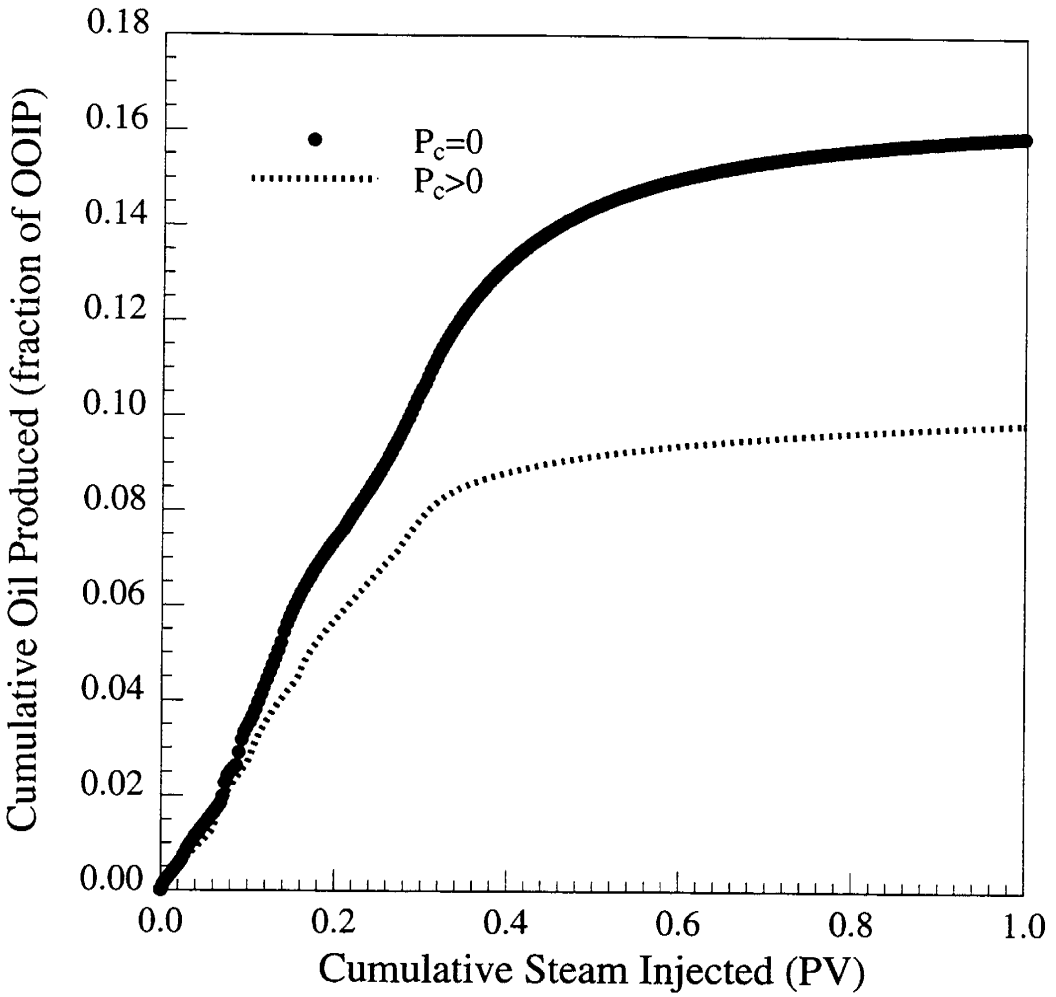

Figure 3.13: Effect on oil recovery of water-oil capillary pressure in fracture.

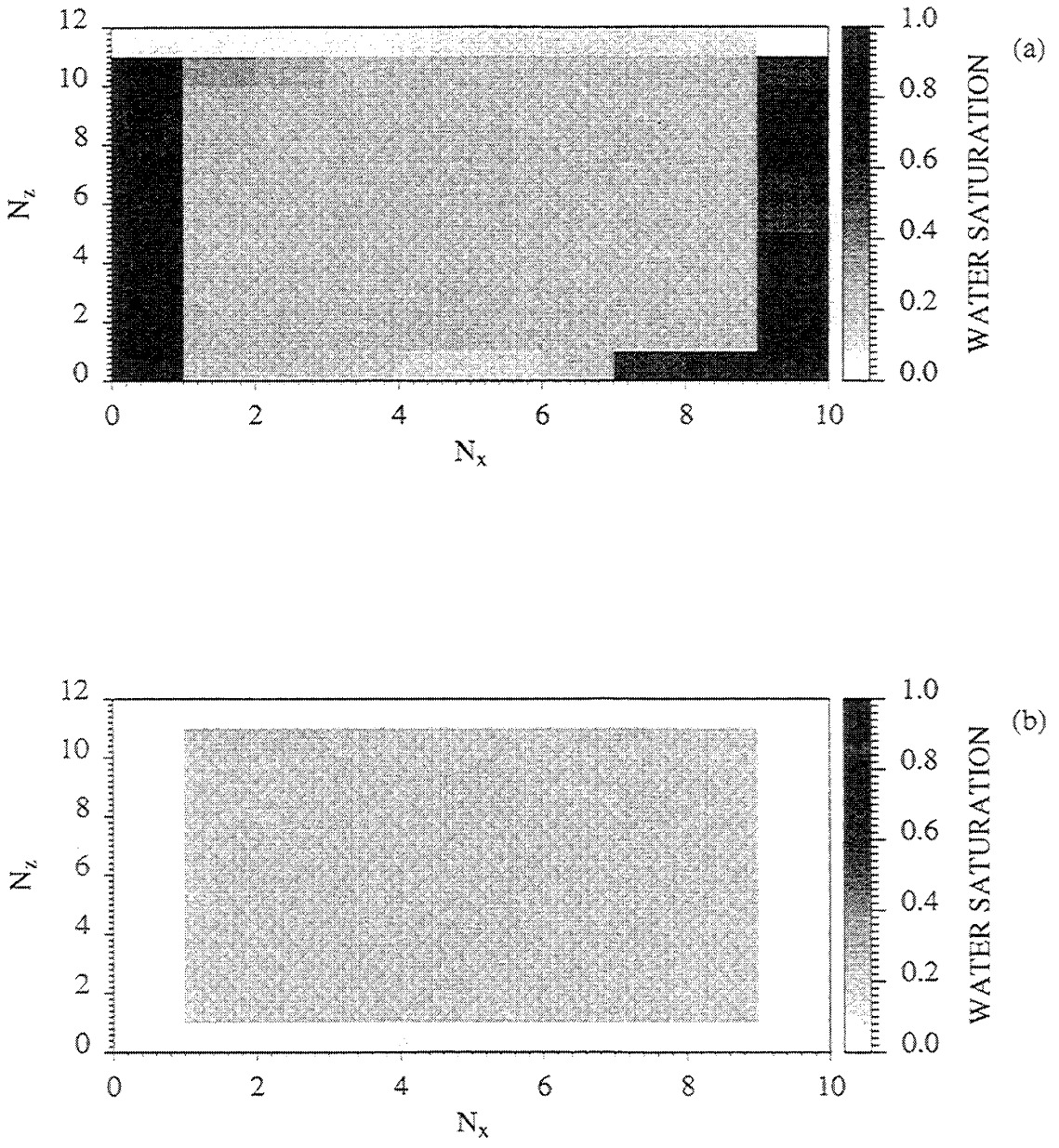

Figure 3.14: Water saturation maps at 0.3 PV steam injected. (a) Zero fracture water-oil capillary pressure. (b) Finite fracture water-oil capillary pressure.

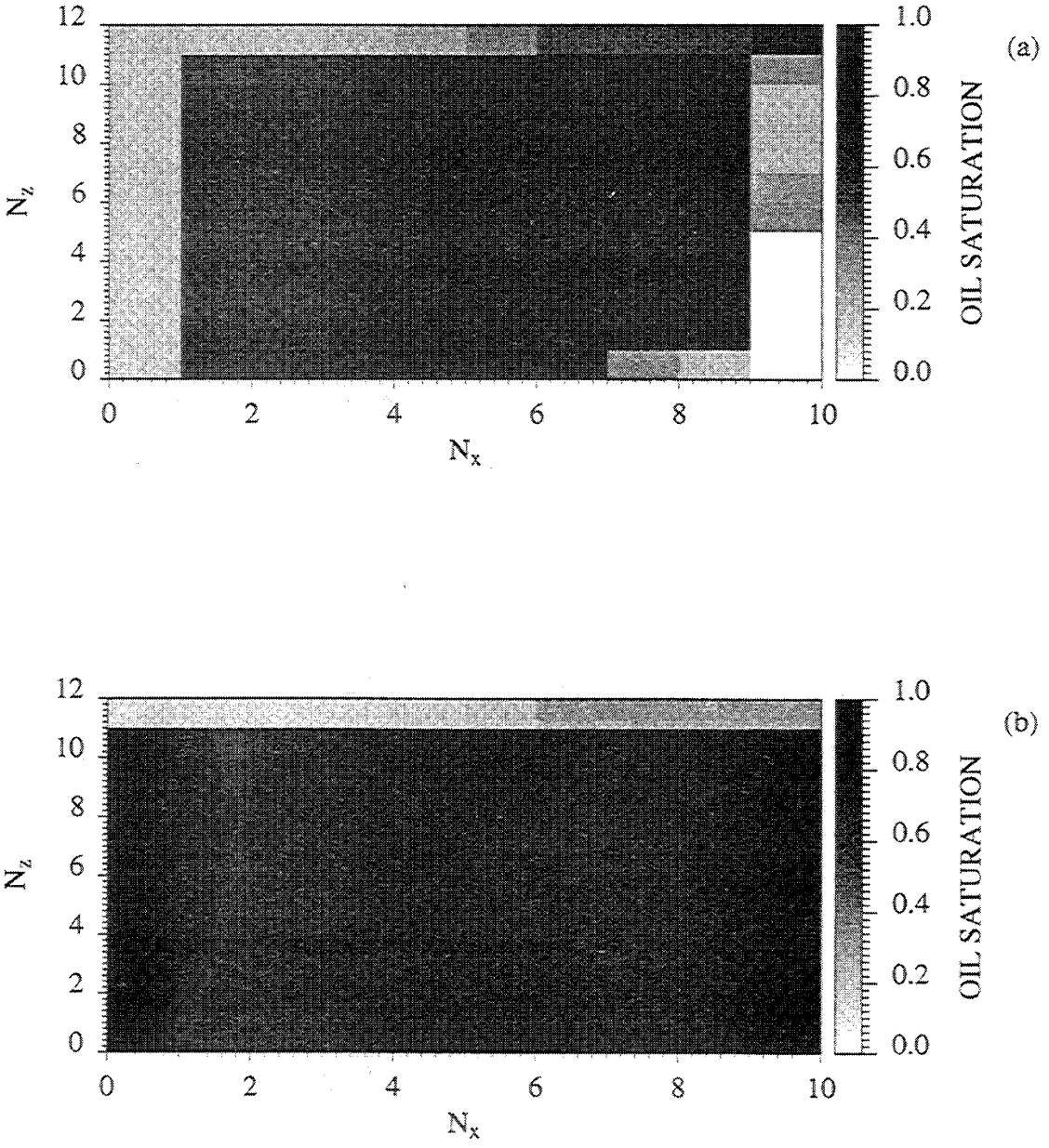

Figure 3.15: Oil saturation maps at 0.3 PV steam injected. (a) Zero fracture water-oil capillary pressure. (b) Finite fracture water-oil capillary pressure.

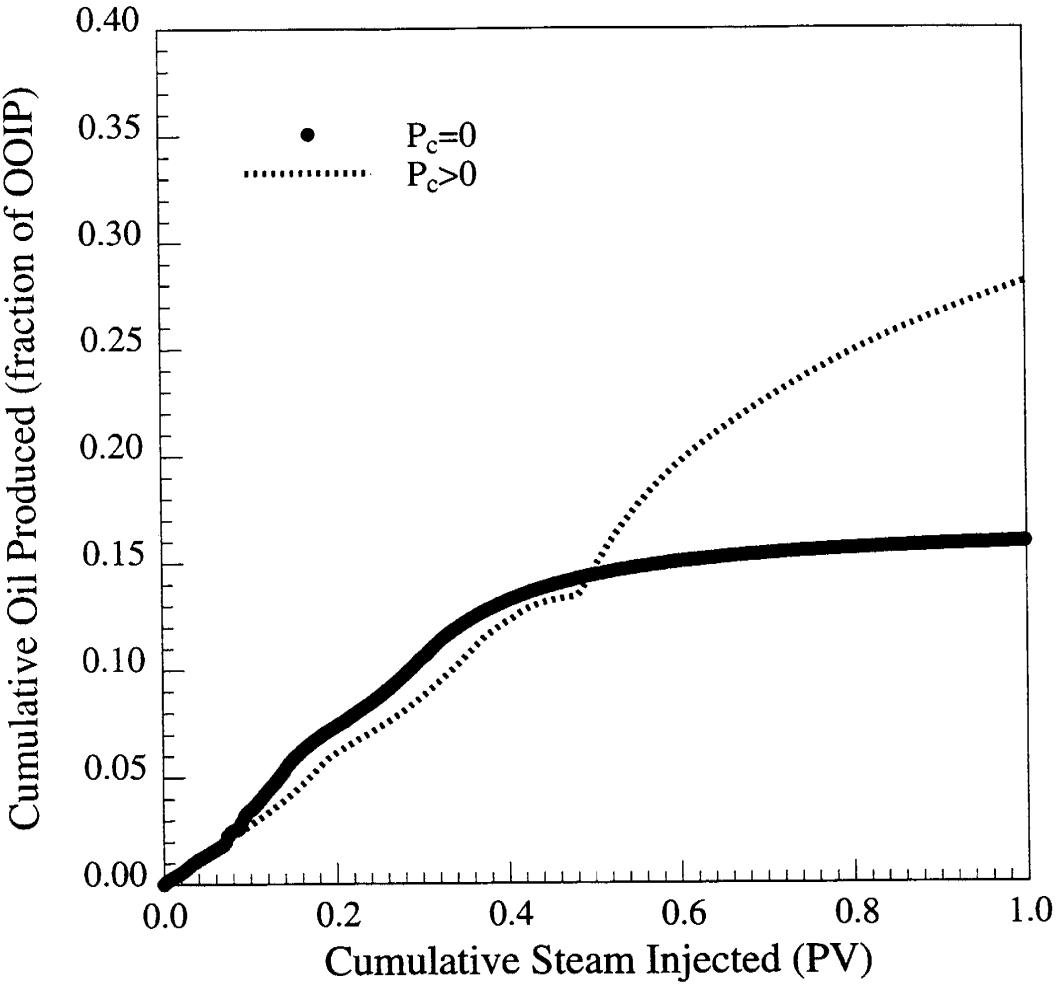

Figure 3.16: Effect of gas-oil capillary pressure of fracture on oil recovery.

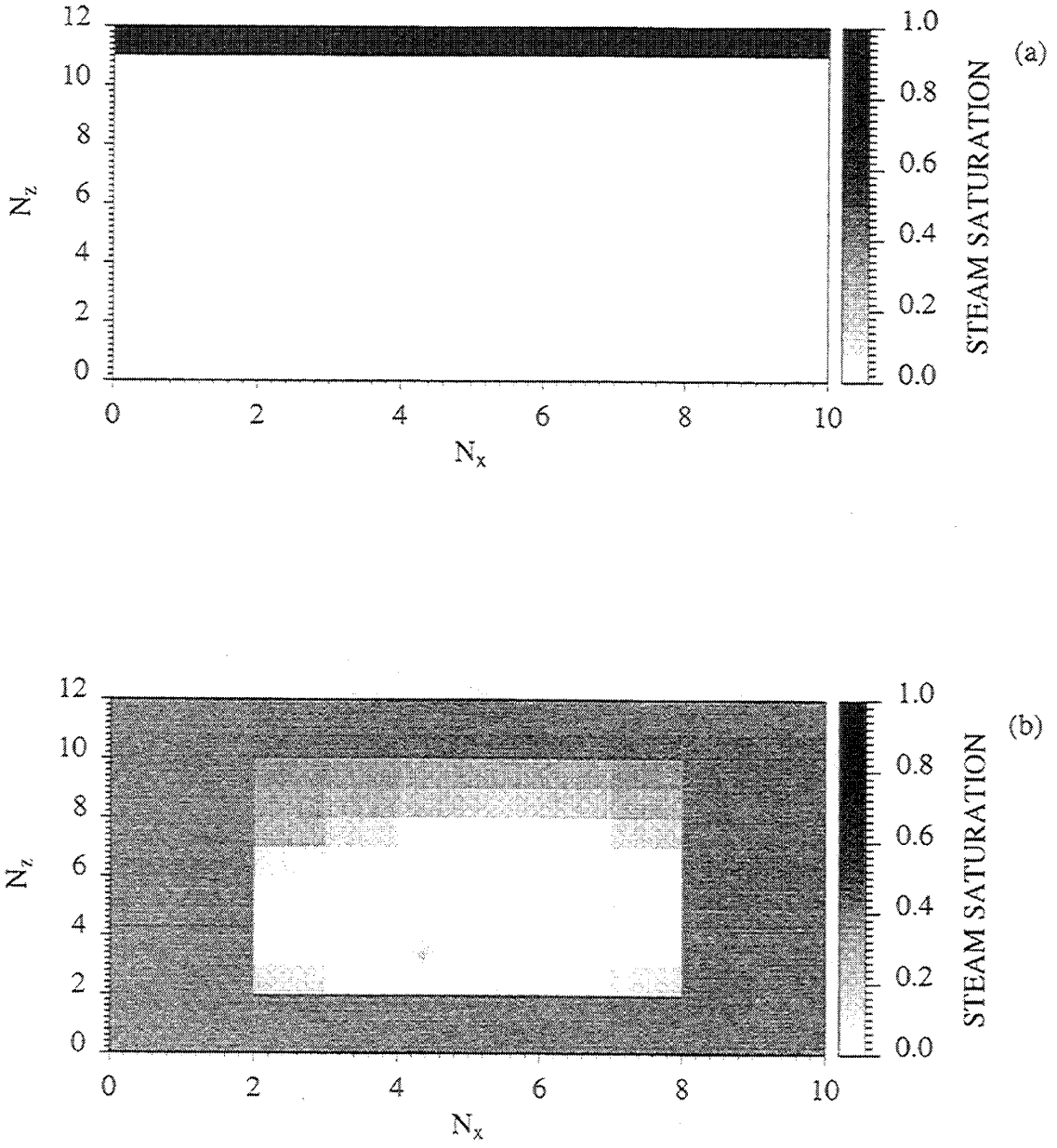

Figure 3.17: Steam saturation maps at 0.5 PV steam injected. (a) Zero fracture gas-oil capillary pressure. (b) Finite fracture gas-oil capillary pressure.

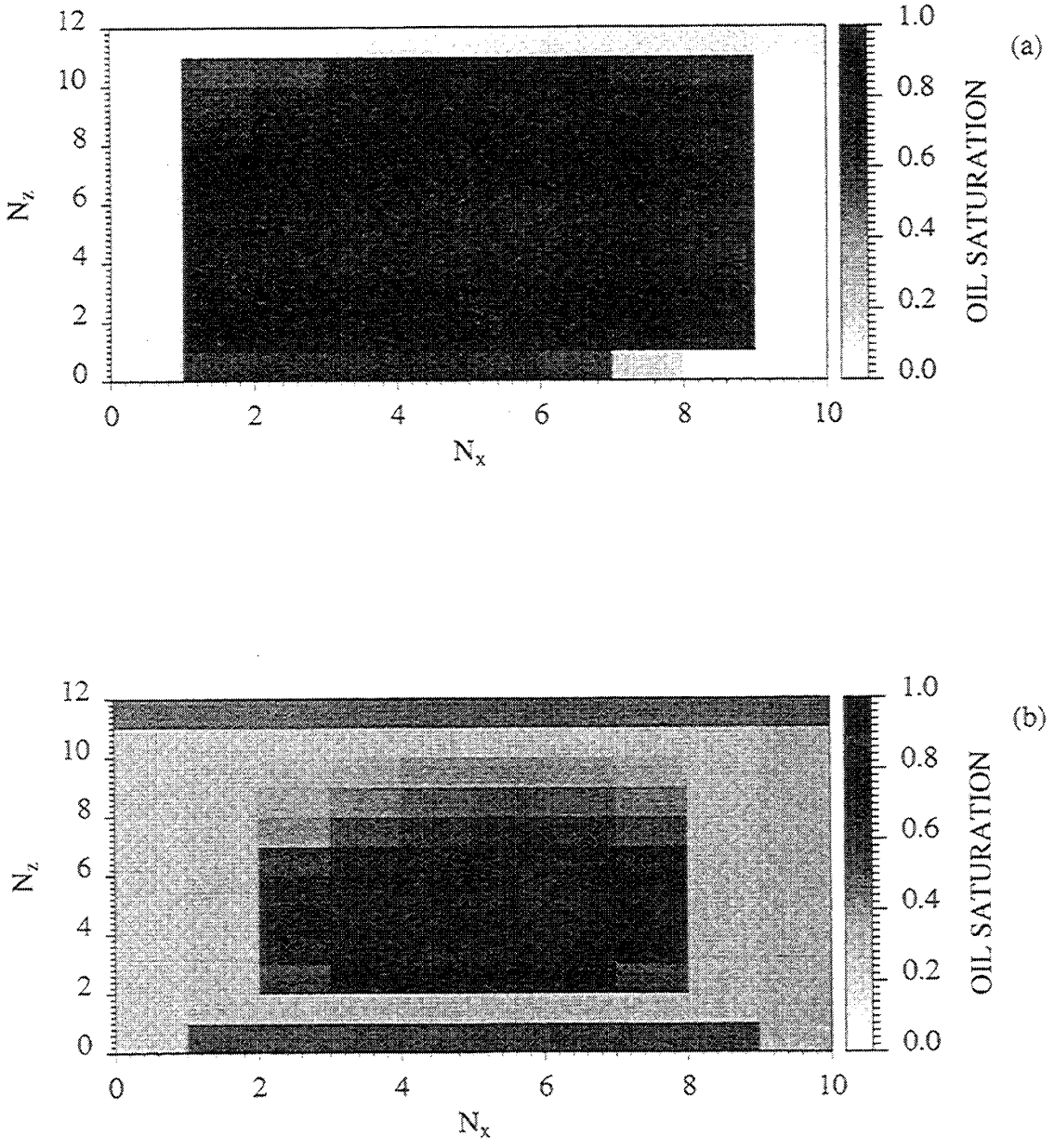

Figure 3.18: Oil saturation maps at 0.5 PV steam injected. (a) Zero fracture gas-oil capillary pressure. (b) Finite fracture gas-oil capillary pressure.

When there is no capillary pressure in the fracture, only the oil in the fracture is displaced (Fig. 3.18a). Only a very small amount of oil has been displaced from the matrix.

When capillary pressure is greater than zero, oil saturation in the matrix has been decreased to almost 0.2 for a large portion of the matrix, particularly near the fracture faces. Note also, in Fig. 3.18b, that the recovery in the upper part of the matrix is greater than the lower part, indicating that gravity effects also have considerable influence on the displacement process.

3.1.3 Effect of Varying Relative Permeability of Matrix

To investigate the effect of the relative permeability of the matrix on oil recovery, two differing sets of relative permeability data were used. The initial simulation runs were made using relative permeability curves typical of a sandstone [61]. They are shown in Fig. 3.19 and will be called as base case relative permeability curves.

Three-phase relative permeability curves for Boise sandstone measured by Saraf [74] were used for the second set of simulation runs. Figure 3.20 shows these curves.

As seen from Figs. 3.19 and 3.20, there are some differences in the end points of these two sets of curves. The base case water-oil relative permeability curve has a higher endpoint relative permeability to oil in the presence of water. However, end point gas relative permeability in the presence of oil for the measured curve is higher than the base curves. Endpoint water relative permeabilities are similar for both measured and base case curves. Critical liquid saturations in gas-liquid relative permeability curves are different from each other. Critical liquid saturation is 0.25 for the base case and 0.4 for the measured gas-liquid relative permeability curves. The effect of matrix relative permeabilities on the oil recovery is shown in Fig. 3.21. The oil recovery from the base case is higher. However, the matrix water-oil capillary pressure curves were not the same for these two cases. Capillary pressure was higher for the base case (Fig. 3.22). Previous sensitivity studies on the matrix water-oil capillary pressure, showed it to be an important parameter affecting the recovery. So, the use of differing capillary pressures may be the reason for the differences in

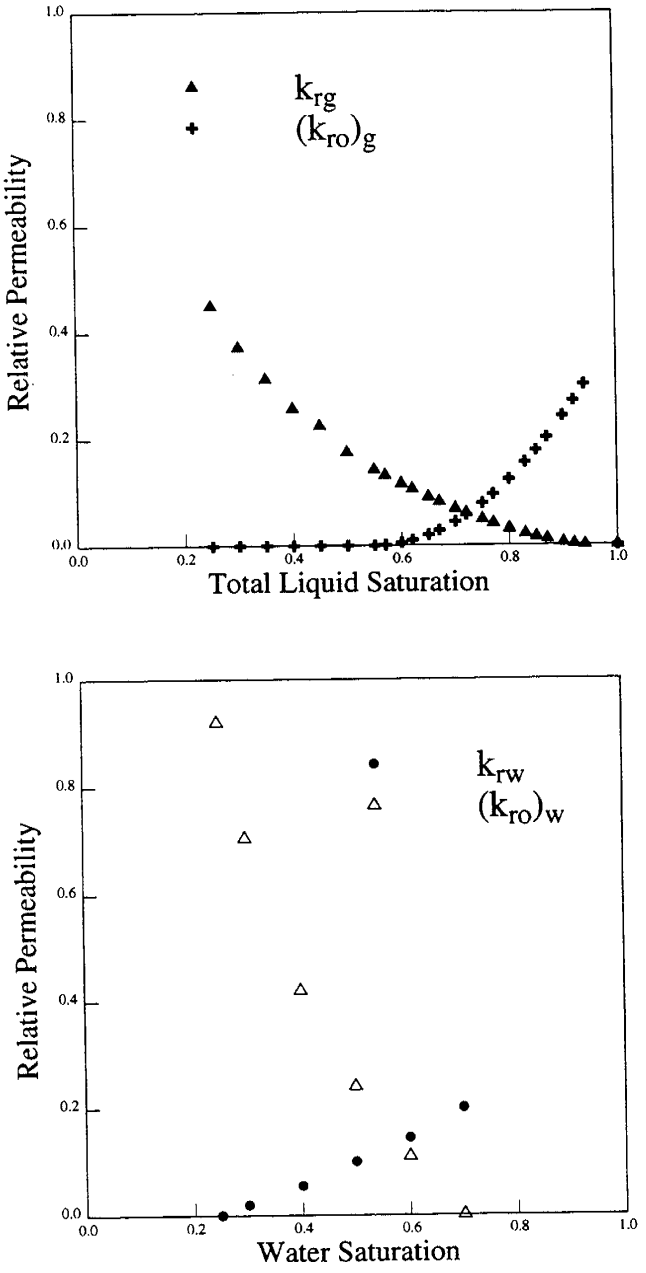

Figure 3.19: Base case relative permeability curves for matrix (Oballa et al., 1990).

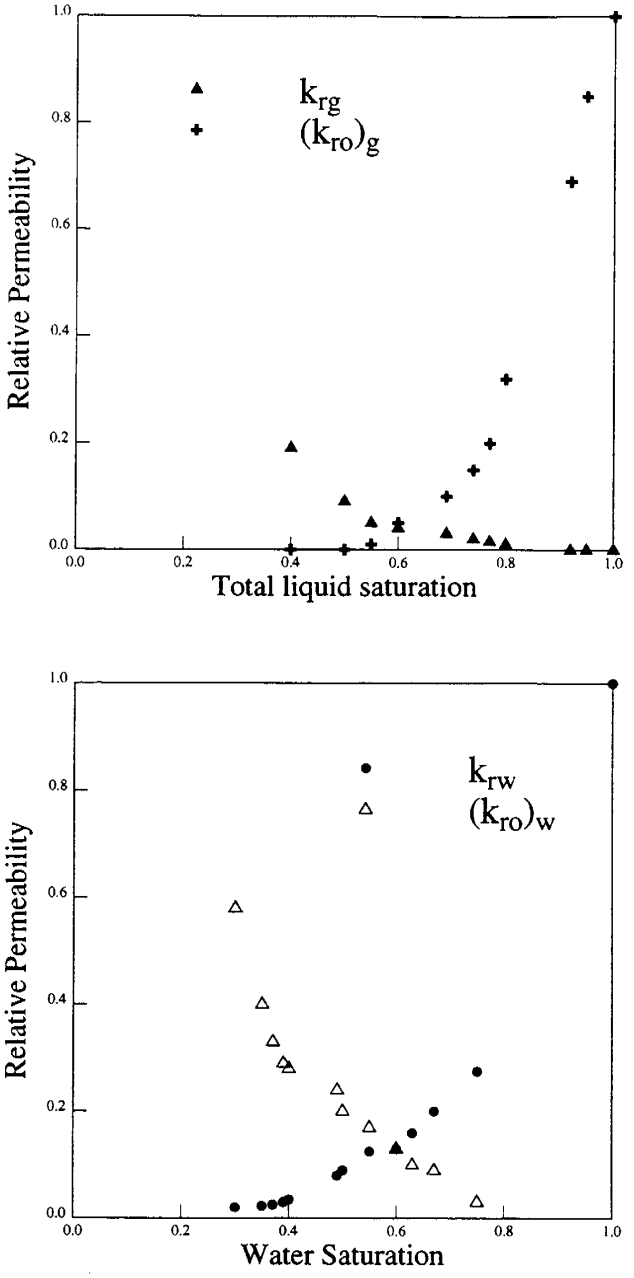

Figure 3.20: Measured relative permeability curves for Boise sandstone (Saraf, 1966).

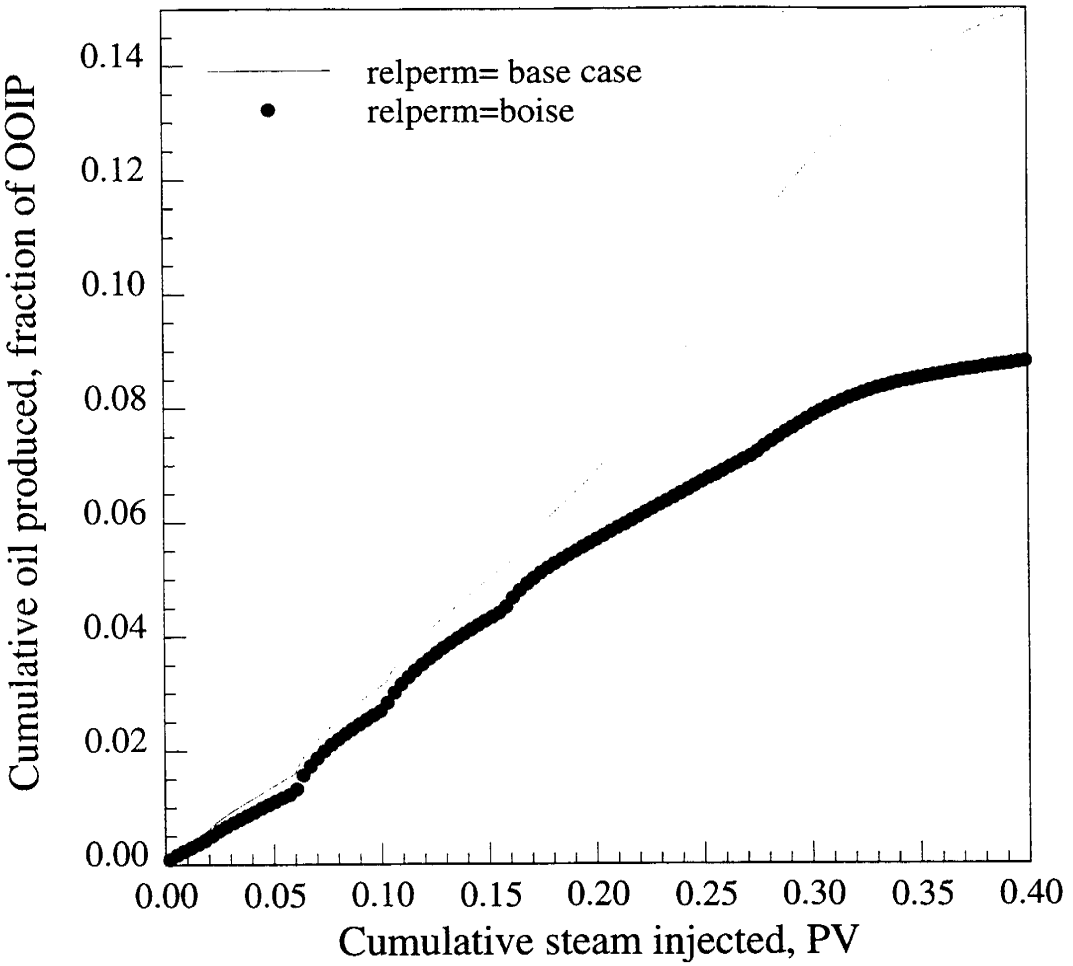

Figure 3.21: Comparison of oil recovery for differing matrix relative permeability and capillary pressure sets.

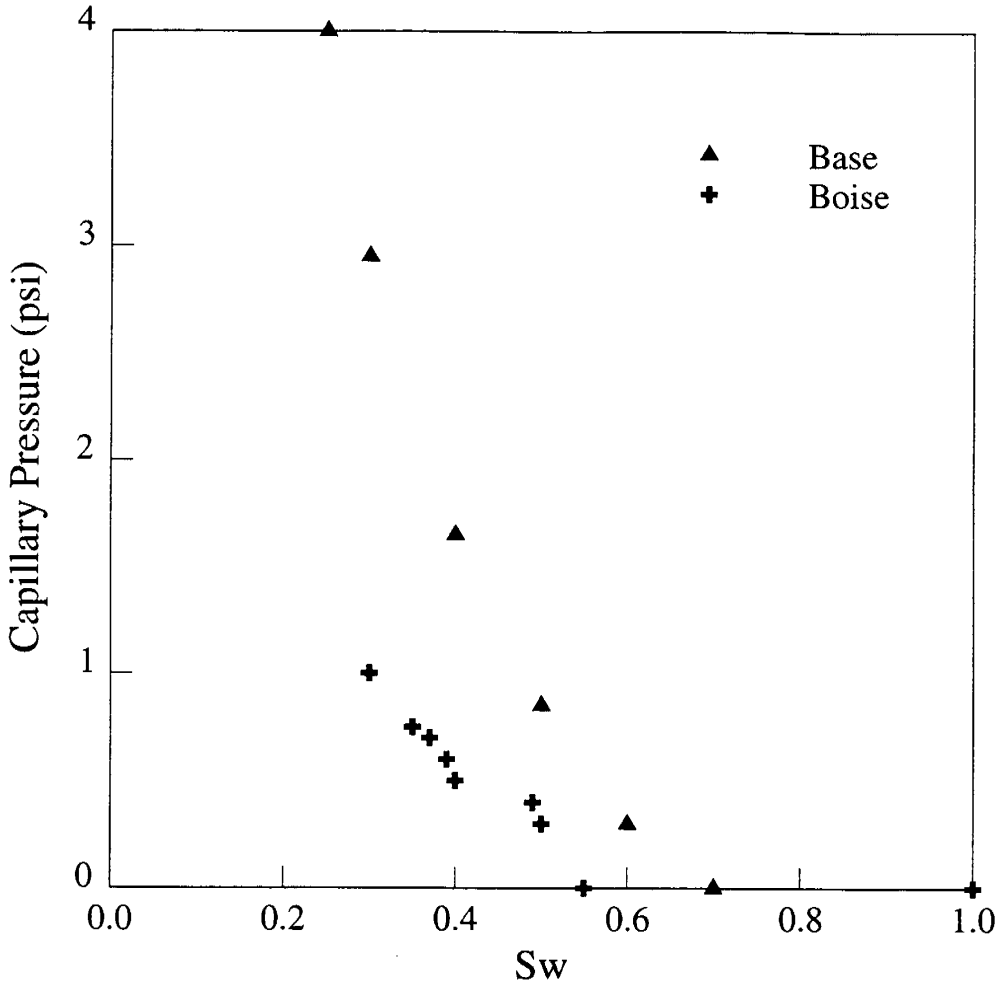

Figure 3.22: Comparison of capillary pressures used in the relative permeability sensitivity studies.

Fig. 3.21. To investigate this effect further, and to isolate the effects of relative permeabilities, capillary pressure was set to zero for the next two runs.

As seen in Fig. 3.23, oil recovery is the same for the two cases even though two different relative permeability curves were used. In the next set of simulations, the same nonzero water-oil capillary pressure data were used with differing relative permeabilities. Oil recoveries from the two cases were again very similar (Fig. 3.24). Thus, the reason for the difference in oil recoveries in Figs. 3.23 and 3.24 is the use of differing capillary pressures. Figure 3.23 shows the oil recovery with zero capillary pressure, and Fig. 3.24 is for finite capillary pressure.

These sets of runs, testing the sensitivity of oil recovery on the relative permeability of the matrix supported the previous capillary pressure sensitivity studies. When gas-oil capillary pressure is nonexistent in the fractures, water-oil capillary pressure of the matrix is the dominant parameter, affecting the oil recovery by increasing water imbibition. Therefore, relative permeability effects are insignificant compared to capillary pressure effects.

3.1.4 Effect of Varying Relative Permeability of Fracture

Different relative permeability curves for the fracture were used to investigate the sensitivity of the oil recovery on this parameter. First, water-oil relative permeability curves for the fracture were modified to see the effect on oil recovery. Water-oil and gas-oil relative permeabilities taken from Oballa et al. [61] were used in the base case simulations. They are shown by the symbols in Fig. 3.25a and 3.25b. Then, conventional straight line relative permeabilities were used in the next simulation run. They are shown by the dashed and solid lines in Fig. 3.25b. The results showed that water-oil relative permeability curves for the fracture had a minor effect on oil recovery (Fig. 3.26).

Next the effects of k_{rg} and $(k_{ro})_g$ curves of the fracture were investigated. Straight line relative permeabilities were used in the base case simulations and they are shown by the solid and dashed lines in Fig. 3.27a. Then, the relative permeabilities were modified for comparison. They are shown by triangle and cross symbols in Fig. 3.27a.

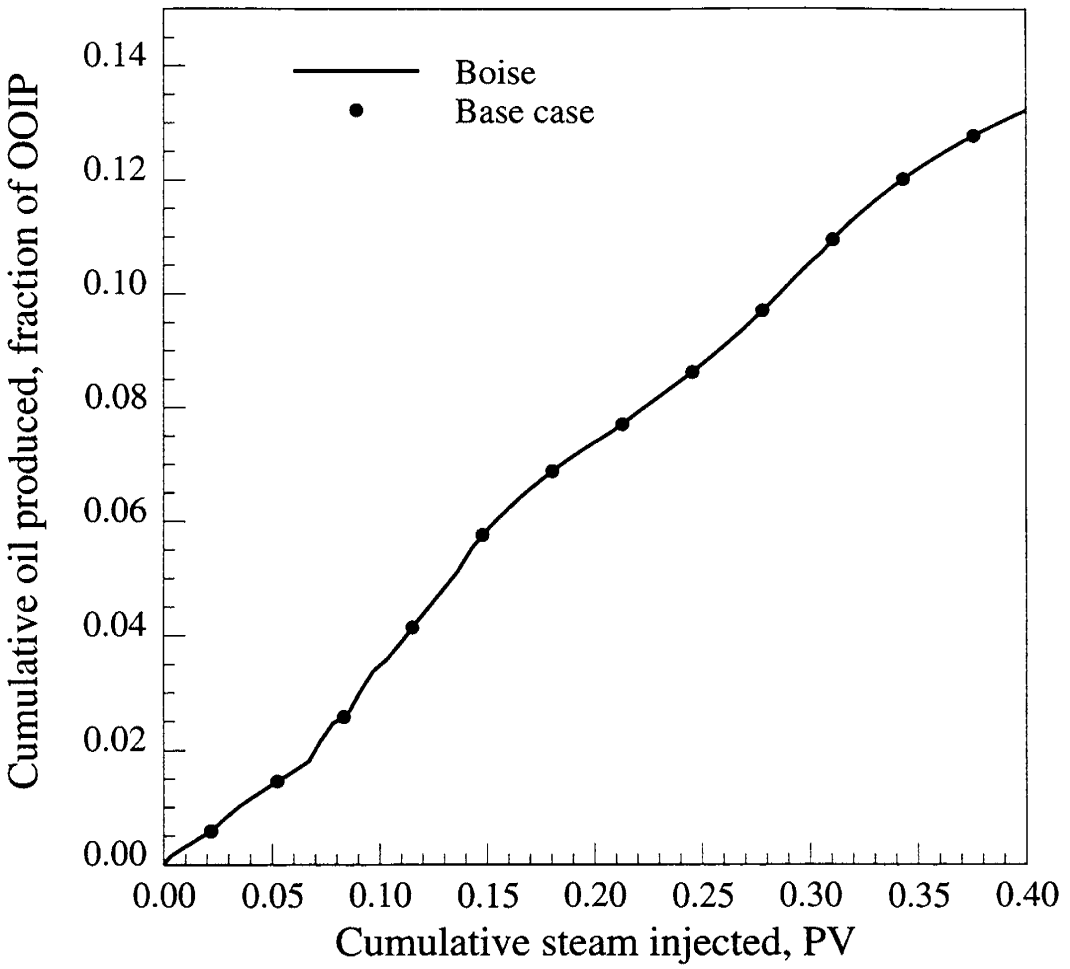

Figure 3.23: Comparison of oil recovery for differing matrix relative permeability sets ($(Pcm)_{wo} = 0$ for both cases).

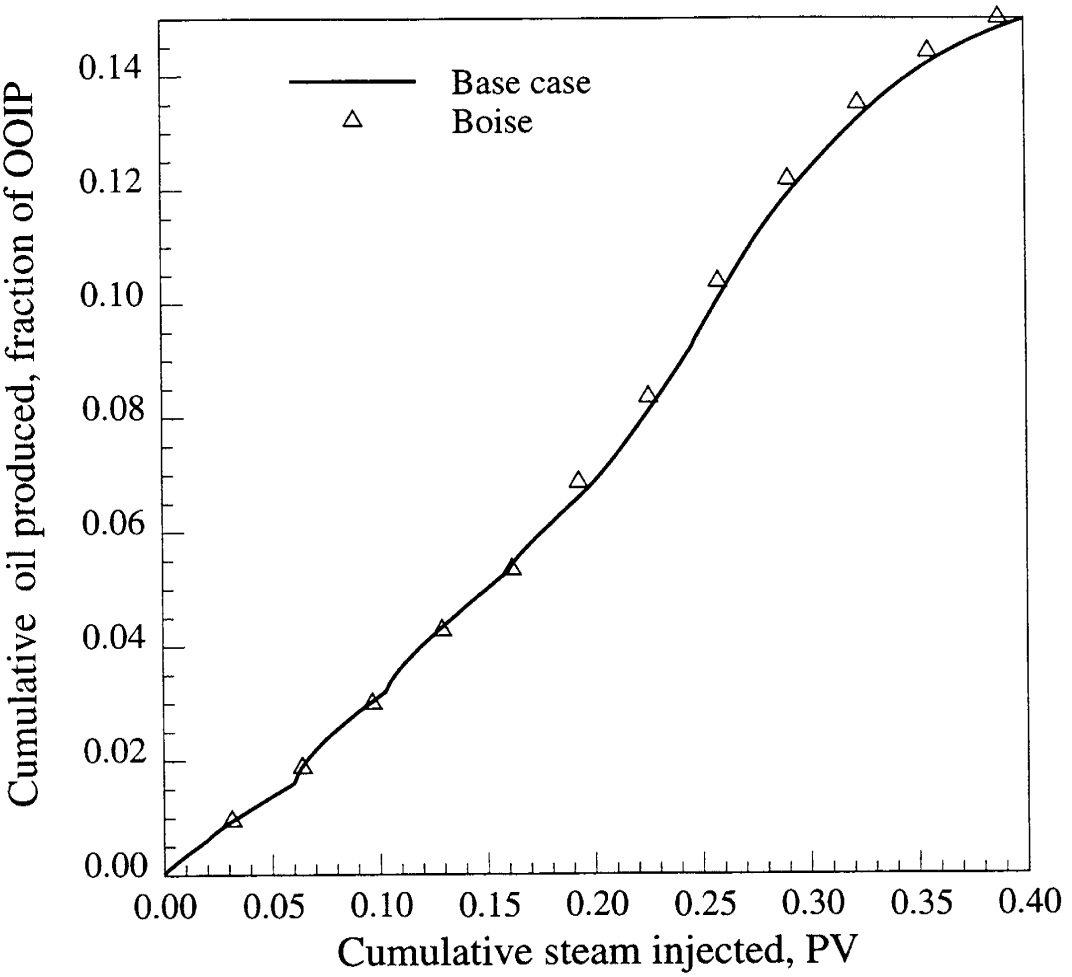

Figure 3.24: Comparison of oil recovery for differing matrix relative permeability sets ($(Pcm)_{wo}$ is the same for both cases).

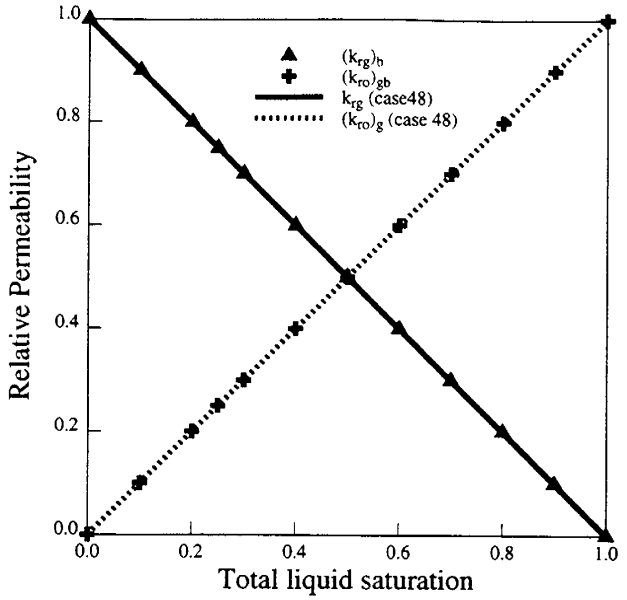

(a)

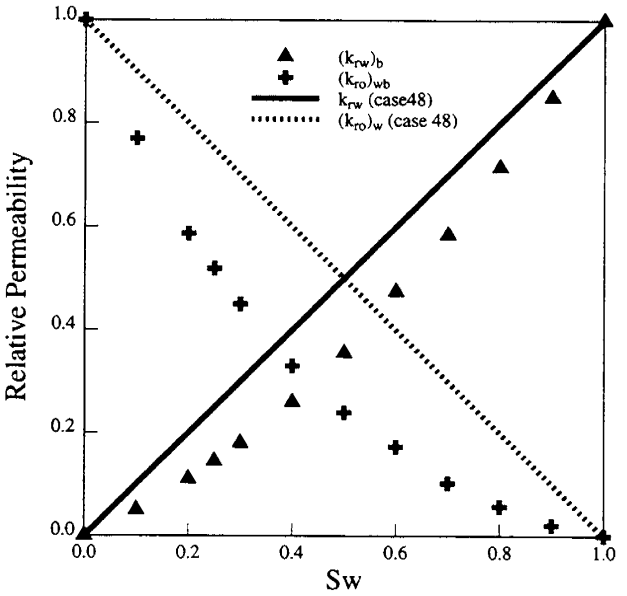

(b)

Figure 3.25: Fracture relative permeability sets used in the simulation run done to investigate the effects of water-oil relative permeabilities (Case48).

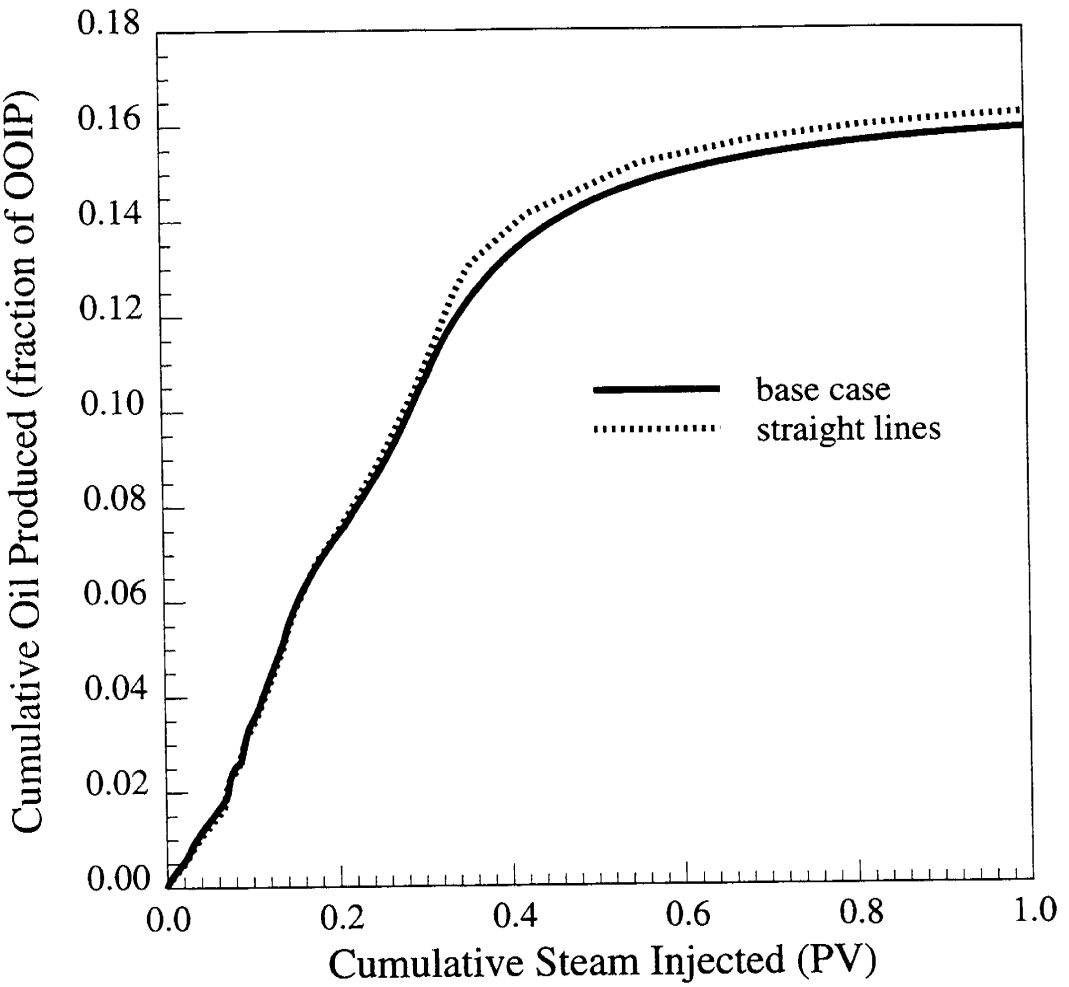

Figure 3.26: Effect of fracture water-oil relative permeabilities on oil recovery.

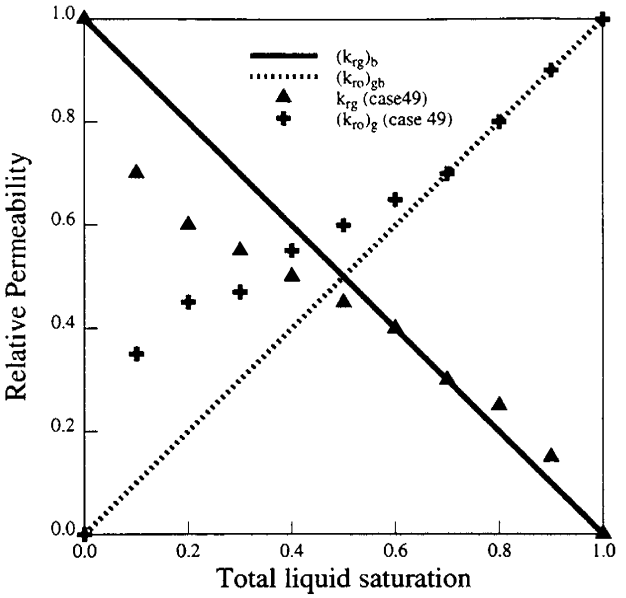

(a)

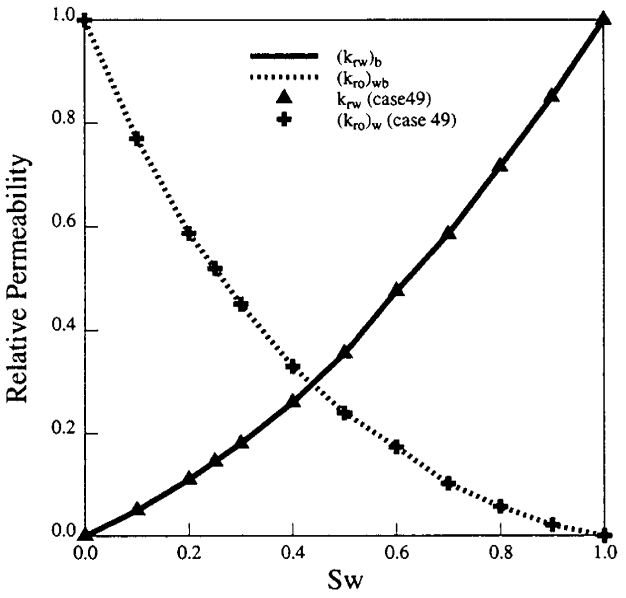

(b)

Figure 3.27: Fracture relative permeability sets used in the simulation run done to investigate the effects of gas-liquid relative permeabilities (Case49).

The oil recovery calculated from the two runs was again similar as shown in Fig. 3.28. This is to be expected since the fracture desaturates very quickly. Steam entering the fracture entirely displaces all the oil on its path.

Results of the fine grid simulations described in this chapter, showed that the water-oil capillary pressure of the matrix, and the water-oil and gas-oil capillary pressures of the fracture had a significant effect on oil recovery. Water imbibition into the matrix and drainage of oil by steam were found to be the most important recovery mechanisms for displacement of oil from a matrix block. Neither matrix nor fracture relative permeabilities were found to be significant parameters in affecting the displacement in this fractured model.

Fine grid simulations were also used to help determine certain experimental parameters such as: steam injection rate, maximum pressure change in the system, and locations and numbers of thermocouples and wells. The details of the experimental design simulations are given in the next chapter.

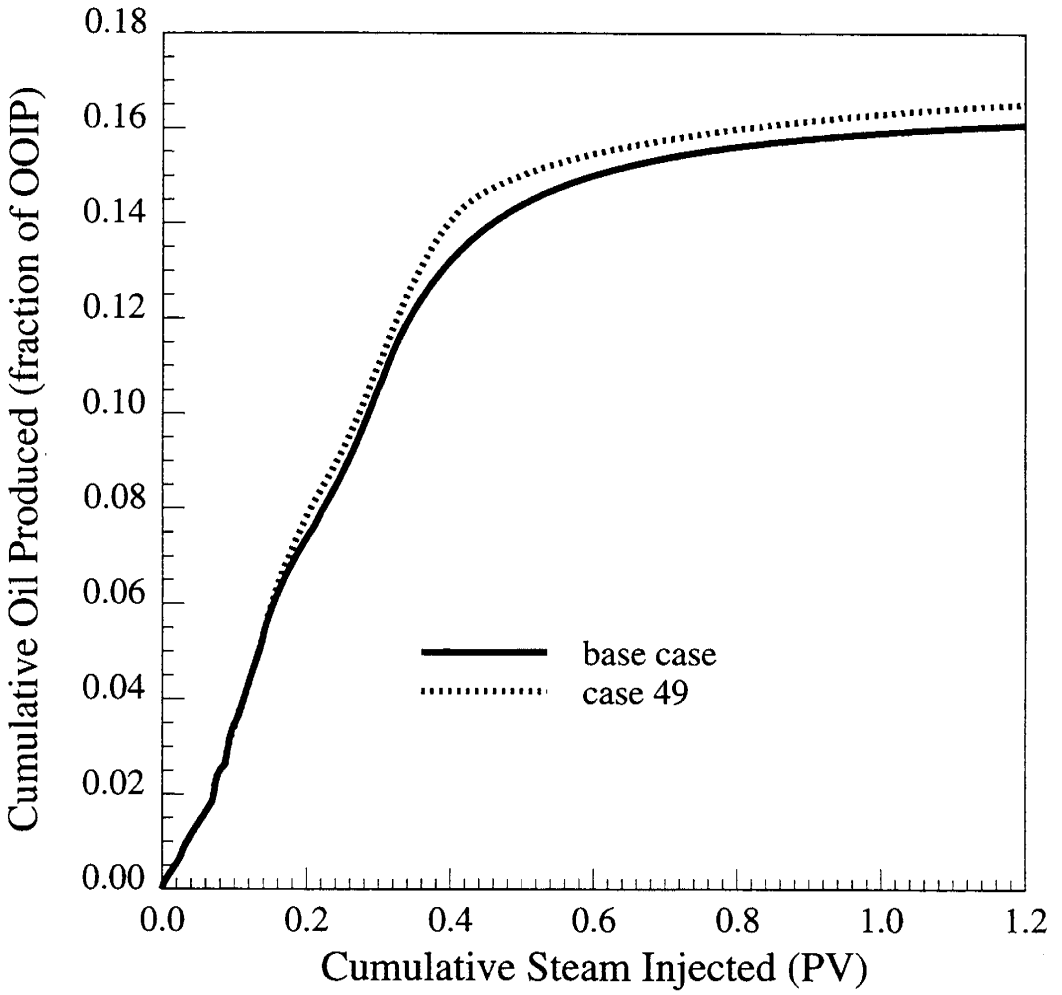

Figure 3.28: Effect of fracture liquid-gas relative permeabilities on oil recovery.

Chapter 4

Experimental Design

Many restrictions affected the design of the core holder for steam injection in fractured systems. The model had to be X-ray transparent, had to have a low thermal conductivity and low thermal expansion coefficient, and it had to be rated against the temperatures and pressures encountered in the steam injection process. Due to these restrictions and the complexity of the design, simulators were used to predict some design parameters. Analytical calculations were also used in the design to determine the expected heat losses from the system.

4.1 Fine Grid Simulations

Several different commercial simulators were used to determine certain experimental design parameters before the core holder and the experimental set-up were built. The number of grid blocks, grid sizes and the grid system used were similar to the ones used in the simulations described in Chapter 3.

Computer Modeling Group's thermal simulator, STARS [17], was used to determine the steam injection rate, maximum pressure change in the system and the numbers and locations of thermocouples. For determining the numbers and locations of the auxiliary wells (injector and producer), two different commercial black oil simulators were used (ECLIPSE [30] and IMEX [16]).

Steam injection rate, in terms of condensed water equivalent, is one of the most

important parameters in the experimental design. The rates should be within the laboratory pump limitations, but also high enough to overcome the heat losses from the model, so that a steam zone can develop in a reasonable time. Four differing steam injection rates (all of them within the pump range of 0-10 cc/min) were used in the simulations. Figure 4.1 shows the effect on the oil recovery of changing the steam injection rate. The highest total oil recovery was observed at the lowest rate (1 cc/min). Furthermore steam was observed in the system even at the lowest rate. Low rates are preferable for experimental purposes because of the timing limitations of the CT-scanner used to measure saturations in the model. A slower displacement rate allows saturation changes to be captured by the scanner.

Pressure distributions calculated throughout the model indicate that spatial variations in pressure are extremely small, indicating that more accurate pressure transducers are required to measure the pressure differences in the system. Calculated pressure in the inlet is 25.30 psi, and at the outlet is 25.20 psi. The pressure diaphragms of the transducers are thin, thus they are rated to measure a pressure difference of less than 5 psi.

The maximum pressure observed in the simulations helped in the core holder material selection. The core holder is made of plastic because of its transparency to X-rays, low thermal conductivity and low thermal expansion coefficient. Metal core holders are not as suitable for CT scanning. Thus, knowledge of the maximum expected pressure is crucial in material selection, since plastics are limited to lower pressures.

Temperatures along the core and the fracture are measured by thermocouples. Thermocouples were placed in the model where major changes in the temperature were predicted from simulation runs. Knowing thermocouple locations beforehand, avoided unnecessary complications in the core holder. In essence, the most significant changes in the calculated temperatures were observed near the matrix/fracture boundaries.

The numbers, locations and types of wells needed to saturate the model before an experiment, and to clean it afterwards, were determined by using commercial black oil simulators [30, 16]. Well locations are important due to the fractures surrounding

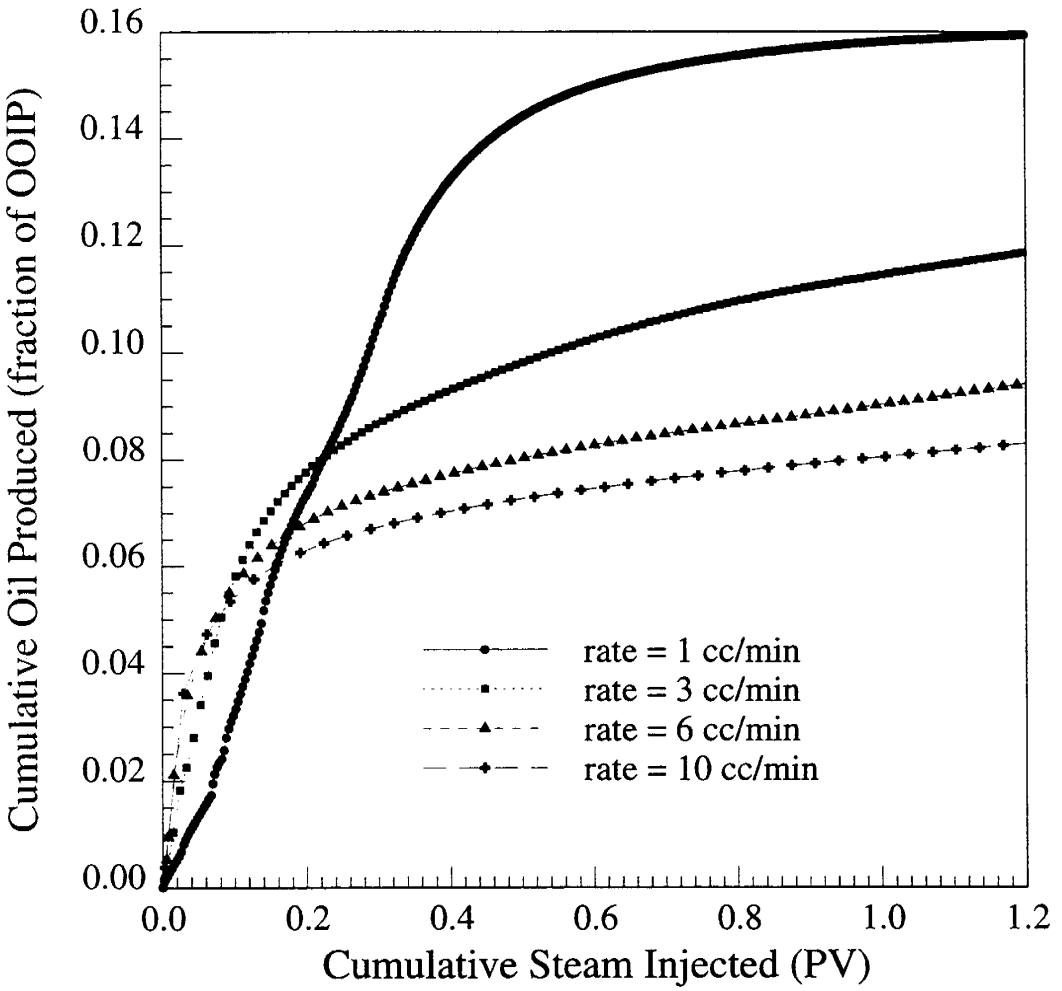

Figure 4.1: Comparison of oil recovery for differing steam injection rates.

the core. They make it difficult to achieve an efficient and thorough displacement. It is very easy for the cleaning fluids to flow only through the fractures and bypass the core.

Computer Modeling Group's black oil simulator, IMEX [16], was used for the simulations to saturate the model. The grid system again used fine gridding to simulate the fracture around the matrix. Initially the system was 100% saturated with water and oil was injected into the system until connate water saturation was reached in the matrix. This is the most commonly used procedure for saturating a core with oil in the laboratory. Both areal and cross-sectional simulations were performed. Differing injection-production schemes were tested, as shown schematically in Fig. 4.2. There are basically five wells in both of the configurations. In the top configuration, there are four injectors located at the corners of the system in the fracture and one producer in the middle of the matrix. In the other configuration, injectors and producer are reversed (four producers and one injector).

Figure 4.3 shows the cumulative water production as a function of oil injected for these two schemes. The configuration with four injectors at the corner and one producer at the center gave the desired result. At the end of 1.5 PV of oil injected, about 79% of the water in the model was displaced, and the desired ($\approx$ 80%) oil saturation in the matrix was obtained. Oil saturation maps shown in Fig. 4.4 confirm these results. At the end of 5.5 PV of oil injection, the matrix had an oil saturation of 0.8, and fractures had an oil saturation of 1.0, with four injectors and one producer. This is the desired initial saturation distribution. On the other hand, with four producers and one injector, oil saturation distribution is far from the optimum.

After determining the number of wells and their locations, a sensitivity study was made on the completion location of the producer. Completion in the middle layer gave the best results. Figure 4.5 shows the comparison of oil recovery for two different completion locations, at the top and in the middle. Nearly 80 % of the water has been produced when the producer was completed in the middle. When the completion was at the top, only 10% of the water was produced. Oil saturation maps show similar results (Fig. 4.6). When the production well is completed in the middle, it showed an oil saturation distribution of 80% in the matrix and 100% in the fracture. When

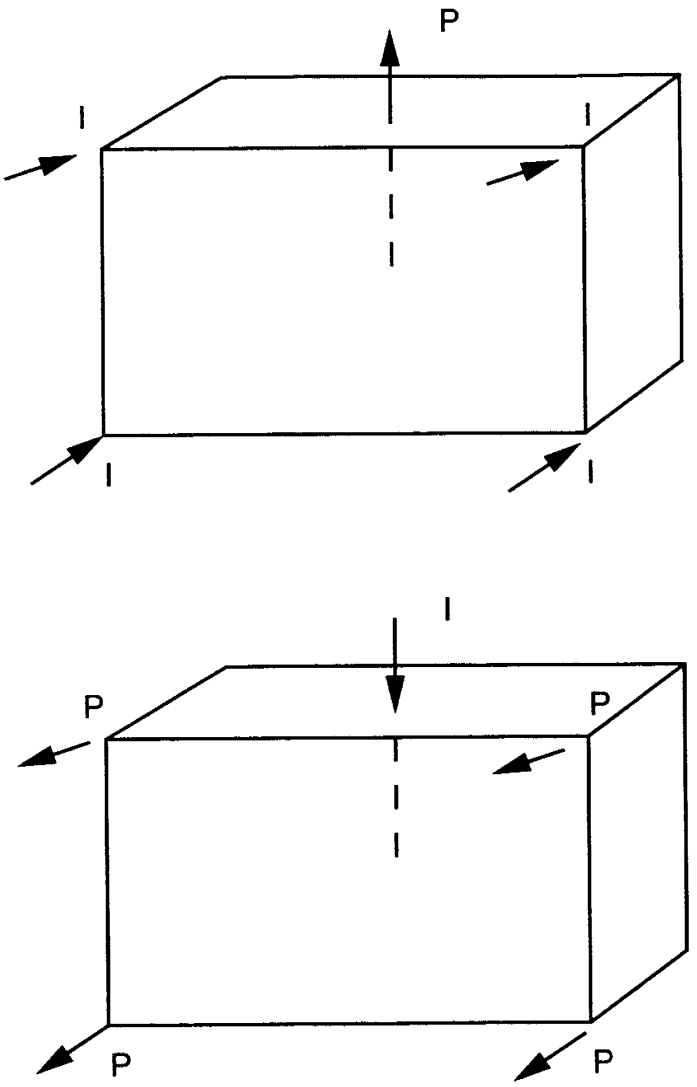

Figure 4.2: Injector-producer configurations for saturation runs.

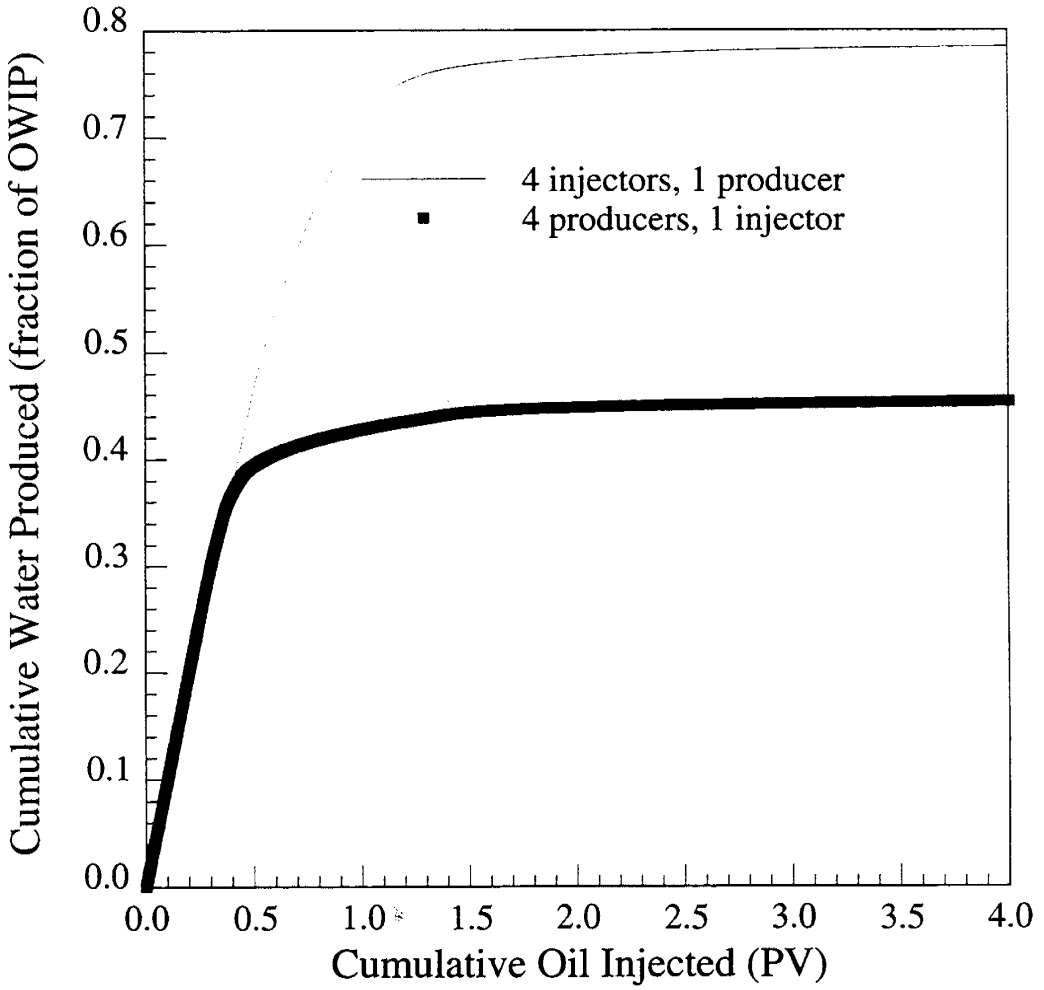

Figure 4.3: Effect of injection-production schemes on the efficiency of the saturation process.

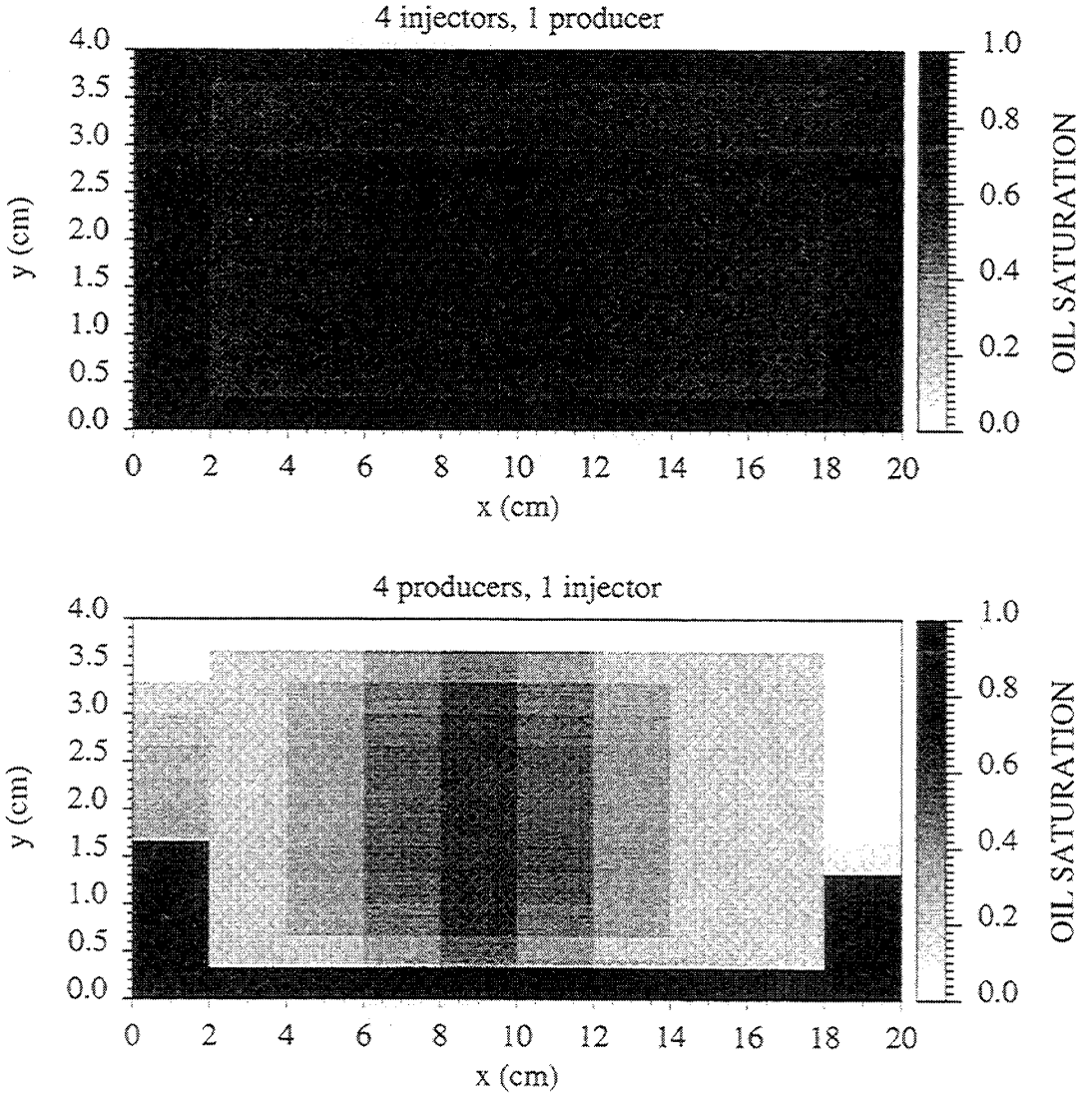

Figure 4.4: Oil saturation maps at 5.5 PV oil injected for saturating the model.

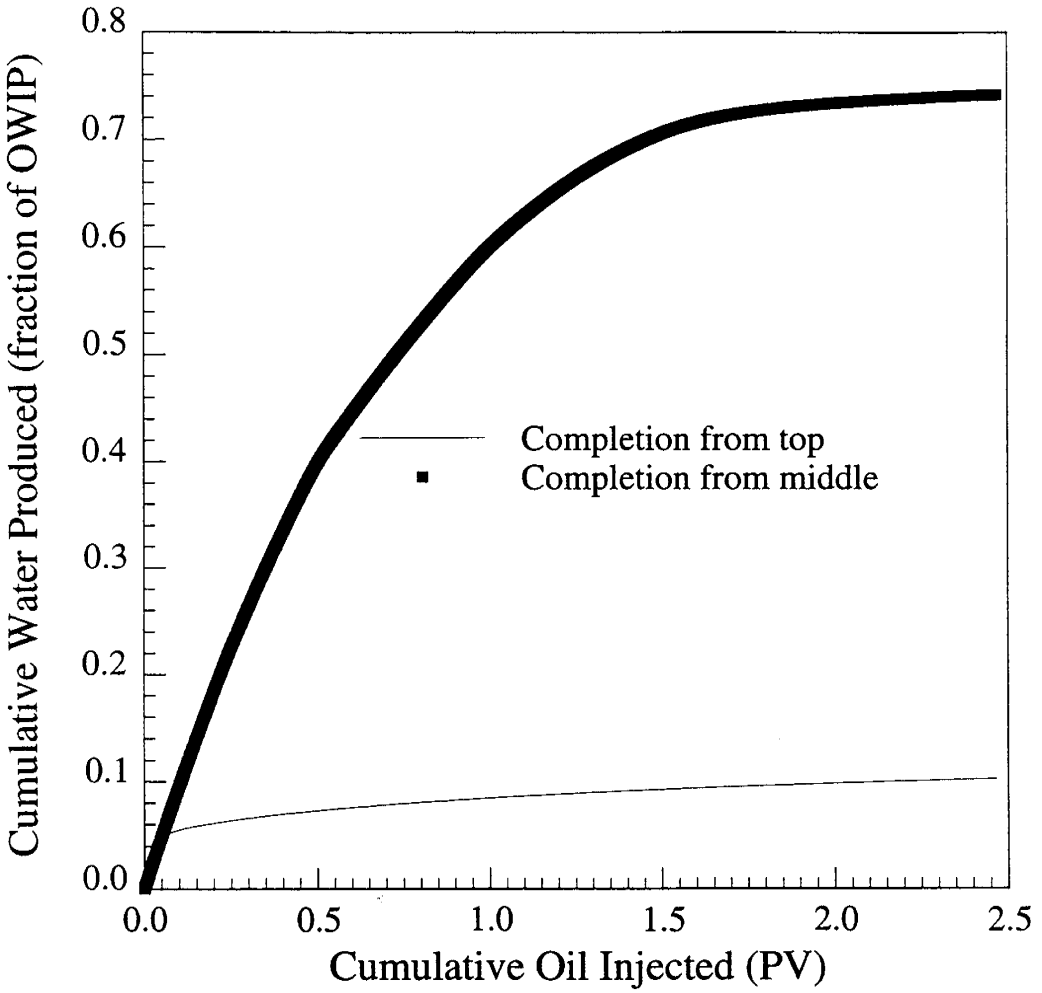

Figure 4.5: Effect of producer completion locations on the saturation process.

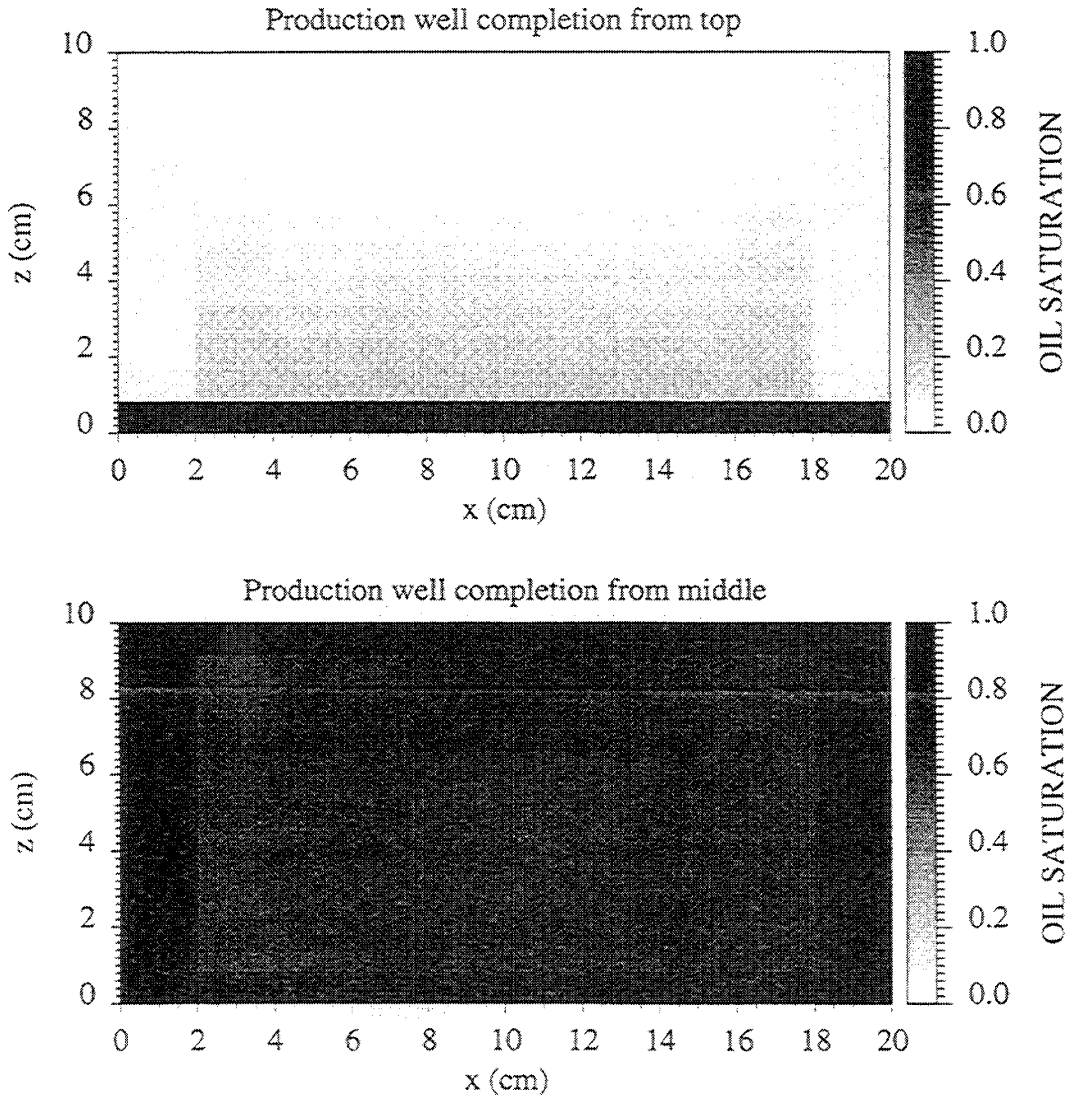

Figure 4.6: Oil saturation maps at 3.7 PV oil injected (Effect of producer well completion location).

the producer was completed at the top, only the fracture at the bottom is filled 100% with the oil, the rest of the system still has a high water saturation.

Another important design consideration is the well locations for cleaning the system after each run. The model has to be cleaned thoroughly of oil, and resaturated with water after each steam injection run, so that the same saturation distribution can be achieved for the start of each run. This cleaning process should be done in-situ without disassembling the core holder. To simulate the cleaning procedure, the pseudo-miscible option of a black oil simulator, ECLIPSE [30], was used.

At the beginning of the simulation run, the system had the saturation distribution similar to the end of a steam injection experiment, where oil had not been displaced thoroughly. Mineral spirits, a solvent used in the laboratory, is injected into the model until oil has been displaced completely. The best results were again obtained with the configuration of four injectors at the corners and one producer in the center.

Figure 4.7 shows the cumulative oil removed as a function of solvent injected. Nearly 100% of the oil was displaced by the solvent for the case with four injectors and one producer. A sensitivity study on production well completion locations gave similar results to the runs for saturating the model. A production well in the middle layer gave the best results. Figure 4.8 shows the comparison of different completion locations for the producer. When the producer was completed at the middle layer, 100% of the oil could be removed. Notice that, even with this configuration, over 30 PV are required to remove all the oil.

4.2 Analytical Heat Transfer Calculations

Analytical heat transfer models were used to predict the maximum expected heat losses from the model to determine the minimum insulation thickness and to determine the time at which steady state is reached.

The reason behind using analytical heat transfer models instead of simulations was because Joshi [48] found that it was not possible to simultaneously predict the experimental heat loss and the displacement by simulator models. Joshi's conclusions are confirmed later in Chapter 8, where the simulator heat loss models, and their

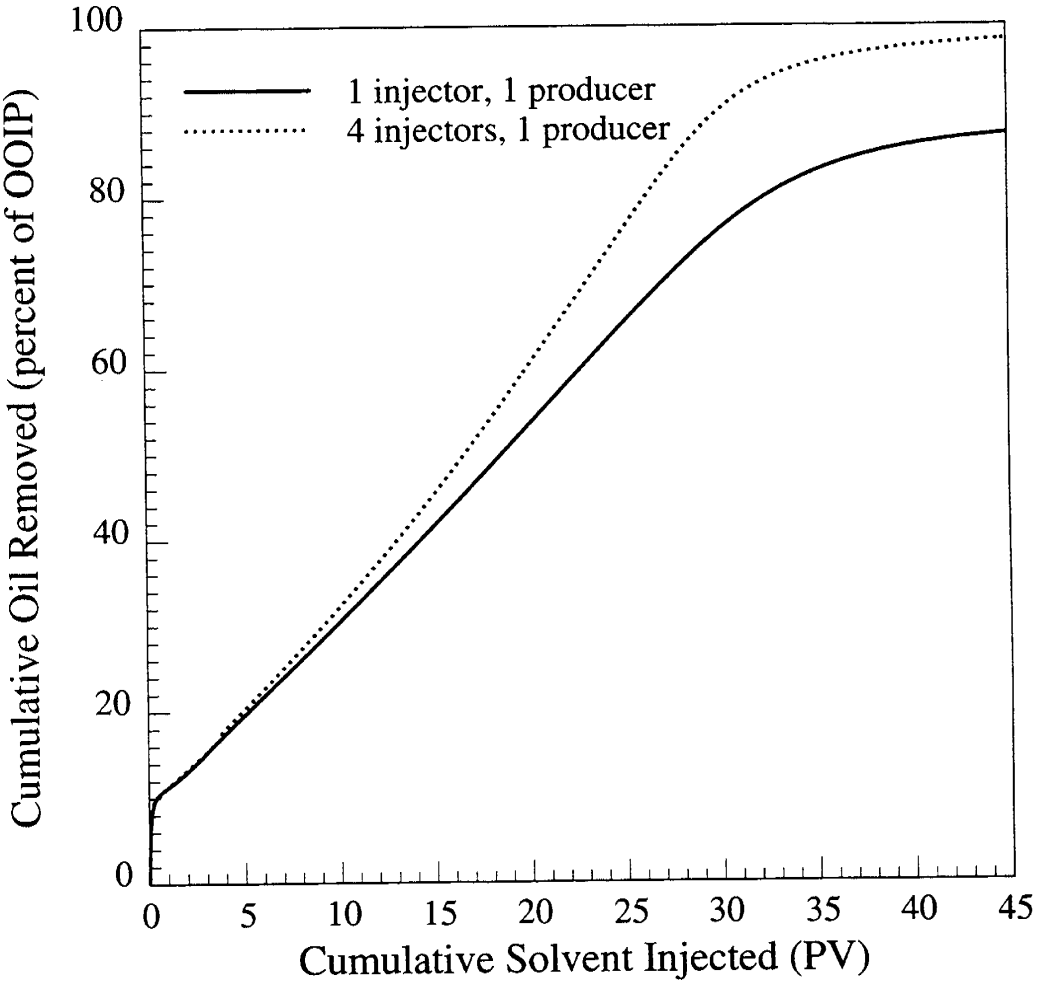

Figure 4.7: Comparison of injection-production schemes for cleaning the model.

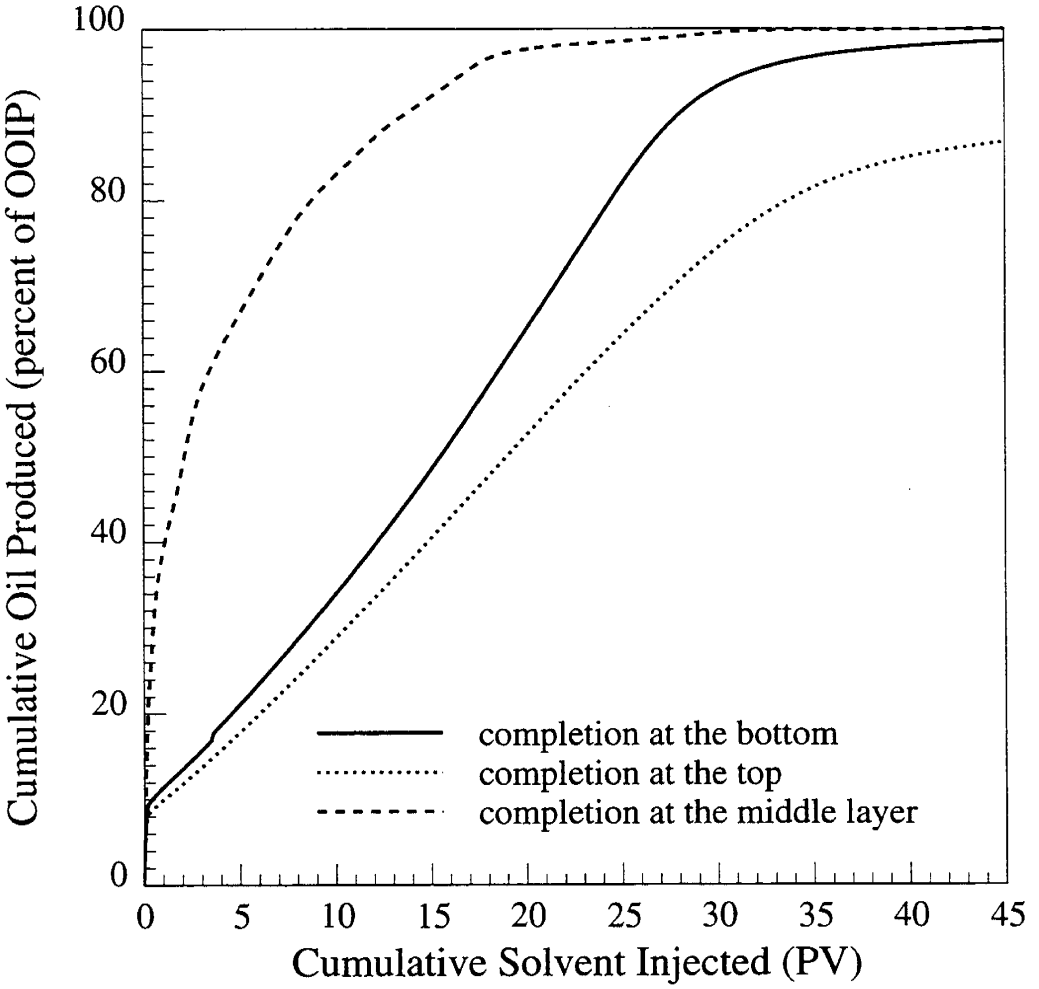

Figure 4.8: Effect of well completion locations on the efficiency of the cleaning process.

validity for simulating laboratory models, are discussed in some detail.

The analytical heat transfer models used for the experimental design will be discussed in the next two sections for steady state and transient heat losses.

4.2.1 Steady State Heat Transfer

In the design of a model for a steam injection run, the maximum heat loss should be calculated to determine the minimum insulation thickness to assure that a steam zone could develop at the minimum planned steam injection rate. Demiral et al. [24] followed a similar procedure in the design of their laboratory model and found that steady state heat losses calculated to determine the insulation thickness were higher than the actual experimental heat losses. Therefore, the insulation thickness calculated by this approach is likely to be conservative enough for model design.

The assumptions that were used in steady state heat loss calculations can be summarized as follows.

- Rock and fracture are at steam temperature.
- Ambient temperature is constant.
- There is conductive heat transfer between the layers of insulation and convective heat transfer between the insulator and the ambient air.

The model consists of two layers. The first layer is the polysulfone core holder which has a fixed thickness. The second layer is the Fiberfrax insulation, the thickness of which should be determined based on the heat loss calculations. The polycarbonate layer behind the polysulfone was not considered in these calculations. As a result, the calculated heat losses should be maximum values.

Since the model is not one dimensional, some kind of a shape factor should be incorporated into the one-dimensional heat loss equation. Heat loss is given by,

$$q = K\Delta T \tag{4.1}$$

where,

q	=	heat loss per unit area
K	=	thermal conductance
ΔT	=	temperature difference

The shape factor for a parallelepiped shell, given by Rohsenow and Hartnett [70], is used in the calculations. The equation for the shape factor is :

$$K = \lambda \left[\frac{S_1}{\delta} + 2.16(a + b + c) + 1.20\delta \right] \tag{4.2}$$

where,

λ	=	thermal conductivity
S_1	=	total inner surface area of the shell
δ	=	thickness of the shell
a, b, c	=	dimensions of parallelepiped

and a, b and c dimensions are shown in Fig. 4.9.

Figure 4.10 shows the steady state heat losses calculated at different injection rates against different Fiberfrax insulation thicknesses. When we look at the curve for the lowest injection rate of 1 cc/min, it is clear that an insulation thickness of at least 0.75 cm is needed to overcome the heat losses at 1PV injected. If higher rates are used in the experiment, Fiberfrax insulation may not even be needed to overcome the heat losses.

4.2.2 Transient One-Dimensional Heat Transfer

Transient heat losses from the system were calculated by solving the one-dimensional transient heat conduction equation. The aim was to determine the time at which the heat loss curves reach steady state.

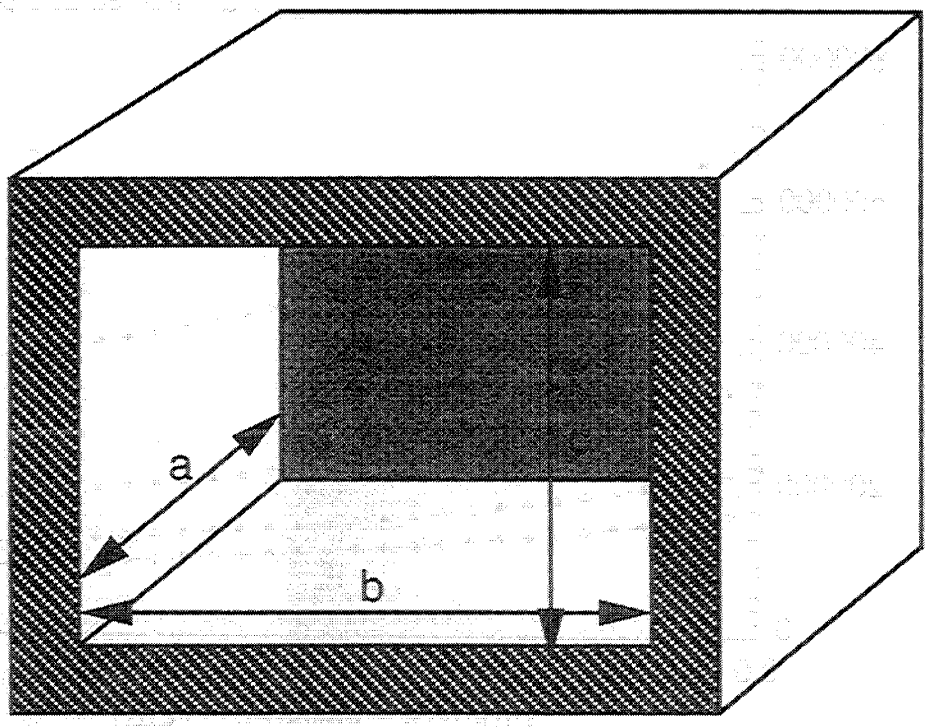

Figure 4.9: Parallelepiped shell model used in the steady state heat loss calculations.

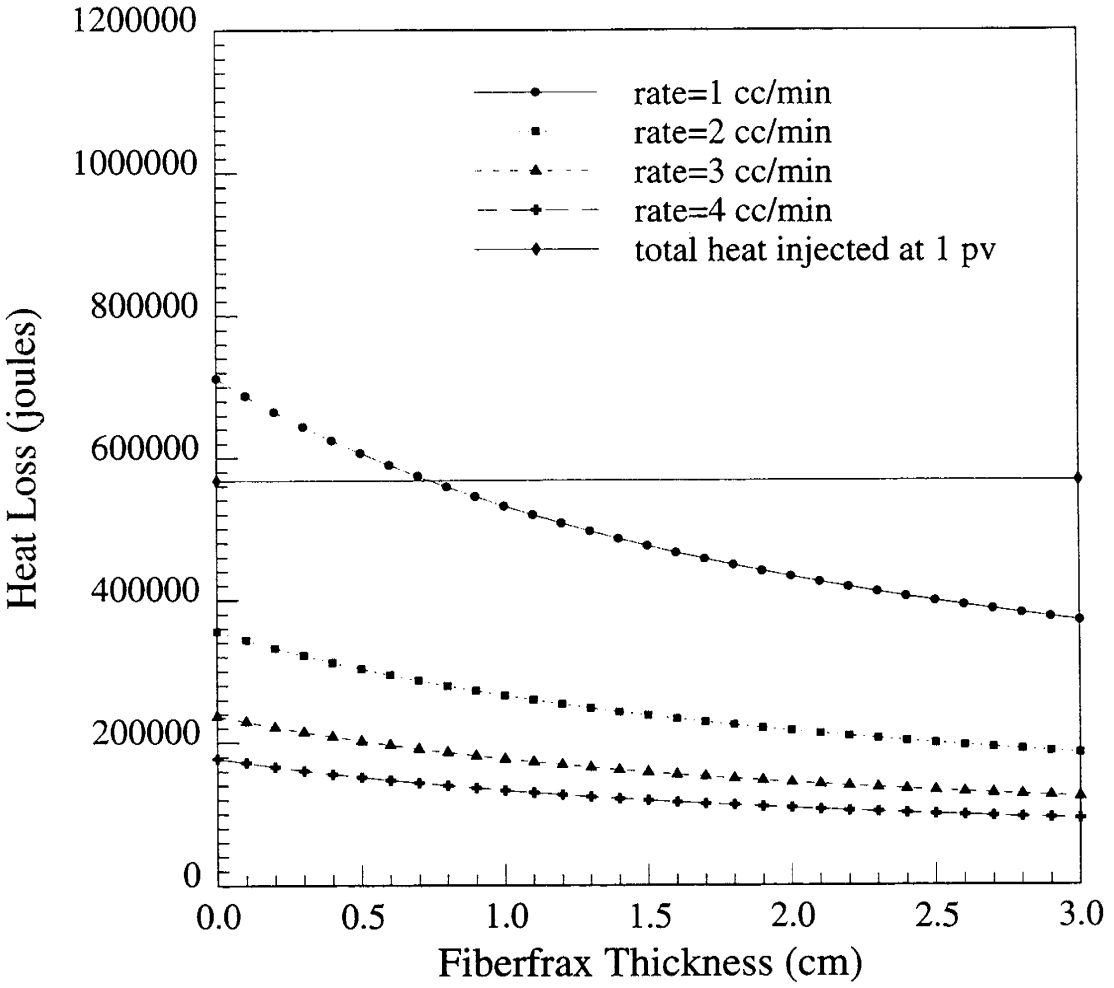

Figure 4.10: Effect of insulation thickness on the steady state heat losses at different rates.

The equation to be solved is given in its general form by,

$$\frac{\partial^2 T}{\partial x^2} = \frac{1}{\alpha}\frac{\partial T}{\partial t} \tag{4.3}$$

where,

T	=	temperature
x	=	distance
t	=	time
α	=	thermal diffusivity

The dimensionless form of the above equation was solved for six cases with two different boundary conditions.

- Case 1: One layer of insulation (infinite polysulfone and constant temperature inner boundary condition).
- Case 2: Two layers (polysulfone and Fiberfrax), constant temperature inner and outer boundary conditions.
- Case 3: Two layers (polysulfone and Fiberfrax), convective inner and outer boundary conditions.
- Case 4: Two layers (polysulfone and infinite Fiberfrax), constant temperature inner boundary condition.
- Case 5: One layer (polysulfone), convective outer boundary condition, constant temperature inner boundary condition.
- Case 6: Three layers (polysulfone, polycarbonate and Fiberfrax), constant temperature inner and outer boundary conditions.

For the cases with constant temperature inner and outer boundary conditions, the inner boundary condition was taken as steam temperature and the outer boundary

condition was taken as the ambient air temperature. When the convective boundary conditions were used at the inner and outer boundaries, they can be written as,

$$\text{at } x = 0 \quad h_{f_1}(T_s - T_1) = -\lambda_1 \frac{\partial T_1}{\partial x} \tag{4.4}$$

$$\text{at } x = b' \quad h_{f_2}(T_2 - T_\infty) = -\lambda_2 \frac{\partial T_2}{\partial x} \tag{4.5}$$

where,

h_{f_1}	=	convective heat transfer coefficient from the system to the insulation
h_{f_2}	=	convective heat transfer coefficient from the insulation to the surroundings
λ_i	=	thermal conductivity of each layer (i=1,2 or 3)
T_s	=	steam temperature
T	=	temperature
T_∞	=	ambient air temperature
x	=	distance
b'	=	total thickness of the insulation

The Laplace transformation method was used in the solution of the transient heat conduction equation and the solutions in Laplace space were inverted by the Stehfest Algorithm [81]. Figure 4.11 shows the dimensionless cumulative heat losses calculated from the six different cases (with different boundary conditions).

When the two infinite insulation solutions, (Cases 1 and 4) were compared, it was observed that adding an additional layer of insulation to the system decreased the heat loss. The two-layer solution gave less heat loss than the single layer solution due to increased thermal resistance. For these cases of course, steady state never developed as shown by the continuous decrease in heat loss rates given in Fig. 4.12. Steady state is characterized by a plateaus in the dimensionless heat loss rate curves of the finite systems (Fig. 4.12).

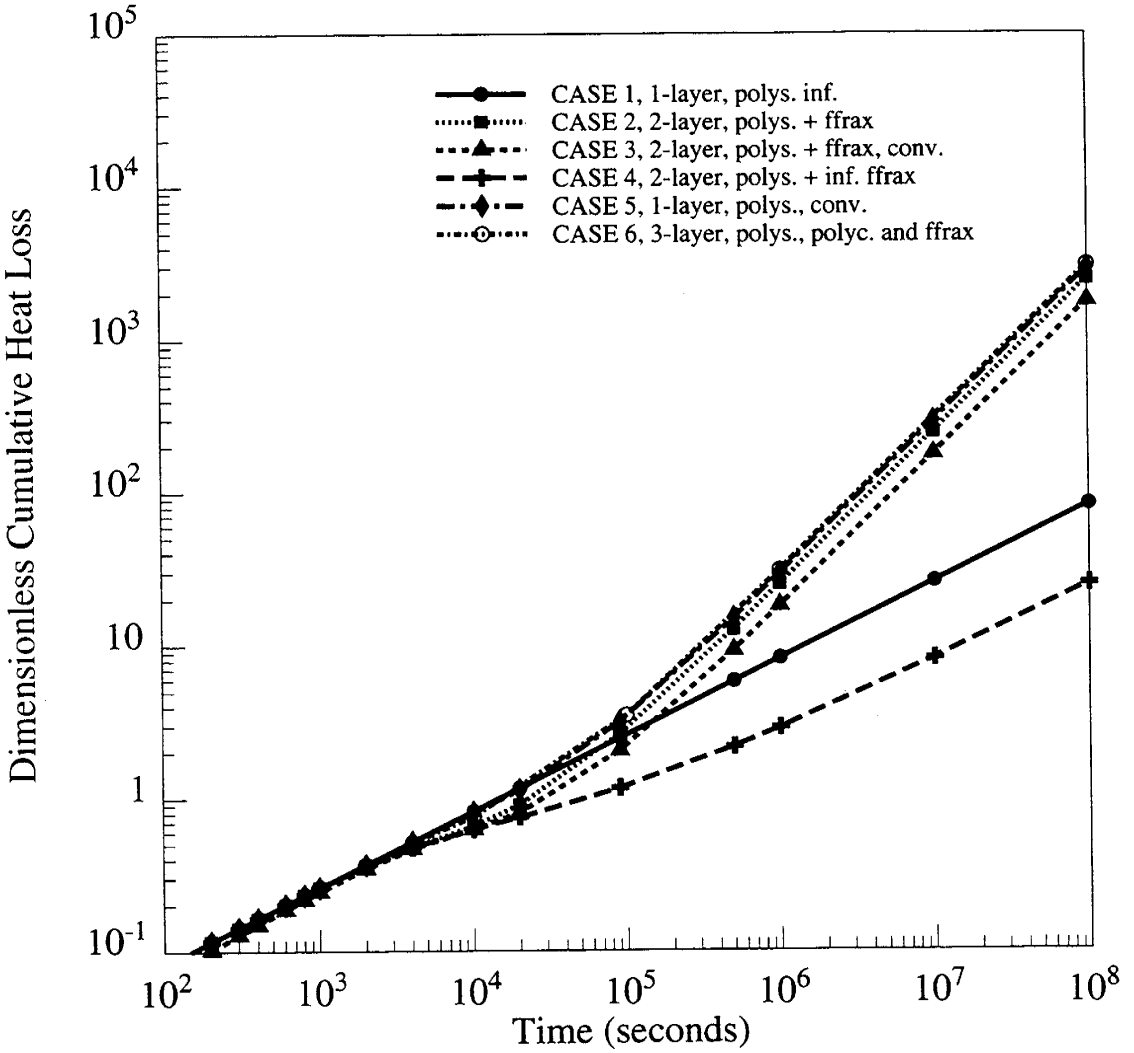

Figure 4.11: Dimensionless cumulative heat loss calculations from transient conduction equation.

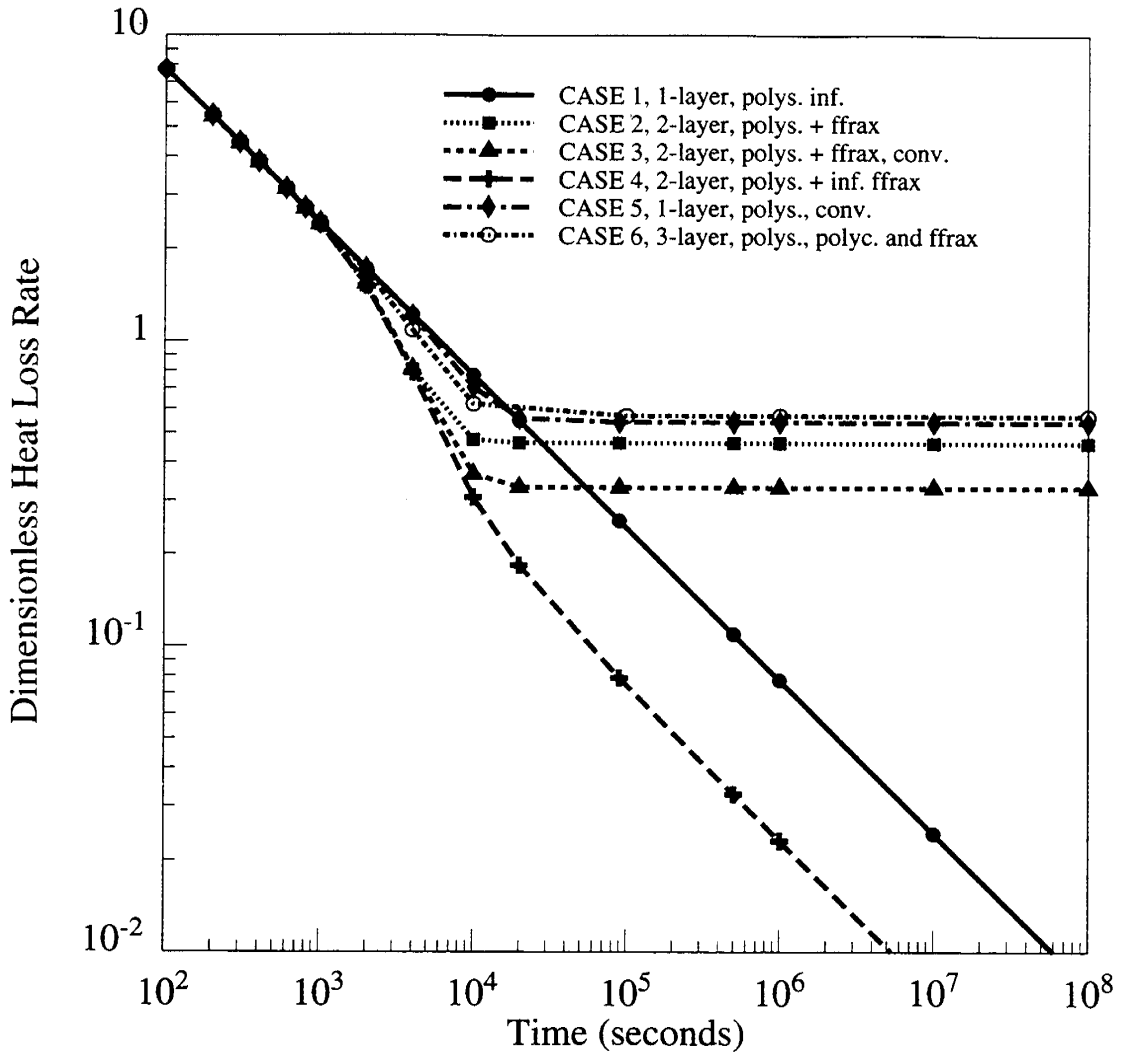

Figure 4.12: Dimensionless heat loss rate calculations from transient conduction equation.

Among the cases with finite insulation thickness with constant temperature inner and outer boundary conditions (Cases 2 and 6), the three layer solution showed a cumulative heat loss slightly higher than the two layer solution. This unexpected behavior is due to the thickness of the third layer which was decreased in Case 6 to keep the total thickness the same as in Case 2. The difference in the cumulative heat losses calculated from the two layer and three layer solutions were not very significant. Using a two layer solution may be appropriate to model the heat losses from the experiment.

The only differences between Case 2 and Case 3 are the inner and outer boundary conditions. Case 2 has constant temperatures at the inner and outer boundaries, while Case 3 has convective boundary conditions. The cumulative heat loss calculated for Case 3 was slightly less than Case 2 due to the extra resistance from the film layer. Even the one-layer solution with a convective outer boundary condition shows a heat loss rate less than the 3-layer solution with constant outer boundary conditions, due to this extra resistance from the film layer.

One common feature of all the cases with finite insulation thicknesses is that it takes nearly three hours to reach steady state. The estimated time to reach steady state is relatively large with respect to the estimated duration of the experiments. This shows that neglecting the early time behavior, in modeling the experimental heat losses, is a bad assumption for this problem.

The heat transfer calculations discussed in Section 4.2 were done to get a feel about the heat losses expected in the experiment to help in the design of the insulation for the core holder. Actual measured heat losses were later modeled analytically with more complex boundary conditions. These results will be discussed in Chapter 8.

Chapter 5

Experimental Apparatus

The description of the experimental apparatus used in this study, will be given in the following sections.

- Core holder
- Fluid injection system
- Fluid production system
- Temperature, heat flux and pressure measurement
- Data acquisition system

The schematic of the entire experimental system is shown in Fig. 5.1. Appendix A lists the specifications and distributors of the equipment and parts used, and the commercial suppliers. A detailed discussion follows.

5.1 Core Holder

Since a CT scanner is used to measure saturations in the core, core holder material has to be transparent to X-rays. Furthermore, heat losses must be small compared to injected heat. Therefore, metals were not considered for the core holder material. Different high temperature plastics were considered. Polysulfone, which is a high

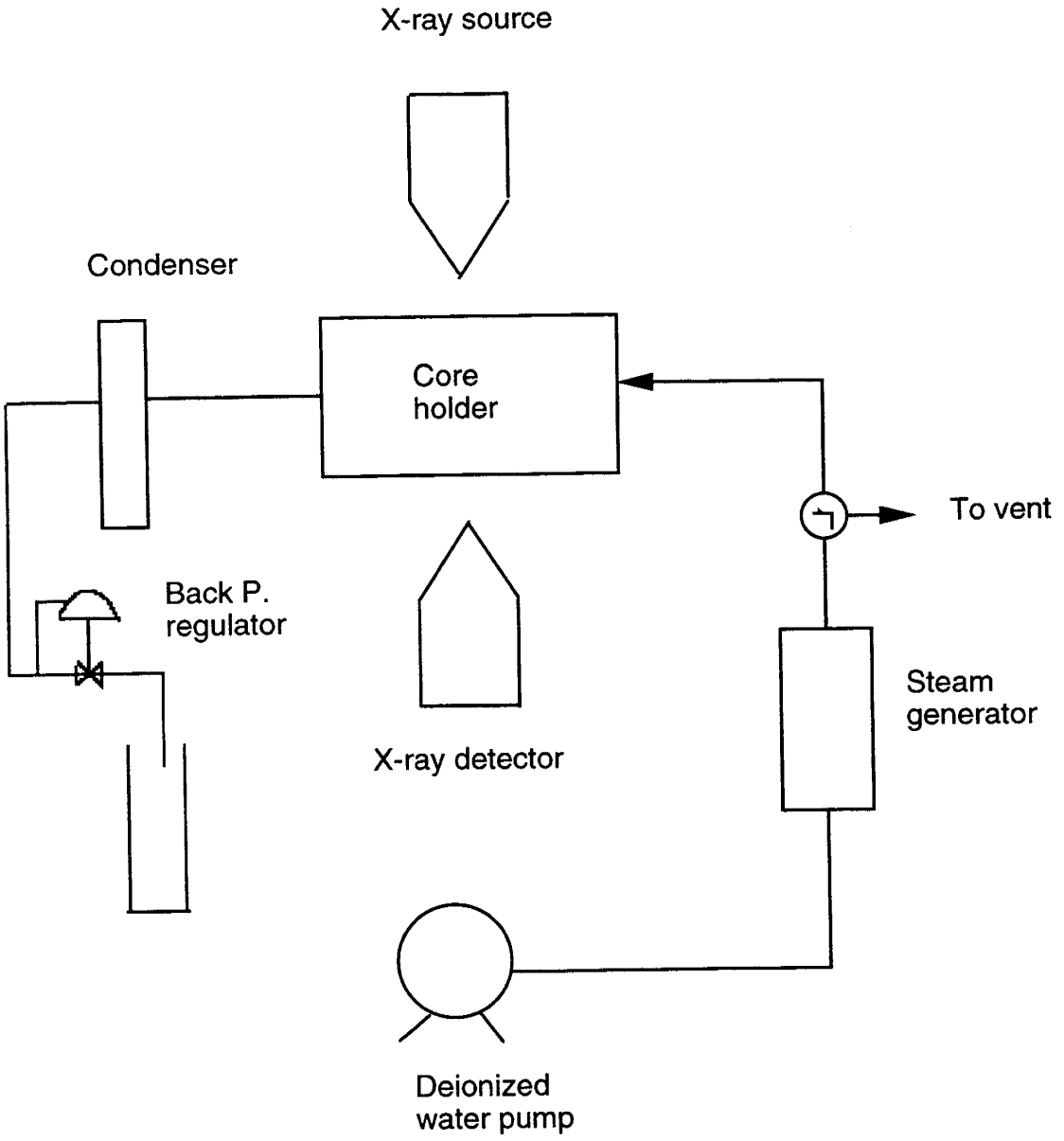

Figure 5.1: Overall schematic of the experimental set up.

strength, transparent thermoplastic having an operating temperature range between $-150°$ F and $300°$ F was chosen for the core holder material. Basically the term, polysulfone, denotes a class of polymers prepared by radical-induced copolymerization of olefins and sulfur dioxide [58].

Polysulfone has a low thermal conductivity which is essential for controlling the heat losses. It can also handle high temperatures and the operating pressures (30 psig maximum). It is resistant to steam and is compatible with the solvents, alcohols and oils that are used in the laboratory experiments. It also has a low thermal expansion coefficient, which enables us to control the fracture aperture at high temperatures.

The external dimensions of the core holder frame are $25.5 \times 3.7 \times 15.5$ cm. Its wall thickness is 2.8 cm. It is rectangular in shape and a Boise sandstone slab of dimensions $19.9 \times 3.55 \times 10$ cm is placed inside it. Polysulfone spacers, of 0.07 cm thickness, are put between the core and the core holder to form a clear space to simulate the fractures on all six sides. They are square shaped with an area of a little less than 1 cm^2. They are placed on the sides of the model, two on each side halfway between the thermocouple locations at all sides. Figure 5.2 shows the front view of the core holder frame with the core placed inside.

Back and front plates of the core holder are removable and are also made of polysulfone. Sealing between the back and front plates and the frame is made possible by using silicone engine gaskets applied to both sides of the frame. Spacers of 0.07 cm thickness are put between the front and back plates and the core to simulate the fractures in that direction. The polysulfone plates are 2 cm thick. Additional polycarbonate plates of 1 cm thickness are put on the outside of the polysulfone plates to provide extra resistance against internal pressure forces. The polycarbonate plates are located only on the front and back faces of the model since they have the largest area exposed to internal pressure. Figure 5.3 shows the front view of the core holder with the polycarbonate plate visible.

Twenty 3/8" OD bolts (as indicated by the bolt holes in Fig. 5.3) made of Torlon are used to squeeze the gasket and seal the model. Torlon was chosen because of its high tensile strength, which yields less under temperature and pressure than other plastics. To avoid bulging of the front and back plates under pressure, four aluminum

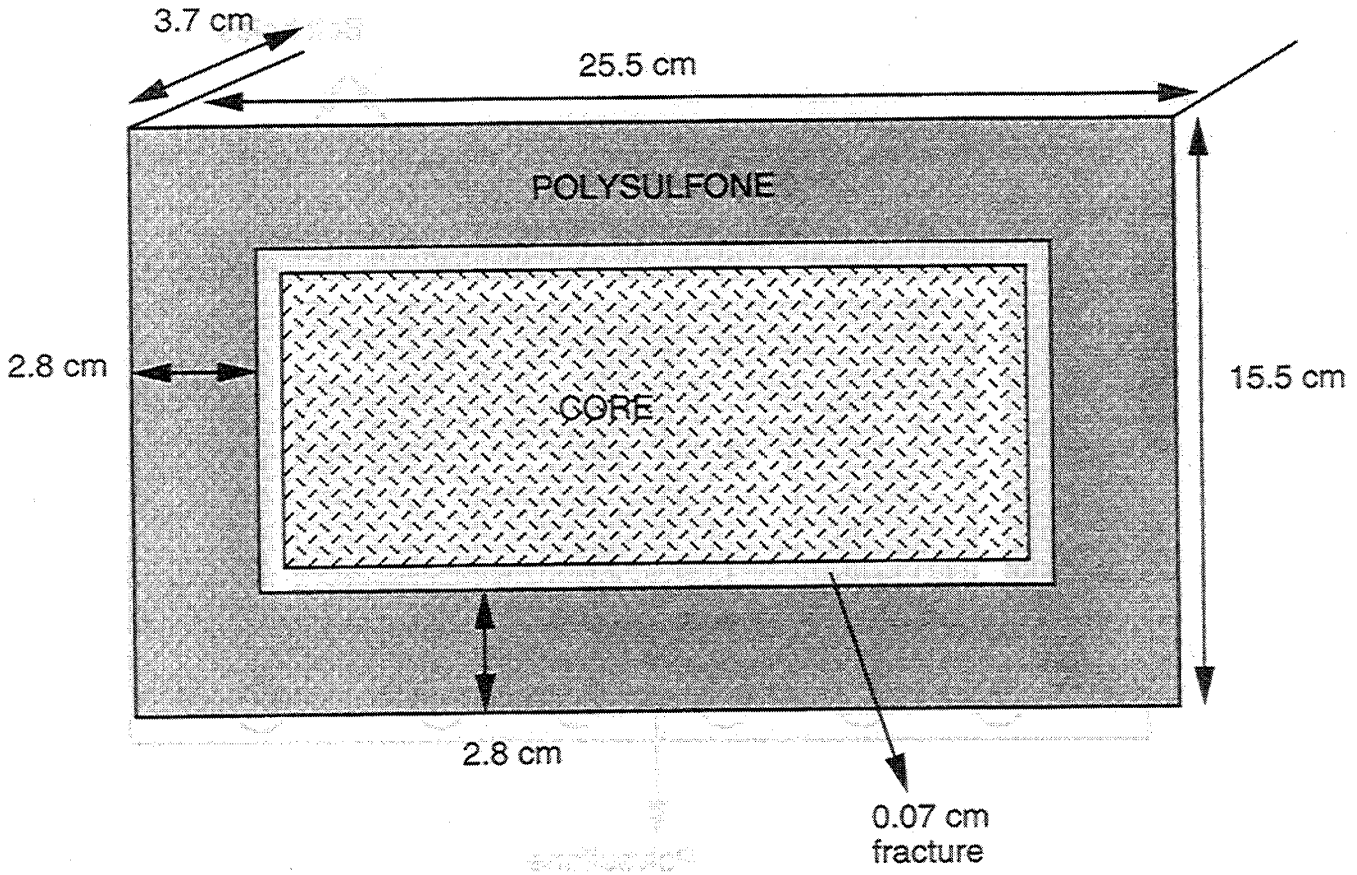

Figure 5.2: Front view of the core holder frame and the core.

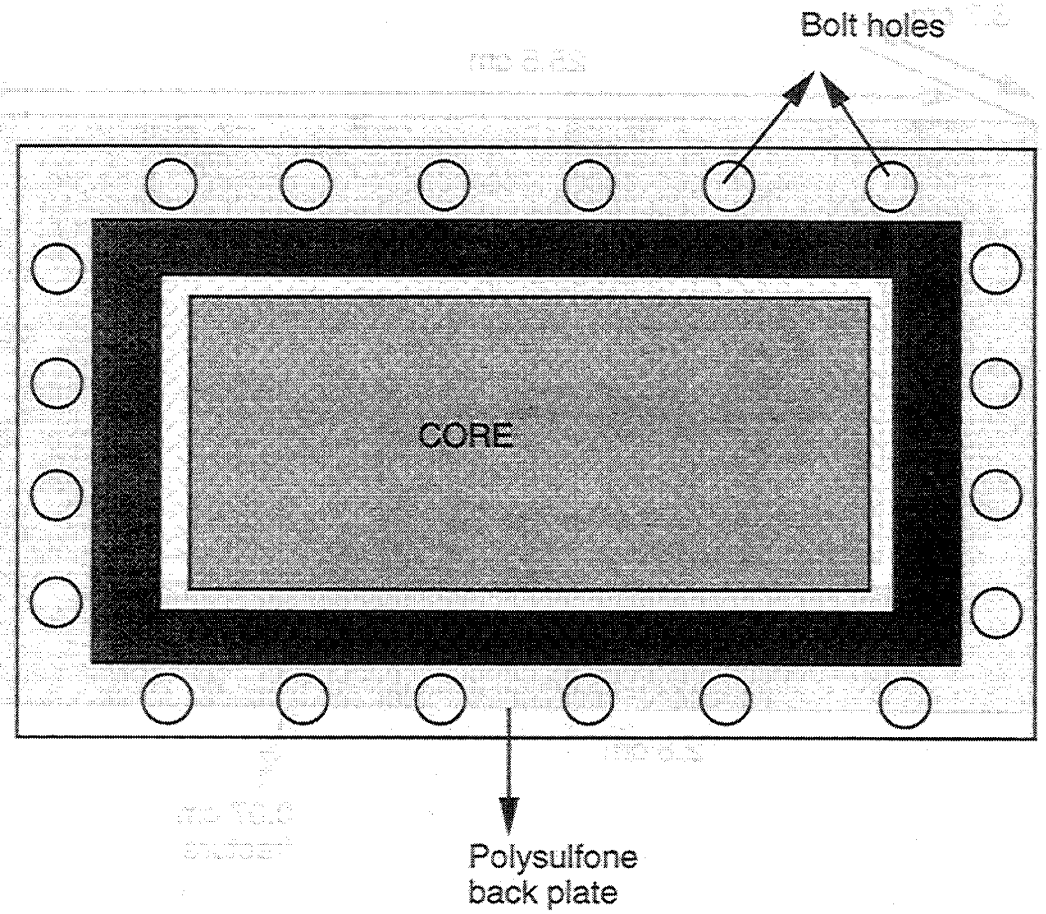

Figure 5.3: Front view of the core holder showing the back plate and the frame.

slabs of square cross section were assembled on the front and back plates. Figure 5.4 shows a front view of the core holder, with locations of the bolts and aluminum slabs.

Pressure is measured in two locations and temperature is measured at thirteen locations in the core holder. To seal the pressure ports and the thermocouples, 1/16" ID fittings are used in the core holder. Due to scanner restrictions, only plastic fittings were considered. Since the thermal expansion coefficient of polysulfone is low compared to conventional nylon Swagelok fittings, they can cause cracks in the polysulfone, as proven by a test on a prototype polysulfone model. Therefore, chromatography fittings made of PEEK were used, since PEEK has a low thermal expansion coefficient. Top, bottom and end views of the core holder show the locations of the thermocouple and pressure fittings more clearly (Figs. 5.5 and 5.6).

All the fittings are located at the center plane of the core holder, to enable scanning at both sides of the fittings. Two pressure taps of 1/16" OD PEEK tubing are located at the top of the model extending into the center of the core (Fig. 5.5). The taps are also used as auxiliary wells during the cleaning and saturation processes, which will be described in the following sections.

There are four wells located at the corners of the core holder. These can be used interchangeably for different injection-production schemes. During a steam injection experiment, to be discussed later, there is one injector and one producer, located diagonally. All of the corner wells are vertical and perforated in such a way that we can inject into and produce from the fracture itself. The two auxiliary wells that are used as pressure ports can also be used as producers or injectors in the center of the core.

To fix the core holder on the scanner table, two plates were manufactured from thick aluminum sheets, to be attached to the front and back polycarbonate plates on the core holder and also to the scanner positioning table. Semi-circular shaped fire bricks were also assembled at the top and bottom of the core holder to eliminate some of the scanning artifacts due to its rectangular geometry. Figure 5.7 shows a sketch of the front view of the core holder with fire bricks.

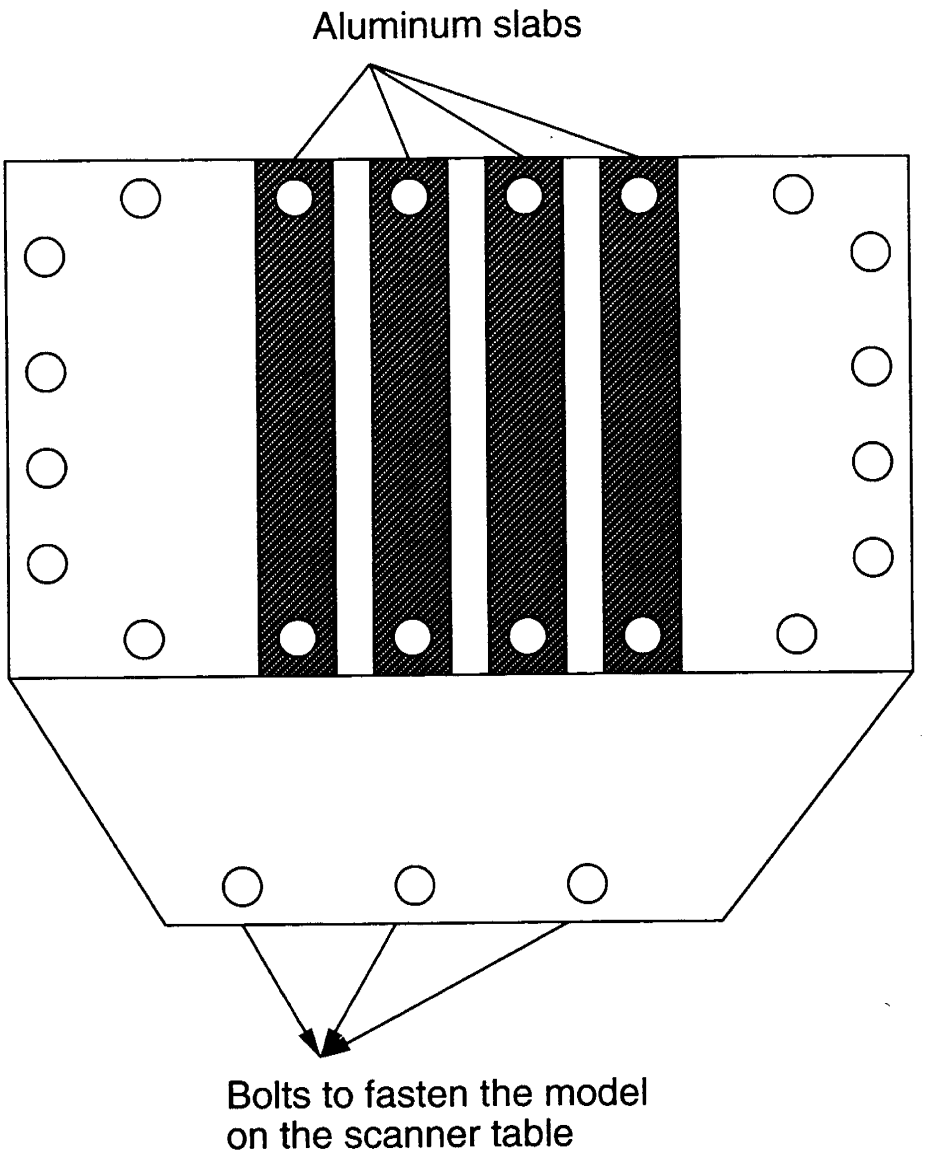

Figure 5.4: Front view of the assembled core holder.

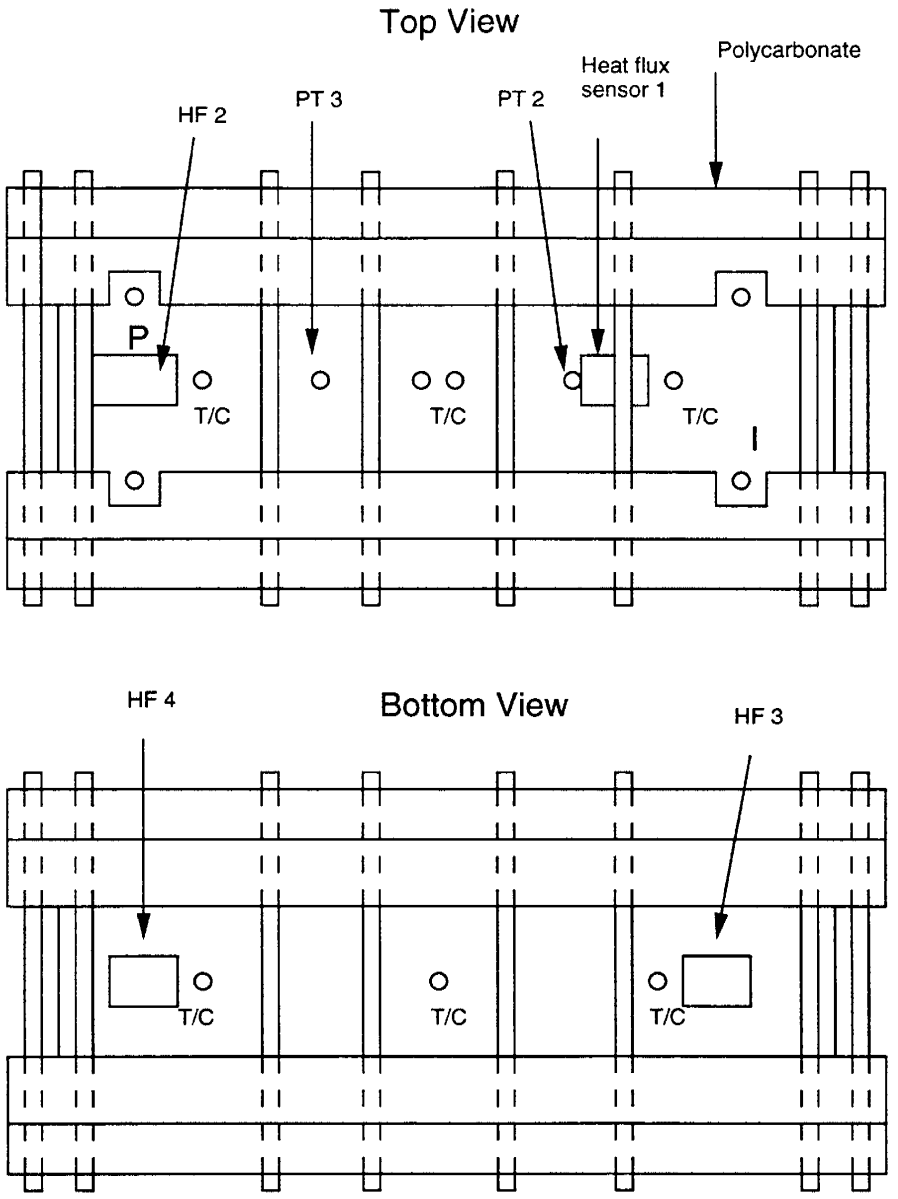

Figure 5.5: Top and bottom views of the assembled core holder.

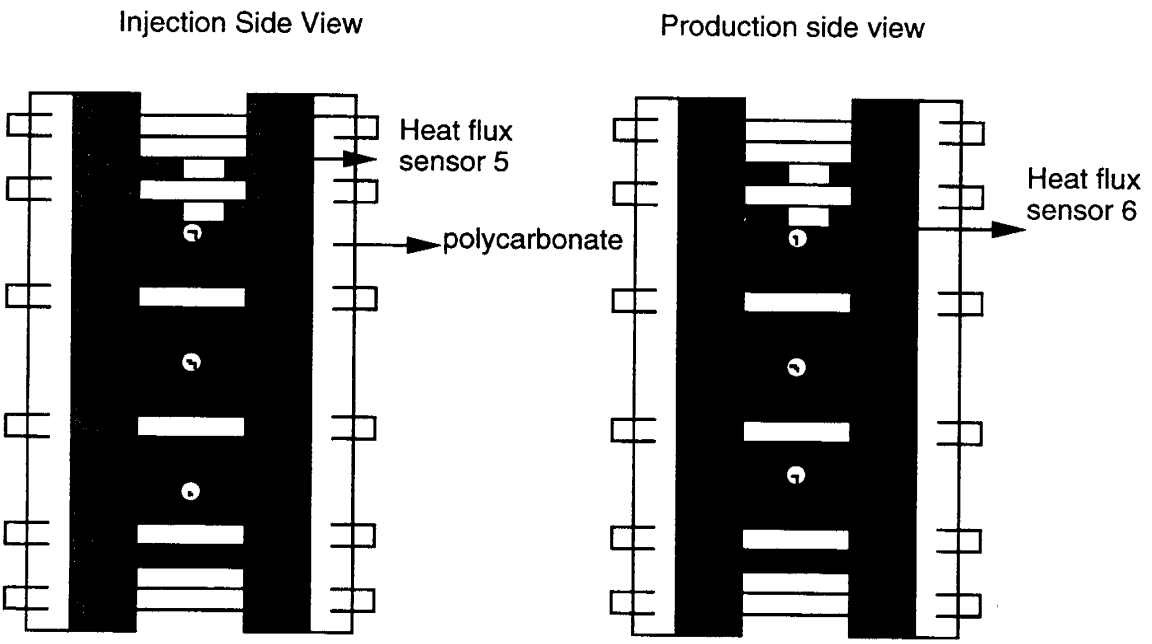

Figure 5.6: End views of the assembled core holder.

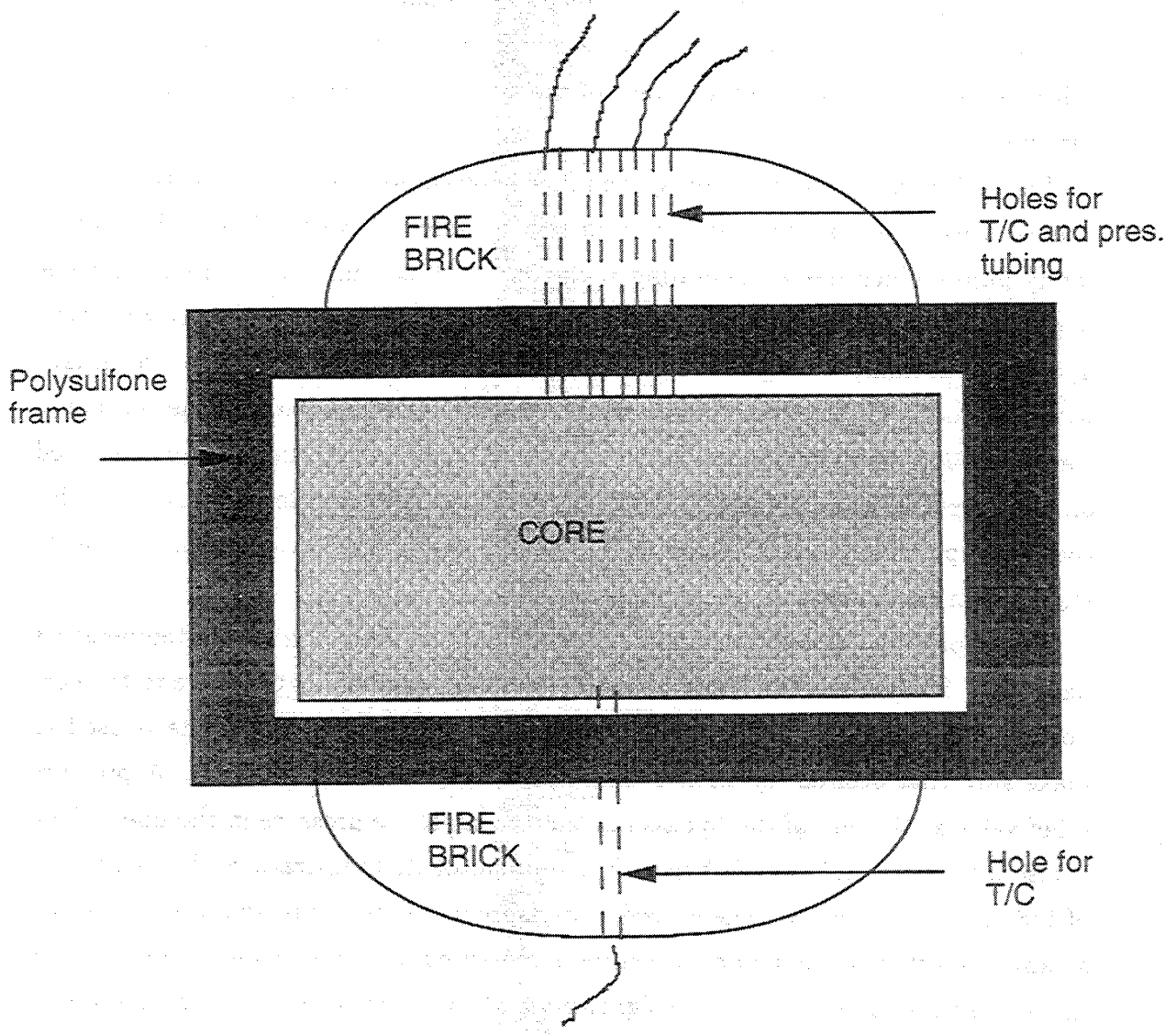

Figure 5.7: Sketch showing the front view of the core holder with fire bricks.

5.2 Fluid Injection System

The fluid injection system will be described in two parts. First, the flow lines and plumbing system of the apparatus that are used in the steam injection experiments will be described. Next, are the details of the system for cleaning and saturating the core holder.

Figure 5.8 shows the injection system flow diagram for the steam injection experiments. Deionized water is pumped from a water reservoir with a liquid chromatography pump which has an operating range of 0 - 10 cc/min. An inline filter helps to eliminate contamination to the pump. Deionized water is pumped through a 1/8" nylon high pressure tubing to the steam generator. The steam generator is a furnace with a coiled 1/8" 316 SS tubing located inside. The temperature of the furnace is controlled by a temperature controller. The temperature controller is adjusted based on the response from a Type J SS thermocouple located inside the furnace. This thermocouple is kept in contact with the wall of the furnace at all times for steady state steam generation.

Water passing through the furnace is circulated through a 3-way high temperature ball valve. Steam from the steam generator is either directed by the valve to the core holder, or is vented to the atmosphere through a bypass line. This line is used to make sure that desired injection pressure and temperature is achieved. A pressure relief valve at the end of the bypass line helps control the pressure in the line. There is also a thermocouple in the bypass line to monitor its temperature. A cross fitting of 1/8" ID in the injection line is used to measure its temperature and pressure before steam is injected to the model. Pressure is measured by a gauge and temperature is measured by a thermocouple, the signal from which is displayed by a digital temperature indicator. All the injection tubing is 1/8" 316 SS from the steam generator up to the point where it enters the core holder. At that point, it is converted to 1/16" 316 SS tubing. All the injection lines are covered with fiberfrax insulation of 3 to 4 cm thickness to reduce the heat losses.

Before the injection tubing goes into the core holder, another cross fitting is used

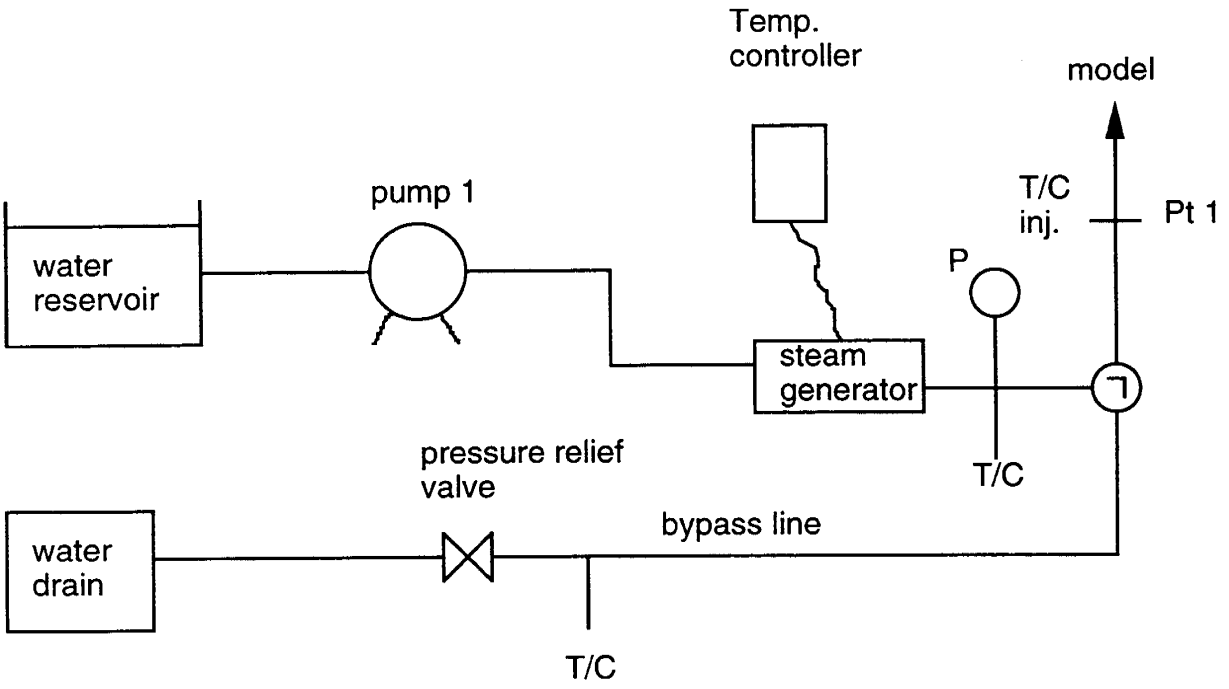

Figure 5.8: Flow diagram for injection lines (steam injection) .

Table 6.3: Permeability Measurements by Mini-Permeameter

Direction	Mean (md)	Standard deviation (md)
x	1205	295
y	1362	258
z	1077	155

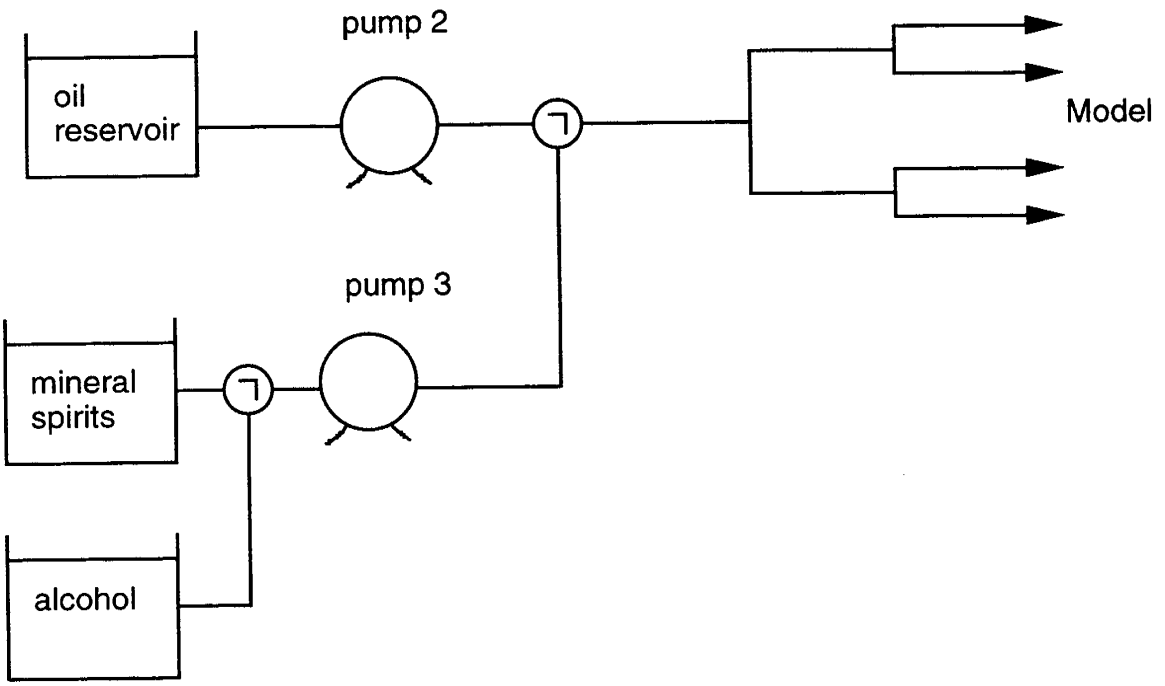

Figure 5.9: Flow diagram for injection lines (cleaning and saturating) .

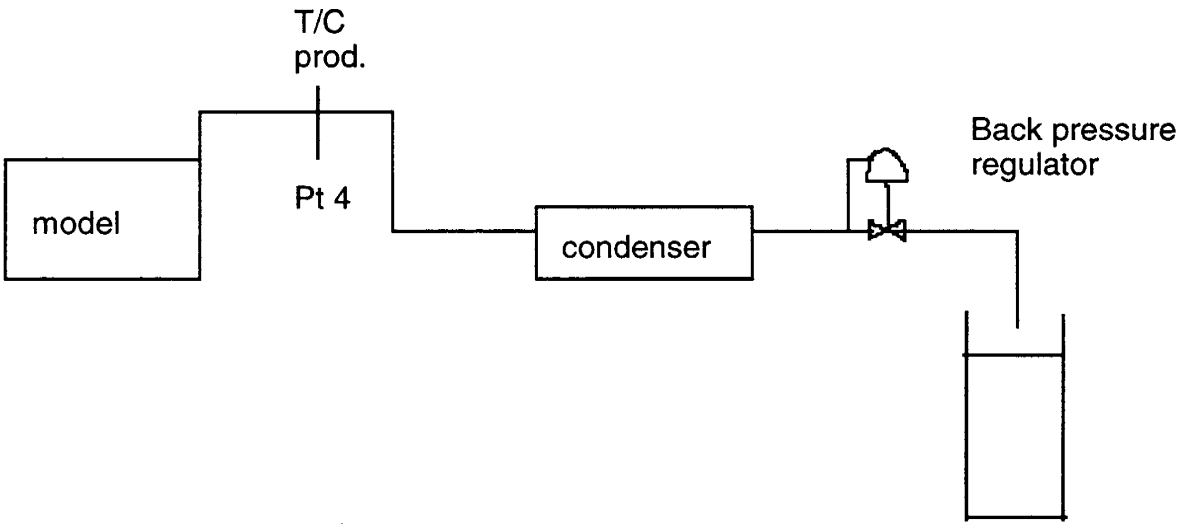

Figure 5.10: Flow diagram for production lines (steam injection) .

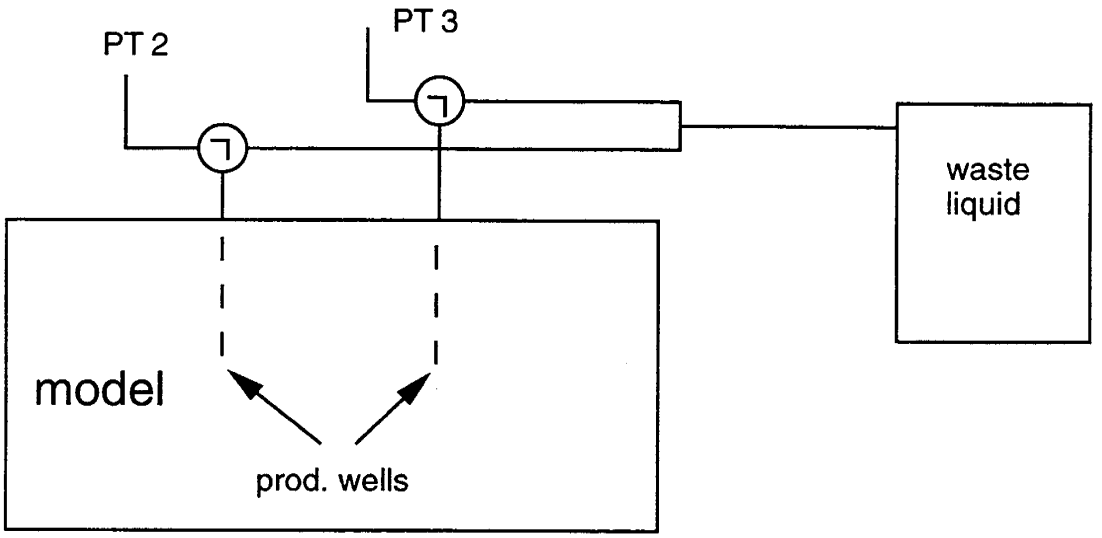

Figure 5.11: Flow diagram for production lines (cleaning and saturating) .

5.4 Temperature, Heat Flux and Pressure Measurement

Thirteen thermocouples are placed in the core holder to measure the temperature both in the core and in the fracture. The thermocouple locations were chosen so that maximum changes that take place in the core holder can be measured, as shown in Fig. 5.12. All thermocouples are 1/16" SS Type J thermocouples, and type J thermocouple wire is used to connect the thermocouple leads to the data logger.

Since heat losses from the system will be inevitable, thin film heat flux sensors are assembled on the core holder to record the heat losses. Six heat flux sensors were used in most of the experiments. Later, two more are added at the back and front plates of the core holder. Heat flux sensors are attached to the model with high temperature resistant tape. The locations of the six sensors are shown in Figs. 5.5 and 5.6. Each sensor also has a thermocouple attached to it which measures the temperature at the sensor. A detailed description of the working principles of the thin film sensors can be found in Shallcross and Wood [77].

Pressure drop along the core is measured by using four differential pressure transducers. One measures the inlet pressure, two measure the pressure at two ports along the core, and the last one measures the pressure at the outlet end. The locations of the pressure ports are shown in Fig. 5.13. The diaphragms used in the differential pressure transducers are 5, 3, 3 and 25 psi corresponding to Transducers 1, 2, 3 and 4 respectively. These pressure ranges were chosen by considering the maximum pressure drops expected at different locations along the system. A higher range is used in Transducer 4 because it measures the differential pressure to the atmosphere while the others measure differential pressures in the model.

The pressure transducers should be calibrated prior to each experiment. To make the calibration process simple, the plumbing was designed so that it is not necessary to remove the transducers to calibrate them.

Two three-way ball valves are used for each pressure transducer, as shown in Fig. 5.14. Valves A are connected either to the calibration line or to the pressure port. Valves B are either connected to Valves A or to a loop which applies zero pressure

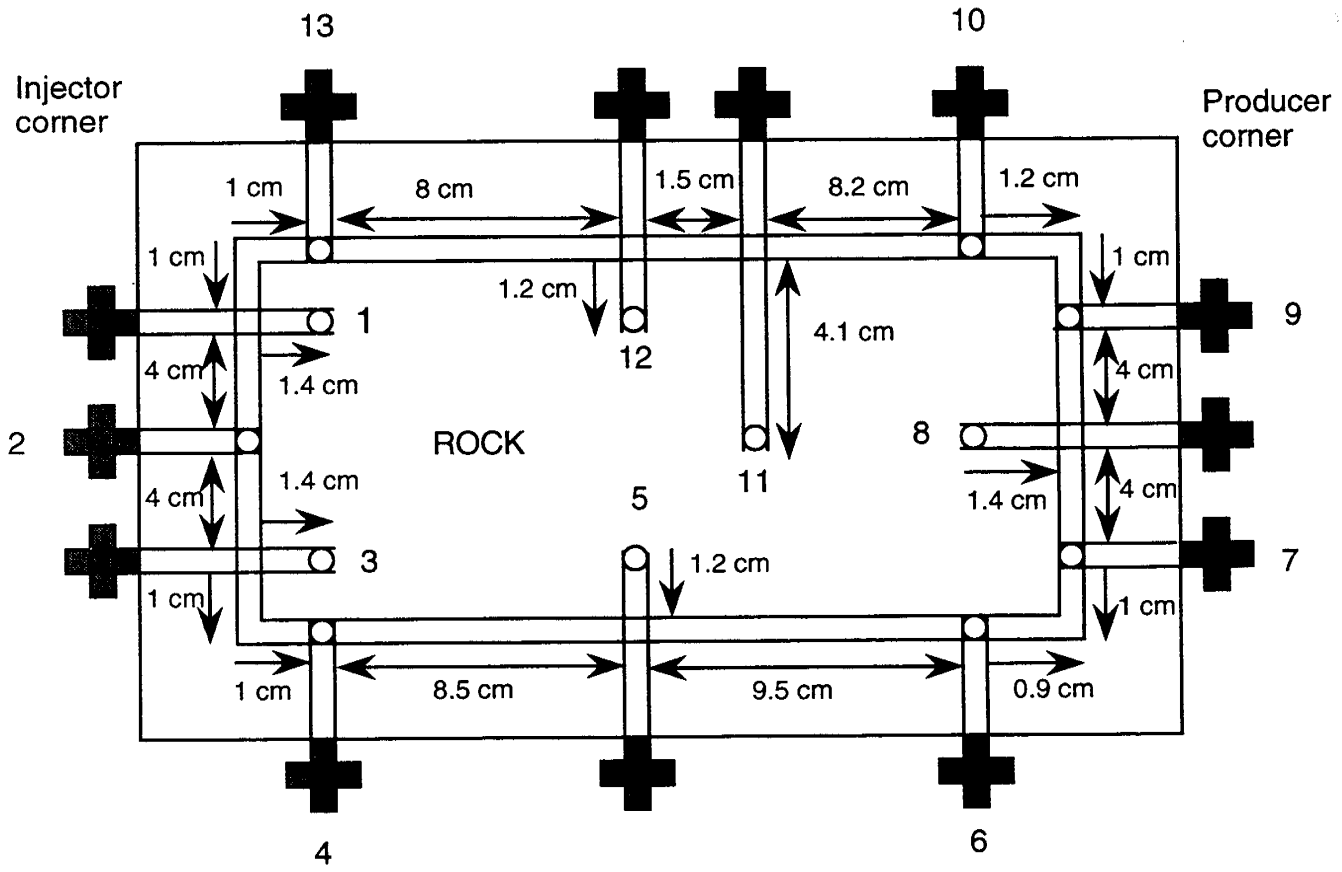

Figure 5.12: Thermocouple locations.

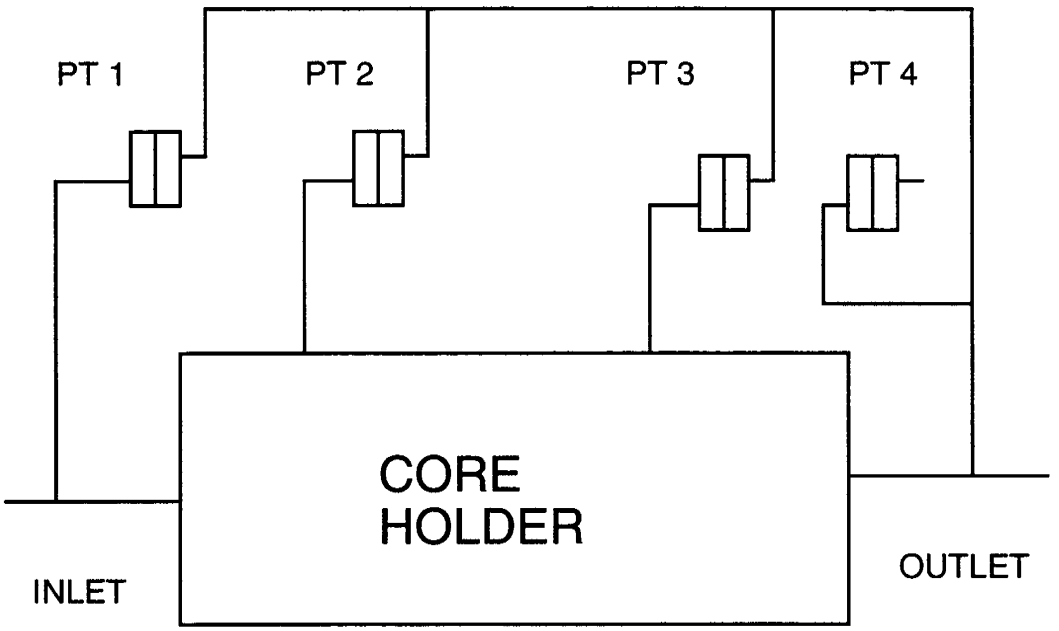

Figure 5.13: Locations of the pressure transducers.

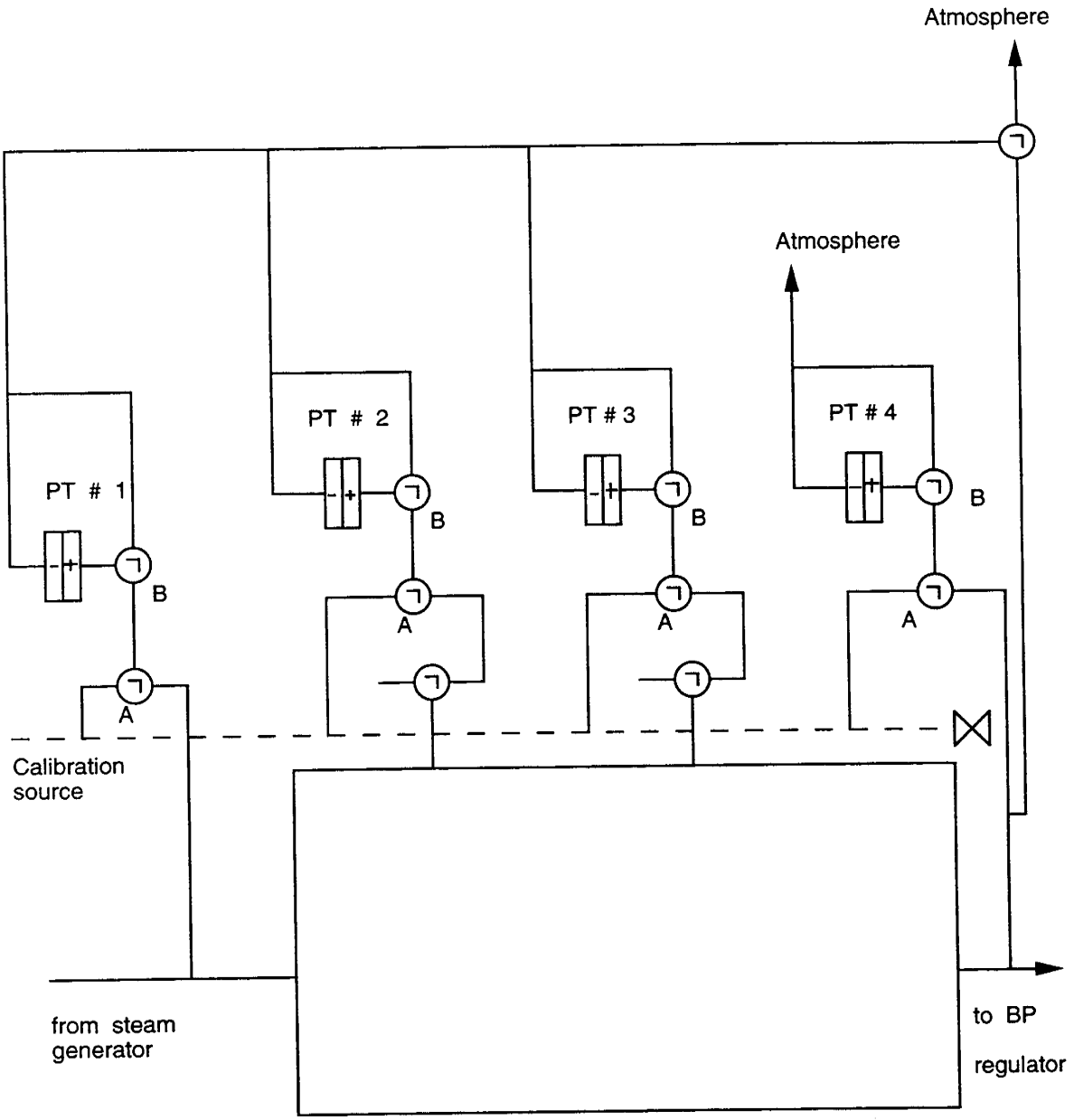

Figure 5.14: Plumbing diagram for the pressure transducers.

drop on the transducer. The positive sides of the transducers are connected to the pressure ports and the negative sides are connected to the core outlet. The negative side of Transducer 4 is open to the atmosphere. This enables the measurement of the absolute pressure rather than the pressure drop, from which the pressures at the other ports can be calculated. There is also an additional three way valve that either opens the entire system to atmosphere for calibration, or to the core outlet for pressure measurement.

During calibration, all of the A valves are open to the calibration source , shown as a dashed line in Fig. 5.14. For applying zero pressure drop on the transducers, the B valves are open to the loop, and, for applying full scale pressure, they are open to the A valves. During the pressure measurement process, the A valves are open to the pressure ports. Two additional valves are used on pressure Transducers 2 and 3. These ports are switched from the pressure measurement system, as used during an experiment, to production wells when cleaning and saturating the model. A Heise precision gauge, calibrated by a dead weight tester, is used to calibrate the transducers.

5.5 Data Acquisition System

Pressures, temperatures and heat fluxes are measured and recorded during an experiment, as shown schematically in Fig. 5.15. The signals from the pressure transducers are sent to the demodulators, from which the analog signals are sent through a terminal block to a cable that goes to the data logger relay multiplexer card. Thermocouples measuring temperatures in the model, thermocouples in the injection and production line, furnace and the heat flux sensor thermocouples, are all connected to the data logger relay multiplexer card, with thermocouple compensation via Type J and T thermocouple wires.

Heat flux sensor outputs are connected to the same cable that carries the transducer signals through a terminal block located on the cart housing the valves, pumps, transducers and demodulators for the experiment. The cable is then connected to the relay multiplexer card inside the data logger.

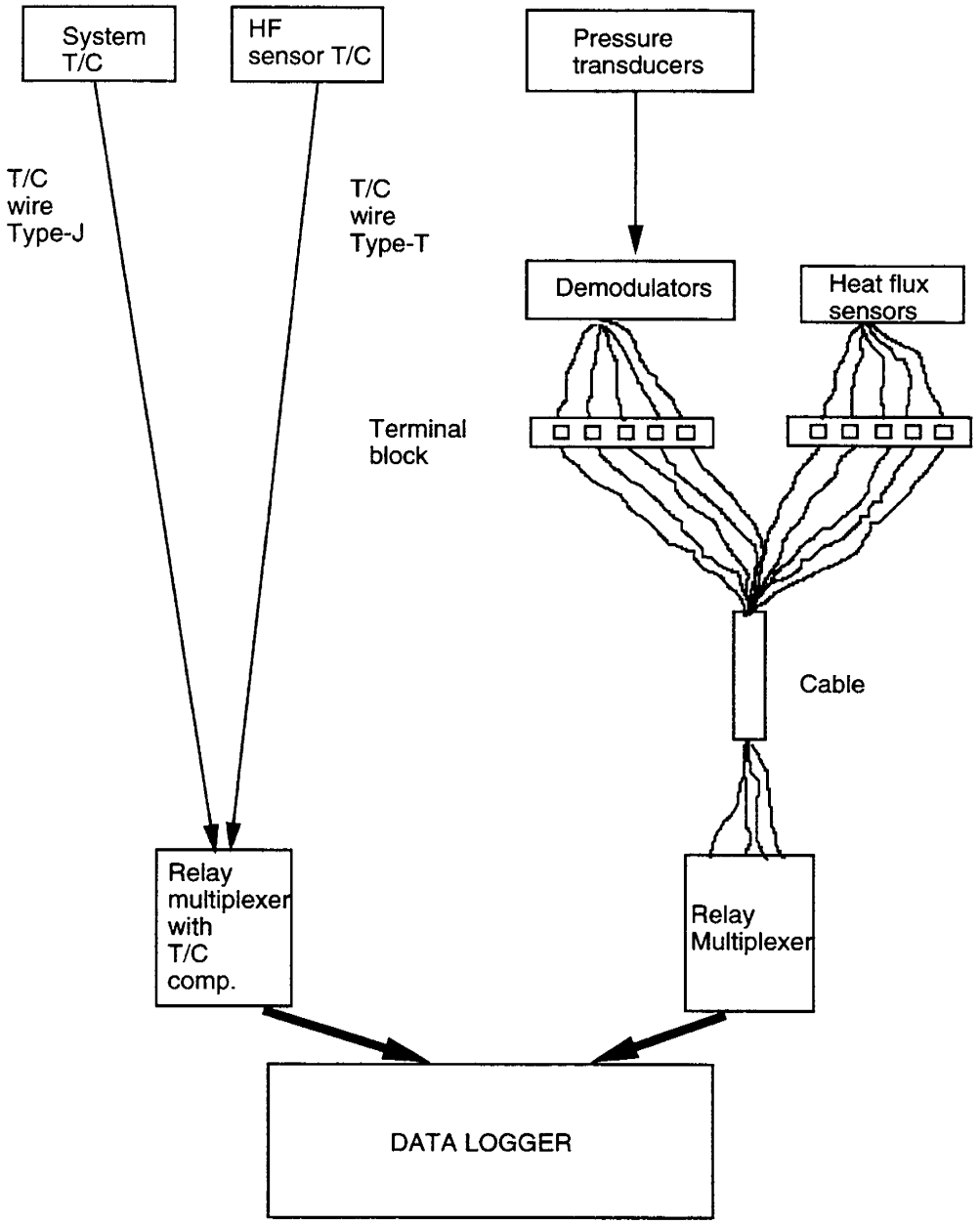

Figure 5.15: Schematic of the data acquisition system.

Software, written in QuickBasic, and interfaced with HPIB command language, records and displays the data during an experiment. This software is listed in Appendix B.

Chapter 6

Flow Properties Determination

The consolidated sandstone that was used in this study is Boise sandstone. It is a coarse grained feldspathic sandstone with angular grains; very poor sorting, large angular feldspar grains in a matrix of small quartz, feldspar and Fe-Ti minerals; and small clay content. It consists of approximately 50 % quartz, 45 % feldspar and 5 % clay and opaque minerals [73].

Porosity and permeability of the Boise core were measured in the laboratory by using differing methods.

6.1 Porosity Measurements

Porosity of the core was measured using two methods, the saturation method and computerized tomography.

6.1.1 Saturation Method

In the saturation method of determining porosity, a clean dry sample is saturated with a fluid of known density and the pore volume is determined from the gain in weight of the sample [3]. Rectangular core plugs of Boise sandstone $9.9 \times 2.5 \times 2.5$ cm in size, were used in these porosity measurements. The plugs were first dried in the oven and then were weighed with an analytical balance. Next, they were evacuated

for twenty four hours. Then, water was allowed to saturate them under vacuum. The cores were allowed to sit overnight under water and then were weighed again. Porosity was calculated by using the following material balance formula.

$$\phi = \frac{W_{wc} - W_{dc}}{\rho V_{bu}} \tag{6.1}$$

where,

W_{wc} = Weight of water saturated core, gm
W_{dc} = Weight of dry core, gm
ρ = Density of water, gm/cc
V_{bu} = Bulk volume of the core, cc

Table 6.1 shows the porosities measured in this study compared to Boise sandstone values from the literature. The results are in reasonable agreement with previous studies.

Table 6.1: Porosity of Boise Sandstone.

Sample # 1	0.294
Sample # 2	0.307
Sanyal [73]	0.32
Guzman [36]	0.251-0.266

6.1.2 Measurement by Computerized Tomography

Measurement of porosity by CT (Computerized Tomography) is an effective nondestructive technique that is now used widely in industry and research organizations. Several investigators have used this technique, as discussed next.

Chatzis et al. [11] developed porosity maps for a Berea sandstone core of 29.2 cm in length and 3.87 cm in diameter by scanning at 12 locations and averaging the results. The core was scanned dry, saturated with water and saturated with 2 wt % NaCl + 1 wt % NaI brine. Two different energy levels were used for all the scans. Thus, six sets of porosity maps were drawn. The average of all six maps was taken for the average porosity calculation. The calculated overall porosity was in good agreement with the porosity measured gravimetrically. Table 6.2 shows the comparison of porosity values measured by CT scanning and gravimetrically.

Table 6.2: Porosity Measurements by Two Methods (Chatzis et al. (1988)).

CT scanning	20 ±2 %
Gravimetric measurement	20%

Peters and Afzal [63], characterized a laboratory sand pack by CT imaging. They developed a porosity histogram for the sandpack. The average porosity obtained by CT compared favorably with material balance calculations. The porosity map for the core cross section showed a porosity distribution that was far from being homogeneous. Porosity heterogeneities were introduced due to the packing procedure. Heterogeneities were also present in the porosity map for the longitudinal section of the sandpack. In this study, CT imaging was used successfully to characterize a sandpack that was used in flow experiments.

MacAllister et al. [57] used CT scans to develop porosity maps for a 3 in long, 0.73 in diameter, Baker dolomite. The porosity distribution was found to be relatively homogeneous compared to typical reservoir carbonates.

A CT scanner is also used in this work to characterize the Boise sandstone that was used in the experiments. The porosity calculations from CT scans are done on a voxel by voxel basis by fully saturating the sample by two different fluids with strong density contrasts to produce large CT number differences. To calculate porosity accurately, two different scan locations were determined for the core. After deciding

on the proper energy levels and scanner settings, the core was positioned, evacuated with a vacuum pump, and scanned dry.

Deionized water was allowed to saturate the core under vacuum. After saturation was complete, the core was scanned at the same two scan locations. The porosity was calculated from these two scans using the CT processing software (CATSOFT) [8]. The equation used in the porosity calculations is given by,

$$\phi = \frac{CT_{wc} - CT_{dc}}{CT_w - CT_a} \tag{6.2}$$

where,

CT_{wc} = CT number for the core saturated with water
CT_{dc} = CT number for the dry core
CT_w = CT number for pure deionized water
CT_a = CT number for air

Figure 6.1 shows the porosity maps for the two slices at two locations. The average porosity was calculated to be 0.294 for Slice 1 and 0.291 for Slice 2. These average porosity values agreed well with the previously measured porosity value of 0.307 by the saturation method.

As shown in the porosity maps (Fig. 6.1), the porosity distributions are similar for the two slices. They both tend to show a higher porosity value in the center of the core compared to the sides. Since the porosities were calculated from unprocessed raw CT numbers, these high values may be due to the artifacts introduced because of the rectangular shape of the core. Also notice there is a tendency for the porosity values to be higher along the diagonals. This too, is due to the core shape. The image processing, and artifact and noise filtering techniques, used for the saturation calculations, will be discussed in Chapter 7.

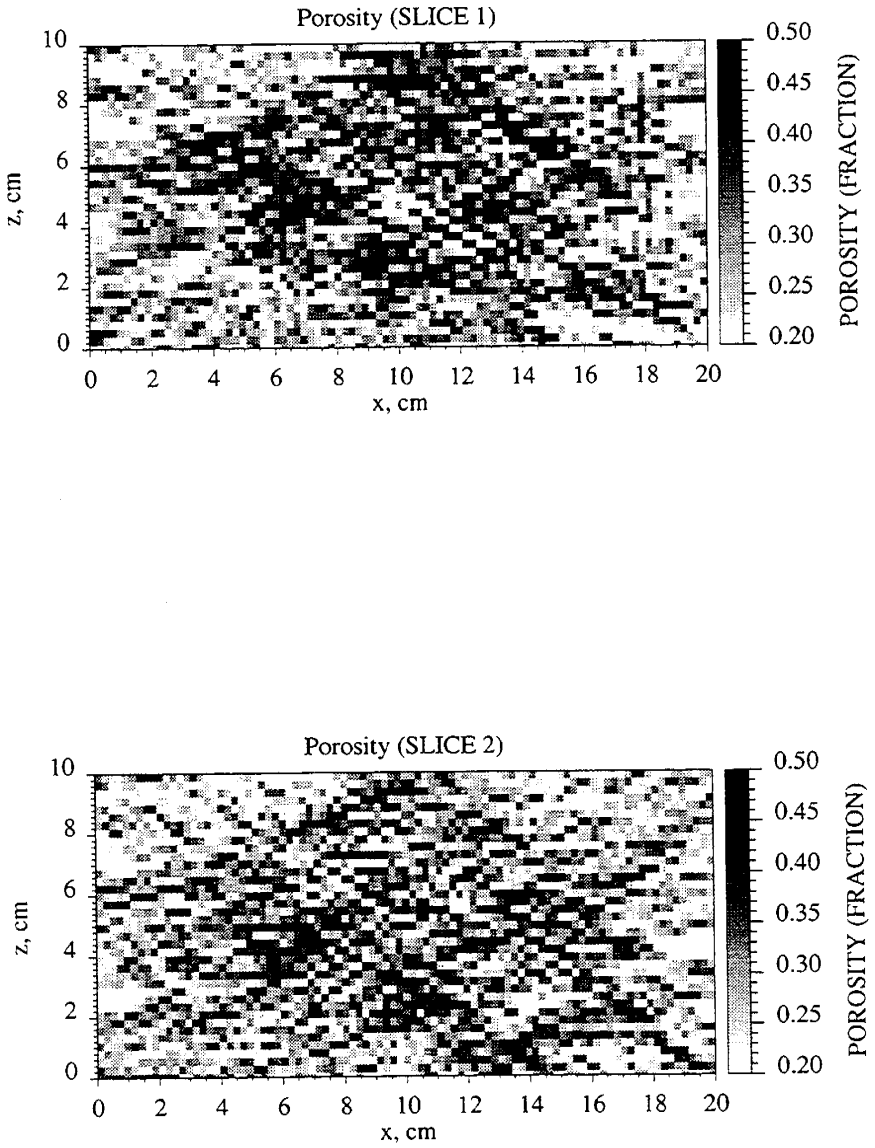

Figure 6.1: Porosity maps for two different core slices.

6.2 Permeability Measurement

Knowing the permeability of the porous medium is crucial in any flow experiment since it is one of the main flow parameters used in simulations. To measure the permeability of the Boise sandstone used in the experiments, two techniques were used; the conventional Ruska liquid permeameter, and measurement of point permeabilities by a minipermeameter.

6.2.1 Ruska Liquid Permeameter

Permeability measurements with the liquid permeameter are made by determining the time required for a given volume of liquid to flow through a core of known dimensions at a recorded pressure and temperature. This calculation is based on Darcy's law [19].

Cylindrical 1 in diameter core plugs were drilled in different directions from a large square block of Boise sandstone. The core plugs were evacuated and saturated with deionized water, which is used for the permeability measurement. Following the saturation, the cores were installed in the liquid permeameter. The following describes the procedure used in this measurement [19].

- The system is connected to a nitrogen supply and the regulating valve is closed.
- The core plug is assembled in the core holder.
- The separatory funnel is filled with the test fluid, which is deionized water for these tests.
- The fluid is allowed to fill the core holder and to fill the burette from the top.
- After the liquid level in the burette is above the index mark, the core holder valve is closed.
- The regulating valve is opened and the pressure is adjusted to a constant value and that value is recorded.

- The discharge-fill valve is turned to discharge.
- The time required for the liquid level in the burette to drop, from the upper to the lower index mark, is recorded by a stop watch.

The liquid permeability is calculated by Darcy's equation, given below.

$$k = \frac{\mu V L}{A t \Delta p} \tag{6.3}$$

where,

k	=	Absolute permeability, Darcys
μ	=	Viscosity of the liquid used at the measured T and P, cp
V	=	Volume of liquid between the two index marks, cm^3
t	=	Recorded time, sec
Δp	=	Pressure difference, atm
L	=	Length of the sample, cm
A	=	Cross-sectional area of the sample, cm^2

Permeability measurements using the above procedure ranged from 900-1700 md depending on the cut directions on the large Boise core block. Horizontal permeabilities ranged from 900-1400 md, and vertical permeabilities ranged between 1200-1700 md.

6.2.2 Measurement of Permeability by a Mini-permeameter

The second method that is used to measure permeability is the use of a mini-permeameter. The mini-permeameter is a simple gas-flow measuring device designed to make a large number of very fast and nondestructive permeability measurements (Goggin et al. [35]). The mini-permeameter is used extensively both in the laboratory and the field.

Eijpe and Webber [29] constructed a mini-permeameter for rocks and also adapted it for unconsolidated sands, and for use in the field. It consists of a narrow tube, pressed against a flat clean rock surface. Air is injected to the pores and flows around

the tube. A constant pressure drop is applied and the gas flow rate is measured. Calibration curves, that relate the permeability to the air flow rate, are developed first for known rock samples. The permeability of the sample can be calculated from the observed flow rate by using these calibration curves.

Daltaban et al. [22] designed an electronic field mini-permeameter for making nondestructive permeability measurements of outcrops. Their instrument measures flow rate and injection pressure electronically, with individual measurements taking no more than 30 seconds. This field permeameter was used to sample 3-D shallow marine sandstone deposits at scales ranging from centimeters to kilometers. The measurements obtained from the permeameter were interpreted and simulated by numerical models.

A simple permeameter was built, and Goggin et al.'s [35] method was used to calculate the permeability point by point at certain locations on the Boise block that was used in the experiments.

The equipment consists of a metal tubing, with a silicone rubber stopper (00 size, center-bored with 1/4" diameter cork bore) attached to its end. The silicone rubber stopper acts as a seal. The flow rate is measured by a rotameter. The geometrical factor calculated by Goggin et al. was used in Darcy's law and the permeability is estimated from the measured injection pressure and temperature. The geometric factor handles the complexities associated with the geometry of flow. It is a function of the tip seal size and sample dimensions. Goggin et al. developed curves for geometric factor versus tip dimensions by a series of simulation runs for different dimensionless core sizes. These curves were used to calculate the geometric factor corresponding to the core sample dimensions and tip size used in the measurements.

The procedure followed to measure point permeability is as follows.

- Calibrate the rotameter at the pressure of interest.
- Inject nitrogen through the tubing at the desired pressure.
- Press the tubing with the silicone rubber seal on the core at the point of interest.
- Record the rotameter reading.

- Calculate the corresponding flow rate from the calibration curve.
- Recalculate the rate at the pressure of interest.
- Determine the geometric factor, G_o by using the inner and outer diameter seal dimensions.

The permeability is calculated from the following formula,

$$k_{app} = \frac{q_1 \mu p_1}{a G_o (p_1^2 - p_o^2)/2} \tag{6.4}$$

where,

k_{app}	=	Apparent permeability, cm^2
μ	=	Viscosity of nitrogen at T_1 and p_1, Pa.s
p_o	=	Atmospheric pressure, Pa (absolute)
p_1	=	Injection pressure, Pa (absolute)
q_1	=	Calibrated rotameter reading at p_1, m^3/s
G_o	=	Geometric factor
a	=	Internal radius of the tip seal, m

Permeability contour maps were developed by using the permeameter and measuring permeabilities at different directions at several locations on the Boise sandstone block that was used in the experiments. The permeabilities were in close agreement with results from the Ruska liquid permeameter. Figs. 6.2, 6.3 and 6.4 show the x, y and z-direction permeability contour maps. The permeability ranged between 800 md and 1700 md depending on the location. Table 6.3 shows the means and standard deviations of the permeability measurements in different directions.

Conventional permeability measurement techniques only allow the determination of a single average permeability value for each core plug. Thus, average values were calculated by measuring the permeabilities from several individual core plugs cut from a single block. Average permeabilities measured by the Ruska permeameter ranged from 970-1900 md and the standard deviations ranged from 26-280 md.

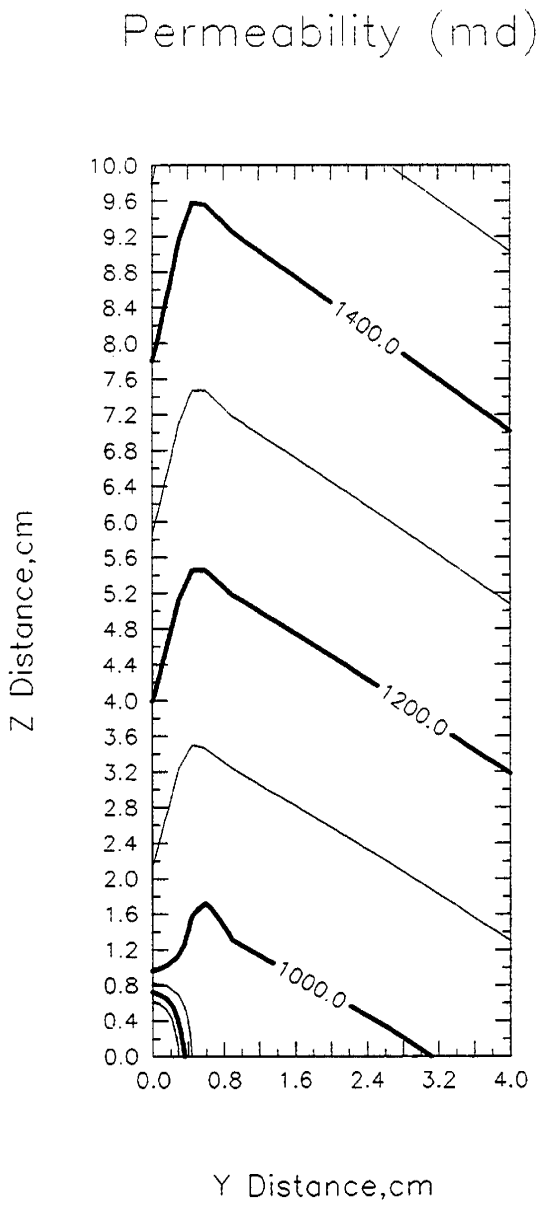

Figure 6.2: Permeability map of Boise (x-direction)

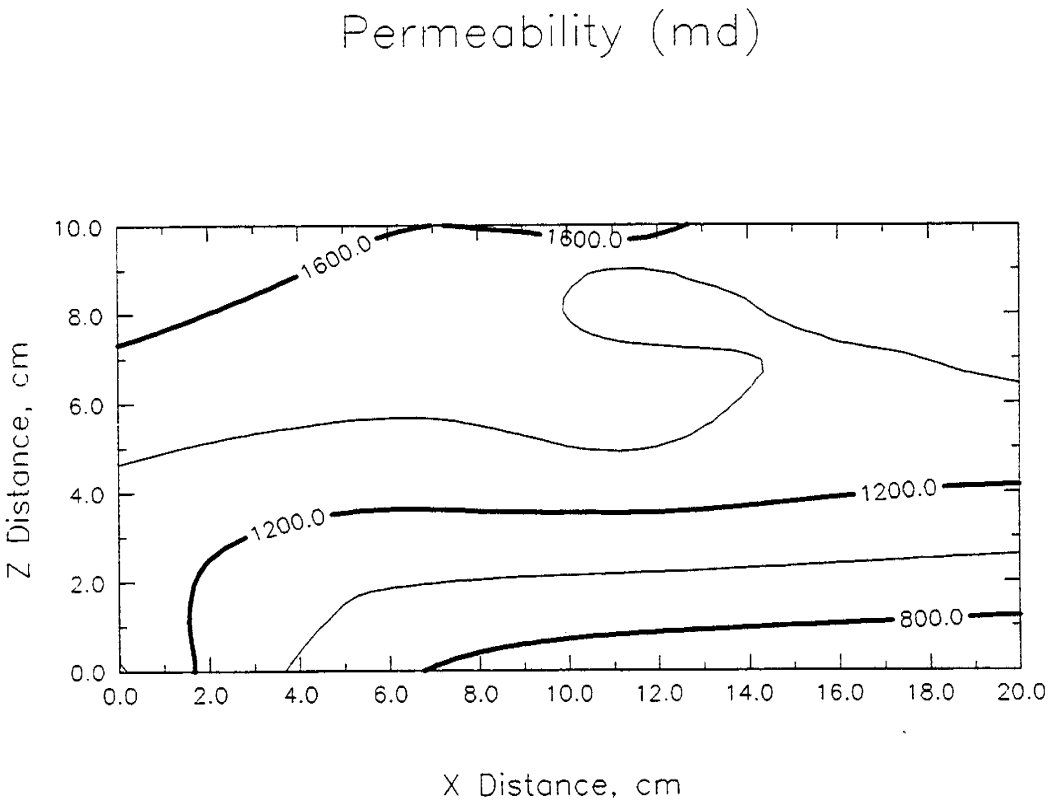

Figure 6.3: Permeability map of Boise (y-direction)

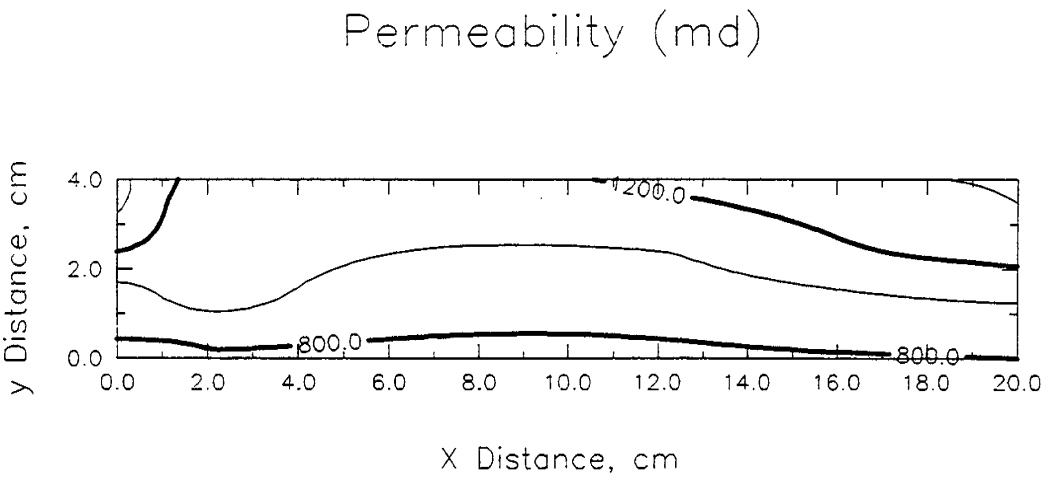

Figure 6.4: Permeability map of Boise (z-direction)

Table 6.3: Permeability Measurements by Mini-Permeameter

Direction	Mean (md)	Standard deviation (md)
x	1205	295
y	1362	258
z	1077	155

Chapter 7

Experimental Procedure and Results

The first section of this chapter summarizes the procedures followed to prepare the apparatus for steam injection runs. Then, the procedure is described for the steam injection experiments.

The experimental effects of differing operating parameters are discussed in the third section. Finally, a summary of these results and important experimental observations are given.

7.1 Preliminary Scans

In addition to the conventional measurements in steam injection experiments, such as pressure and temperature, saturations were measured in-situ using the CT-scanner.

One of the major accomplishments in this study, is the in-situ pixel by pixel measurement of two phase steam-water saturations both in the fracture and the rock matrix. To quantify the two-phase saturations the following equation was used.

$$S_w = \frac{CT_{ws} - CT_{dc}}{CT_{wc} - CT_{dc}} * 100 \tag{7.1}$$

where,

CT_{wc} = CT number for the core saturated with water
CT_{dc} = CT number for the dry core
CT_{ws} = CT number measured when two phases (water-steam) are present
S_w = Water saturation, percent

The steam saturation is calculated from a material balance.

$$S_g = 100 - S_w \tag{7.2}$$

where, S_g is the steam saturation, in percent. In these equations it is assumed that the CT numbers for a dry core and a steam saturated core will be identical. This is a good assumption, since the density of the steam in these experiments is very low.

As seen in Eq. 7.1, to calculate steam/water saturations, three different CT numbers are required (dry core, core saturated with water and core saturated with two phases). Since saturation calculations are done on a pixel by pixel basis, the exact scan locations and the optimum scanner settings had to be determined prior to each run so that scanner settings and the scan locations were consistent for each experiment. In other words, exact scan locations and the same scanner settings should be used for dry scans, saturated scans and steam injection runs.

After assembling the core holder on the scanner positioning table, the electrical connections for the thermocouples and the heat flux sensors, and the connections for injector/producer and pressure ports were completed. Considering all the metallic objects around the core holder, such as thermocouples, tubing and wires, two appropriate scan locations were selected. The locations for the two scan slices were determined accurately with the help of the CT positioning table. Figure 7.1 shows these locations. The scan slices are planes in the x-z direction and are parallel to the center plane where thermocouples and pressure taps are located. Slice 1 is the slice at the front closer to the injection well, and Slice 2 is at the back closer to the producer.

After the scan locations were fixed, the model was evacuated and was scanned dry at these two locations. Different settings were used on the scanner to determine the settings for the image with least noise and artifacts.

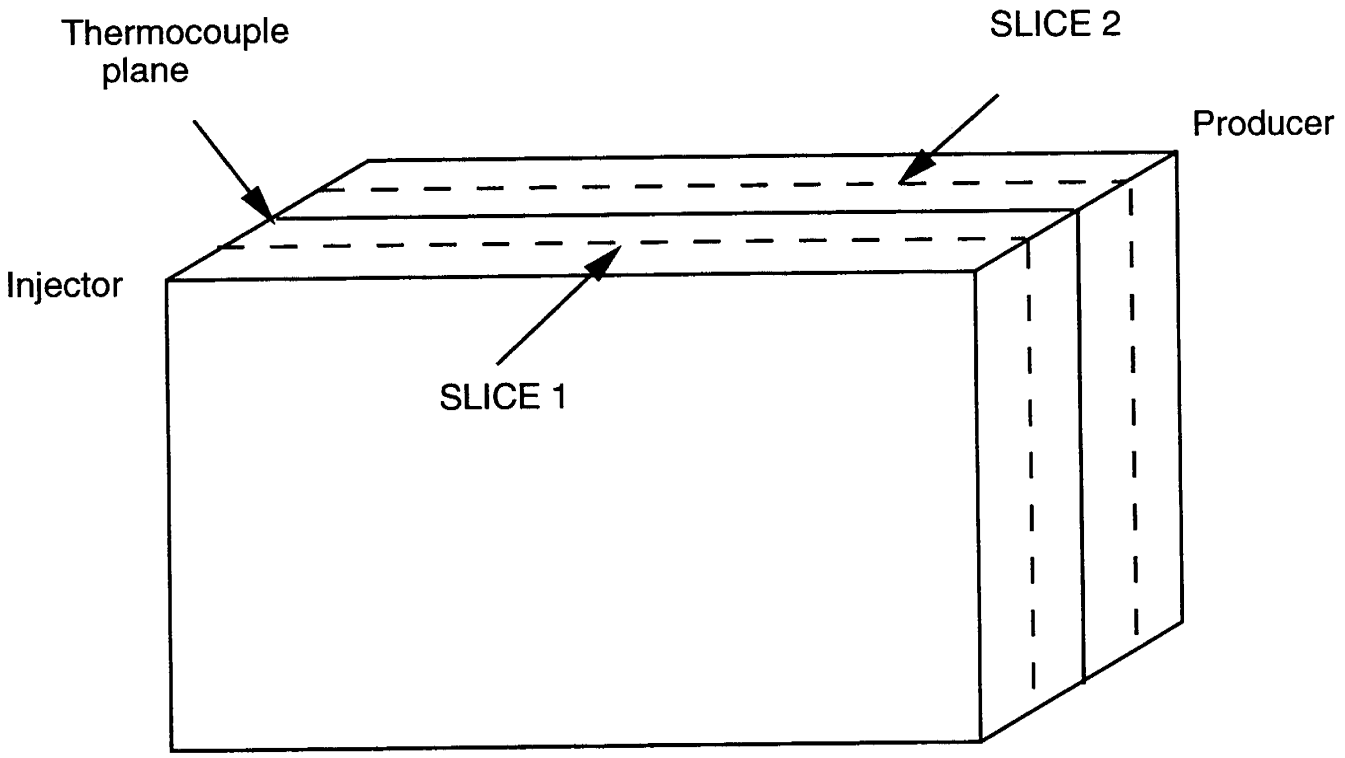

Figure 7.1: Scanning plane locations.

The EMI 5005 scanner has two different scanning speeds, normal and slow. Both speeds were used to compare the resulting images. As seen in Fig. 7.2, the two CT number maps are quite similar in terms of both image quality and noise. Therefore, normal scan speeds were used in the experiments. This enabled us to more rapidly capture the saturation changes expected in the experiments.

Next, different energy levels in the scanner were tested to decide on the best energy level for our system. Energy levels of 100 kV and 140 kV were used for comparison. Figure 7.3 shows a comparison of 140 kV and 100 kV dry scans. The darker colored regions in these CT maps show the areas with higher density (i.e., higher CT numbers) and the areas with lower density are shown by lighter colors. Fractures surrounding the core are characterized by negative CT numbers, close to the CT number for air.

Following the dry scans, the model was evacuated again followed by carbon dioxide injection. The evacuation and the carbon dioxide injection cycles were repeated several times. Carbon dioxide was used because of its higher solubility in water than air, so that subsequent water injection could dissolve all the gas. Deionized water was then allowed to saturate the model by gravity, and under vacuum. After water saturation was complete, the model was scanned again at the same two energy levels. Figure 7.4 shows the CT number maps for the water saturated core at the two different energy levels. Again, the darker areas correspond to higher CT number regions, like the core, and the lighter areas show the fractures around the core. Since the fractures are filled with water, the CT numbers are different than with air, but are close to the CT number for deionized water. CT numbers are higher when the core is saturated with water, since water is more dense than air.

The CT number map for the saturated core at 100 kV shows significant cross shaped artifacts in the scans. In fact at these locations, nonphysical CT numbers were measured. This is because the 100 kV energy level was too low for the density of the core holder and the core. These artifacts are not desirable since they can affect the saturation calculations. Therefore, 140 kV was chosen for the energy level used in the steam injection experiments. Even though 140 kV scans look much better, in terms of artifacts and noise, some artifacts are still inherent in the scans due to the rectangular shape of the core holder. These artifacts are the lines located

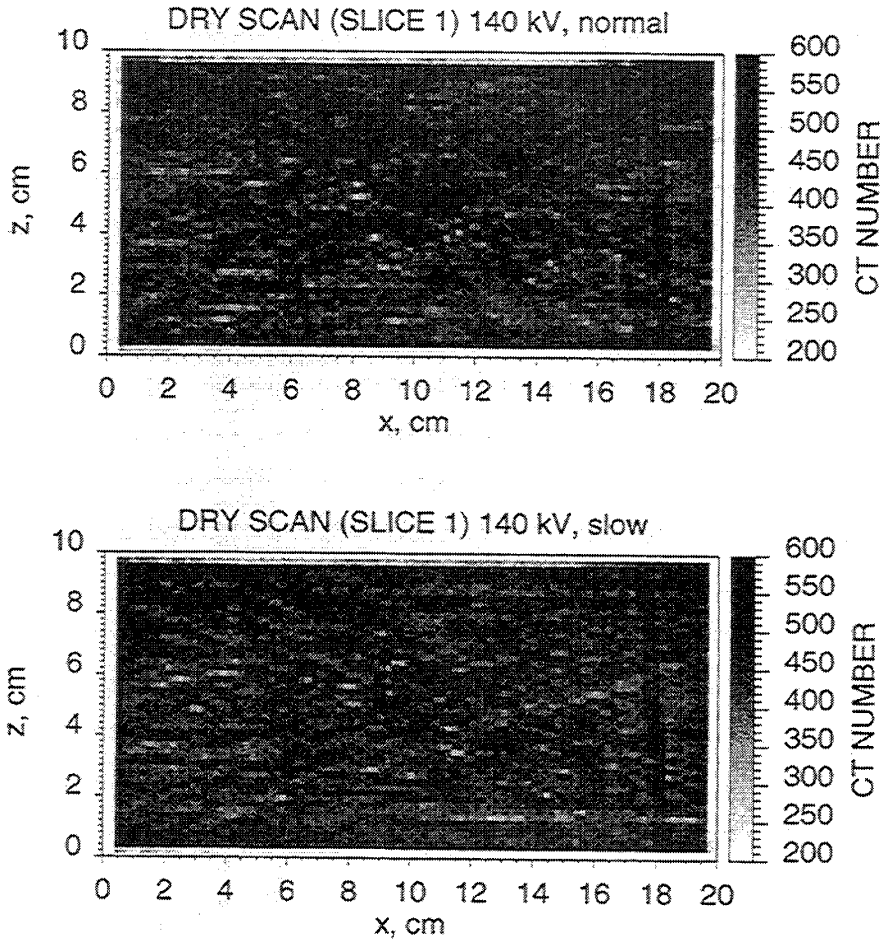

Figure 7.2: Effect of scan speeds on images.

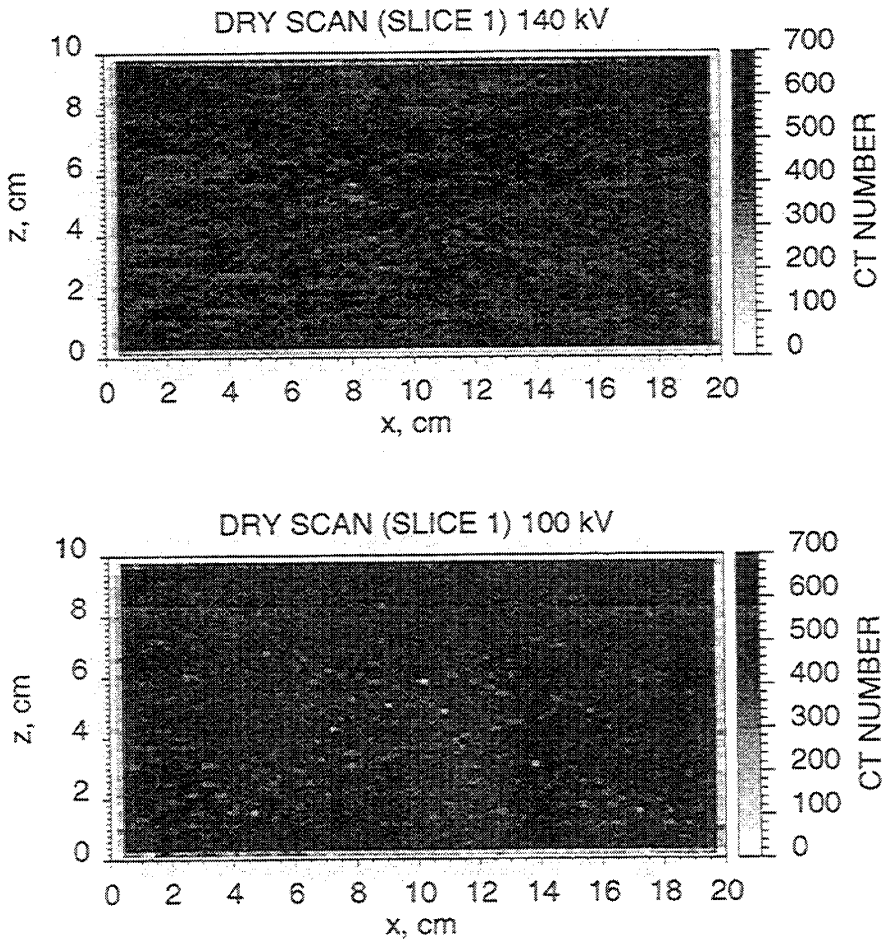

Figure 7.3: Effect of energy levels on scanning results (dry scans).

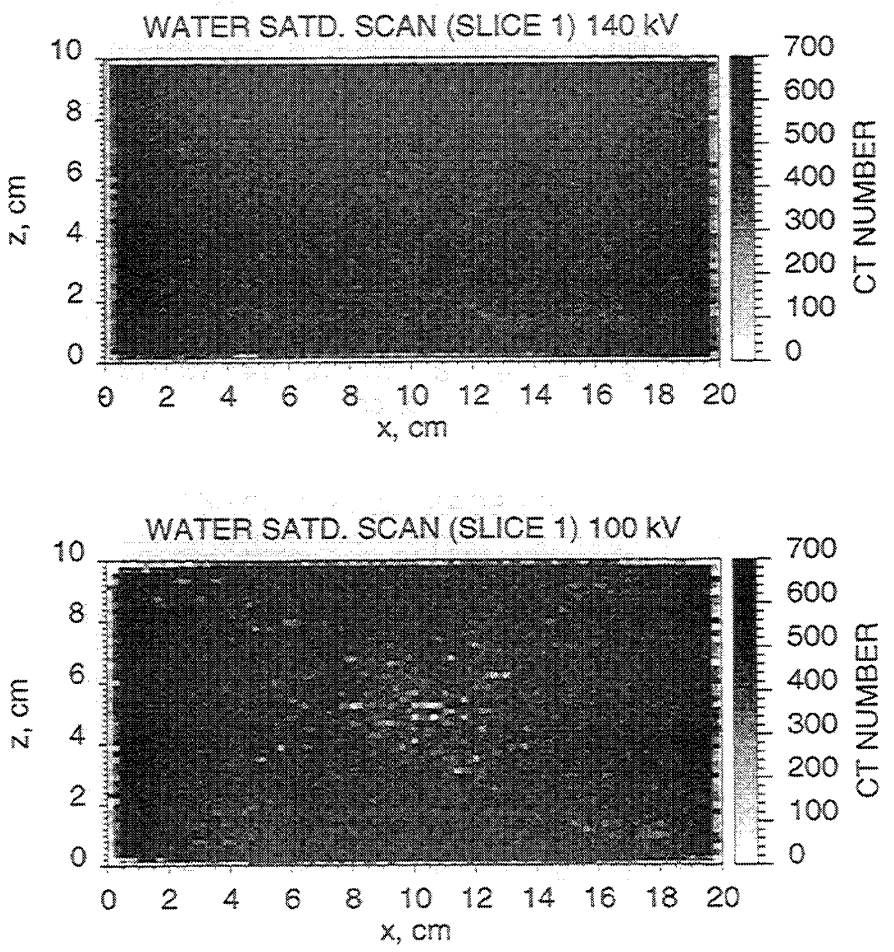

Figure 7.4: Effect of energy levels on scanning results (water saturated scans).

diagonally at various locations in the CT maps, originating from the corners; and they are inevitable. Image processing techniques, like subtraction and smoothing, helped eliminate some of the noise and artifacts. These procedures will be described in Section 7.5.

7.2 Procedure for Steam Injection Experiments

The procedure followed in all the steam injection experiments can be summarized as follows.

Before each steam injection run, the chromatography pump is calibrated and is set at the desired injection rate. Then, the temperature controller for the steam generator is set to the desired temperature. Deionized water is pumped to the steam generator. The steam is diverted through a bypass line to a vent until it is at the desired injection temperature. In the meantime, pressure transducers are calibrated. Once steam is observed in the bypass line outlet, back pressure is applied to the core outlet and the injection valve is opened to the model. Slightly superheated steam is injected to the system. This is done so that the enthalpy of the injected steam is known accurately.

The injection well is completed at the bottom and the producer is completed at the top of the model. They are located at the two diagonal corners of the model. During the experiment, temperatures, pressures and heat losses are recorded every thirty seconds by the data logger, and CT scans are taken every fifteen minutes. Once a steam injection run is finished, the furnace is turned off and cold water is continuously injected to the model until the entire system is cooled. Cooling of the system was necessary because any existing steam in the system could cause shrinkage when it condenses, and could create a vacuum in the system. Excessive vacuum is not desired since it can cause leakage or damage to the core holder.

7.3 Effects of Changing Operating Parameters

In all the steam injection experiments that will be described in this work, initially the core is 100% saturated with water and steam is injected into the water saturated core. Differing combinations of steam injection rates, back pressures and injection temperatures were used in the experiments. In all the runs presented here, rate, injection temperature and back pressure are held constant unless otherwise stated. The results from these runs are described in detail in the following sections. Table 7.1 gives a summary of the experimental runs presented.

Table 7.1: Summary of Runs

RUN #	Rate (cc/min)	Back pressure (psig)	T_{inj} (°C)
RUN 26	6	0	118
RUN 27	6	0	118
RUN 29	6	12	117
RUN 34	6	0	108
RUN 39	2	12	115
RUN 40	6	12	116

7.3.1 Effect of Steam Injection Rate

Steam injection rate is one of the most important operating parameters in any steam injection project. The effect of rate on the oil recovery has been investigated widely for homogeneous reservoirs, however studies on fractured/fissured reservoirs are scarce. Multidimensional systems have not been examined thoroughly.

Dreher and Kenyon [27] studied the effect of steam injection rate on recovery, both experimentally and numerically. They used fractured carbonate disks in their

experiments. They concluded that steam injection rates determine the efficiency with which heat moves from fractures to the matrix.

Jensen [45] conducted an experimental and numerical study on steam injection to fractured sandstone and carbonate cores. He first waterflooded the cores and then injected steam. Both the numerical sensitivity studies and the experimental results showed that the slower the injection rate, the more time is available for imbibition; therefore higher oil recoveries are observed initially in the waterfloods with the slower injection rates. But at the end, oil recoveries become almost identical. Once steam flooding had started, the system reacted faster to the thermal front at higher injection rates. However, the final oil recoveries and oil saturations in the system, at the end of steam flooding, changed little at differing rates.

In this study, a wide spectrum of rates (within the limits of the chromatography pump) were used in the steam injection experiments. The rates are all stated in terms of cold water equivalent (cc/min). For comparison purposes, results from runs at two different rates will be shown here. The high rate and the low rate used are 6 cc/min and 2 cc/min, respectively.

As described in Chapter 5, there are thirteen thermocouples distributed in the model in both fracture and matrix. The temperature histories of these thermocouples show the effect of injection rate on the heat propagation in the system. Figure 7.5 shows the temperature histories of the thermocouples installed in the fracture (fracture thermocouples). Solid lines show the high rate runs in these graphs. The physical locations of these thermocouples are shown in Fig. 7.6, repeated from Chapter 5 Fig. 5.12.

The thermocouples closest to the injection side like #2 and #13 respond to the injection faster than the rest of the thermocouples. The responses of the thermocouples at the bottom and away from the injector are the slowest (#6 and #7). The thermocouples close to the producer are heated faster than the bottom thermocouples since they are located in the flow path of the steam (#9 and #10). Thermocouple #4, even though it is at the bottom, is heated faster than Thermocouple #6 since it is close to the injector.

The propagation of the heat front is slightly faster when high rates are used.

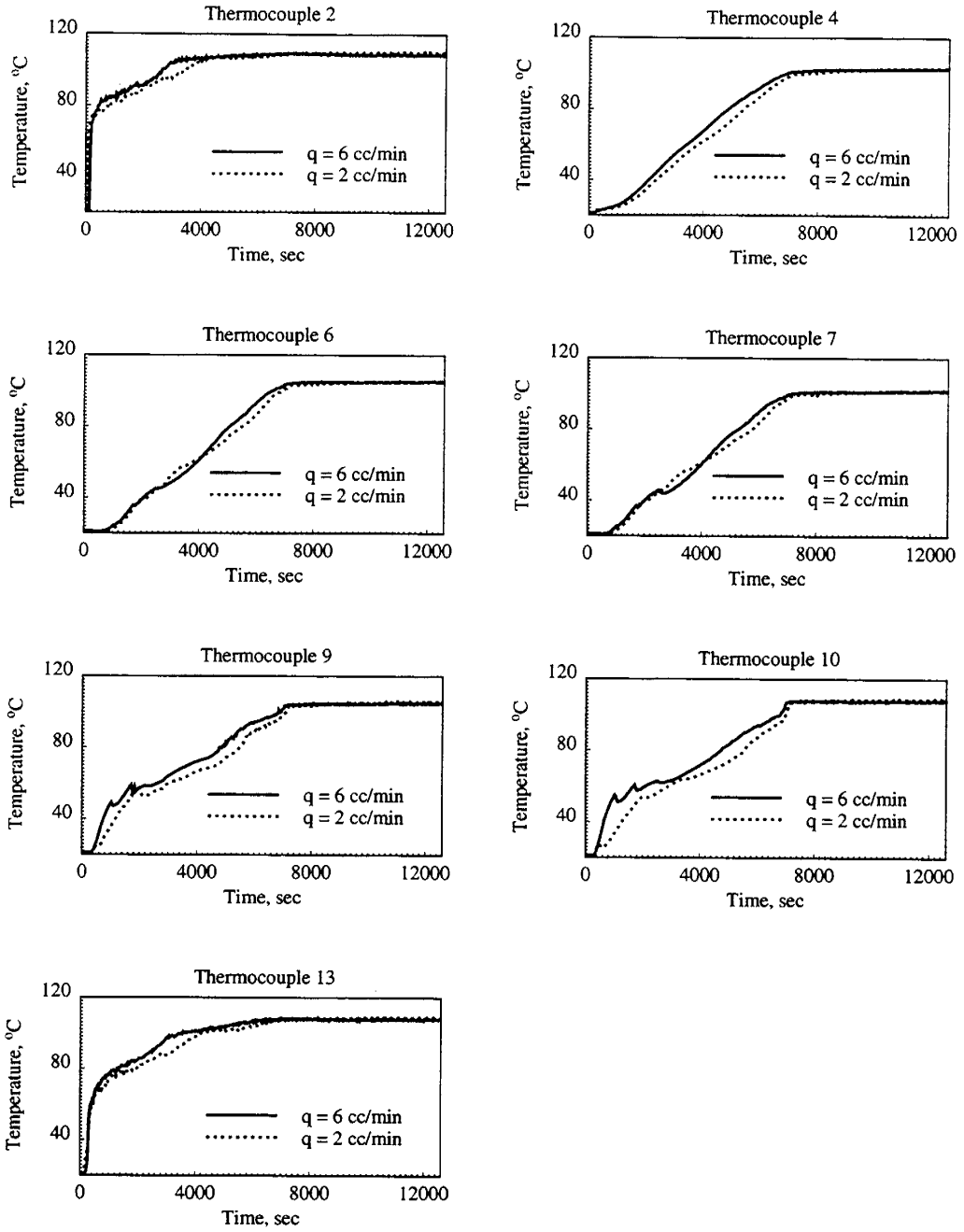

Figure 7.5: Fracture thermocouple histories (rate comparison).

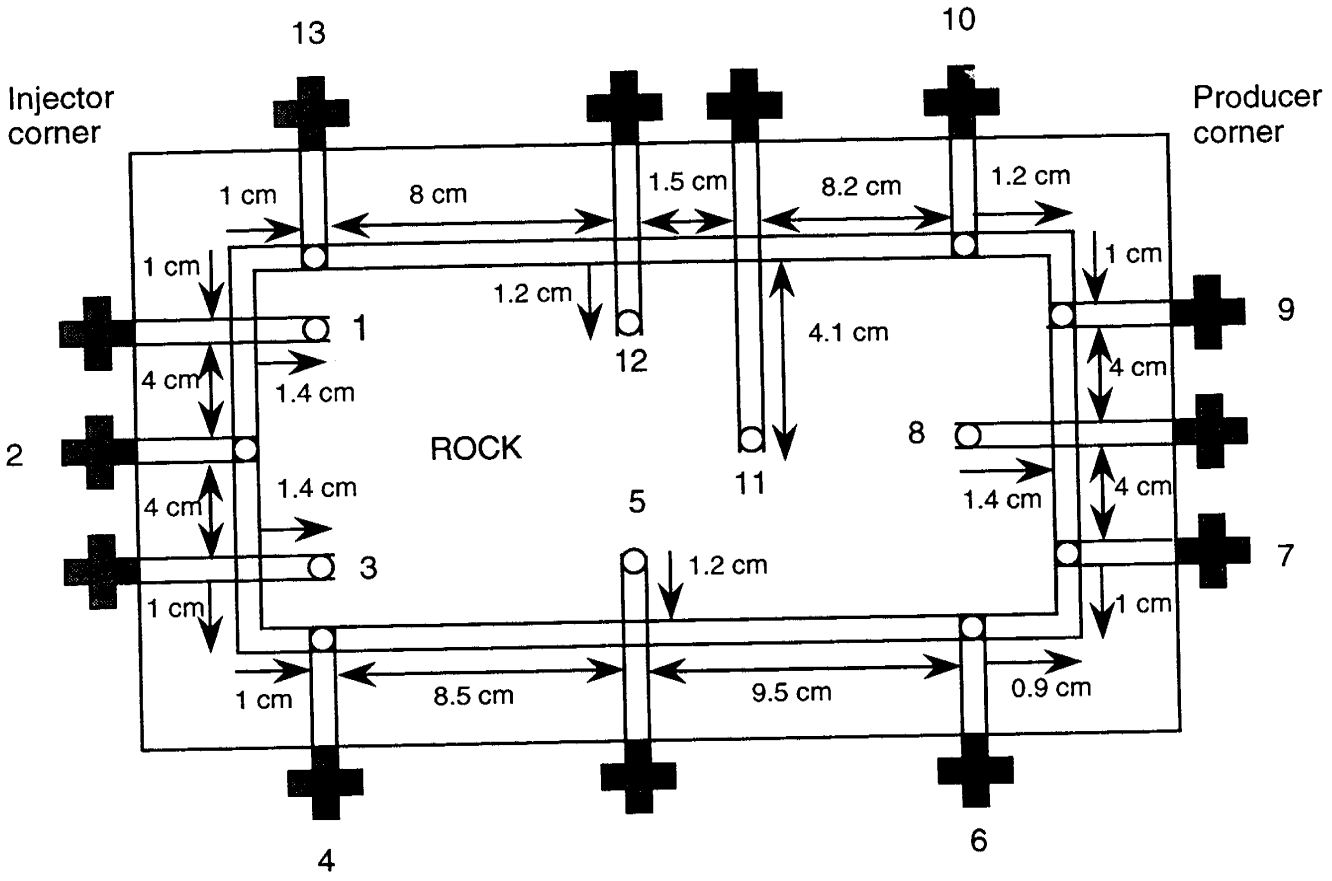

Figure 7.6: Locations of the thermocouples.

However, temperatures measured in both rates become identical when they reach steady state. The same behavior is also observed for the thermocouples installed in the matrix (Fig. 7.7). The matrix is heated from top to the bottom. Thermocouples #1 and #12 are at the top and #5 is at the very bottom.

Initially, higher steam volume is injected into the system with the high rate, and this causes the system to heat slightly faster. However, after the transient period is over, temperatures reach steady state for both rates; determined only by the back pressure on the system, independent of the rate.

The effect of steam injection rate is not very significant, especially if one considers the differing steam injection temperatures in these runs. Since the injection temperature is controlled by the furnace temperature and the temperature controller, it is very difficult to maintain the same injection temperature for all runs, since even a change in the room temperature can affect the heat losses from the furnace. Injection temperature histories for both runs measured in the inlet line are shown in Fig. 7.8. Although the average injection temperatures are similar for these two runs, the histories are slightly different. Initially, the injection temperature is slightly higher in the 6 cc/min run. Eventually, the two injection temperatures become nearly equal. This behavior is also observed in the injection enthalpies. This shows that the initial differences in temperatures inside the model may have been due to the slight differences in injection temperatures and enthalpies. Therefore, temperature effect due to various injection rates may not be very significant for this system.

The same behavior is observed when heat flux histories are compared. Heat losses from the six sensors located on the core holder at different locations are shown in Fig. 7.9. The locations of these sensors are shown in Fig. 7.10. The heat losses are higher for the sensors at the top and bottom, #1-4 than the sensors at the sides (#5 and #6). The sensors at the top show a heat flux reading higher than the bottom sensors initially since they are close to the locations where steam flows and temperature increases rapidly. Initially, heat losses are higher with the high injection rate. This is because the higher rate of steam injection heats the model sooner. Later, heat losses become identical at both rates as interior temperatures approach the same steady state temperature value. The fluctuations in the heat loss measurements for Sensor

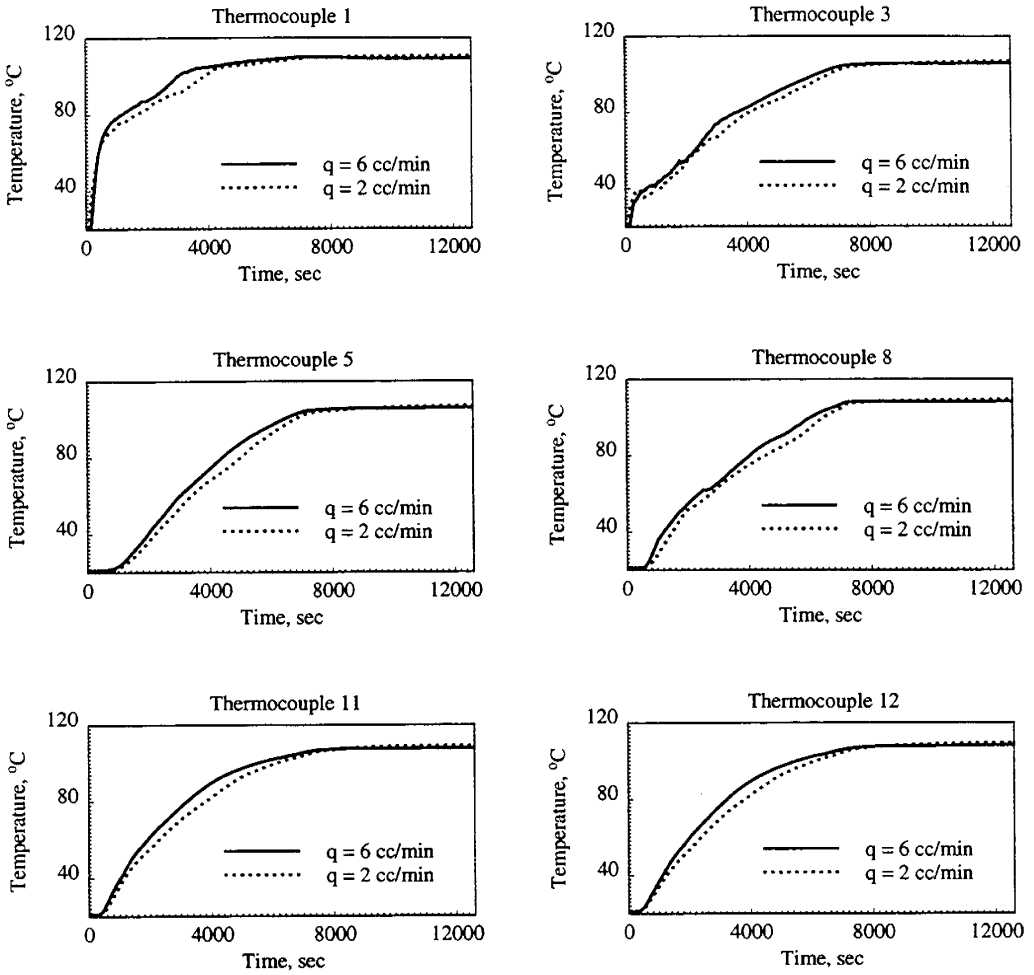

Figure 7.7: Matrix thermocouple histories (rate comparison).

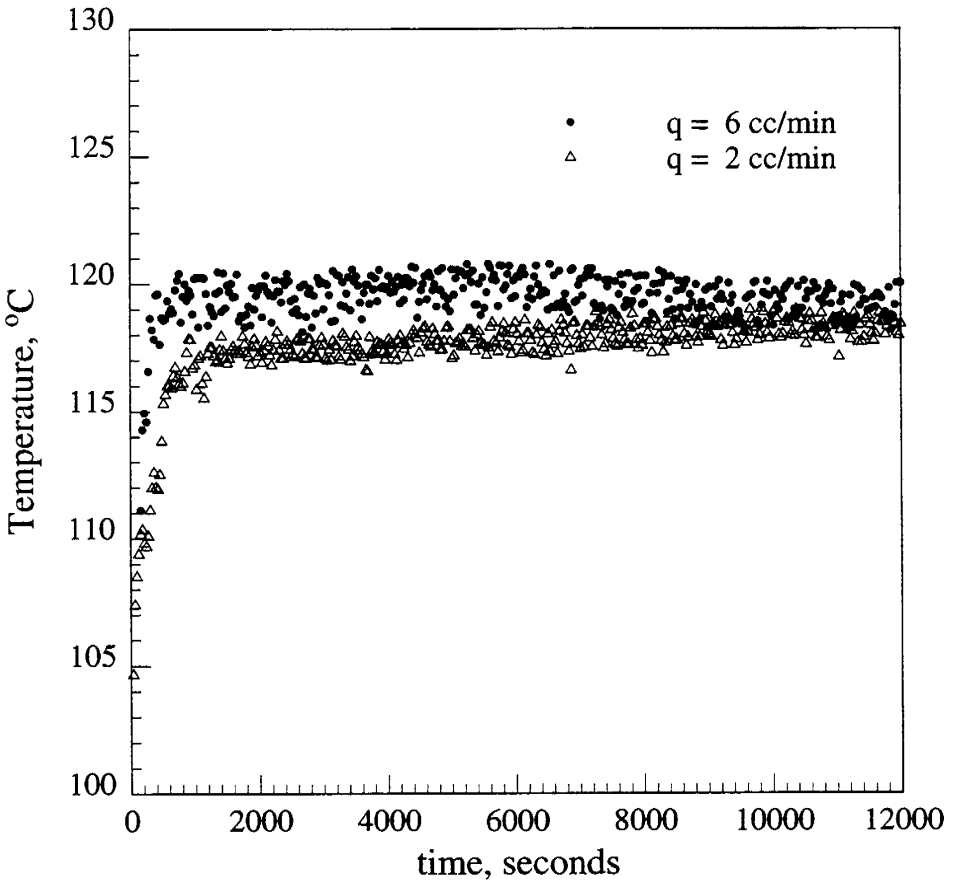

Figure 7.8: Injection line temperatures (rate comparison).

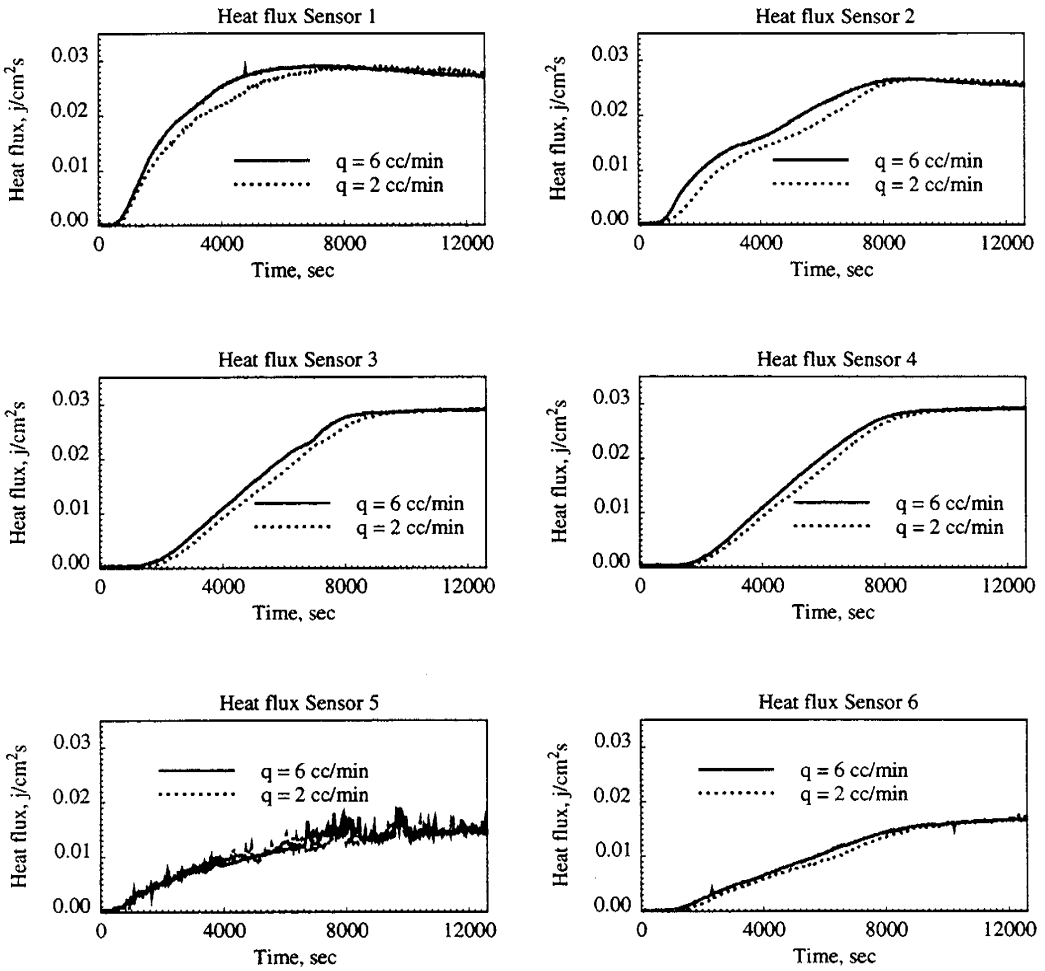

Figure 7.9: Heat losses measured from the sensors (rate comparison).

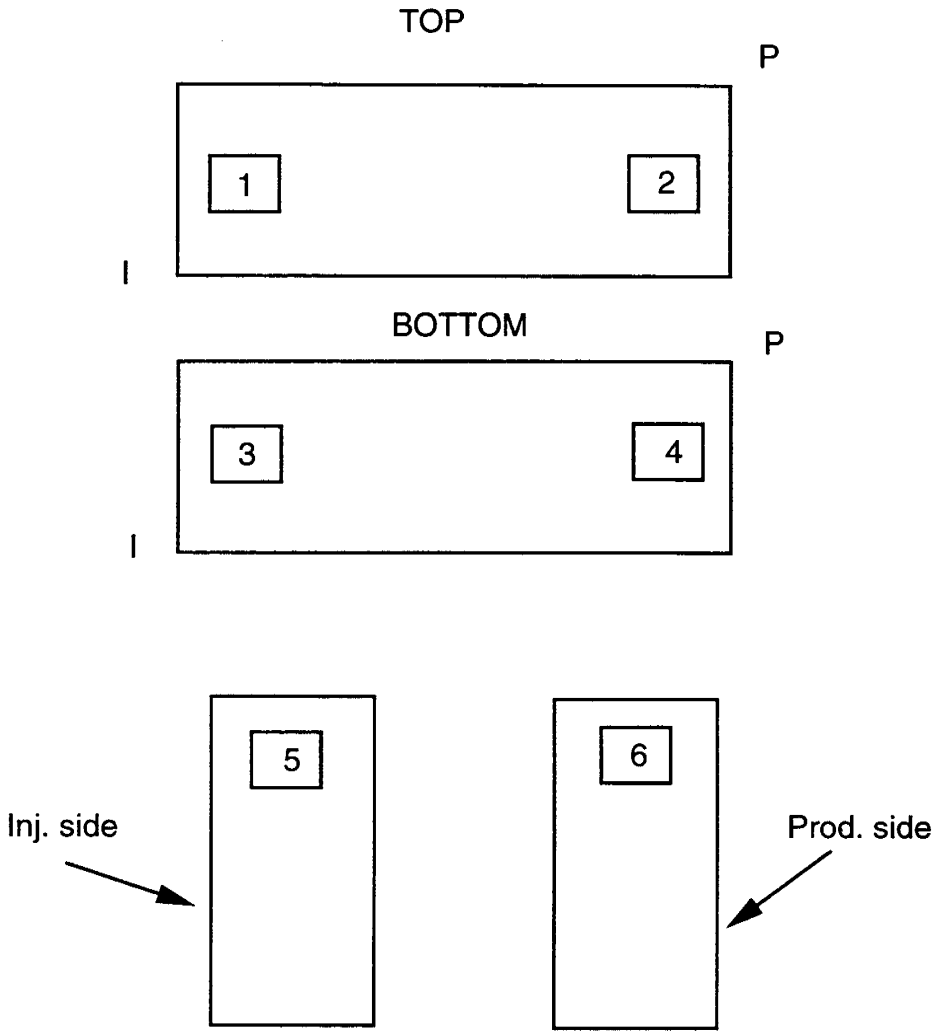

Figure 7.10: Locations of the heat flux sensors on the core holder.

5 was due to the movement and dislocation of the Fiberfrax insulation attached to that side from the back and front movement of the core holder while taking scans.

7.3.2 Effect of Back Pressure

The second operating parameter that was changed in the experiments, was the back pressure on the system. Differing back pressures were used in the experiments to investigate their effect on the process. The temperature of the steam coming from the steam generator was kept the same for both runs. Results will be compared for runs with 12 psig and 0 psig back pressure on the regulator. The actual model outlet pressure is slightly different from the pressure on the regulator, and it is measured by the outlet pressure transducer. When the back pressure is 0 psig, the outlet of the system was opened to the atmosphere.

Figure 7.11 compares the thermocouple temperature distributions along the center of the model with the steam saturation maps calculated from CT numbers. These maps show the temperature and steam saturation distribution at a short time after the steam injection has started (t = 65 min).

Temperature maps show that when the back pressure is 0 psig, the system has a larger heated area than for the 12 psig run. Steam saturation maps also follow the same trend. Steam flows in the injection side and the top fracture for the low back pressure run. On the other hand, when the back pressure is 12 psig, no steam saturation developed in the fractures at this time. Therefore, there is a less efficient conductive heat transfer into the matrix.

The apparent nonzero steam saturations in the matrix are caused by the noise in the CT scan images. Ways to deal with these artifacts and partially eliminate them will be discussed in the coming sections of this chapter. Analysis of the inlet injection temperatures and the saturation temperatures calculated from the inlet pressures help to explain the differences in the temperatures in the system for the two runs with differing back pressures.

The saturation temperature curve was calculated by using the pressures measured

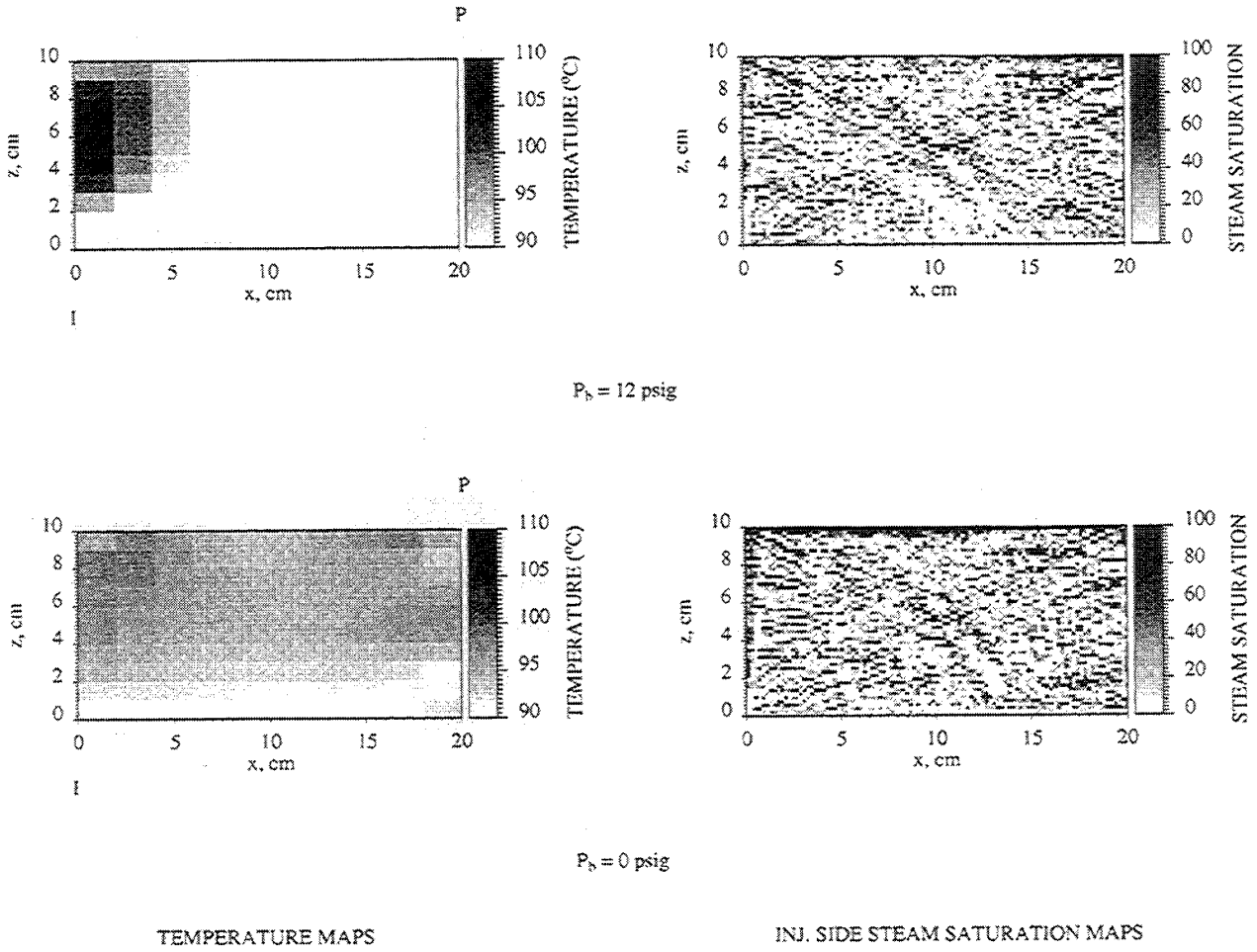

Figure 7.11: Temperature and steam saturation maps at 65 min, for 0 and 12 psig back pressure.

in the injection line. The following correlation [31] was used.

$$T_s = 115.1 p_s^{0.225} \tag{7.3}$$

where,

T_s = Saturation temperature, °F
p_s = Measured pressure, psia

A cross-fitting located in the injection line enabled measurement of temperature and pressure at the same location. When both the calculated saturation temperature and the measured temperature are plotted, it shows whether the injected steam is saturated or superheated (Fig. 7.12). When the back pressure was 0 psig, injected steam was more superheated than for the run with 12 psig back pressure. In fact, when the back pressure was 12 psig, the steam temperature was only slightly above saturation temperature. Therefore enthalpy due to superheat is higher for the low back pressure run, and the system is heated faster than for the 12 psig run.

Once steady state is reached, later in the run, the temperature behavior inverts from the earlier response. Figure 7.13 shows the temperature and steam saturation maps at 180 min. The two steam saturation maps are almost identical. Steam flows mainly in the fractures, in the injection side to the left, and in the top fracture. Final temperatures throughout the model are higher with the high back pressure, since its saturation temperature is higher.

Heat loss measurements from the heat flux sensors complement the observed temperature behavior in the model. Initially heat losses are higher for the low back pressure run (Fig. 7.14). Then, as temperatures increase in the high back pressure run, heat losses become higher. The fluctuations in the heat flux measurements from Sensor 5 are again due to the movement of the Fiberfrax insulation, as discussed before.

One important observation from these experiments is that, due to the higher total enthalpy difference available to heat the rock with the lower back pressure, steam

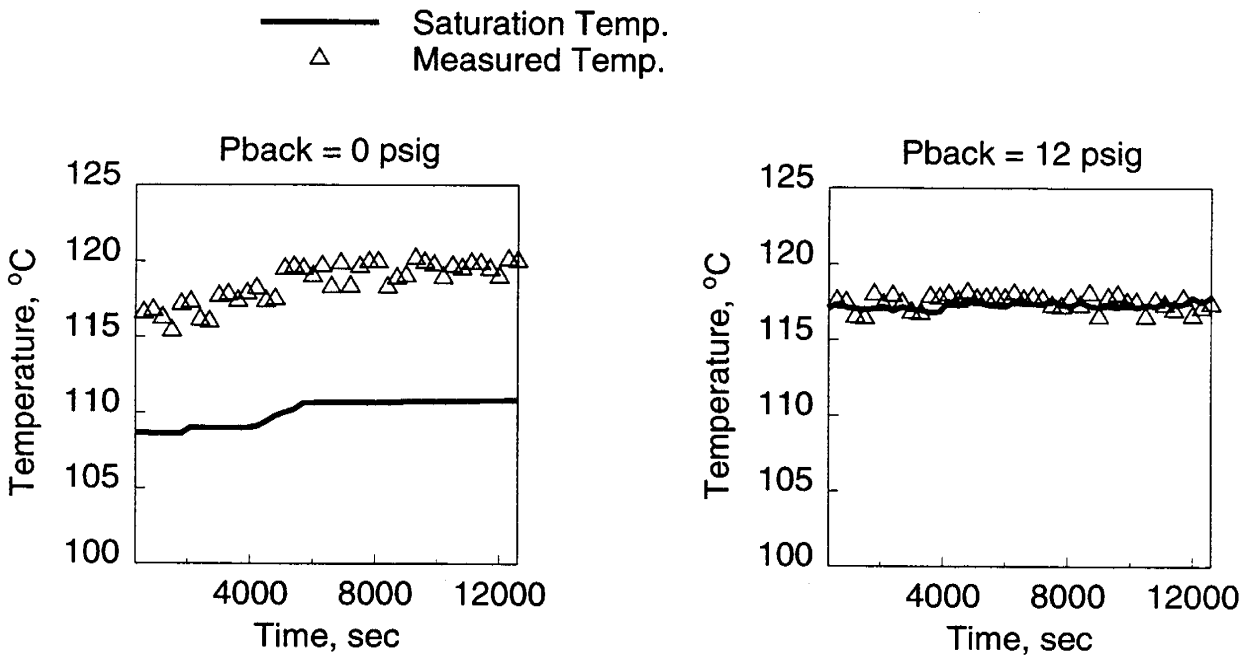

Figure 7.12: Injection line and saturation temperatures for 0 and 12 psig back pressure runs.

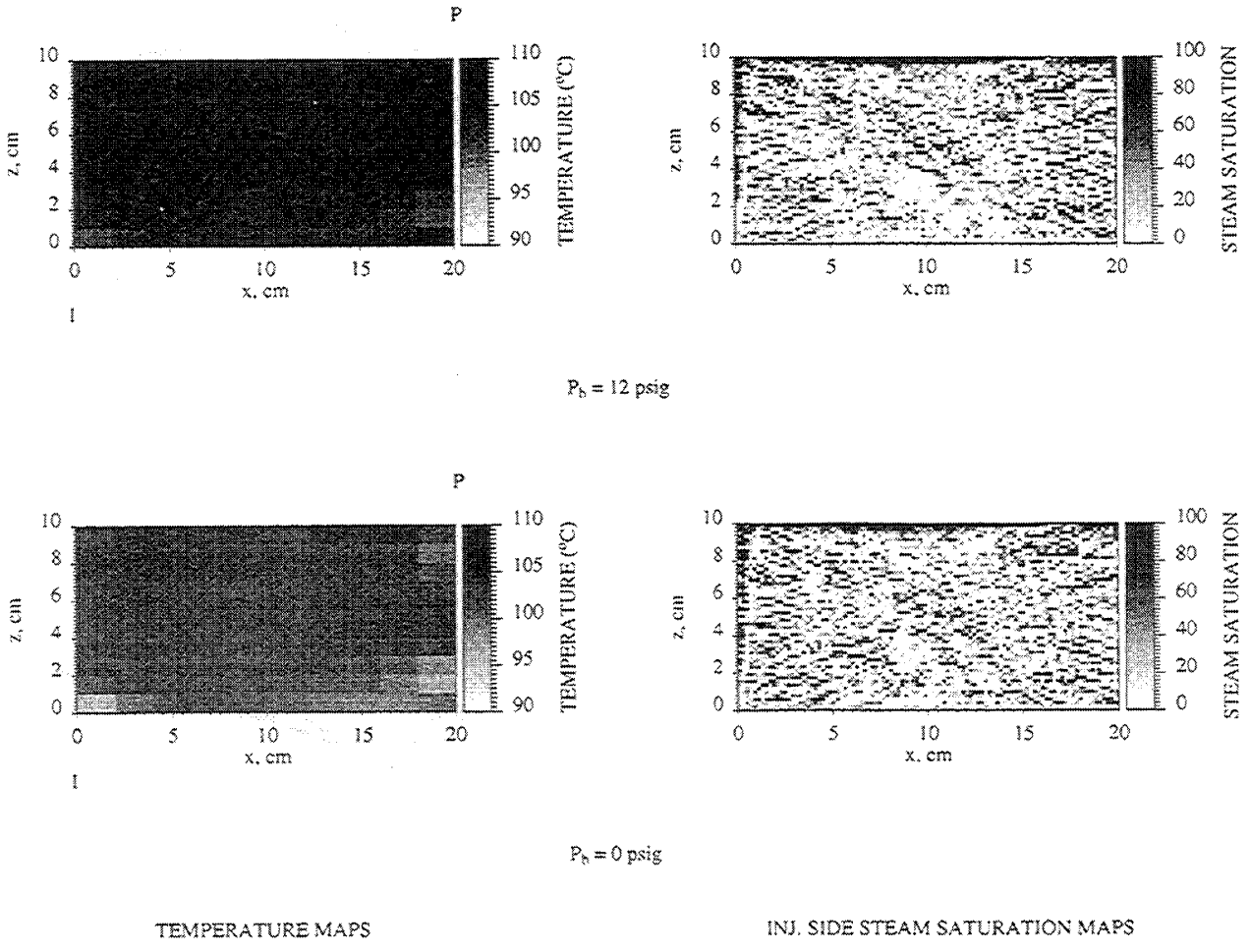

Figure 7.13: Temperature and steam saturation maps at 180 min, for 12 and 0 psig back pressures.

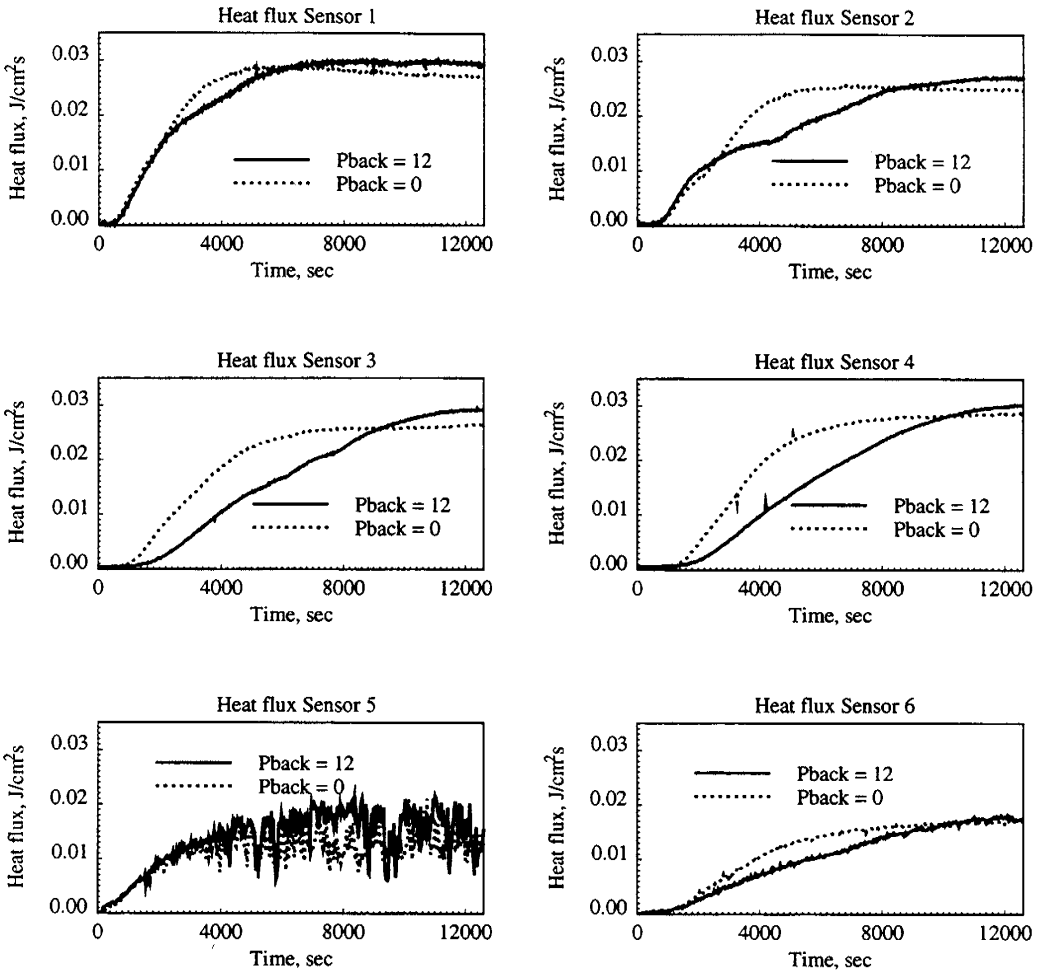

Figure 7.14: Heat losses measured from the sensors (back pressure comparison).

saturation developed faster, and therefore caused faster heating of the matrix. Thus, one can easily speculate that, for a matrix filled with heavy oil, this would have caused a faster viscosity reduction of the oil, and a higher initial oil recovery rate.

7.3.3 Effect of Injection Temperature

Injection temperature of steam is also an important operating parameter since it determines how the reservoir can be heated effectively. Differing injection temperatures were used in the experiments to decide on an injection temperature that would heat the model in a reasonable run time.

Figure 7.15 shows the injection temperatures measured in the injection line from two different runs. The constant rate used in these runs was 6 cc/min and the back pressure was 0 psig. The injection temperature was changed by adjusting the furnace (steam generator) temperature with the temperature controller.

Injection temperature was approximately 10°C higher in Run 26 than in Run 34. The effect of this temperature difference on the heating of the model is shown by the temperature maps in Fig. 7.16 at 210 min. The top map shows the temperature distribution for the lower temperature run, and the bottom shows the same data for the higher temperature run. As expected, the temperature distribution is higher with the higher injection temperature.

7.4 Summary of Experimental Results

One important finding obtained from all runs is that steam saturation only developed in the fractures, and the matrix is heated by conduction. Figures 7.17, 7.18 and 7.19 show the temperature and steam saturation maps at different times for the run at 6 cc/min and 12 psig back pressure. Since qualitatively the same behavior is observed in all runs, only the temperature and steam saturation history from this run are described. The left hand sides of the maps are closer to the injection corner and the right hand sides are closer to the production corner. In the steam saturation maps, Slice 1 is the plane closer to the injector and Slice 2 is closer to the producer.

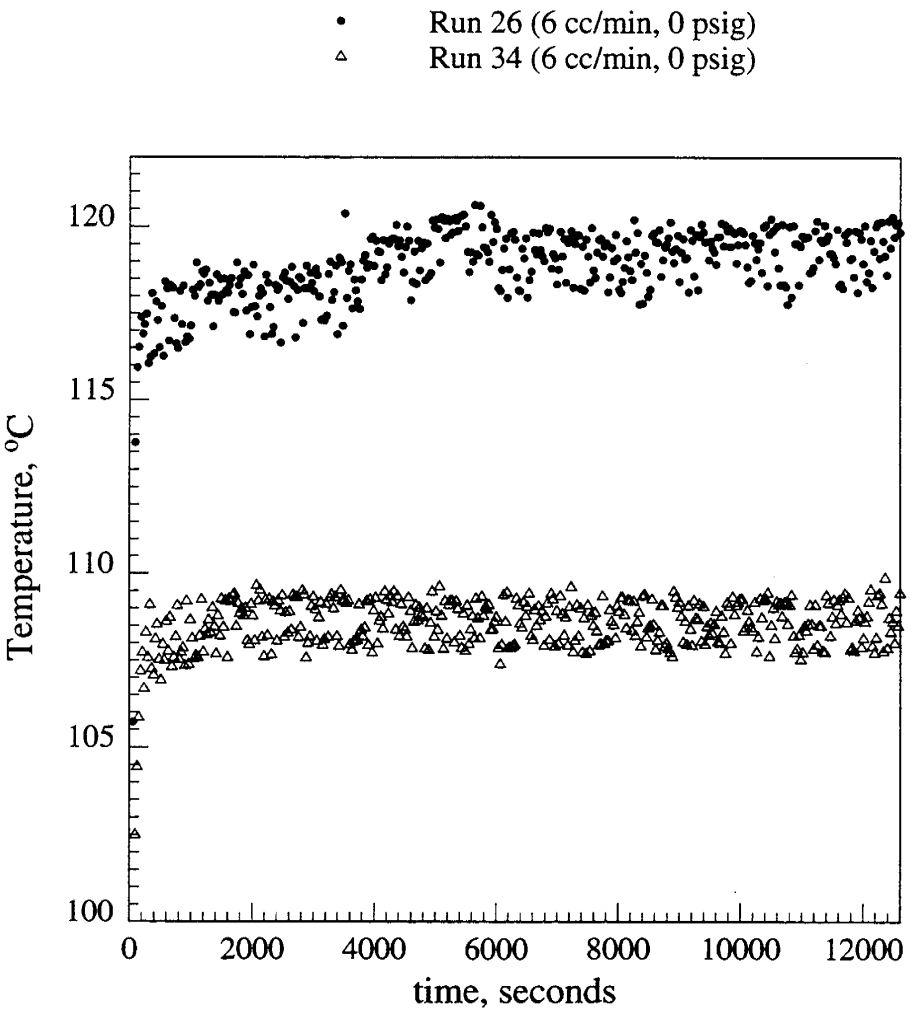

Figure 7.15: Injection line temperatures.

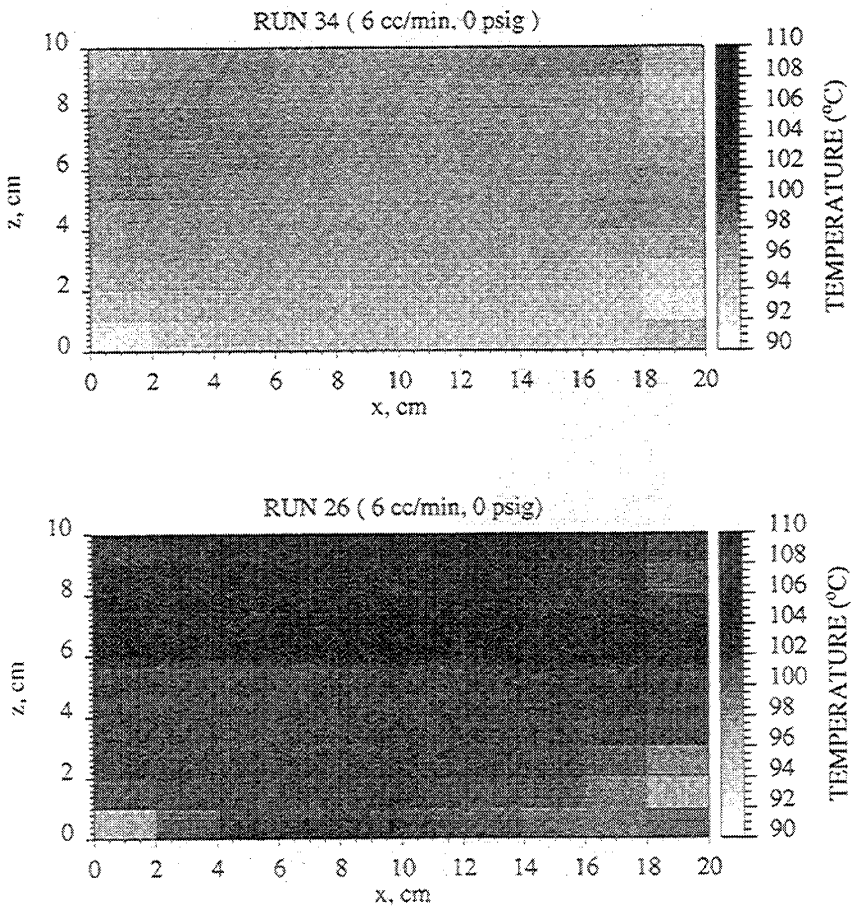

Figure 7.16: Temperature distribution in the model at 210 min for the runs with differing injection temperatures.

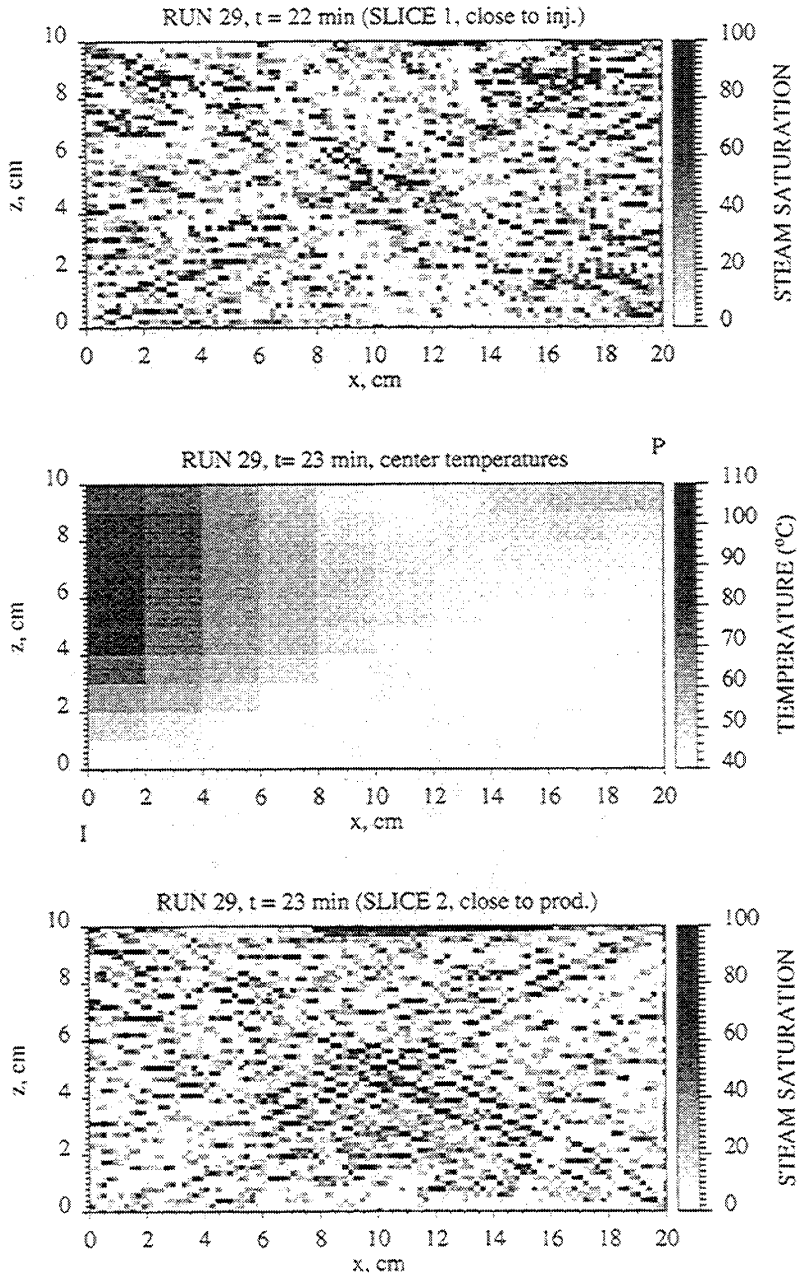

Figure 7.17: Steam saturation and temperature maps measured at 23 min.

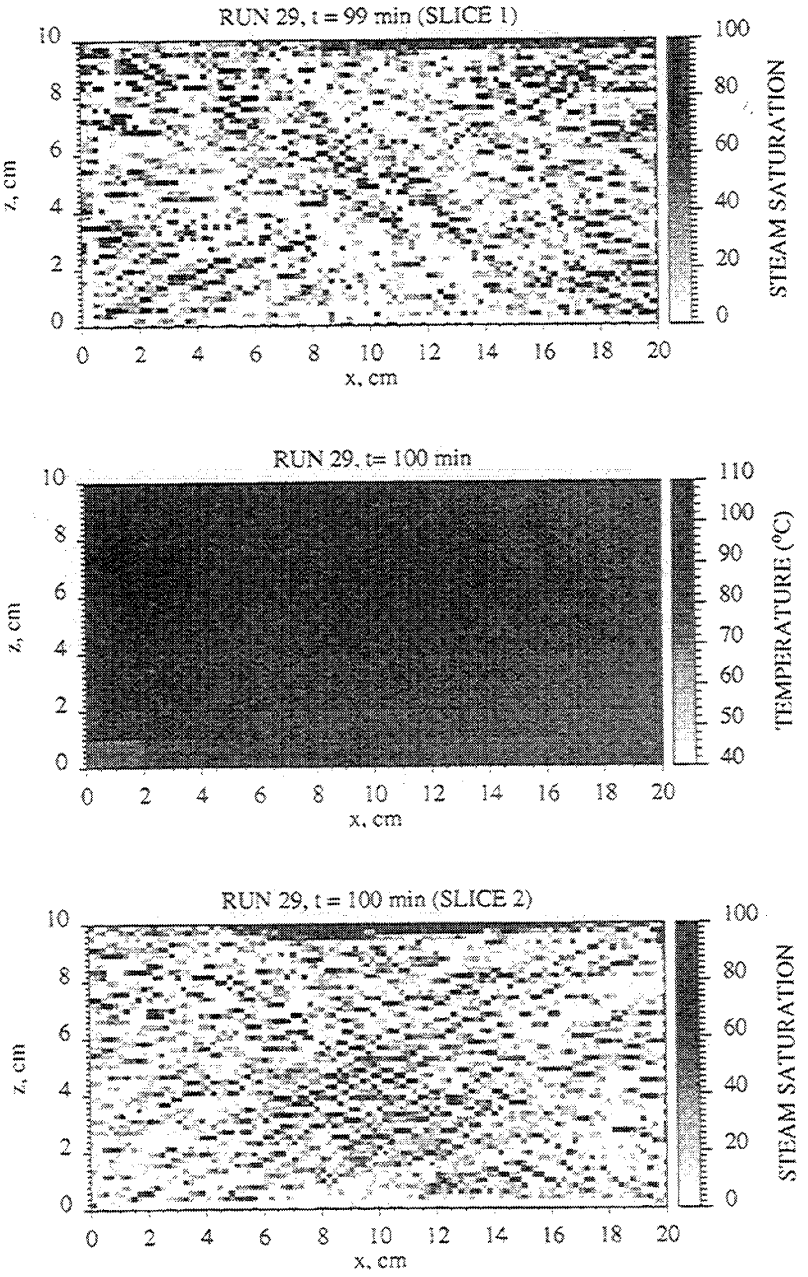

Figure 7.18: Steam saturation and temperature maps measured at 100 min.

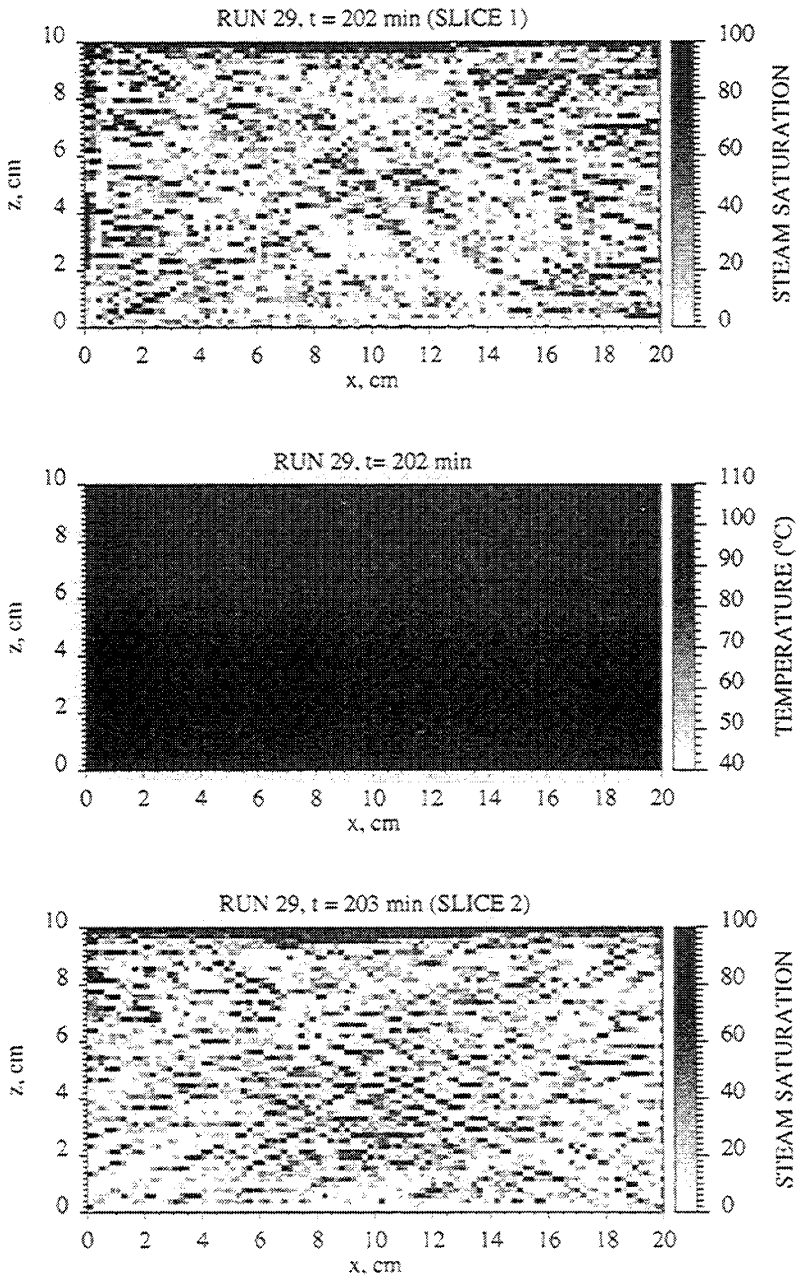

Figure 7.19: Steam saturation and temperature maps measured at 202 min.

In-situ steam saturations are calculated using Eq. 7.1 and the CT image processing software, CATSOFT [8]. At 23 min, steam saturation has not yet developed in the system. Temperature in the matrix has started to increase from left and the top. The fracture in the injector side has the highest temperature, since it is closer to the point where steam enters the system (Fig. 7.17).

At a later time (100 min), the matrix is heated more by conduction (Fig. 7.18). There is a slight steam saturation development at the top fracture due to steam override (Fig. 7.18). Finally, at the end of the run (202 min), the injection side and the top fractures are filled with steam and the entire matrix is heated by conduction (Fig. 7.19). Temperatures are all greater than 100°C in the matrix. Nonzero steam saturations in the matrix, shown in the maps, are due to the artifacts and noise in the CT images. Ways to reduce noise and artifacts will be discussed in the next section.

7.5 Image Processing and Artifact Reduction

When we look at the steam saturations calculated from the CT numbers at the beginning of the steam injection run (before any steam is injected into the system), it is obvious that the nonzero matrix steam saturations are not realistic, and are caused by artifacts and noise. Apparent nonzero steam saturations are calculated in the matrix even at zero time (Fig. 7.20). Unrealistic steam saturations can be filtered, and more accurate steam saturations can be found, by subtracting the image at zero time from the images at later times. The subtraction technique aids in the removal of most of the cross shaped artifacts and the unrealistic steam saturations calculated in the matrix. Subtraction techniques are used widely in medical image processing to reduce unwanted artifacts and noise in the images [55].

Figure 7.21a and b and Fig. 7.22a and b show the effect of subtraction on the steam saturation maps for both slices. The top maps in both figures show the saturation maps before subtraction, and the bottom maps are after subtraction. Subtraction removes most of the artifacts, and most of the unrealistic matrix steam saturations. The diagonal artifacts are almost eliminated. However, we can still see nonzero steam saturations in the matrix. This is because of random noise present in the images due

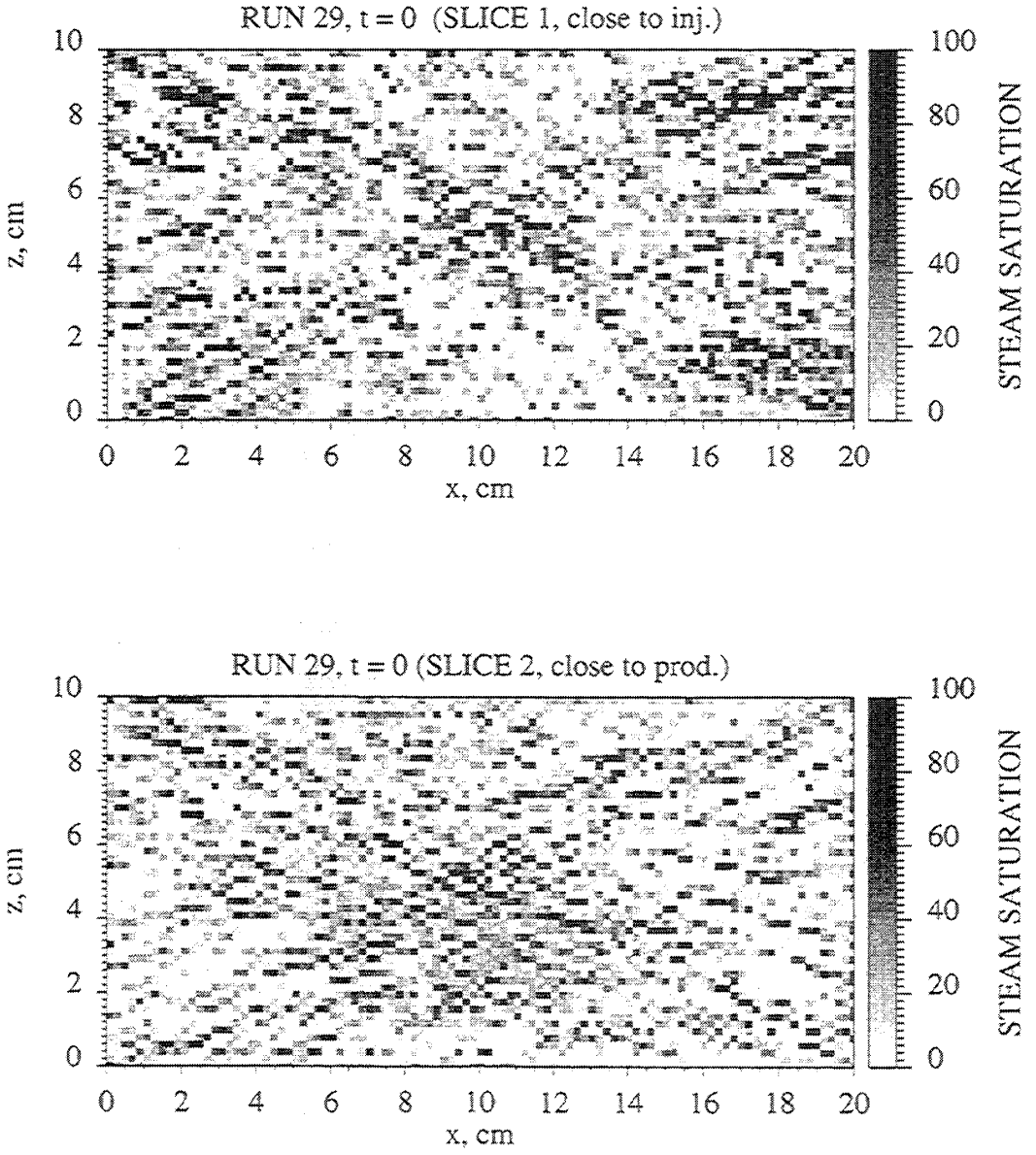

Figure 7.20: Steam saturation maps at time = 0.

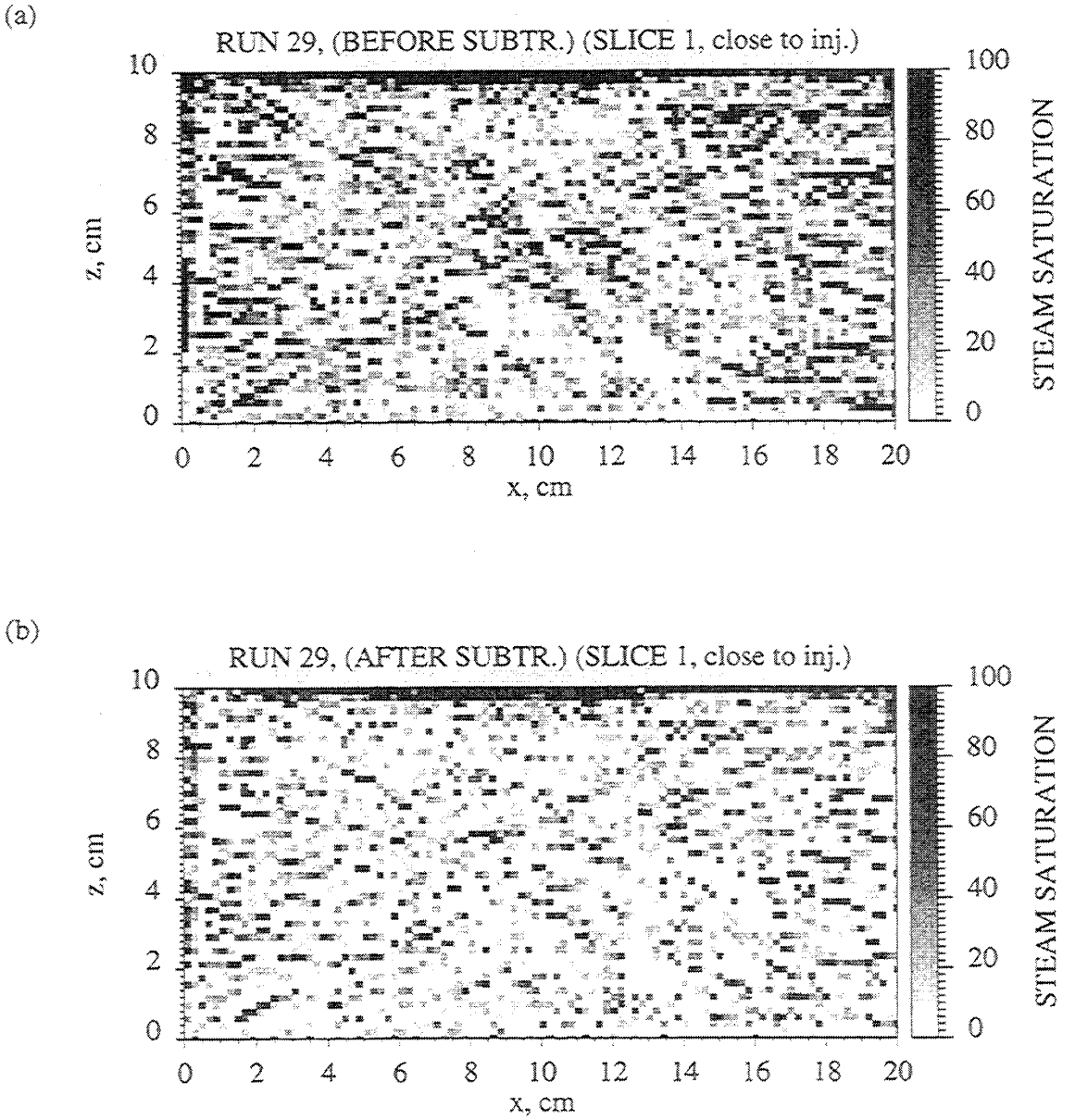

Figure 7.21: Steam saturations in Slice 1 (closer to injector). (a) before subtracting saturations at t = 0. (b) after subtraction.

(a)

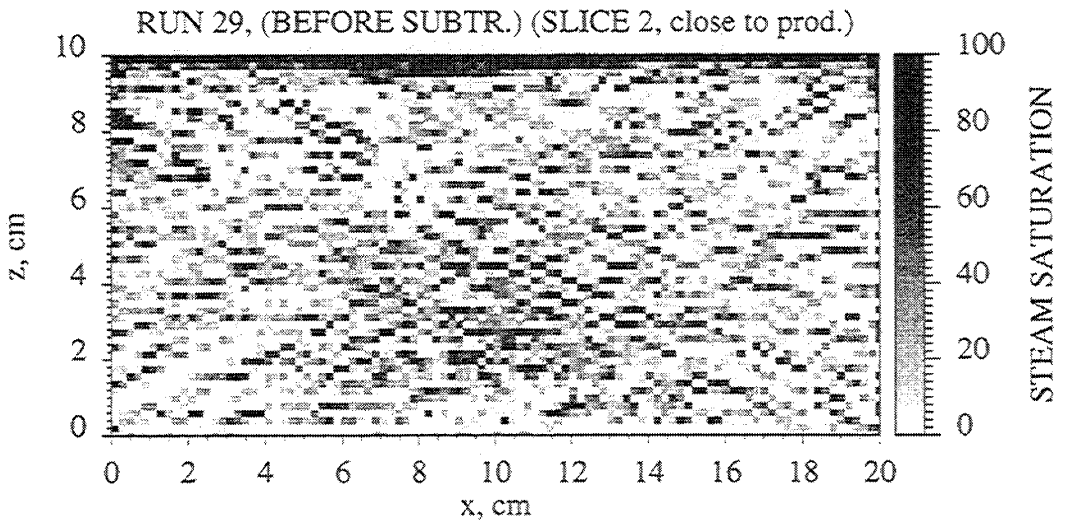

(b)

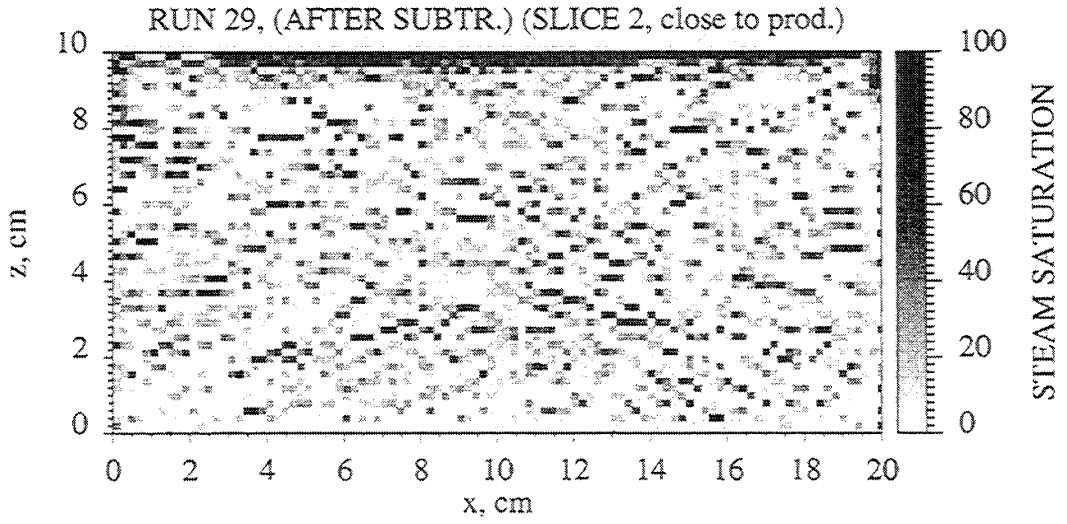

Figure 7.22: Steam saturations in Slice 2 (closer to producer). (a) before subtracting saturations at t = 0. (b) after subtraction.

to the nature of CT scanner measurements. The intensity of the X-ray beam is not homogeneous throughout, and therefore the results are not fully repeatable.

A local averaging and smoothing method was used next to smooth the data and to get better steam saturation maps. The local mean operation is called a smoothing filter [55]. In this method, first the values that are greater than a threshold value are set equal to the threshold. This eliminates unrealistic steam saturations, that are less than zero or greater than one hundred. Then, the domain is divided into a specified number of submatrices. The pixel values are averaged inside each submatrix and the mean is assigned to the center pixel. This process results in a image in which the variation between successive pixels is damped out and therefore the noise is reduced. For our case we took submatrices with dimensions of three by three and took the averages of these nine values. When averaging the data, pixels that correspond to the fractures are also averaged to simplify the calculations. The effect of two-dimensional averaging of the data is shown in Fig. 7.23a and b and Fig. 7.24a and b. The top maps in these figures correspond to the raw unprocessed data and consist of 201×103 pixels. The bottom maps are the averaged data consisting of 67×34 pixels. As a result, the data are smoothed and steam saturations in the fracture are more clearly discernible compared to the saturations in the matrix. The thickness of the fracture shown in the steam saturation maps for the averaged data looks 1.5 times thicker than the raw data because of the averaging process. Such image processing techniques help in the analysis of the data.

When we look at the steam saturation maps after artifacts are reduced, we see that steam only flows in the fractures, and it does not go into the matrix. This is partly due to the permeability difference between matrix and fracture and also due to highly water wet Boise sandstone. This is one of the most important observations from the experiments. However, the matrix is still efficiently heated by conduction. This important finding was made possible by the design of a X-ray transparent core holder and the use of a CT scanner to measure the two-phase steam/water saturations, both in the fracture and matrix. These experimental findings are supported by numerical simulations used to analyze the experimental results. These simulations will be described in the next chapter.

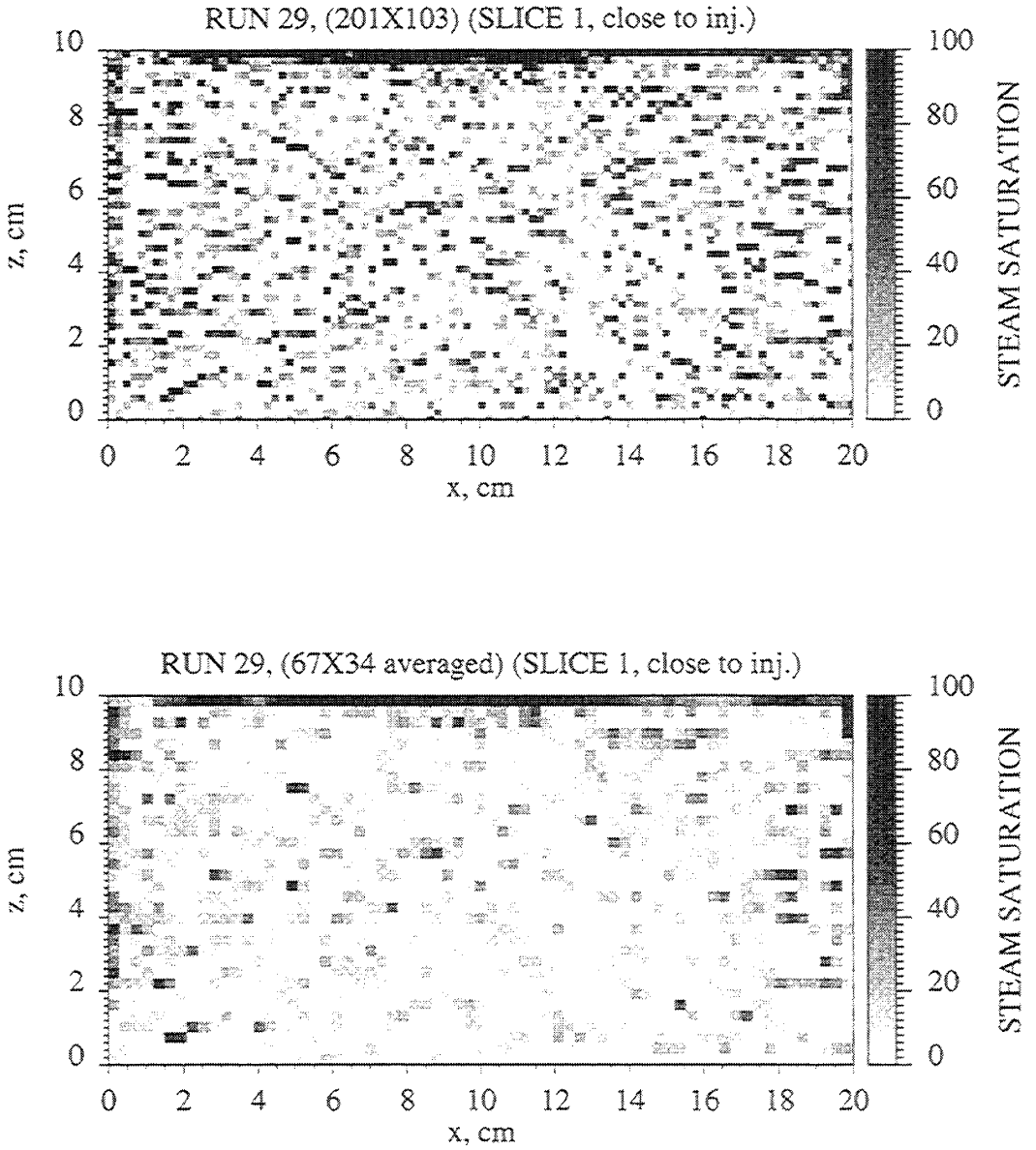

Figure 7.23: Effect of smoothing on the data (Slice 1). (a) Raw data. (b) Smoothed data.

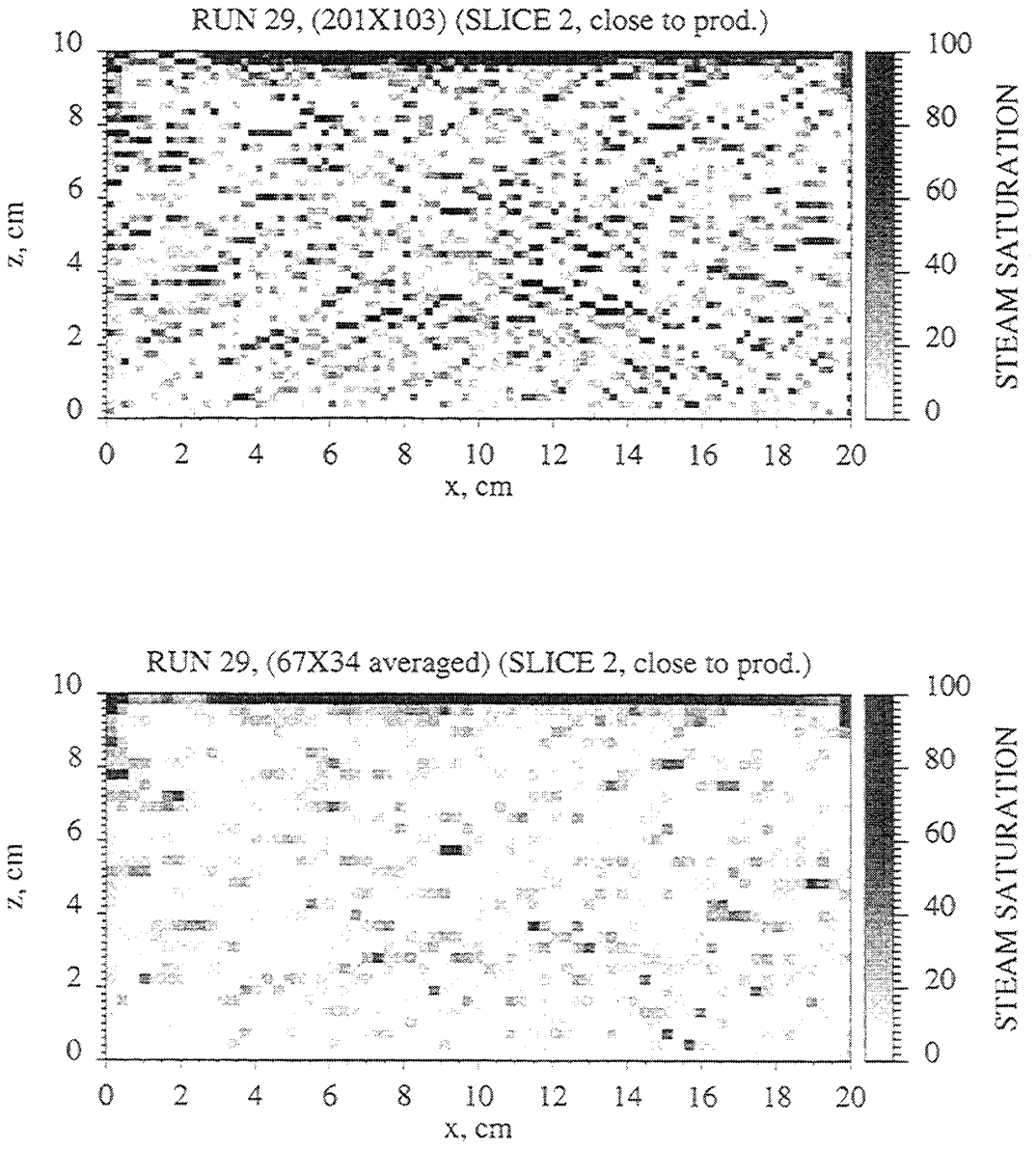

Figure 7.24: Effect of smoothing on the data (Slice 2). (a) Raw data. (b) Smoothed data.

Results from some of the simulations also aided in the design of a pressure cycling scheme, to try to develop steam saturation in the matrix. The results from this pressure cycling experiment will be described in Chapter 9.

Chapter 8

Analysis of the Experimental Data

The experimental data will be analyzed in the following sections. First the heat losses will be modeled by using differing analytical and numerical models. Then history matching simulations will be presented. Finally, a summary of experimental data analysis will be given and the findings will be extended to a case with no external heat losses, similar to what occurs in the field.

8.1 Modeling of Heat Loss

Heat losses from the reservoir to the adjacent formations are important in any steamflood since they determine how fast the reservoir will be heated and how much steam will be required. In fractured reservoirs, the heat transfer to the matrix is also important for it is mainly by conduction from the steam flowing in the fractures.

In any numerical simulation study, heat losses should be accurately modeled before a prediction can be made of the steam saturation and temperature distributions. Generally, when using numerical simulators, it is difficult to model and analyze heat losses found in experiments since most heat loss models used in the simulators are designed for field scale processes.

Computer Modeling Group's, STARS [18] thermal simulator, was used to analyze and history match the experiments. There are two options to model heat losses in STARS.

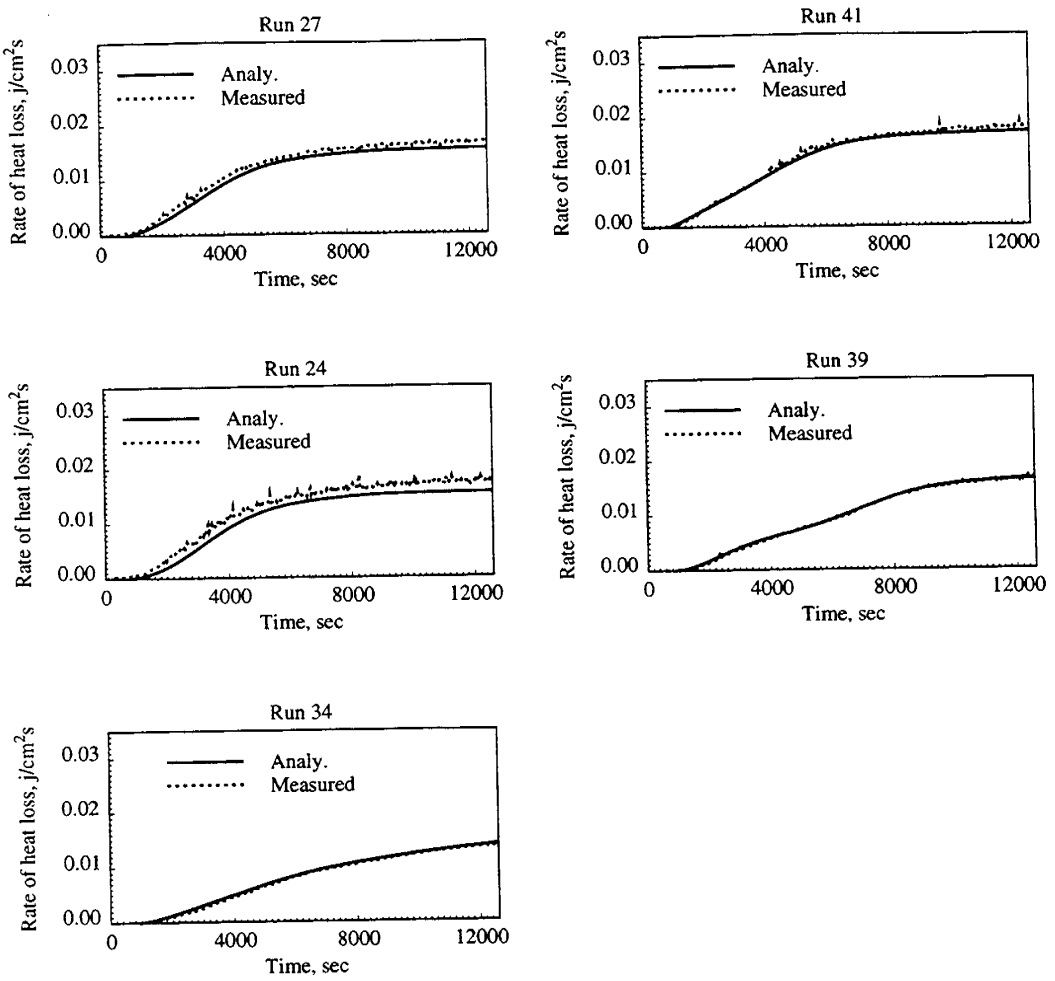

Figure 8.14: Analytical solutions and measured heat losses from the production side for different runs (Sensor 6).

When the fitting function (Eq. 8.1) is inserted into Eqs. 8.2 and 8.3, two algebraic equations result from which p and q can be calculated easily. Once p and q are known, the heat loss from the reservoir to the adjacent formation can be found from the following equation.

$$\lambda \left.\frac{dT}{dz}\right|_{z=o} = \lambda \left(\frac{\Theta}{d} - p\right) \tag{8.4}$$

where,

λ = Thermal conductivity

This model considers the adjacent formations to be infinite, which is a reasonable assumption for most field steam injection processes. However, it is not realistic for a laboratory model with a finite layer of insulation around it.

The second heat loss model, used in the STARS simulator, is the convective heat loss model, where the heat loss from the system to the surroundings is given by the following equation taken from the STARS Users Manual [18],

$$q = h_{conv}(T - T_{amb}) \tag{8.5}$$

where,

q	=	Convective heat loss rate
T_{amb}	=	Ambient or reference temperature
h_{conv}	=	Overall convective heat transfer coefficient
T	=	Temperature inside the system

Both heat loss models were used in the simulations, and the results were compared with the experimental losses measured by heat flux sensors. Since the heat losses measured from the two top sensors are similar to each other, only one heat flux

sensor at the top will be compared with simulator calculations. The same is true for the bottom sensors; only one of the two will be shown.

Figure 8.1 shows the heat loss rates from the experiment and from simulations using the two heat loss models. The dotted lines show the heat loss curves for the infinite overburden model (Eq. 8.4), the solid lines show heat losses from the convection model (Eq. 8.5), and the symbols (dots) show measured data from the heat flux sensors. For all the cases, the infinite overburden model shows an increasing trend first, but then it declines. It never reaches steady state. This is contrary to the experimental heat losses and the losses calculated by the convective model. This result is expected due to the nature of the model. Same behavior was observed with an infinite thickness insulator in the one-dimensional analytical heat transfer calculations that were described in Chapter 4.

The shapes of the heat loss curves are different for the top and the injection side than for the bottom and the production side. The heat loss curves peak for the top and the injection sides since the temperatures inside the system immediately reach steam temperature there. The increase in heat losses are more gradual for the bottom and production sides since they are heated more gradually.

On the other hand, the convective heat loss model first shows a rapid increase in rate and then reaches steady state. This confirms the conclusion that when simulating heat losses from experiments it is not realistic to use the infinite overburden model. However, the transient portion of the convective heat loss curve differs from the experimental curves. The heat losses increase abruptly in the simulator rather than the smooth more gradual measured increases. This shows that the convective heat loss model is also not sufficient by itself to model the experiments accurately.

Next, heat losses from the experiments were analyzed by different analytical models to determine how the results can be used in conjunction with the simulator models to better model the experiments.

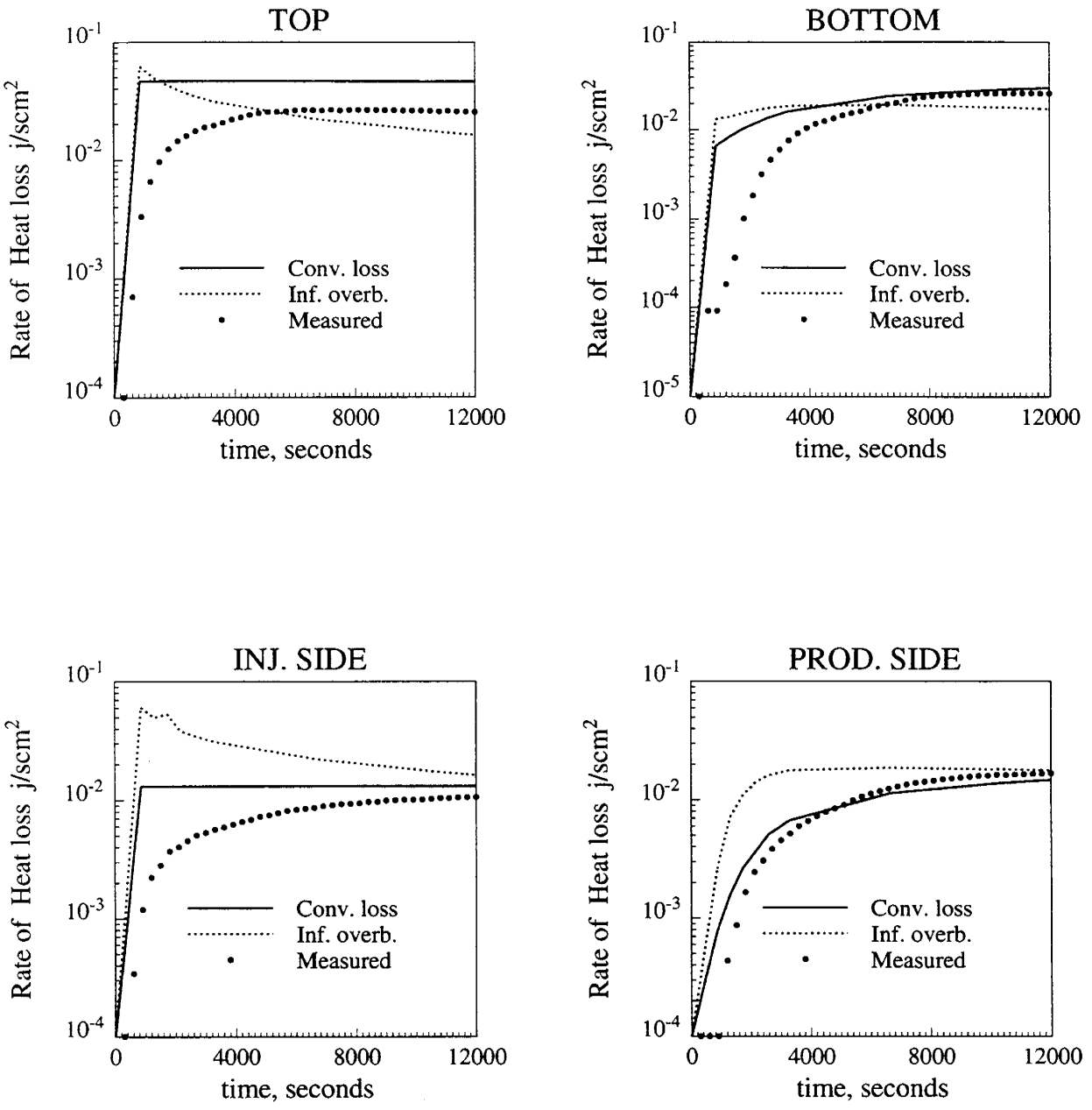

Figure 8.1: Measured heat losses compared to those calculated by different simulator models.

8.1.1 Analytical Heat Transfer Models

To analyze the experimental heat losses, the one-dimensional transient heat conduction equation (Eq. 8.2) was solved analytically. The solutions of this equation were discussed in Chapter 4 for six different cases. These solutions were used in the design of the experiment and were done for different insulation combinations. In this chapter, these solutions are applied to the real model using the exact experimental conditions and core holder thermal properties. Solutions were only done for a single polysulfone layer since the effect of the Fiberfrax was not found to be significant in this system. The Fiberfrax insulation primarily acted as a shield against air currents from the fans so that heat flux sensor readings were more stable.

Laplace transformation was applied to Eq. 8.2 and the boundary conditions. The solution was then inverted to real time by the Stehfest Algorithm [81]. The solutions will be compared in detail with the heat loss measurements from one heat flux sensor located at the top of the model.

Case 1:

Boundary conditions are constant temperature at both inner and outer boundaries.

$$\text{at } z = 0 \quad T = T_s \tag{8.6}$$

$$\text{at } z = a \quad T = T_a \tag{8.7}$$

where,

a	=	Thickness of the polysulfone core holder
T_a	=	Ambient temperature
T_s	=	Steam temperature inside the fracture

Figure 8.2 compares the heat losses calculated from the analytical solution with the heat losses measured by the sensor. The calculated values are much higher than measured. This is expected since the inner boundary does not reach steam temperature

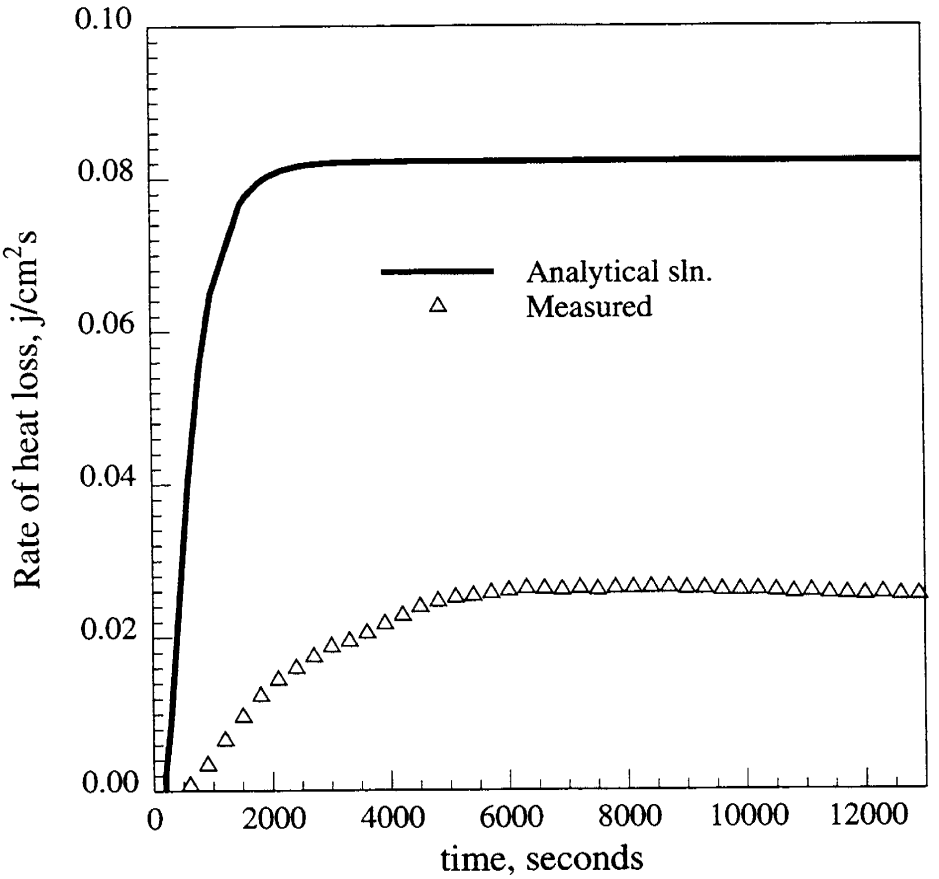

Figure 8.2: Measured heat losses compared to calculations with constant inner and outer boundary conditions.

instantaneously in the experiment, but rather reaches that temperature gradually, as observed from thermocouple measurements.

Case 2:

For this solution, the inner boundary condition is taken as steam temperature, but the outer boundary condition is switched to the convective condition.

$$\text{at } z = 0 \qquad T = T_s \tag{8.8}$$

$$\text{at } z = a \qquad h_f(T - T_\infty) = -\lambda \frac{\partial T}{\partial z} \tag{8.9}$$

where,

T_∞ = Free stream or ambient air temperature

h_f = Convective heat transfer coefficient from the polysulfone core holder to the surroundings

Figure 8.3 compares the heat losses calculated using the convective outer boundary condition with the measured values. The calculated heat losses are lower than in Fig. 8.2 and are closer to the measured values since the convective boundary condition is a more realistic assumption for our system. Also, the temperature changes are more gradual. However, the calculated heat losses are still higher and rise more rapidly than measured, because we assumed a constant temperature at the inner boundary.

Thermocouple measurements in the fracture show that temperatures increase gradually with time. Figure 8.4 shows the temperature measurements from six thermocouples in the fracture at the locations closest to the six heat flux sensors. The thermocouple at the injection side close to the HF 5 rises most rapidly since it is nearest to the injector. The next most rapid rise is in the thermocouple at the top fracture close to HF 1. The slowest rise was observed for the thermocouples at the bottom close to Sensors 3 and 4, which are heated most slowly. It is clear from these measurements that the inner boundary condition should have temperature varying with time to model heat losses.

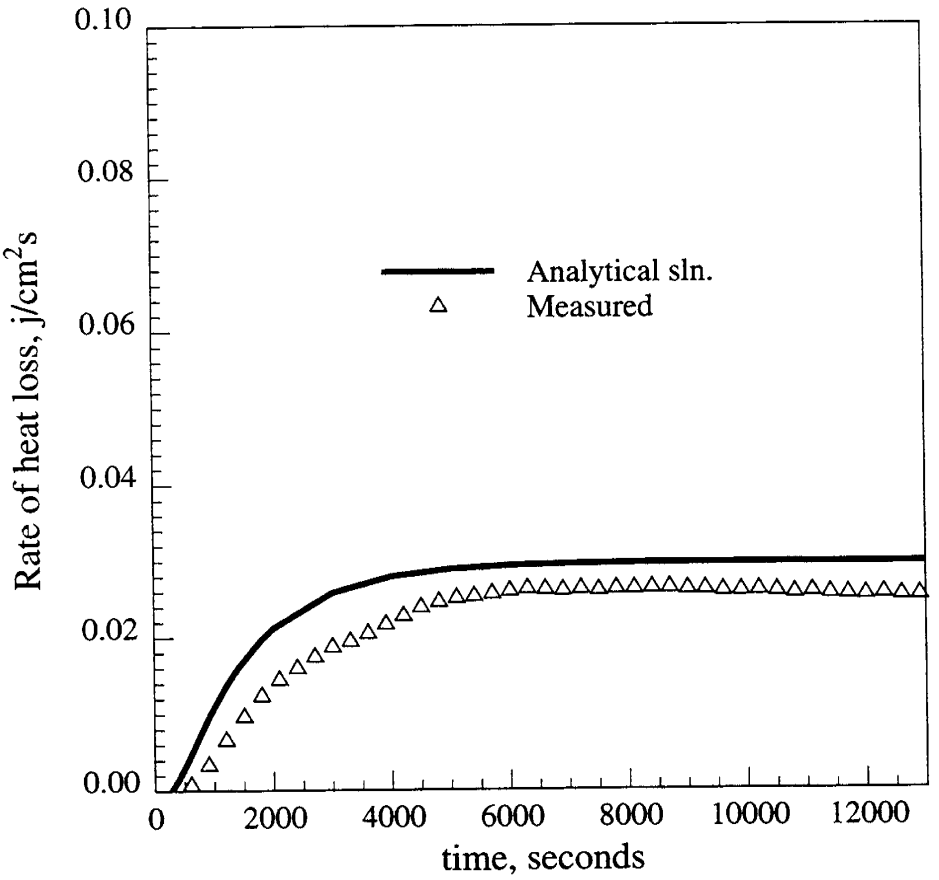

Figure 8.3: Measured heat losses compared to those calculated with convective outer boundary condition.

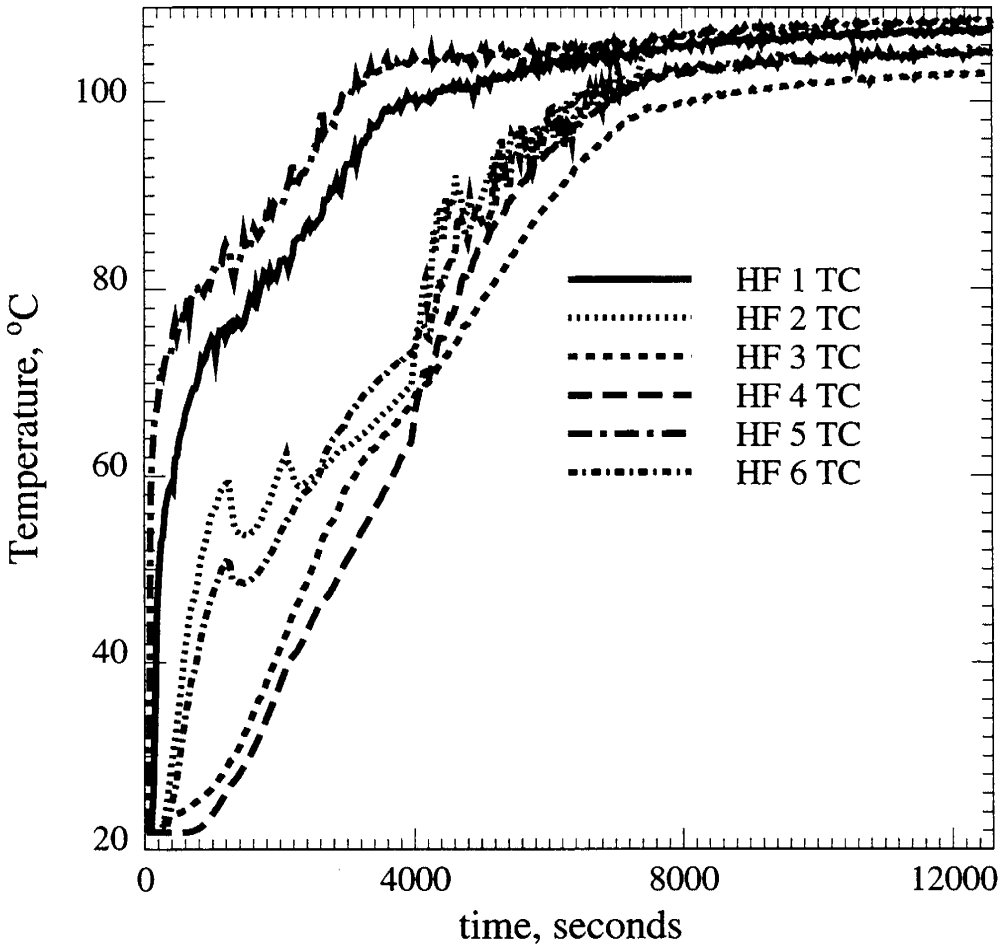

Figure 8.4: Thermocouple measurements.

Case 3:

For this case, the inner boundary condition was taken as variable temperature, and the outer boundary condition as constant temperature.

$$\text{at } z = 0 \quad T = T(t) \tag{8.10}$$

$$\text{at } z = a \quad T = T_a \tag{8.11}$$

To take the Laplace transformation of the temperature function, least squares polynomial fitting was used on the temperatures measured by the thermocouples in the fracture. Figure 8.5 compares the temperatures measured in the fracture, close to Sensor 1 at the top, with the calculated temperatures using a ninth degree polynomial. The fit is quite good. This polynomial was used as the inner boundary condition in the solution.

Some numerical problems occurred due to the Stehfest Inversion Algorithm. The ways to handle those are discussed in detail in Appendix C. The use of double precision in the computer code resulted in completely wrong and unstable solutions. One should use caution, in the type of functions to be inverted and the precision used in the code, to avoid this kind of problem.

Even though the analytical solution was stable and its shape was close to the measured heat losses, there was still a difference between them (Fig. 8.6). Therefore, the outer boundary was switched to the convective boundary condition, and the solution was repeated.

Case 4:

For this case, the boundary conditions were as follows,

$$\text{at } z = 0 \qquad T = T(t) \tag{8.12}$$

$$\text{at } z = a \qquad h_f(T - T_\infty) = -\lambda \frac{\partial T}{\partial z} \tag{8.13}$$

Figure 8.7 compares the solutions with convective and constant temperature outer boundary conditions with the measured heat fluxes. The convective outer boundary solution matched almost perfectly with the measured heat losses. No adjustment was made on the heat properties to achieve this fit. The thermal properties of the

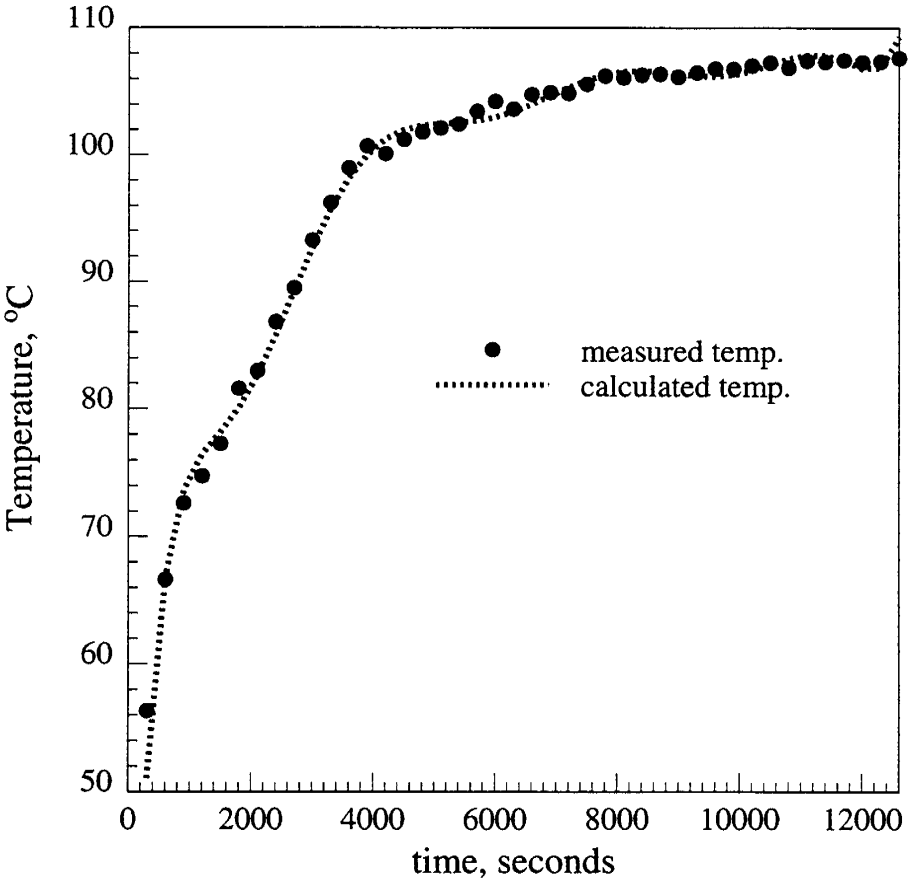

Figure 8.5: Measured temperatures compared to calculations by a ninth degree polynomial.

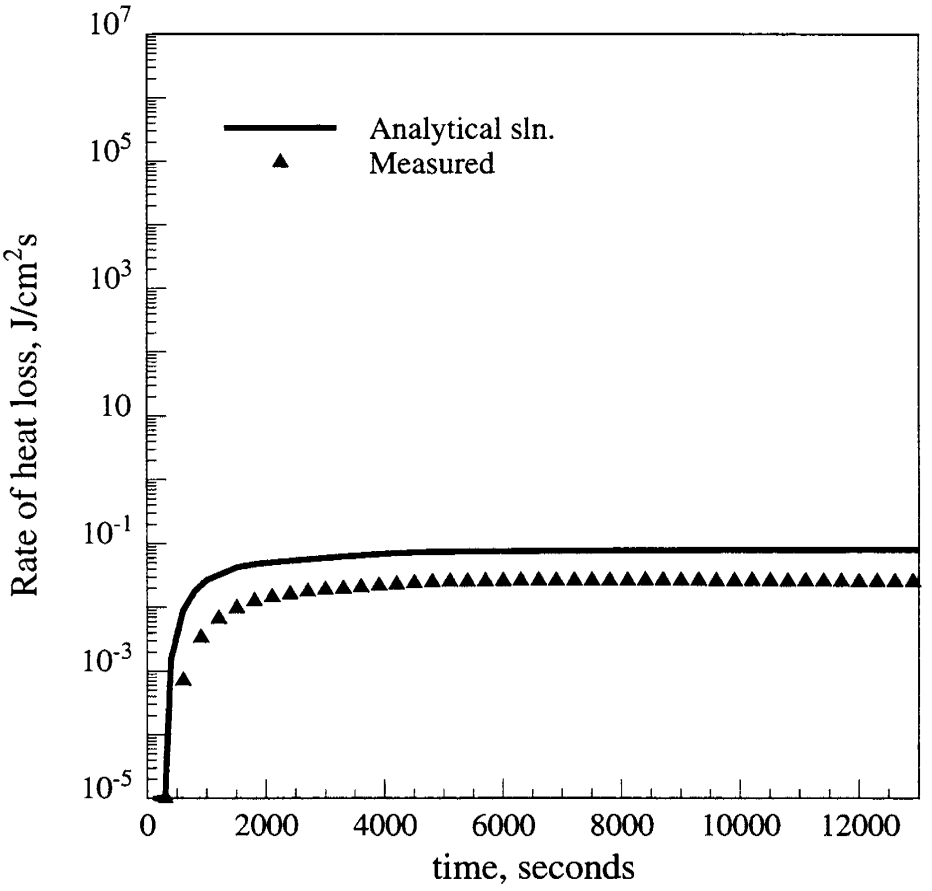

Figure 8.6: Measured heat fluxes compared to calculations by the analytical solution (Case 3).

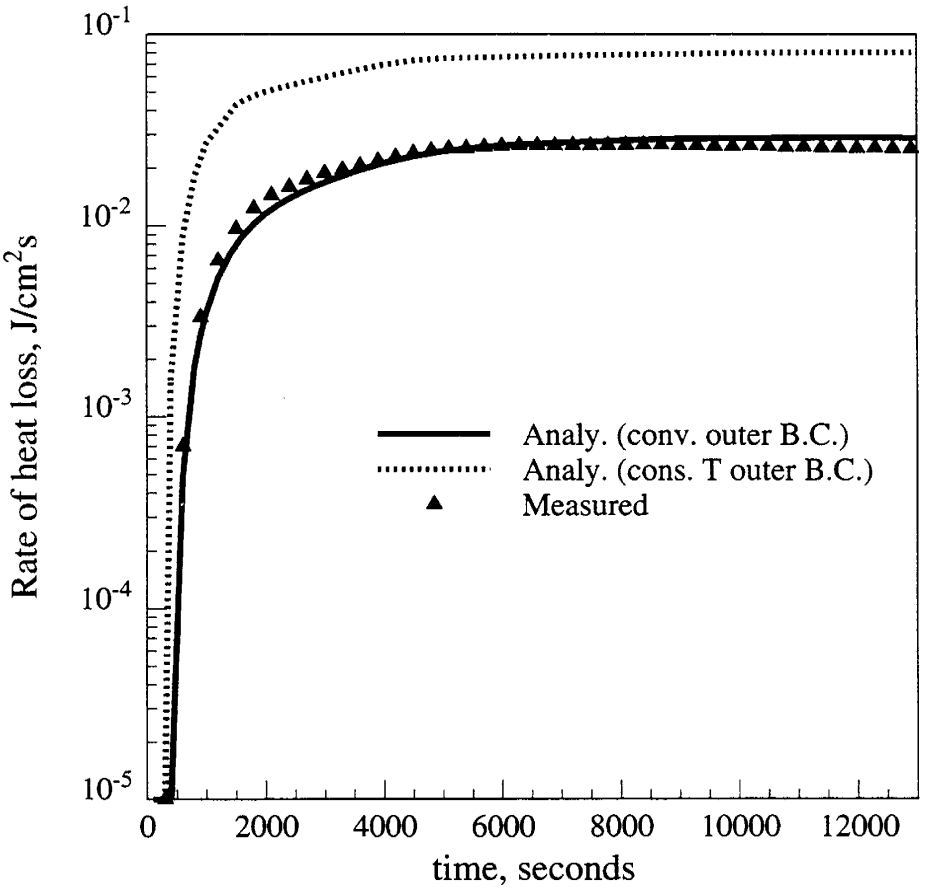

Figure 8.7: Comparison of constant and convective outer boundary solutions with measured heat loss data.

core holder were used for the conductivity and diffusivity and the value of convective heat transfer coefficient was within the range given in the literature [39]. This range is $0.00045 - 0.00065 J/scm^2K$, and the value used in the calculations was 0.00053. The same solution is also shown in Fig. 8.8 with Cartesian scale to emphasize the differences. The agreement is still quite good.

In all of the solutions discussed so far, the ambient air temperature, or free stream temperature was taken as 21°C. A sensitivity study was done on this parameter, and its effect is shown in Fig. 8.9. It is clear from the results that free stream temperature has a large effect on the solutions considering the temperature changes were only ±2°C. The temperature in the room was observed to change from experiment to experiment and the changes were more than 2°C. This indicates that the fit to the measured curves might have been much better if actual free stream temperatures had been monitored during the experiments.

The same solution technique was used to model the remaining five sensors. Figure 8.10 shows the comparison of the analytical solutions with the heat losses measured from all six sensors. The agreement is quite good. The same convective heat transfer coefficients were used for the sensors at the top and bottom (Sensors 1-4). The coefficient was decreased to 0.00015 and 0.00025 respectively for Sensors 5 and 6 which are on the sides of the model. These differences may have been due to differences in air currents from the fans at the sides compared to the top/bottom of the core holder. Furthermore, air velocity is known to affect the thickness of the boundary layer which can cause variations in the convective heat transfer coefficient.

After successfully matching the heat losses with the analytical solution for one experiment, the heat losses from different experiments were analyzed to see whether the same convective heat transfer coefficients would work for all runs. These runs were made at differing injection rates, back pressures and injection temperatures. The calculated and measured heat losses are compared next for four of the sensors; one each at the top, bottom, the injection side and the production side.

Figure 8.11 compares the heat losses calculated and measured from Sensor 1 (top). The same convective heat transfer coefficient was used in all these runs. The matches were good for all the runs. Similar agreement between the analytical solutions and

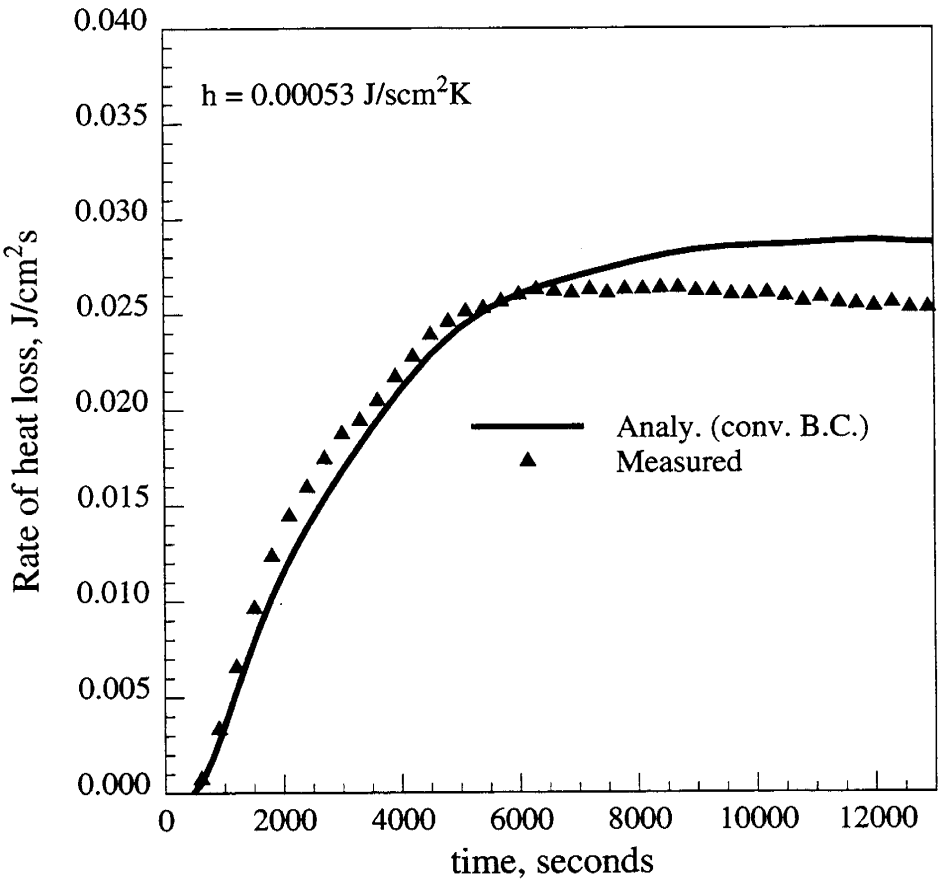

Figure 8.8: Convective outer boundary solution (Cartesian heat loss scale).

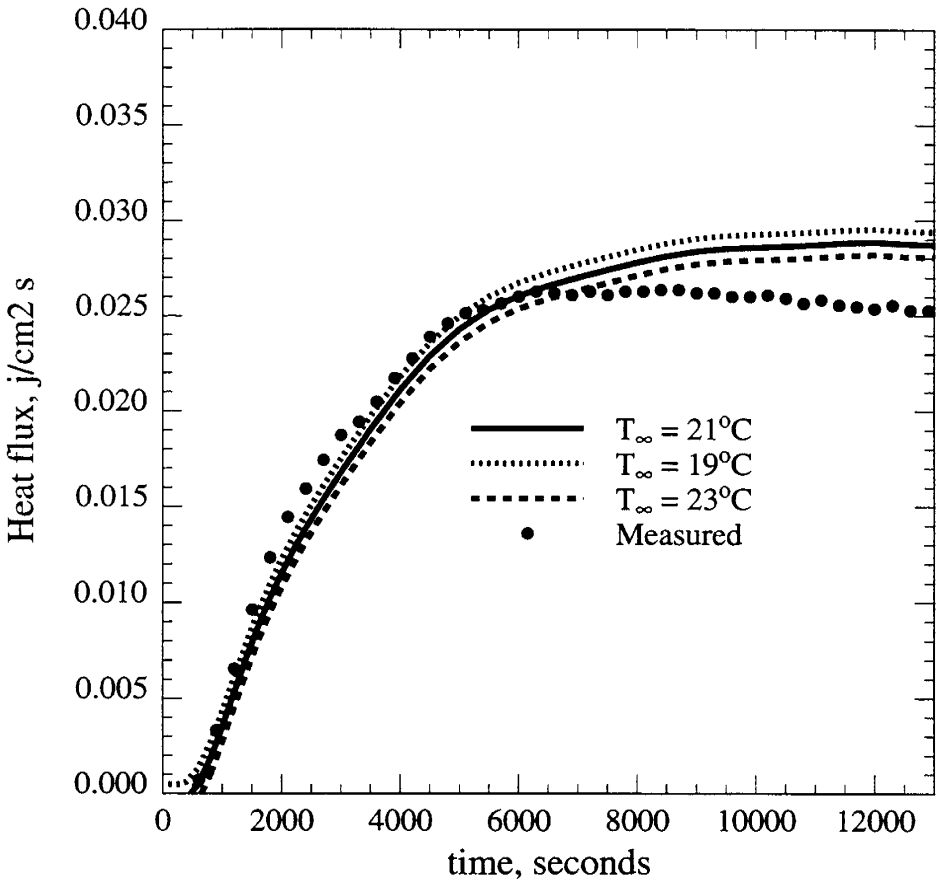

Figure 8.9: Effect of T_∞ on calculated heat losses.

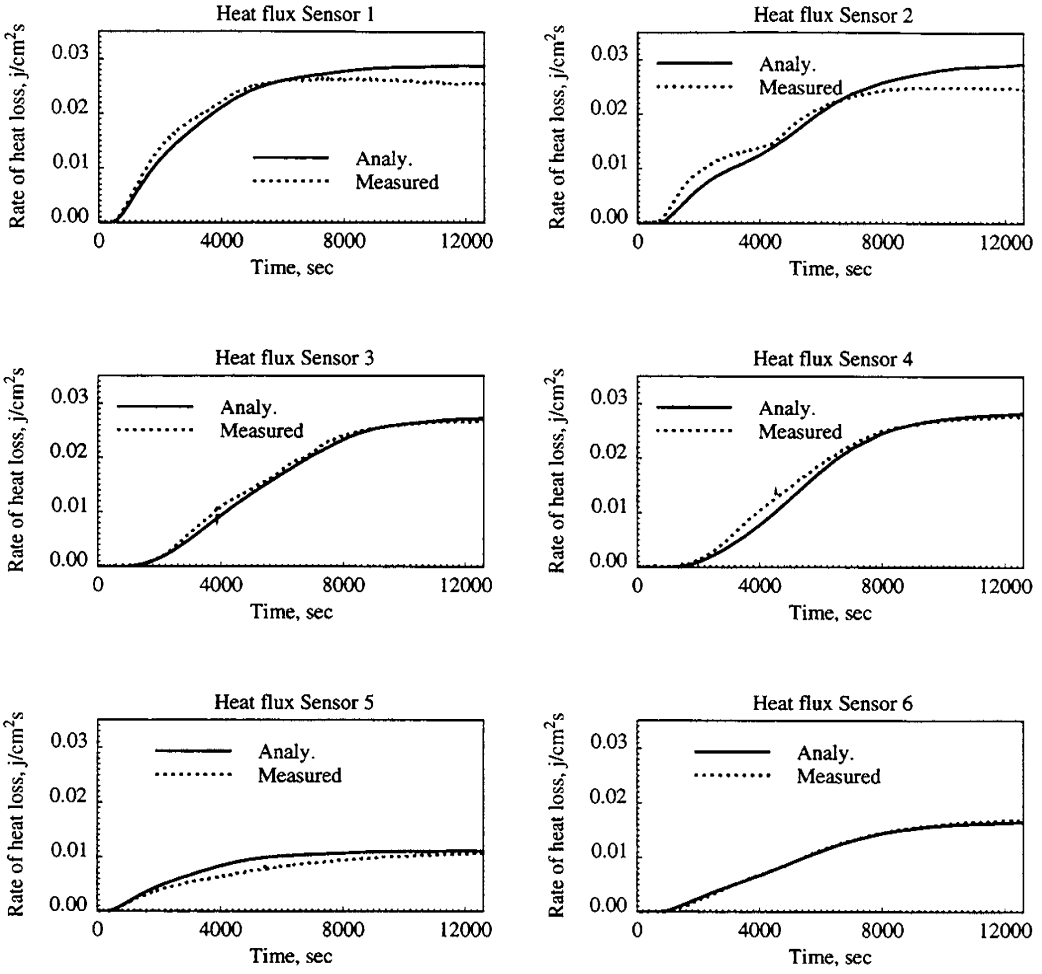

Figure 8.10: Analytical solutions and measured heat losses for the six sensors.

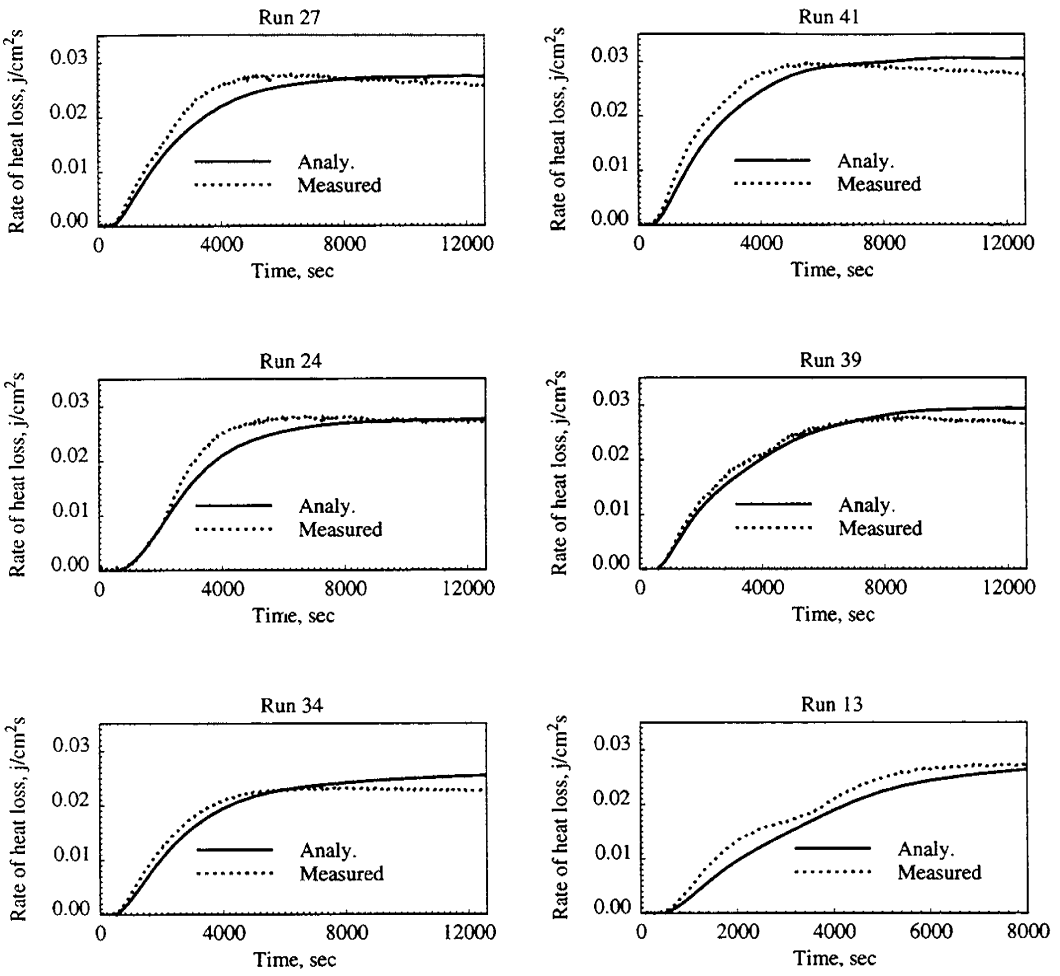

Figure 8.11: Analytical solutions and measured heat losses from the top for different runs (Sensor 1).

measured heat losses was observed for Sensor 3 at the bottom (Fig. 8.12).

Figure 8.13 compares heat fluxes at the injector side of the system (Sensor 5). For most of the runs the matches are close to the analytical solutions. The oscillations and the noise observed in some of the runs are due to the Fiberfrax insulation on that side. The movement of the core holder on the table during scanning caused the insulation to move and affect sensor response. Again, the same convective heat transfer coefficient was used in all of these runs except for Run 41 in which the coefficient for the injector side was increased from 0.00015 to 0.00022 since the fiberfrax insulation was removed from that side for that specific run.

The heat flux sensor located at the production side of the model (Sensor 6) shows similar good matches with the analytical solutions (Fig. 8.14). A comparison for Run 13 is not shown for that sensor due to its malfunction for that experiment.

8.1.2 Heat Loss Data Analysis by Simulations

As discussed before, the conventional simulator heat loss models were not adequate to model the experiments. The analytical solution with the convective boundary conditions showed a good match for most of the runs. The analytical solution basically modeled conductive heat loss through a finite thickness insulation with a convective outer boundary condition.

To implement similar conditions in the simulator, the grid system was modified. Figure 8.15 shows the modified grid system used for history matching, where the shaded area is the insulation. The insulation (core holder) was simulated using grid blocks of zero porosity and permeability and the heat properties of polysulfone. These blocks only conducted heat. Heat losses at the outer block faces were taken as convective, using the convective heat transfer coefficients from the analytical solutions. They were each multiplied by grid block area, and assigned heat transfer coefficients for each outer grid block.

Figure 8.16 compares the resulting heat losses calculated from the simulator with the earlier heat loss models and with the measured heat losses. Heat losses are shown for the top, bottom, injection and production sides of the model. The simulator

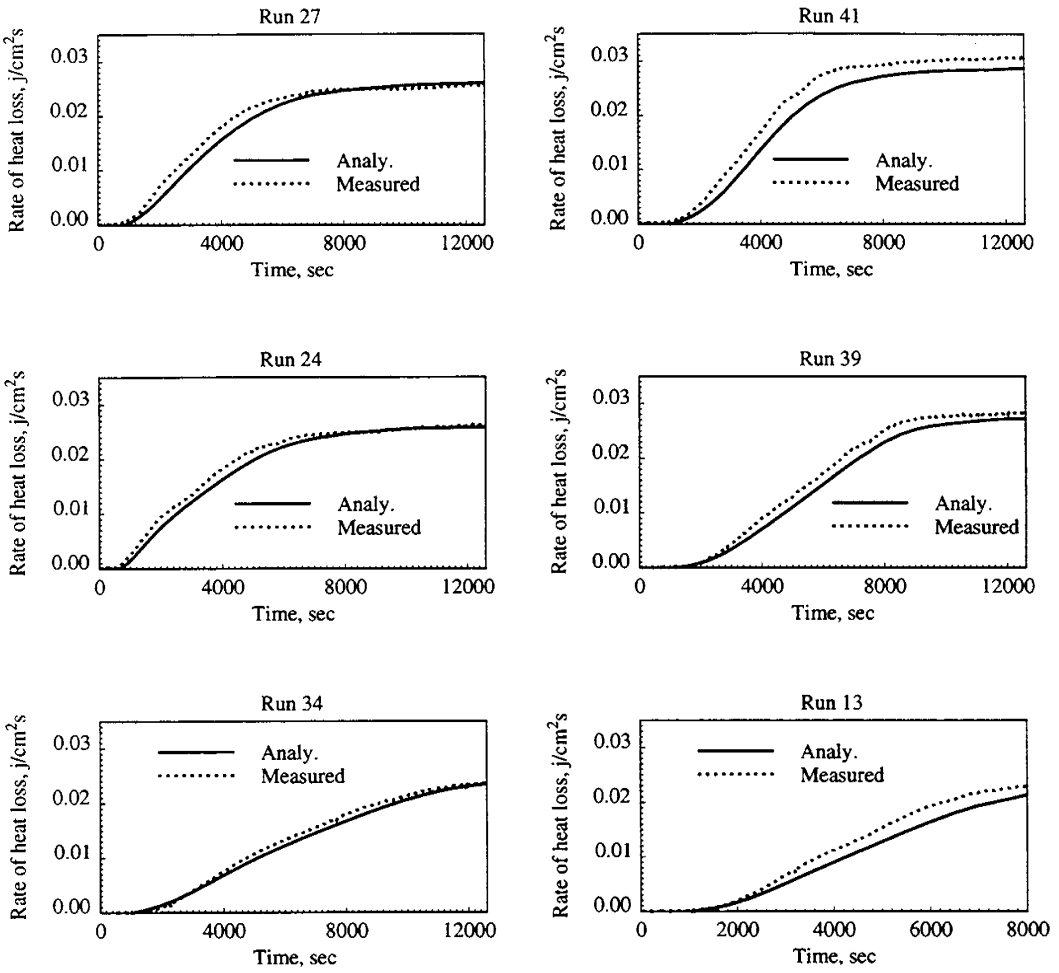

Figure 8.12: Analytical solutions and measured heat losses at the bottom for different runs (Sensor 3).

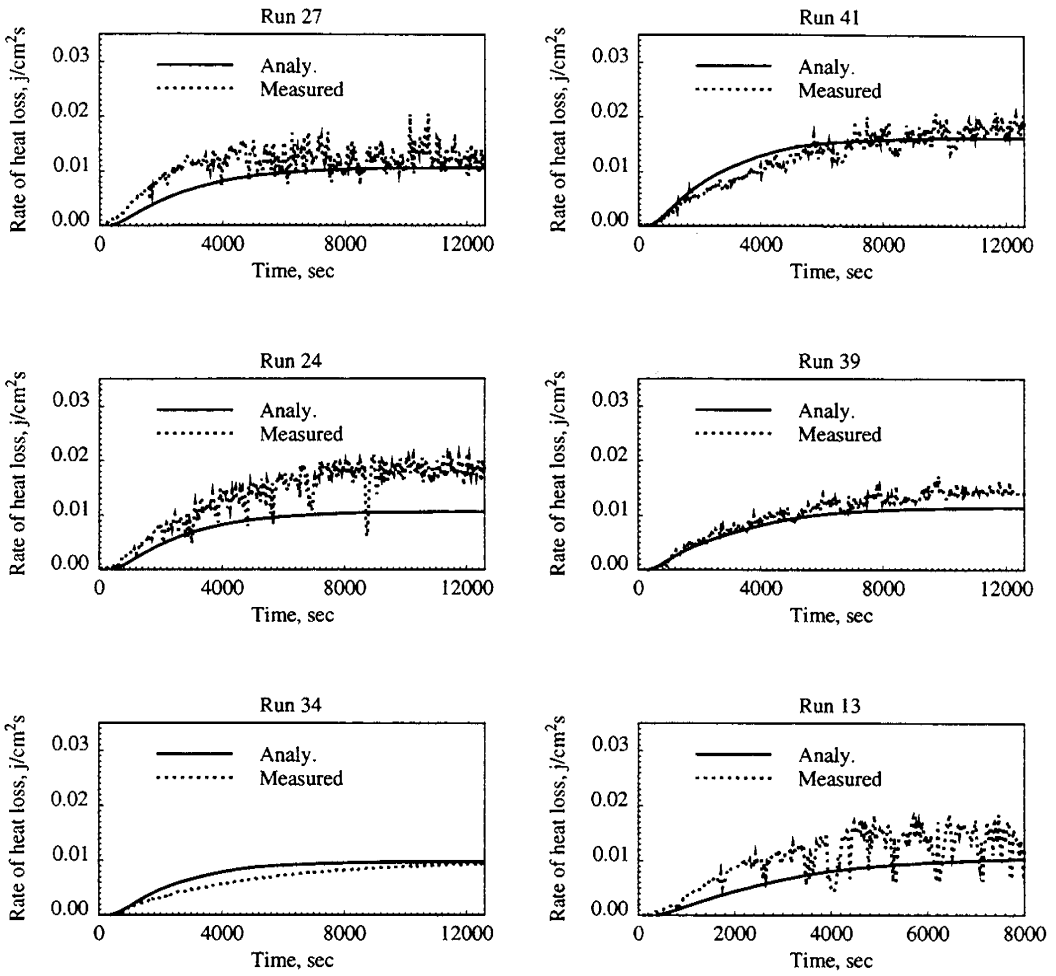

Figure 8.13: Analytical solutions and measured heat losses from the injection side for different runs (Sensor 5).

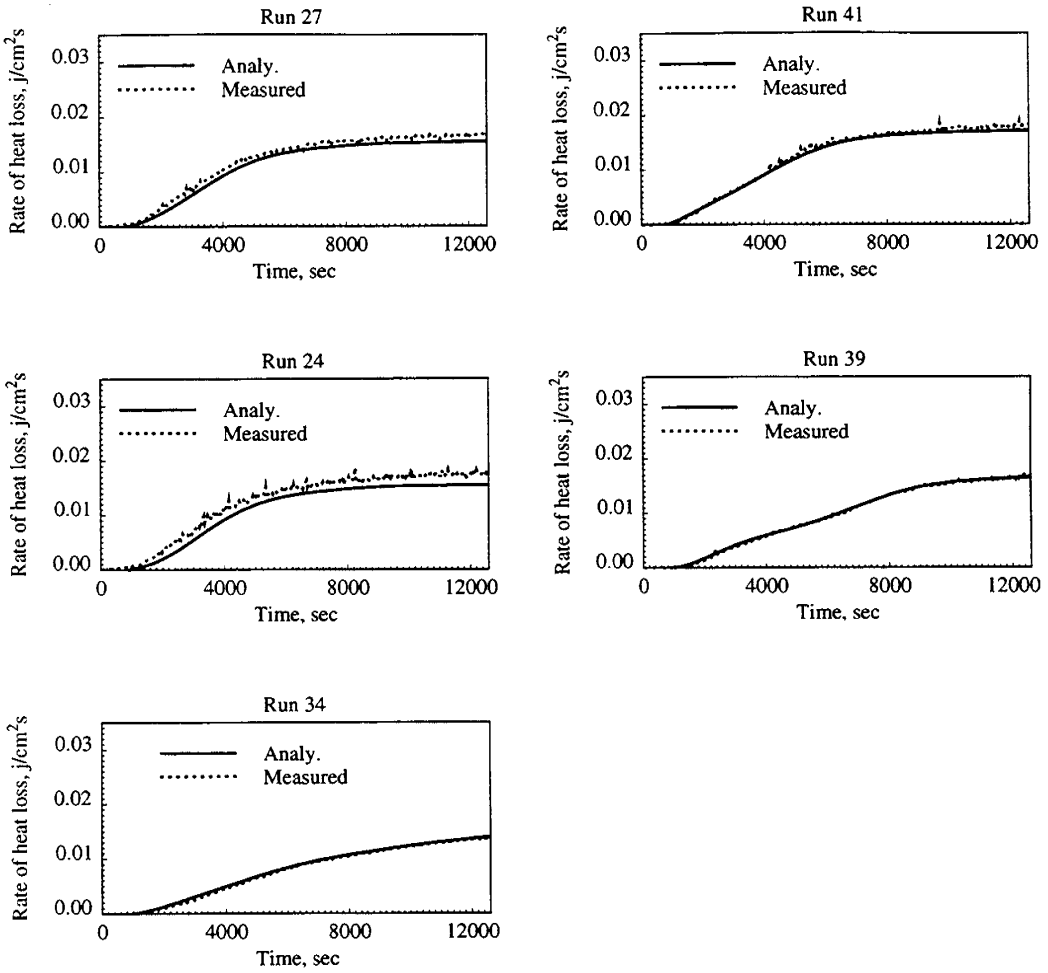

Figure 8.14: Analytical solutions and measured heat losses from the production side for different runs (Sensor 6).

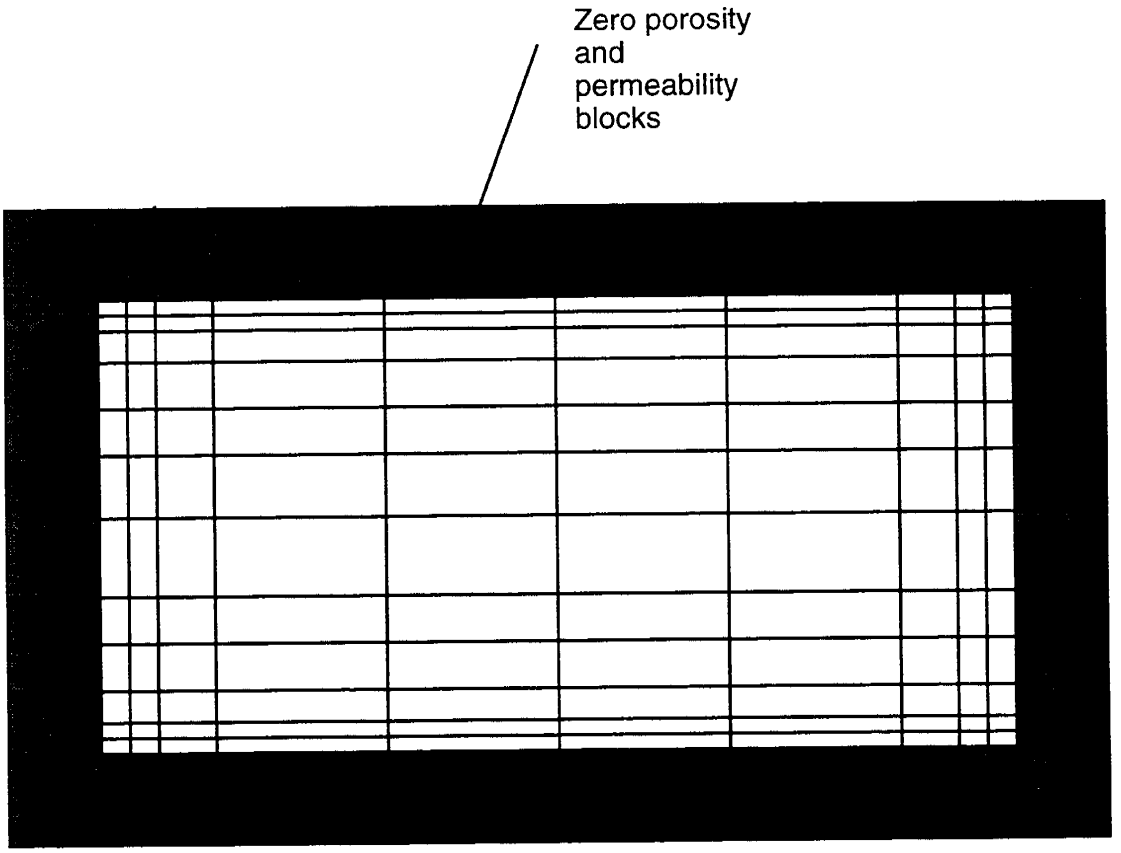

Figure 8.15: Modified grid system for modeling heat loss.

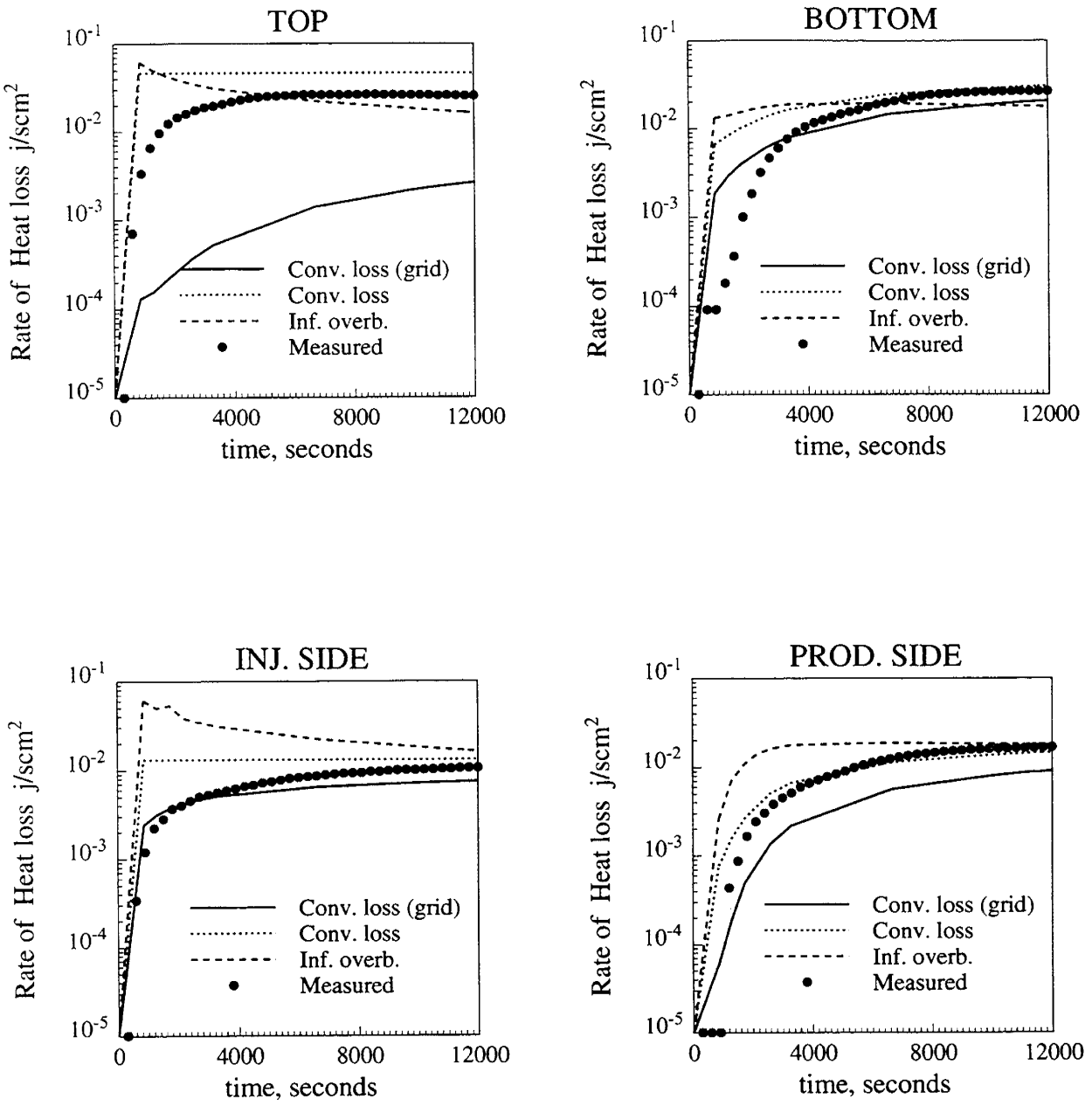

Figure 8.16: Comparison of heat losses calculated with the modified grid, by the conventional models in the simulator to measured values.

heat losses for the injection side agreed well with measurements. The heat losses from the bottom were also in reasonable agreement. The heat losses calculated from simulations were much lower for the top and the production side. However, the predicted shapes of the heat loss curves were much closer to the measured curves than were the other models.

In the simulation described above, only one grid block was used for the insulation. To see the effect of more insulation grid blocks, runs were made with three and six grid blocks, and the results are shown in Fig. 8.17. For the injection, production and bottom sides, increasing the number of grid blocks had little effect on the heat loss calculations. For the top, there was a significant improvement as the number of grid blocks increased from one to three.

Further improvement in the results was observed for the top when the grid block size in the insulation next to the fracture was made finer (Fig. 8.18). The grid block size was decreased from 0.07 cm to 0.035 cm. However, no significant improvement was observed for the bottom, injection and production sides. This simulation run will be called our base case from now on, since none of the physical properties used have been modified. Our best estimates of the properties of the rock and insulation material were used.

Although there are significant improvements in the heat loss calculations with the modified grid system, still the agreement between the simulator and the experiment is not perfect for the base case run. One of the important observations in the experiments was the dominance of conductive heat transfer in heating of the matrix due to flow of steam in the fracture. When the measured temperatures are compared with those calculated in the base case simulations, the measured temperatures were higher at the locations where conduction is dominant, i.e. at the bottom and production sides of the model. Therefore, to attempt to better match temperatures and heat losses, the conductivity of the rock and the steam were increased in the next simulation run. Figures 8.19 and 8.20 compare the temperatures calculated from the base case run, the high conductivity run and the measured temperatures in the matrix and the fractures. In these figures, solid lines show the measured temperatures, the dotted lines show temperatures calculated from the base case simulation and the

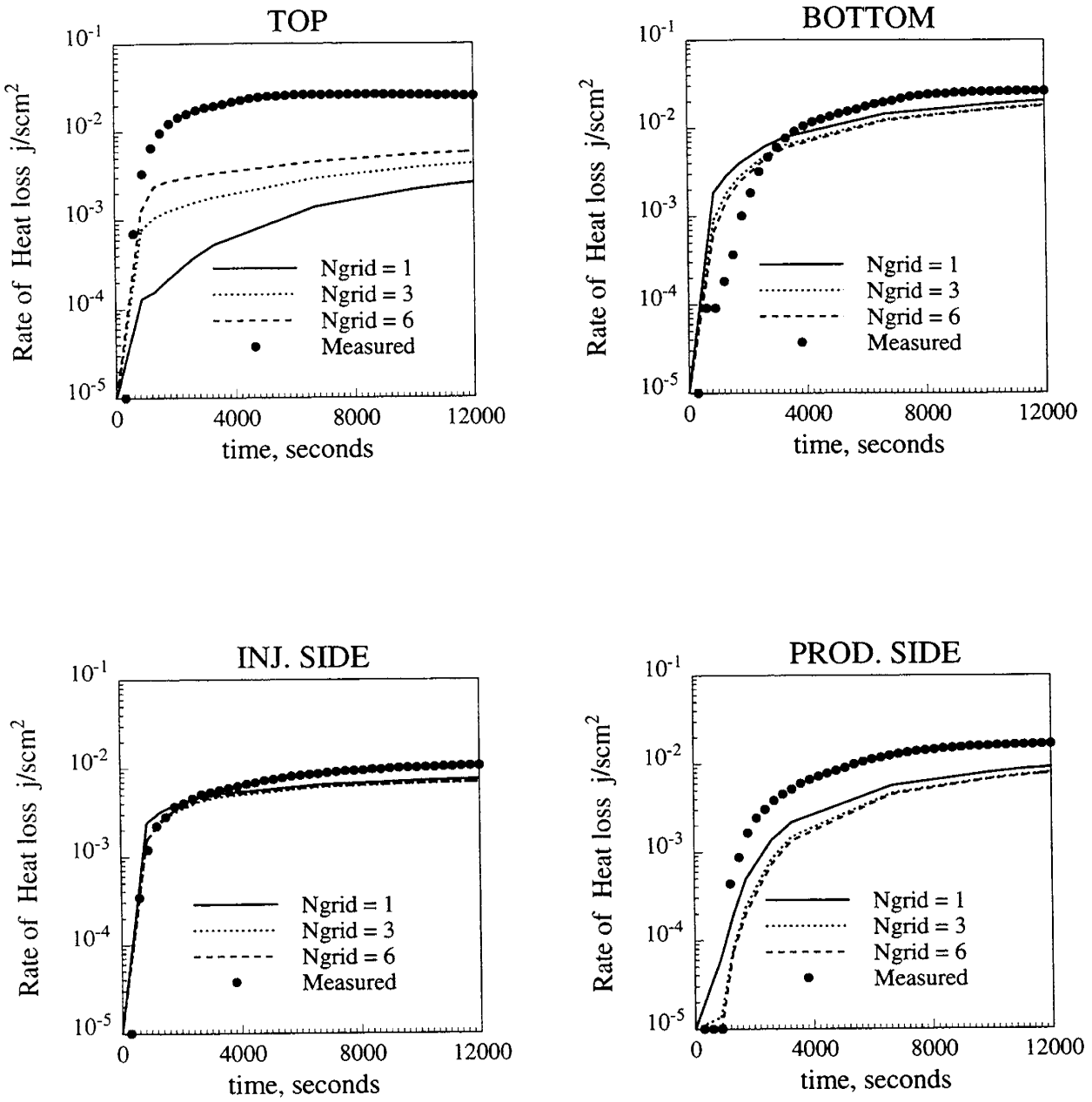

Figure 8.17: Effect of number of insulation grid blocks on heat loss calculations.

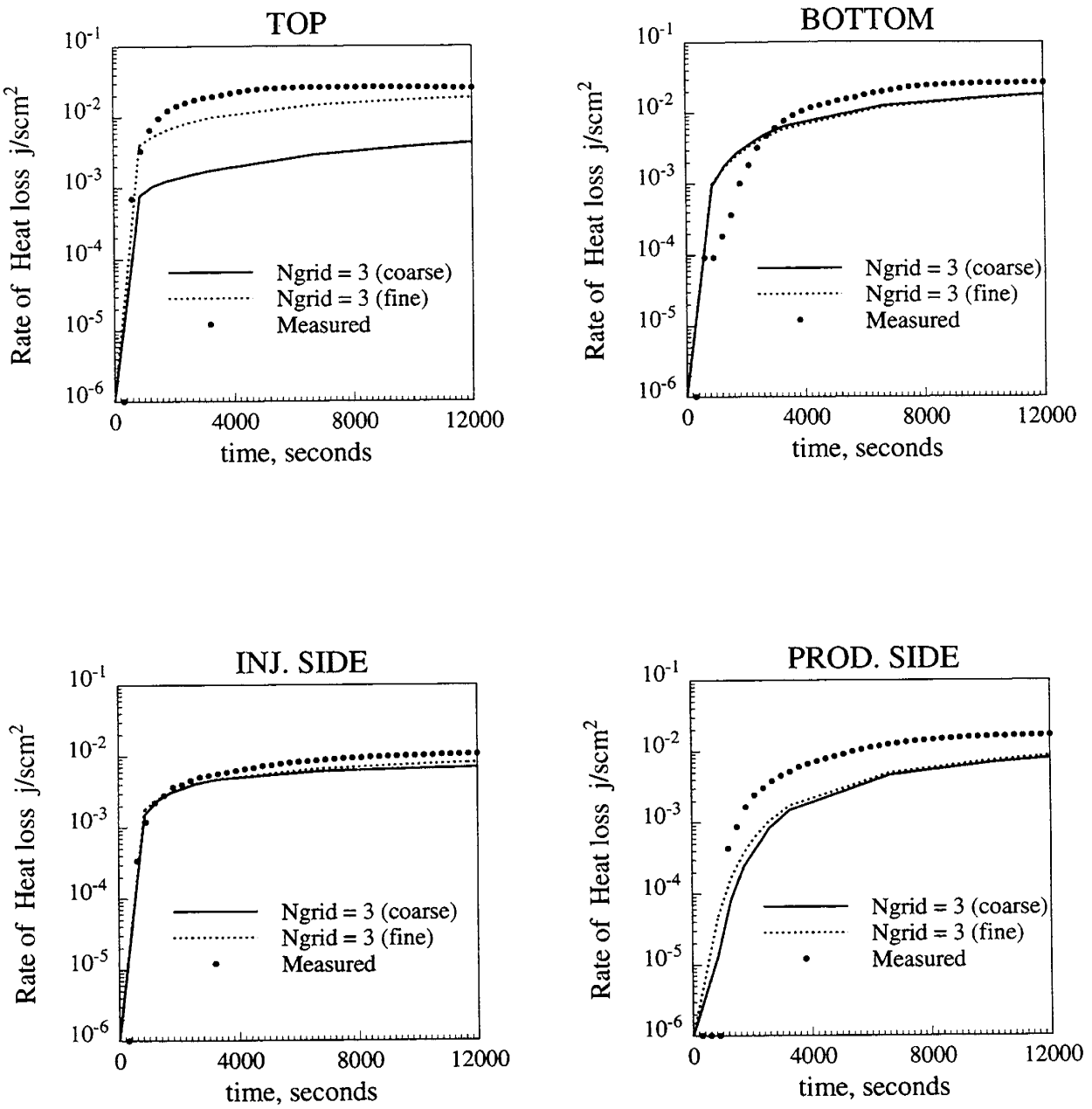

Figure 8.18: Effect of insulation grid block size on calculated heat losses.

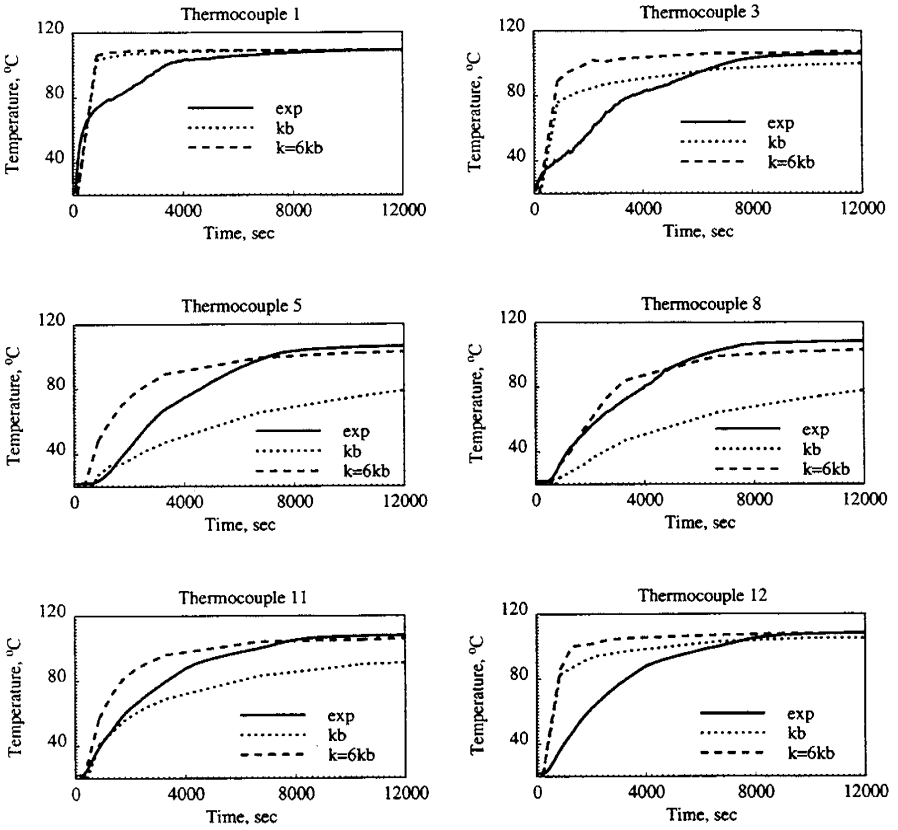

Figure 8.19: Effect of conductivity on calculated temperature histories (Matrix thermocouples).

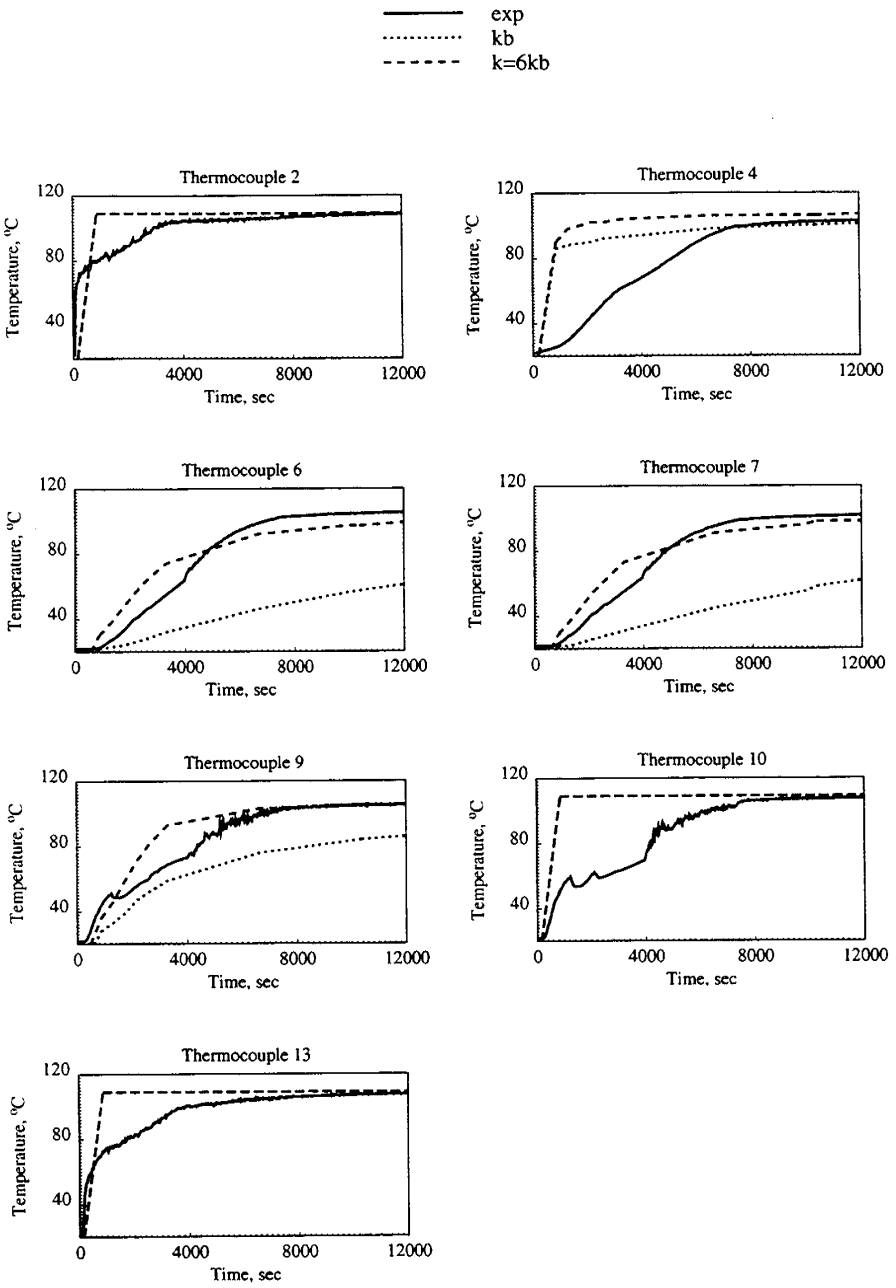

Figure 8.20: Effect of conductivity on calculated temperature histories (Fracture thermocouples).

dashed lines show temperatures calculated with increased thermal conductivities of the rock and the steam. The conductivity of the rock was increased by a factor of six, and the conductivity of steam was ten times higher. The physical locations of these thermocouples were shown in Chapter 5. The figure is repeated here for clarity (Fig. 8.21).

For the matrix (Fig. 8.19), at locations where conduction is dominant, like Thermocouples 5, 8 and 11, there is good agreement between the measured and calculated temperatures from the simulation run with high conductivity. At the locations close to the fractures, Thermocouples 1, 3 and 12, the effect of the rock conductivity is not as significant, since the heat transfer is mainly from steam flowing at these locations.

Similar behavior is observed for the fracture thermocouples. At the bottom and production sides, Thermocouples 6, 7 and 9, the effect of conductivity is significant. The agreement between the experimental and measured temperatures is quite good. At locations where convective heat transfer is dominant, where steam flows, increasing conductivity had little effect (2,4,10,13).

When the heat losses calculated from the high conductivity run are compared with the measured heat losses, the agreement is almost perfect for the top, injection and production sides (Fig. 8.22). The transient portion of the bottom heat loss curve is shorter than measured, this is because calculated temperatures increase faster than measured temperatures at the bottom, especially for Thermocouple # 4 (Fig. 8.20).

All the simulation runs described so far were for a two-dimensional cross-section since the aim was to calibrate the heat loss models in the simulator with the experiments. The heat losses were modeled by increasing simulated conductivities for the rock and the steam. In reality, the physical system is three-dimensional. Therefore, simulation runs were repeated with a three-dimensional grid. Block sizes used in the three-dimensional simulations had to be modified. The matrix grid blocks were not fine near the fracture, as they had been in the two-dimensional cross-section. Instead, uniform gridding was used. The details of the gridding in the three-dimensional system will be described in the next section. The run times were much longer for the three-dimensional simulations due to the increased number of blocks and also due to the numerical difficulties in handling the third dimension. The simulations

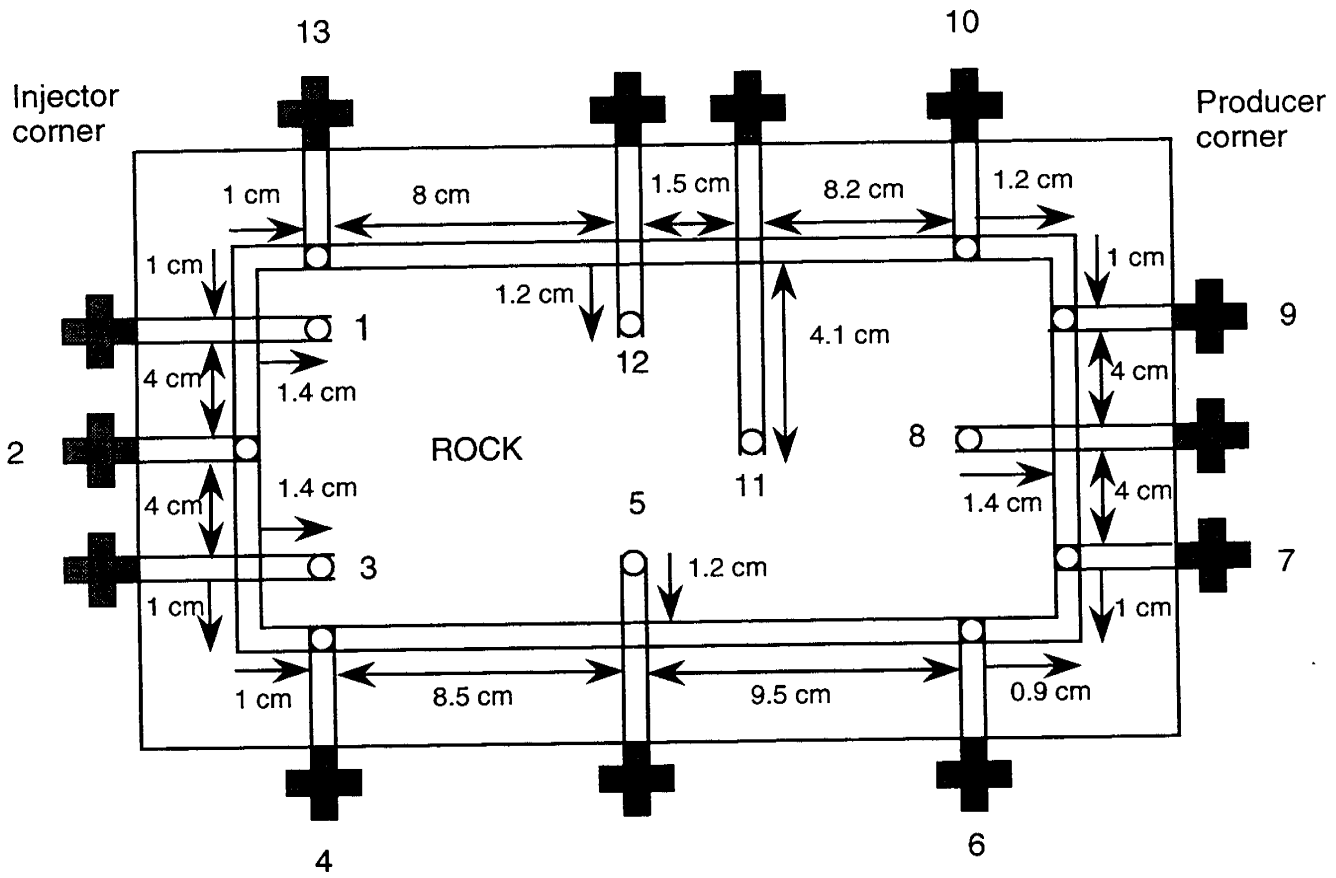

Figure 8.21: Thermocouple locations.

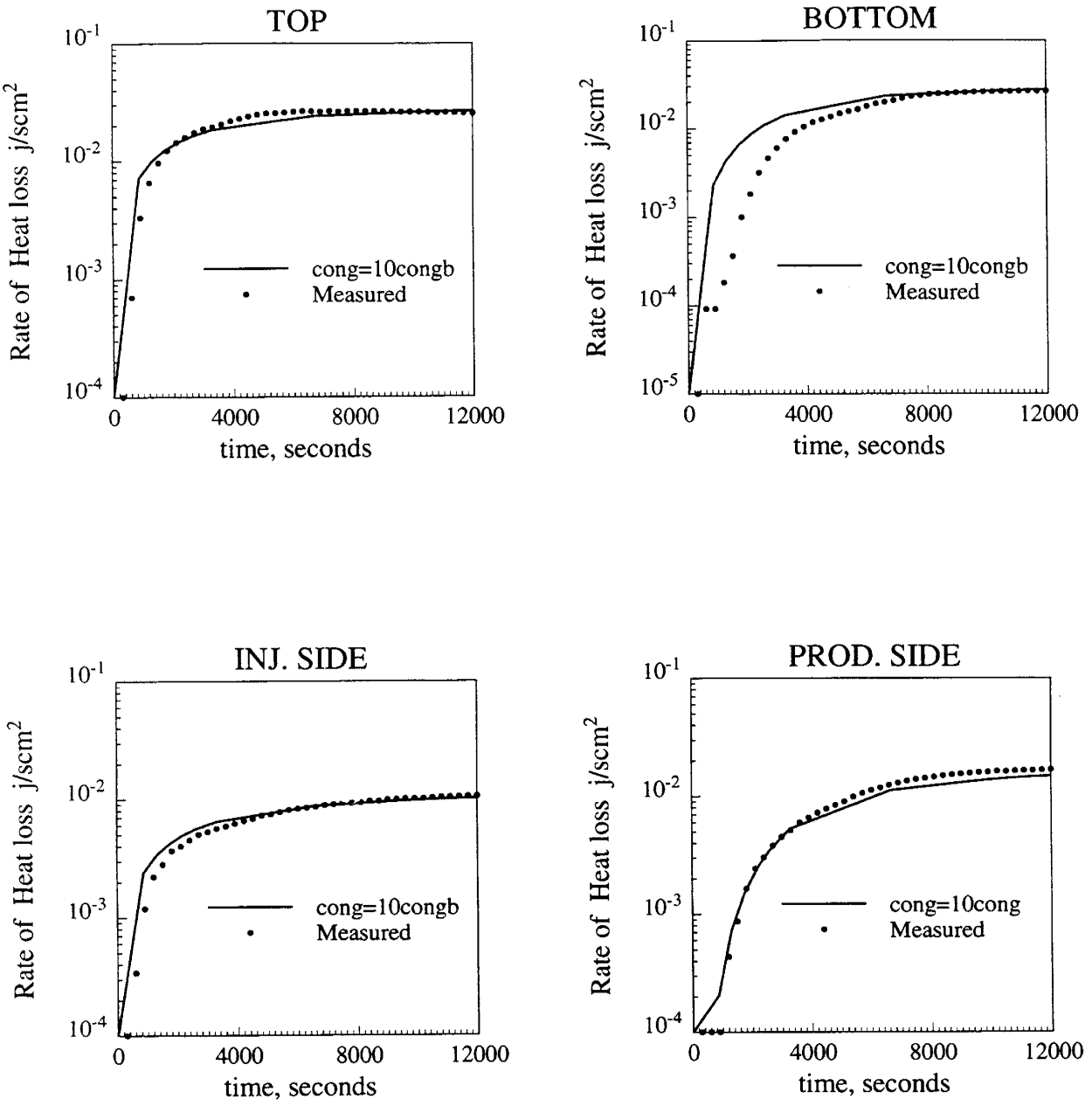

Figure 8.22: Effect of changed conductivity on calculated heat losses.

took almost two days on a DEC Alpha work station compared to 40 minutes for the cross-sectional simulations.

Figure 8.23 shows the heat losses calculated from the simulator with a three-dimensional grid system. The simulator models the heat losses quite well for the bottom, injection and production sides considering the complexity of the core holder geometry. The differences in the heat losses for the transient portion of the bottom heat loss curve are due to calculated temperature faster increases at the bottom. The heat losses from the experiment are slightly higher at the top due to the slight differences in the measured and calculated steam saturations. Calculated steam saturations are 100% at the top fracture. However, in the experiments, there is always some water saturation present. Since the conductivity of water is much higher than steam, measured heat losses are also higher. In fact when the conductivity of steam is slightly increased in the three-dimensional simulations, the heat losses from the top show a better agreement. Since none of the rock and fluid properties has been modified in the three-dimensional simulations, it is obvious that the three dimensional grid system does a better job in modeling the physical system. From now on, three dimensional simulations will be shown to history match the experimental results.

8.2 History Matching

After adjusting and calibrating the simulator for heat losses, simulations were done to match the experiments, using a three-dimensional grid system. Sixteen grid blocks were used in the x-direction, 11 in the y direction and 18 in the z direction. Schematics of front and top views of the grid system are shown in Fig. 8.24. In the grid system, the first three blocks in each direction modeled the insulation, then one grid block was used for the fracture, followed by the grid blocks for the core, and then fracture and the insulation blocks again. Due to the complexity of the grid system, some numerical problems were encountered in the simulator; therefore the core was gridded uniformly. This gridding system was accurate enough, as will be shown by the comparison between the measured and calculated results.

Heat properties of the core holder were assigned to the insulating blocks. Heat

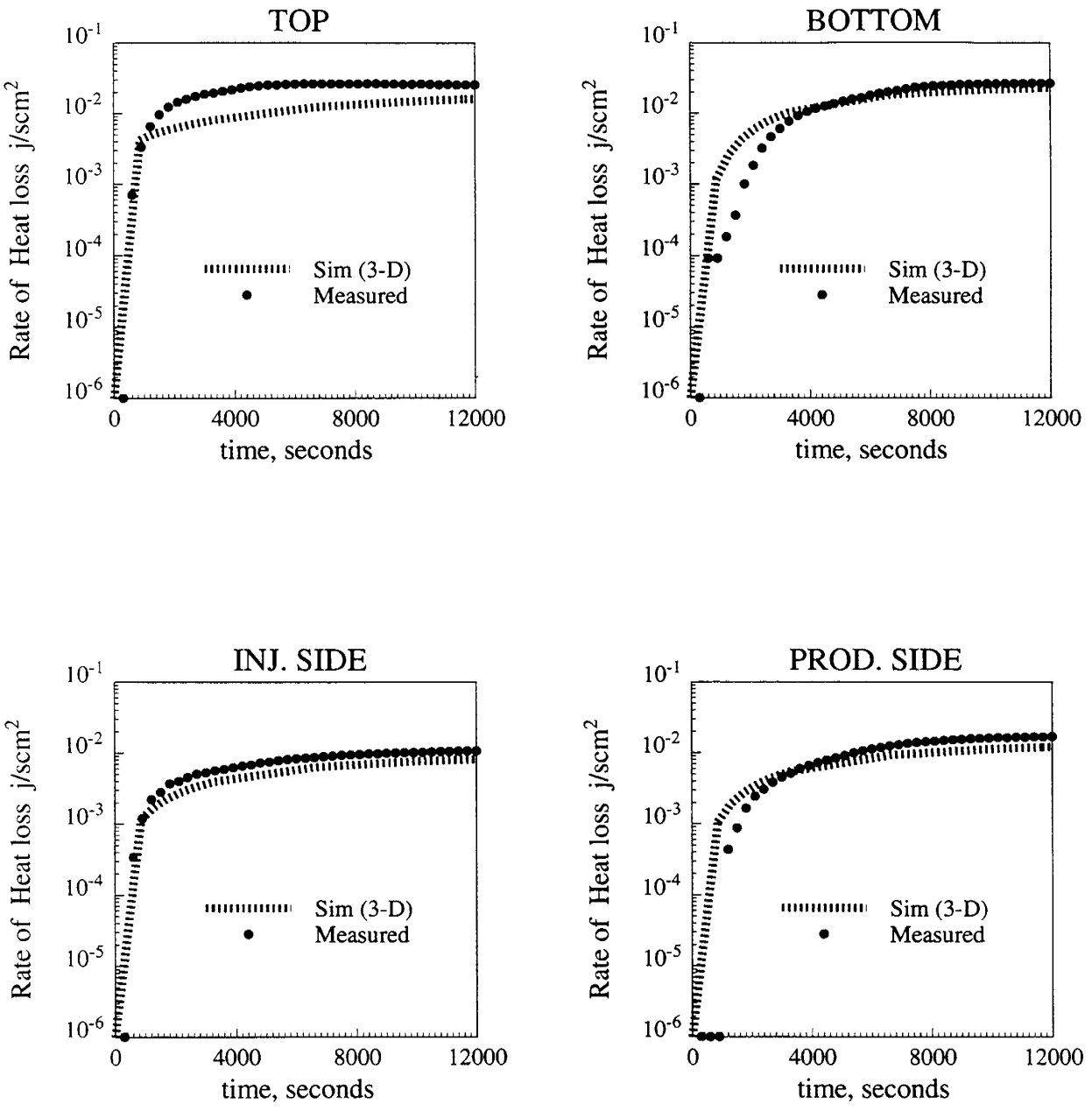

Figure 8.23: Heat losses measured and calculated by 3-Dimensional simulations.

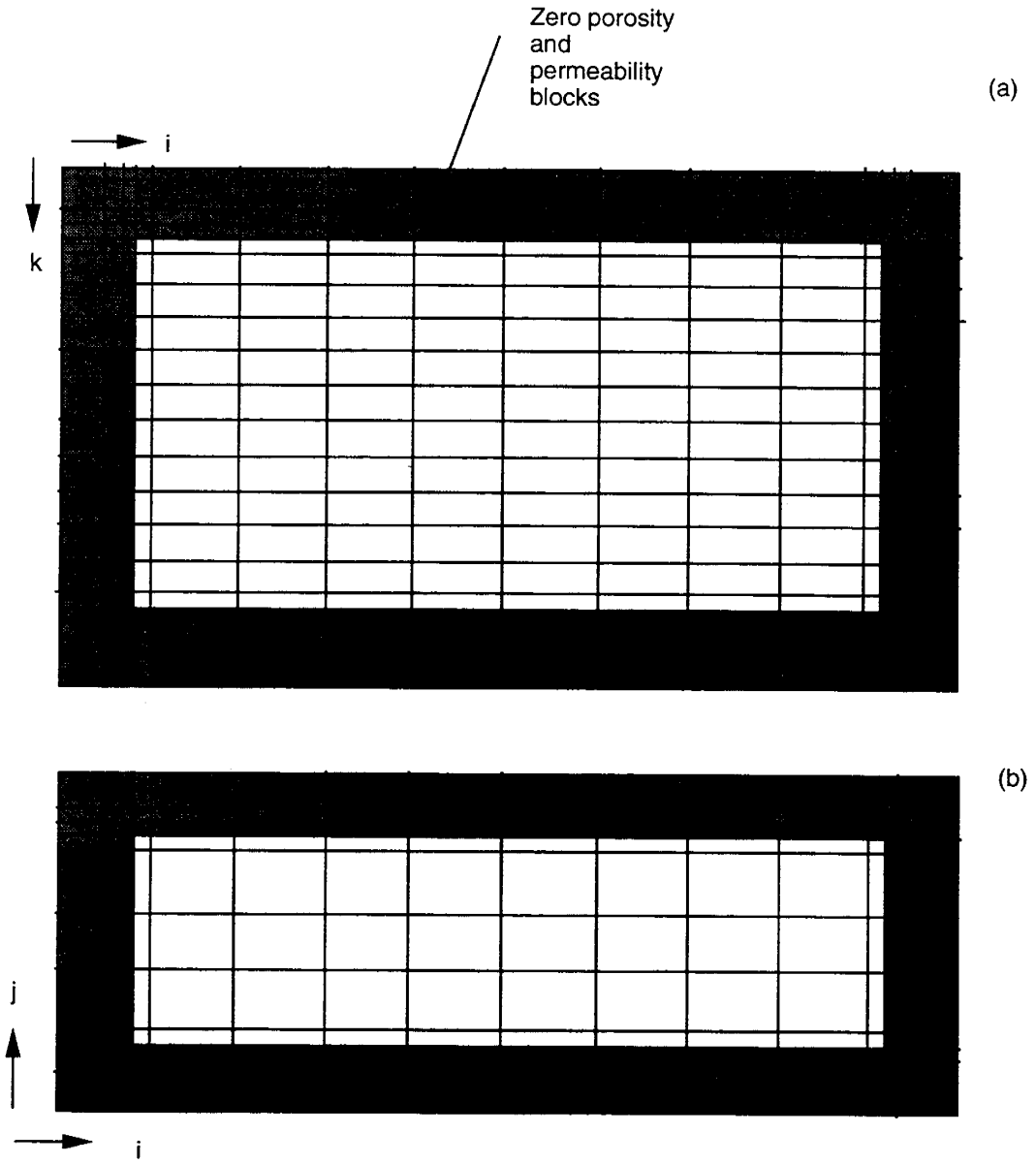

Figure 8.24: Schematics of the three-dimensional grid system, (a) Front view, (b) Top view.

capacity and conductivity of Boise sandstone were taken from the literature [79, 4], while porosity and absolute permeability were measured for the core used in the experiments. The matrix capillary pressure curve was taken from Handy [37]. Capillary pressures were set to zero for the fractures, and straight line relative permeabilities were used there.

Steam-water relative permeabilities are always a controversial issue. There are many differing and contradicting relative permeability curves in the literature. Two differing matrix relative permeability curves from the literature are used in the simulations. They are found to be quite important in this study, as they determine how much steam can flow in the matrix.

The first set of relative permeabilities were from Horne and Ramey [42] (Fig. 8.25). These curves were developed using field test data. Simulations using these curves developed some steam saturations in the matrix, contrary to the experimental observations. The second set of relative permeabilities were from Sanchez and Schechter [72] (Fig. 8.26). The calculations using these curves were similar to the experiments, in that no steam saturation was observed in the matrix. Therefore, these curves were chosen as appropriate for our system.

Simulation results for the run with 7.0 psig back pressure and 6 cc/min injection rate (Run 29) will be presented first. Analytical heat transfer calculations were done first to determine the necessary convective heat transfer coefficients to use in the simulator. Figure 8.27 shows the calculated and measured heat loss curves for this run. The locations of these sensors on the core holder are shown in Fig. 8.28. The noise and the fluctuation in Sensor 5 are due to the movement of the Fiberfrax insulation, as discussed earlier in Chapter 7. Apart from that, the agreement between the measured and calculated heat losses is quite good. These convective heat transfer coefficients were input to the simulator.

The temperatures measured by the fracture thermocouples and the temperatures calculated by the simulator are compared in Fig. 8.29. One common feature of these curves is that the transient portions differ for the simulations and the experiment. There is a rapid increase in temperature for all the calculated fracture thermocouples contrary to the smooth increases measured. The same behavior is also observed in

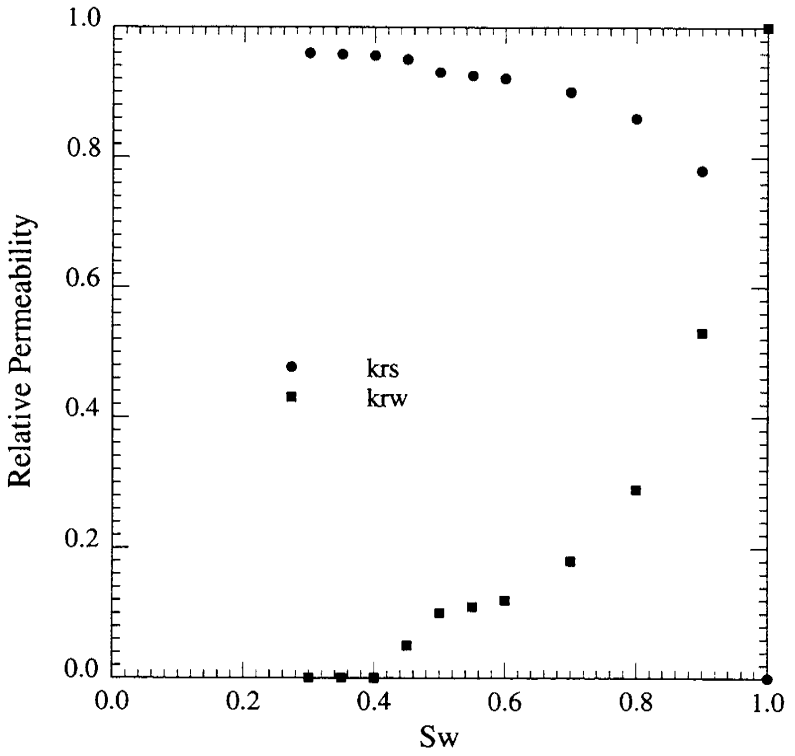

Figure 8.25: Steam/water relative permeability curves (Horne and Ramey, 1978).

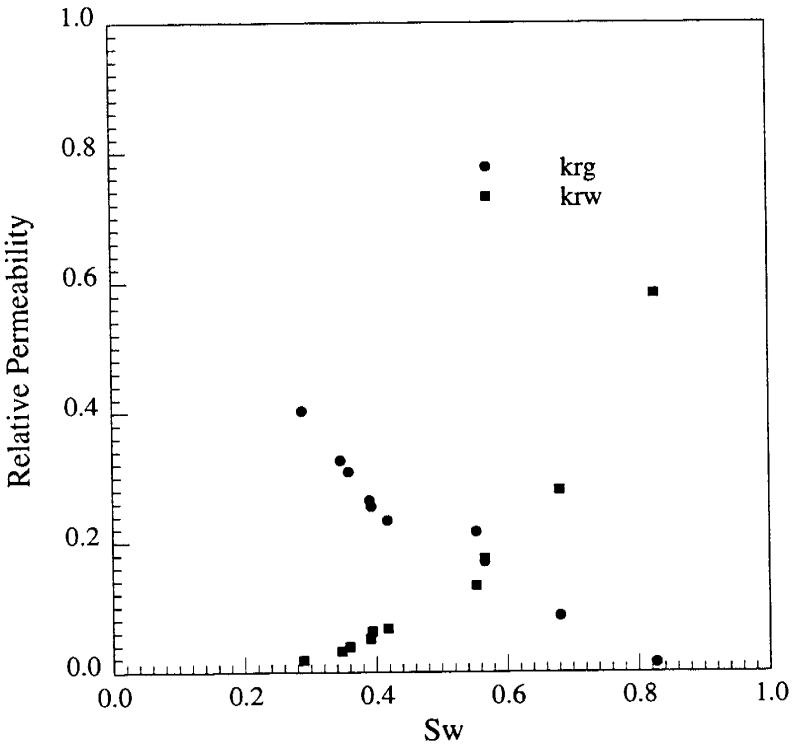

Figure 8.26: Steam/water relative permeability curves (Sanchez and Schechter, 1987).

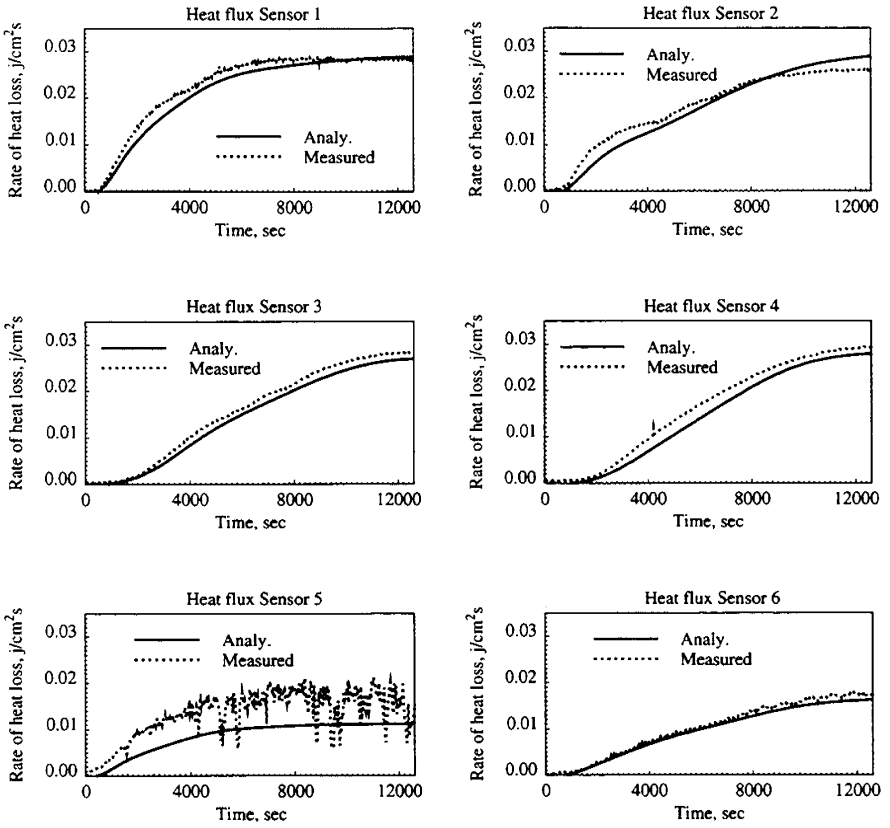

Figure 8.27: Comparison of heat losses from the experiment with analytical calculations.

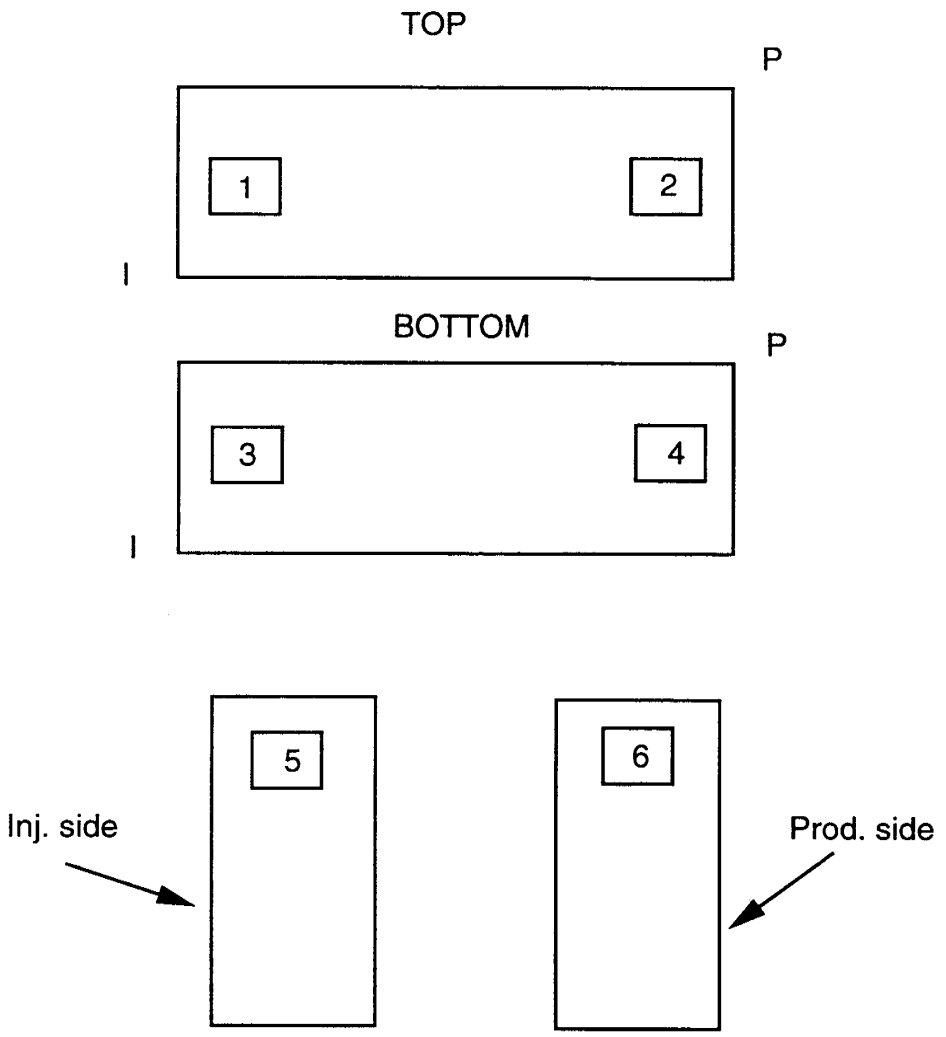

Figure 8.28: Locations of the heat flux sensors on the core holder.

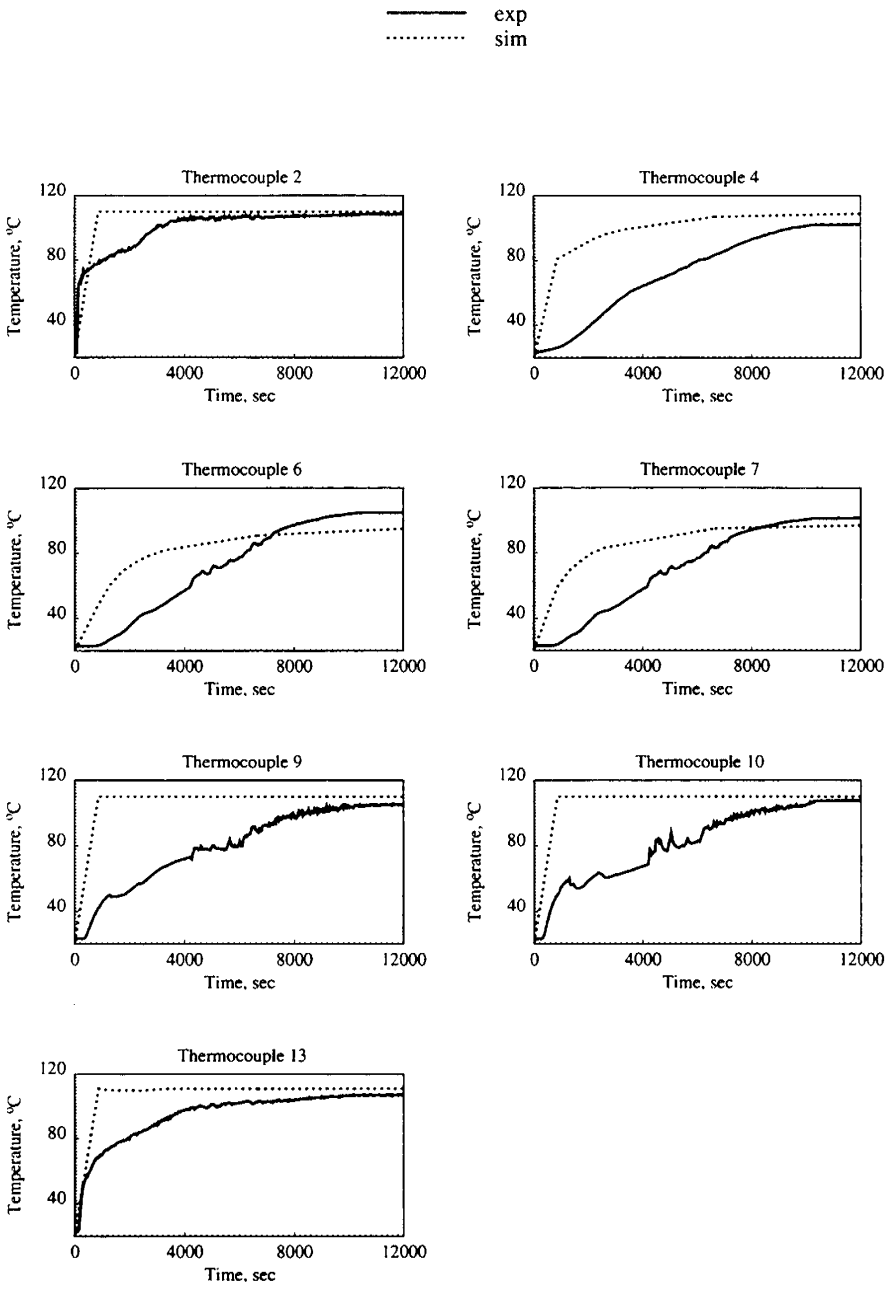

Figure 8.29: Temperatures measured and calculated in the fracture at various locations (Run 29).

the transient regions of the matrix temperature curves (Fig. 8.30). Eventually, when steady state is reached, the calculated and measured curves become similar except for the thermocouple at the bottom (6) and the thermocouple at the bottom production side (7) (Fig. 8.29). The measured temperatures are slightly higher at those locations. The final steam saturation distributions calculated from the simulations are similar to the experiment. Steam is only found in the fracture; it does not enter the matrix.

The discrepancies between the measured and the calculated temperatures at the beginning may have been due to the heat losses between the point where steam leaves the steam generator and the point at which it enters the core holder. Even though the lines are insulated, heat losses occur and the lines take some time to heat up. Because of the physical constraints, caused by the core holder being on the scanner table, steam cannot be circulated throughout the injection line before it is injected into the system. Also heat losses are present at the injection well, and have not been considered in the simulations.

One possible solution to this problem is to set the temperature of the steam generator at a higher value so that steam at a higher temperature can be injected to overcome some of the heat losses. This procedure was tested by conducting a steam injection experiment with the same operating conditions as the previous run (Run 29), but the temperature of the controller for the generator was set to 500° F (Run 41) instead of 390° F. Figures 8.31 and 8.32 show the temperature measurements from the run at higher inlet temperature and the calculated temperatures from simulation. The matches improved considerably compared to the previous run. However, still there is a difference in the transient regions of the curves especially for Thermocouples 3, 4, 9, 10 and 13. These locations are mostly in the fracture at the locations where steam flows.

When we look at the steam saturation maps for the simulation run, it is apparent that 100% quality steam is injected into the fracture. That is why the fracture is calculated to immediately be at the saturated steam temperature (Thermocouples 2, 9, 10 and 13). Thermocouples 10 and 13 are at the top fracture, and 2 and 9 are at the injection and production sides. The calculated immediate heating of the fracture by steam also causes the matrix to heat faster. However, in reality

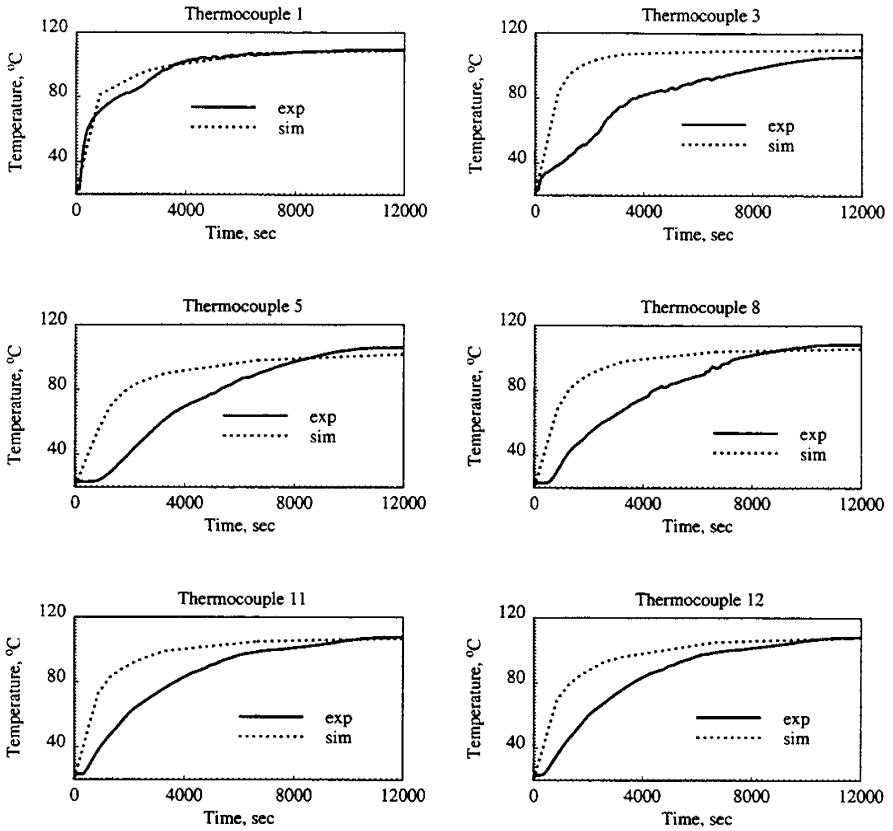

Figure 8.30: Temperatures measured and calculated in the matrix at various locations (Run 29).

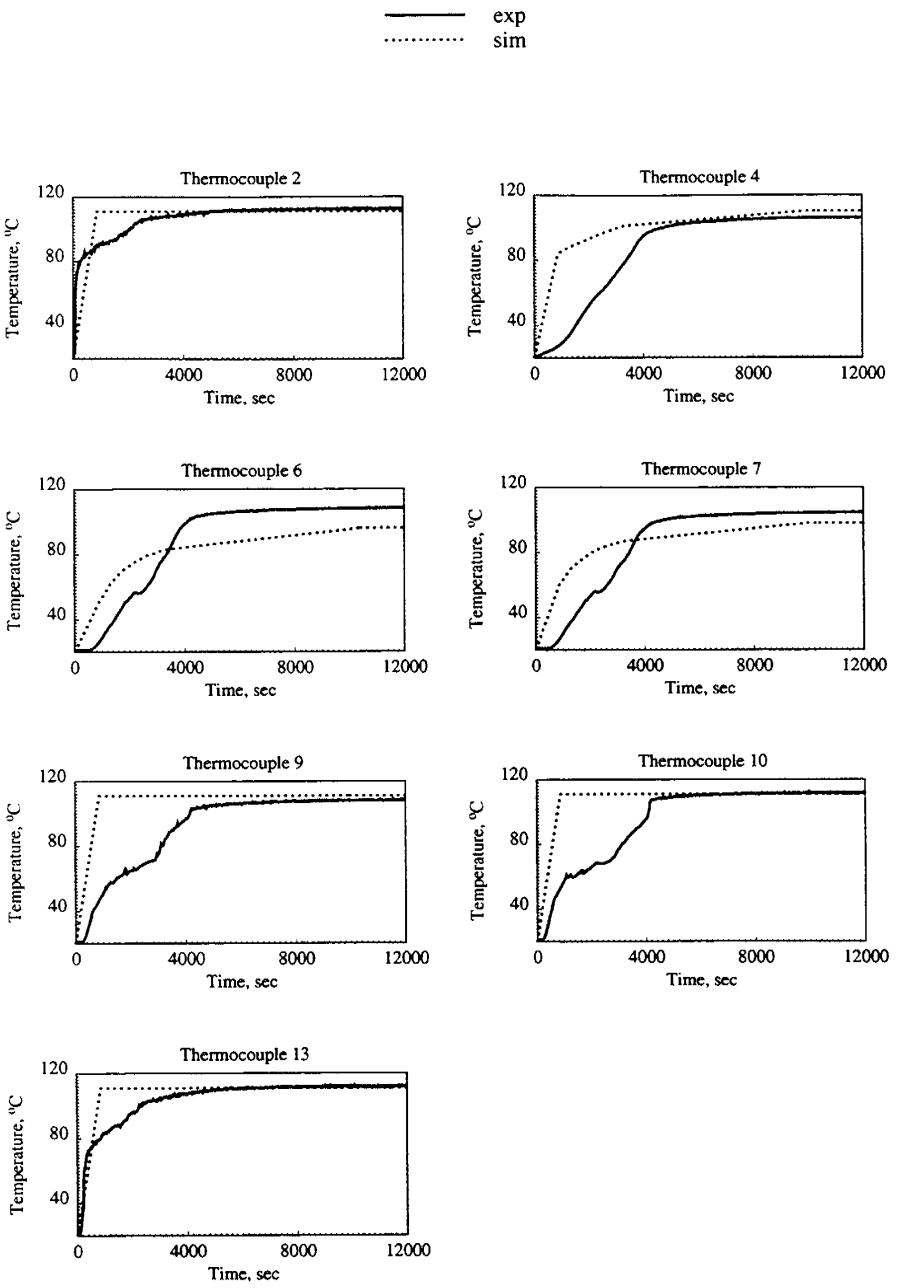

Figure 8.31: Temperatures measured and calculated in the fracture at various locations (Run 41).

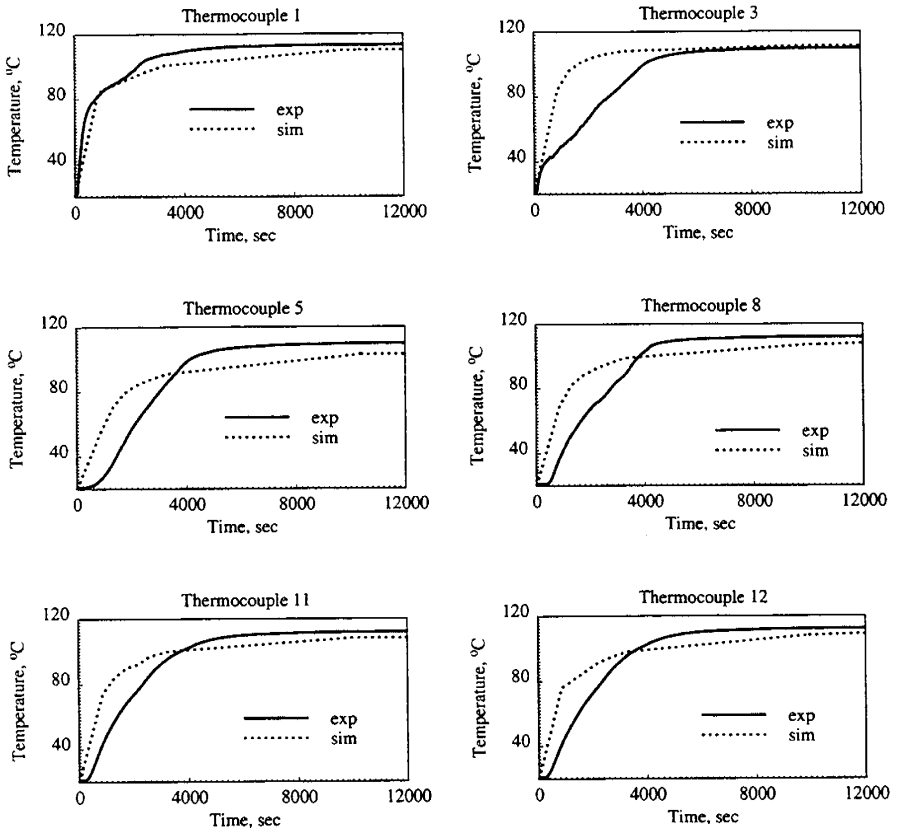

Figure 8.32: Temperatures measured and calculated in the matrix at various locations (Run 41).

although slightly superheated steam is generated, steam condenses due to heat losses, and enters the core holder as hot water. This behavior is confirmed from the CT scanner measurements. For up to about 70 minutes of injection, no steam saturations developed in the system (Fig. 8.33). Thus, to match the initial part of the data, the simulation run was repeated with lower steam quality injected initially.

Different steam quality histories were used in the simulations. The best match was obtained by injecting steam of 25% quality for 72 minutes, and then switching to 100% quality. Figure 8.34 shows the calculated and the measured temperatures for the matrix thermocouples. The agreement between the measured and the calculated temperatures is good for all matrix thermocouples except Thermocouple 5 which is at the bottom.

When we look at the fracture thermocouples, the agreement is good for all except 4, 6 and 7 (Fig. 8.35). Thermocouple 4 is at the bottom close to the injection corner. In the simulations, the injection well location is at the bottom-most corner of the model. In the physical model, the location is slightly above the corner, further from the bottom. The sudden increase in temperature observed in the simulation may have been due to this difference.

For Thermocouples 6 and 7 (at the bottom and the bottom production side), the differences between measured and calculated temperatures may have been due to the nonuniformities in the fracture aperture in the physical model, causing permeability differences in the fractures surrounding the matrix. These nonuniformities may be due to the imperfections in machining and variations in the spacer thicknesses.

Thus, for the next simulation run, the permeability of the fracture at the bottom was increased to see its effect. The match improved for the bottom fracture Thermocouples 6 and 7 and matrix Thermocouple 5, confirming the nonuniformity of the fractures around the matrix (Figs. 8.36 and 8.37). Heat losses and steam saturation maps also agreed with the simulations for this run (Figs. 8.38 and 8.39).

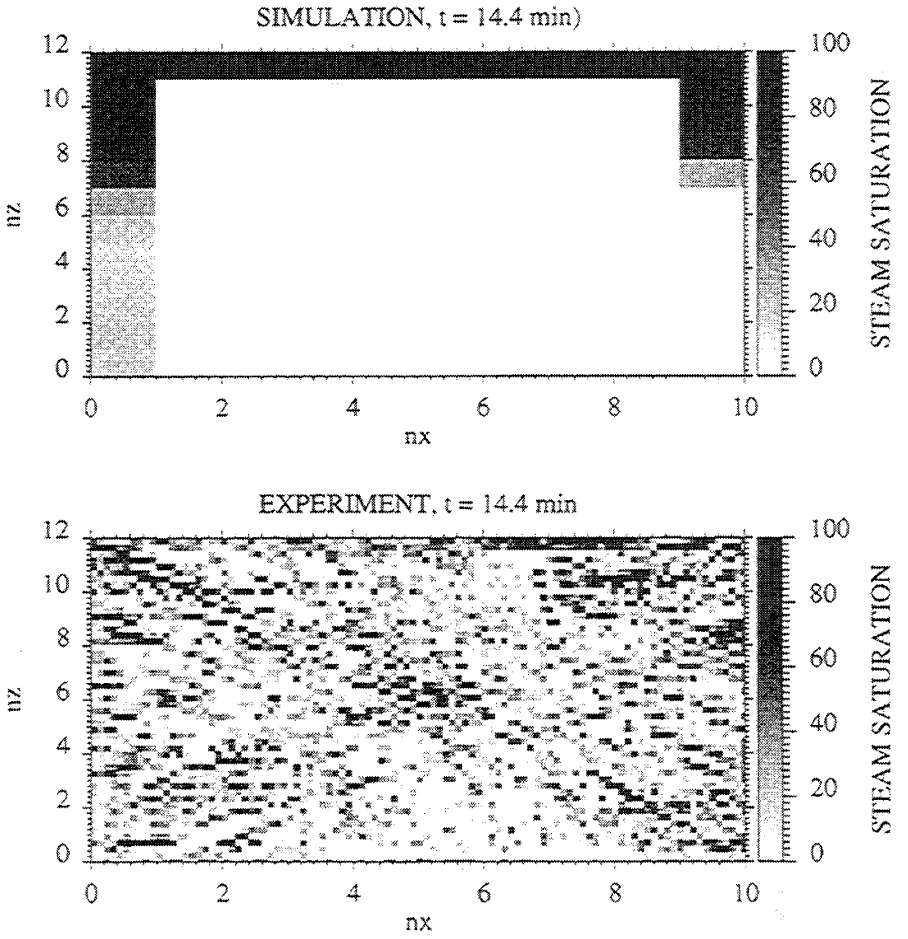

Figure 8.33: Comparison of simulated and measured steam saturations at t = 14.4 min.

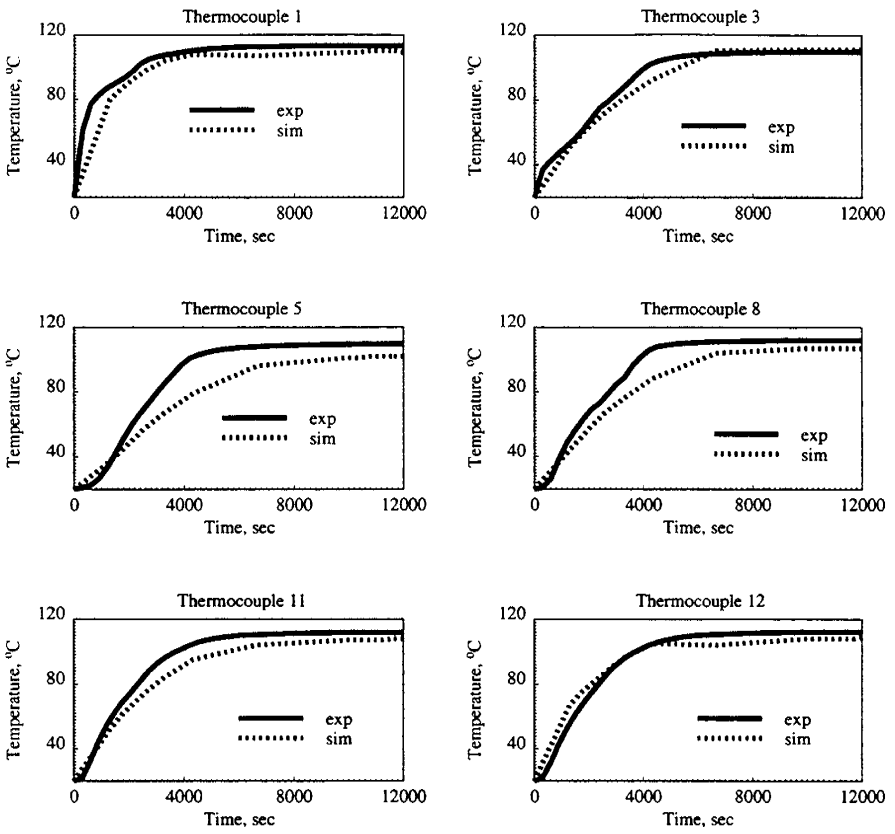

Figure 8.34: Temperatures measured and calculated in the matrix at different locations (Run 41). Variable injected steam quality in the simulation run.

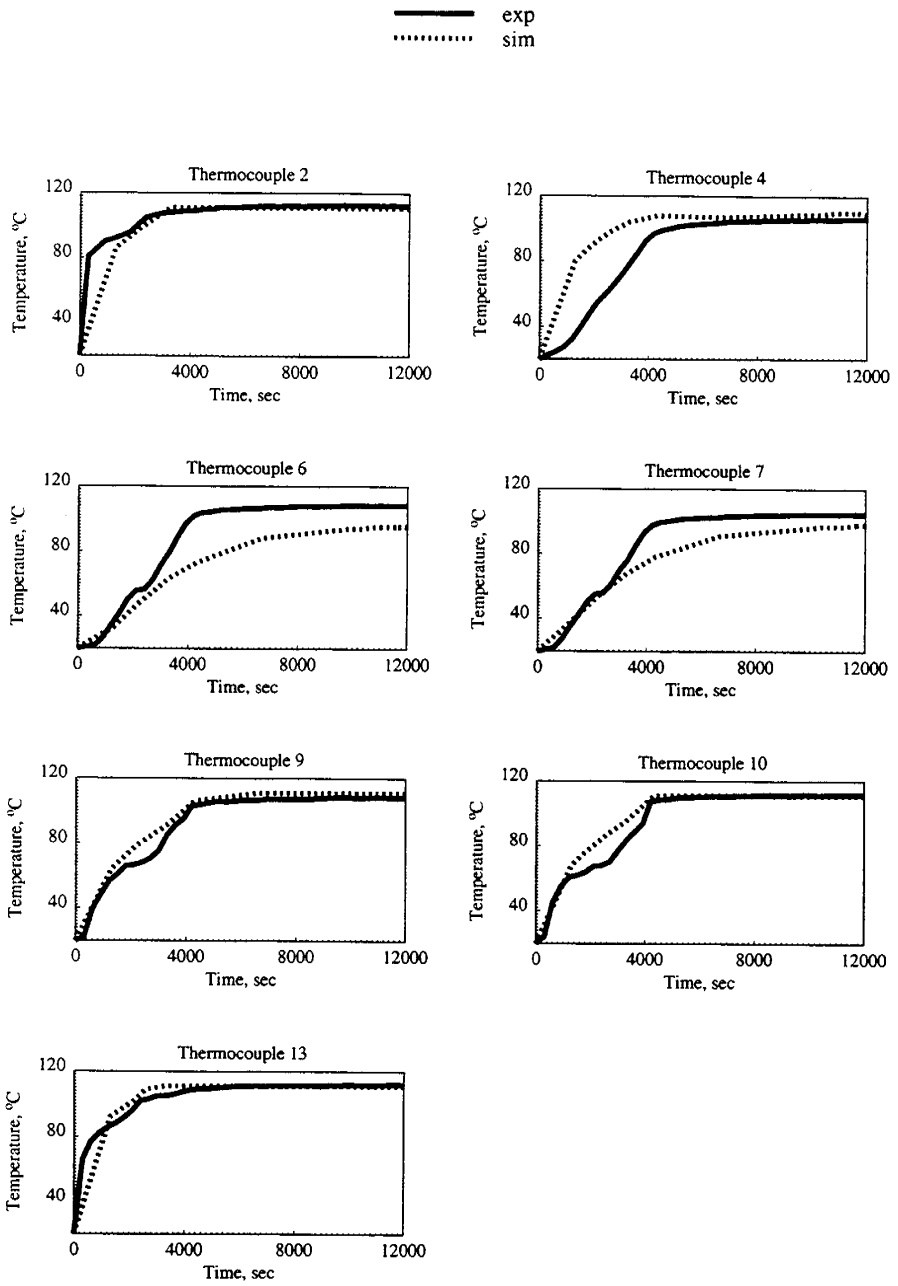

Figure 8.35: Temperatures measured and calculated in the fracture at different locations (Run 41). Variable injected steam quality in the simulation run.

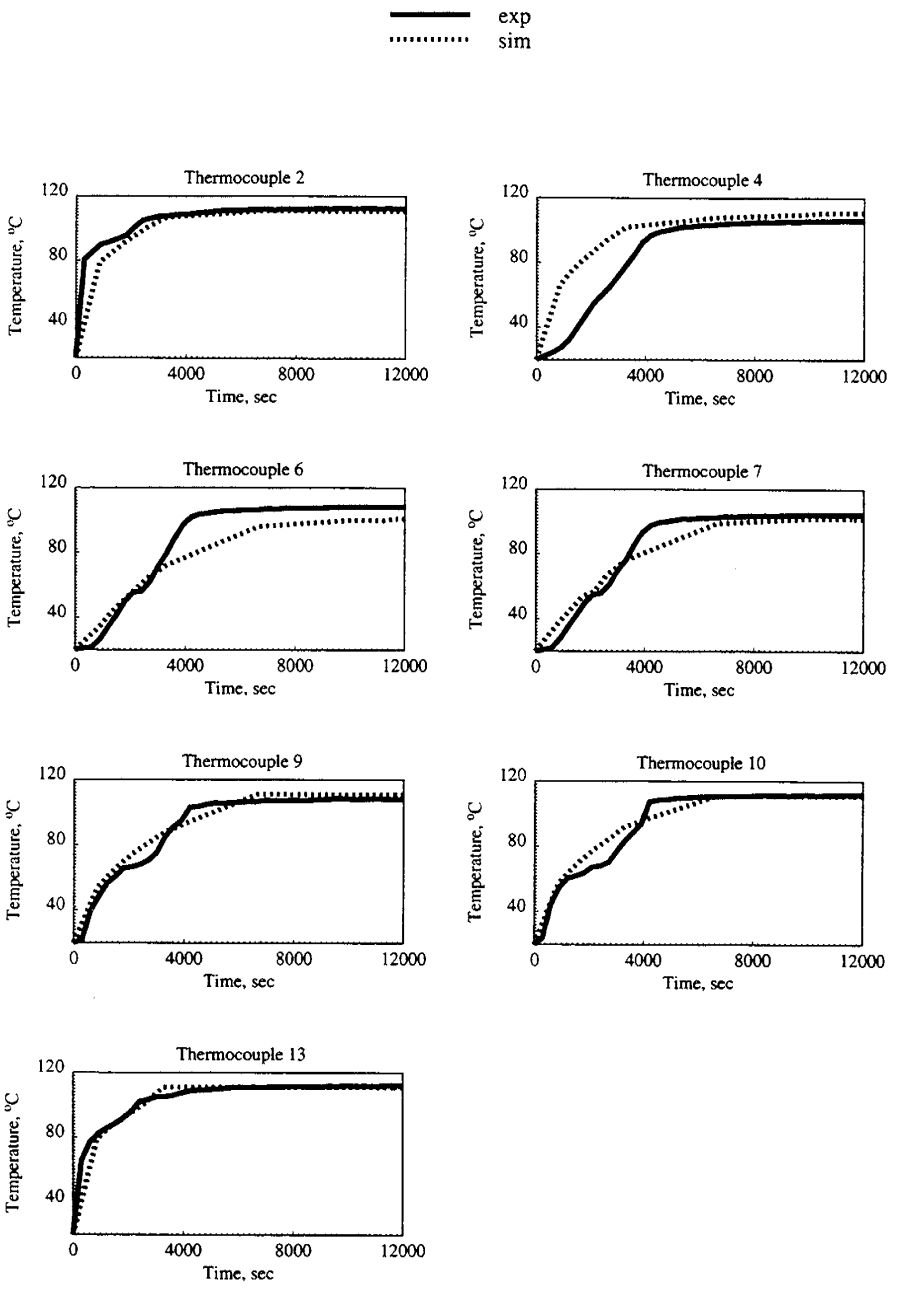

Figure 8.36: Temperatures measured and calculated in the fracture at different locations (Run 41), increased bottom fracture permeability in the simulation run.

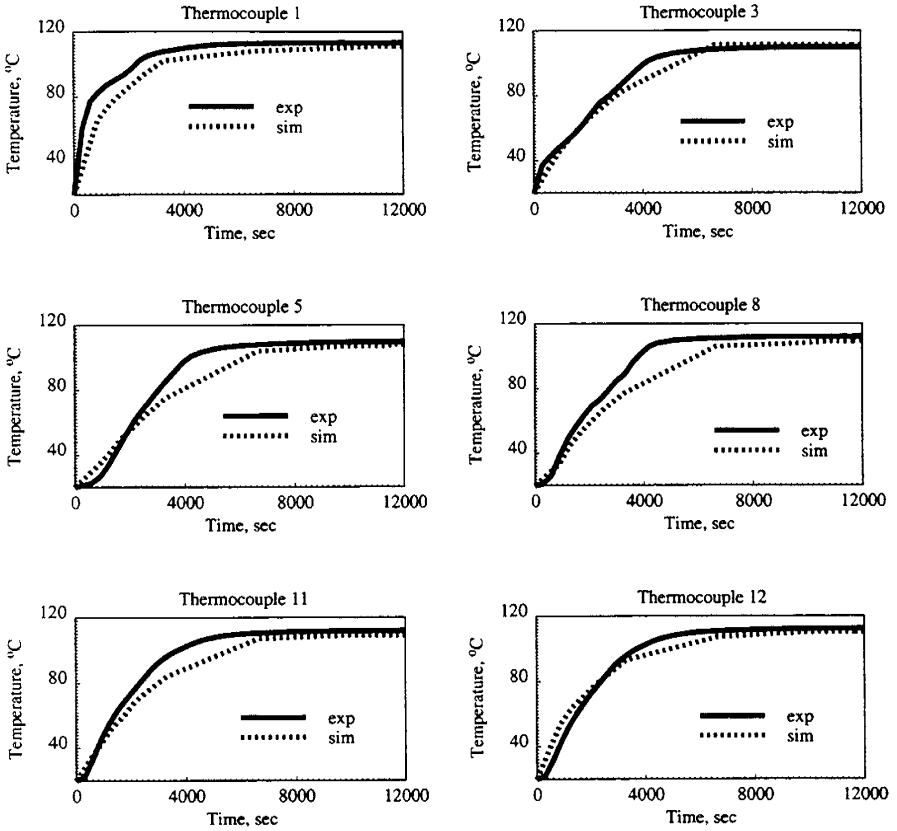

Figure 8.37: Temperatures measured and calculated in the matrix at different locations (Run 41), increased bottom fracture permeability in the simulation run.

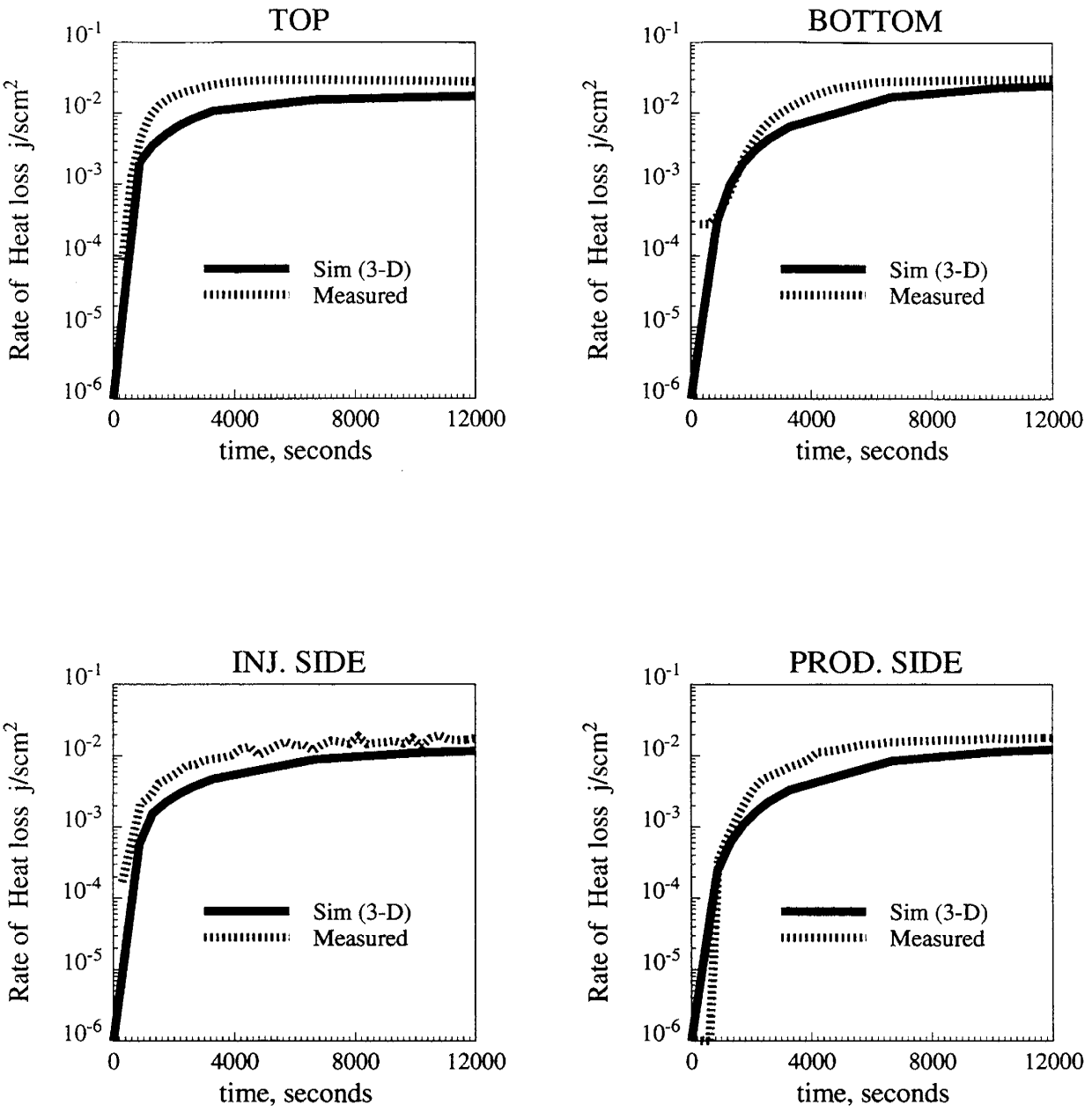

Figure 8.38: Heat losses measured and calculated at different locations (Run 41), increased bottom fracture permeability in the simulation run.

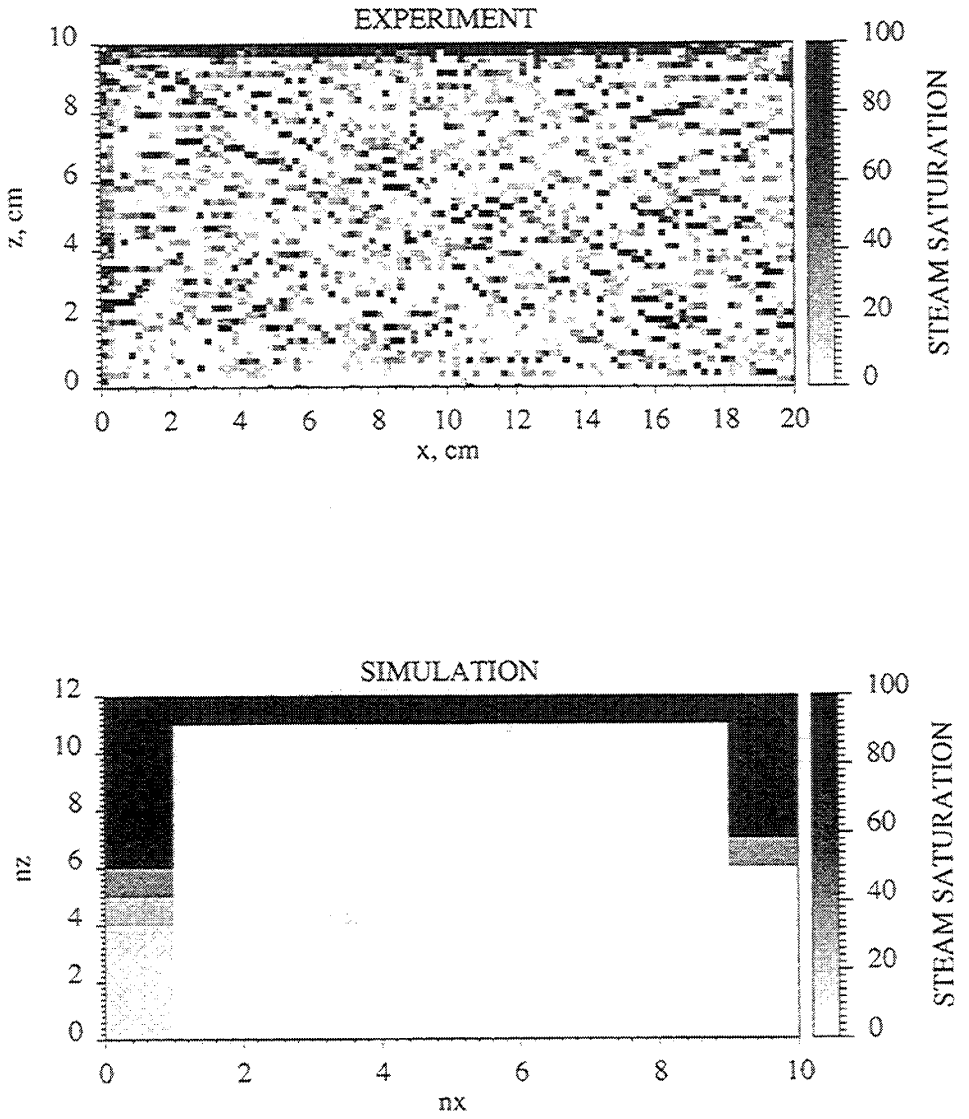

Figure 8.39: Steam saturations measured and calculated (Run 41).

8.3 Summary and Discussion

The first step in the analysis of the results was modeling heat losses from the experiment. To do that, heat loss models in the simulator had to be modified. Simple analytical solutions were used, and the heat transfer coefficients determined from these solutions were used as simulator input. The grid system used also had to be modified to describe the conductive heat loss in the core holder.

After these modifications, the experiments were successfully matched with simulations. Two-dimensional, cross-sectional simulations worked quite well when the thermal conductivities of the rock and the gas phase were increased. Three-dimensional simulations showed good agreement with experiments without modifying the conductivities. However, since three-dimensional simulations are more difficult and more costly to use, two-dimensional simulations can be used for additional simulation studies.

One important finding from the simulations was that there was no steam saturation inside the matrix. Contrary to our expectations, steam only flows in the fracture. The same behavior was observed in the experiments. However, heat transfer by conduction heated the matrix to a high temperature. As a result, steam injection in fractured systems can enhance oil recovery when heavy oils are present. Conduction heating can lower the oil viscosity and improve the oil recovery. This concept will be discussed in detail in Chapter 10.

The analysis presented so far was for a laboratory model where heat losses are a major factor affecting steam saturation development in the system. Heat losses are inevitable in a laboratory experiment. We were able to calibrate our numerical simulations with laboratory data; in terms of heat properties, relative permeabilities and capillary pressures. Next, the same fractured system was simulated by eliminating external heat losses. This was done to more closely mimic the processes taking place in the field (no heat flux, or reflection boundary, between arrays of matrix blocks). Two-dimensional simulations were used in this study since the saturation behavior was found to be similar to three-dimensional simulation results.

The steam saturations obtained with no external heat losses were similar to the

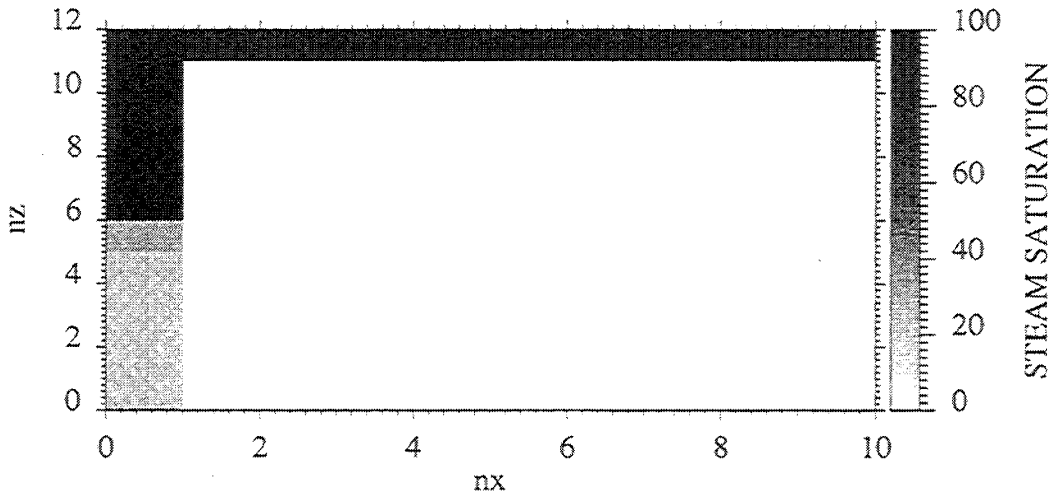

Figure 8.40: Steam saturations at the end of the simulation run (no external heat loss).

experimental results. No steam saturation developed in the matrix (Fig. 8.40). This showed that even for a system with no heat losses as in the field, steam will not enter the matrix with continuous steam injection. Therefore, a different steam injection scheme, cyclic steam injection, was investigated, both experimentally and numerically, for the same fractured system. This is discussed in the next chapter.

Chapter 9

Cyclic Steam Injection

The experimental results and analyses presented so far were for continuous steam injection into fractured systems. Both experimental and numerical simulation results indicated that steam saturation did not develop in the matrix, with steam flowing only in the fractures. Extension of the results to a simulation with no external heat losses also showed no steam saturation in the matrix.

Cyclic steam injection is a widely used method for fractured/fissured reservoirs. This chapter discusses the application of cyclic steaming in fractured systems. The first section describes results of the cyclic steam injection experiment. The second section discusses a numerical simulation run done to analyze the experiment. The final section describes a simulation run with no external heat losses, which would more closely mimic the field.

9.1 Cyclic Steam Injection Experiment

The cyclic steam injection experiment consisted of an initial steam injection period at a constant back pressure (8 psig) up to the time until the entire system is heated. Then the back pressure was lowered to the atmosphere. Steam injection was continued at this low back pressure. Then the back pressure was increased again to 8 psig, simulating the buildup period, and steam injection continued. This process was continued for three cycles. During this time, the core holder was scanned to monitor

any steam saturation changes in the matrix.

Figure 9.1 shows the steam saturations calculated from the CT numbers (after the pressure had been lowered), before the buildup periods. The figure shows all three cycles. These saturation maps are for the slice closest to the injector (Slice 1). Since the behavior was similar for the slice closest to the producer (Slice 2), only the saturation maps for Slice 1 are shown here.

As can be seen in Fig. 9.1, the saturation maps are similar to each other and similar to the results from the previous experiments. Steam flows only in the fracture, and pressure cycling did not develop steam saturation in the matrix. The apparent steam saturations observed in the matrix are not real, and are due to scan artifacts as discussed in Chapter 7.

Figures 9.2-9.4 compare steam saturations measured before and after the back pressure is lowered for the three cycles. These figures also indicate that steam saturation did not develop in the matrix. The top maps (before pressure lowering) and bottom maps (after pressure lowering) are identical. The small differences observed at some pixels are typical of the variations in the X-ray beams from scan to scan.

In summary, the results from the pressure cycling experiment were similar to the previous steam injection experiments at constant pressure. Contrary to our expectations, steam saturation did not develop in the matrix.

The pressure cycling experiment was simulated numerically and the results are compared next.

9.1.1 Numerical Simulations

The same procedure followed for history matching continuous steam injection was used for the pressure cycling experiment. Analytically determined heat transfer coefficients were used together with the same grid block arrangement. Also all flow and thermal properties were the same as the ones used in the previous simulations.

The simulation grid system used was a two-dimensional cross-section. Two-dimensional simulations worked well for modeling the previous experiments, when the conductivities of the rock and steam were modified. The computer cost of

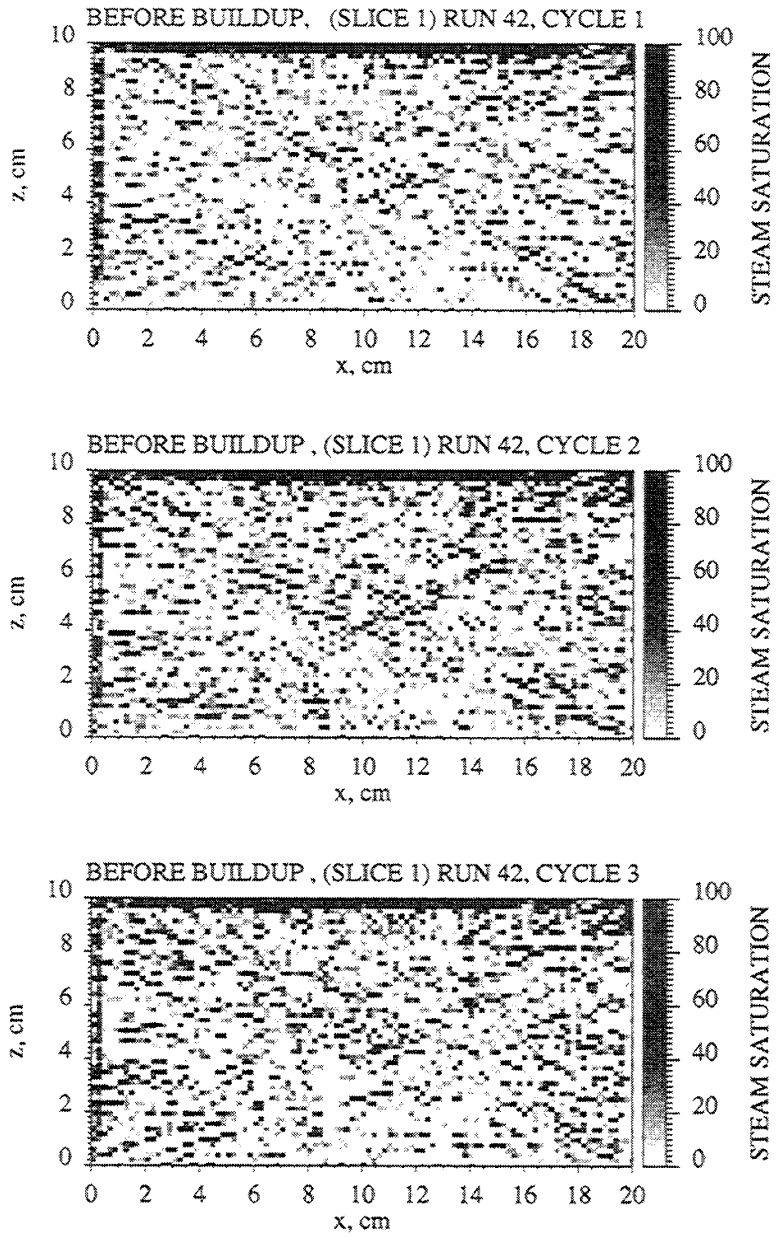

Figure 9.1: Steam saturations before the buildup periods (Pressure Cycling Experiment, Run 42).

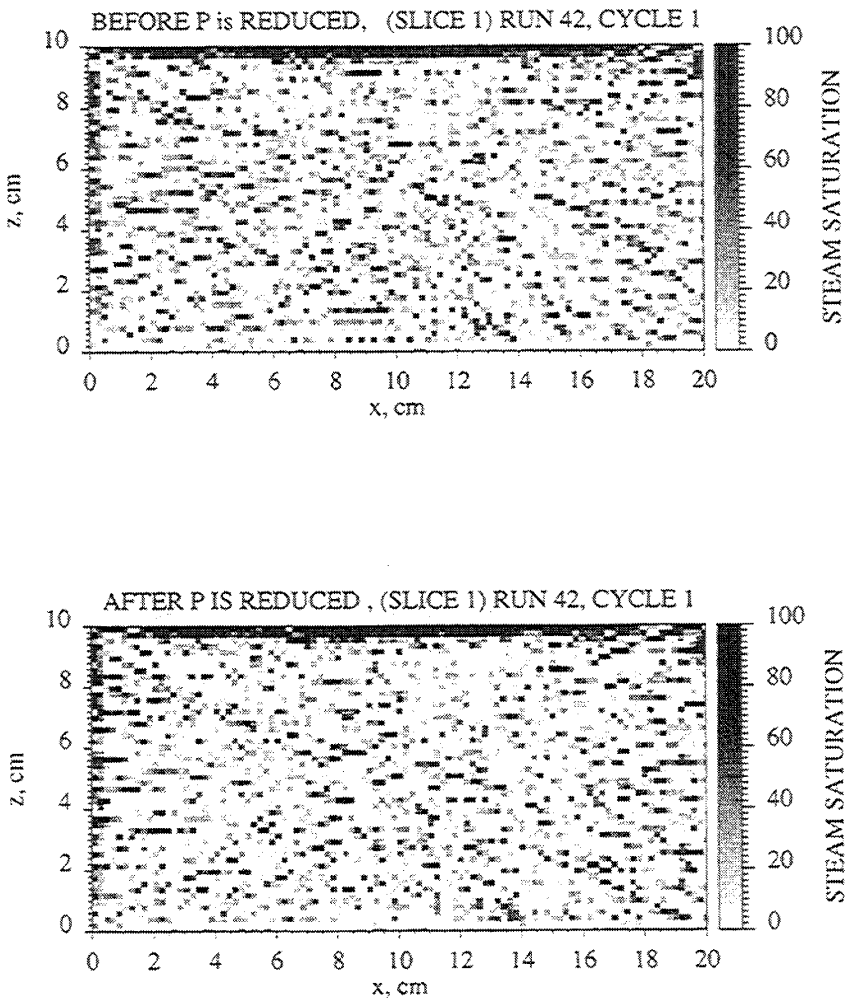

Figure 9.2: Steam saturations before and after pressure is reduced (Cycle 1).

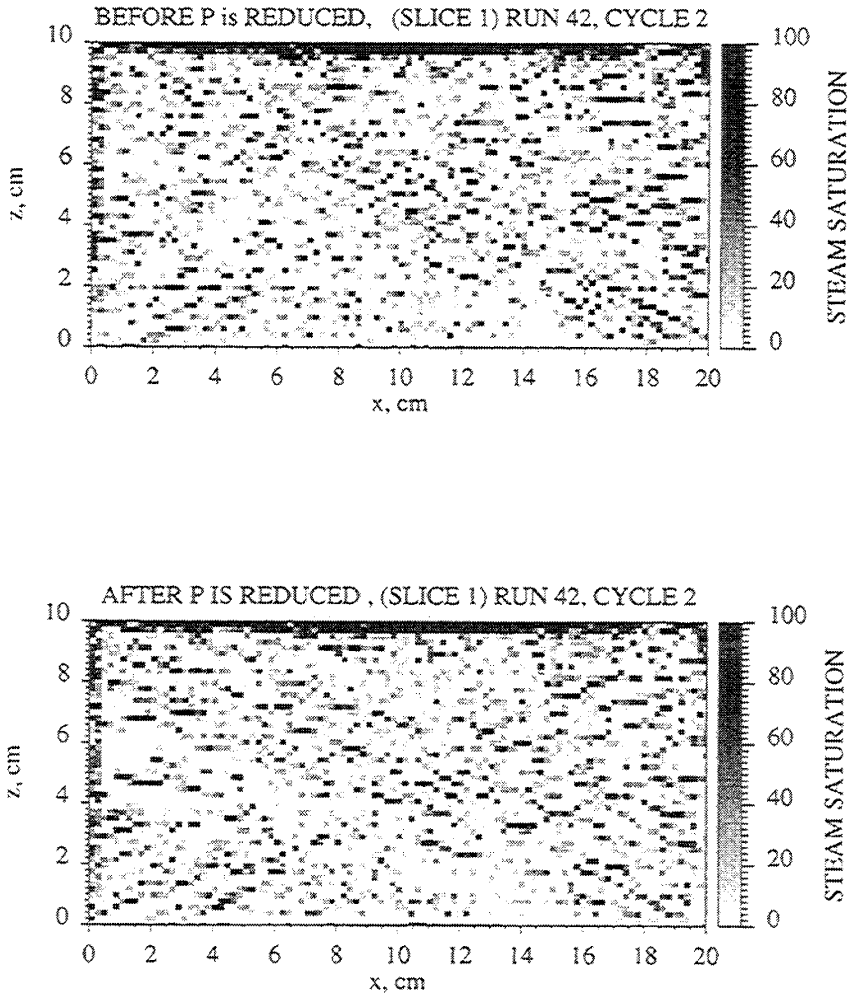

Figure 9.3: Steam saturations before and after pressure is reduced (Cycle 2).

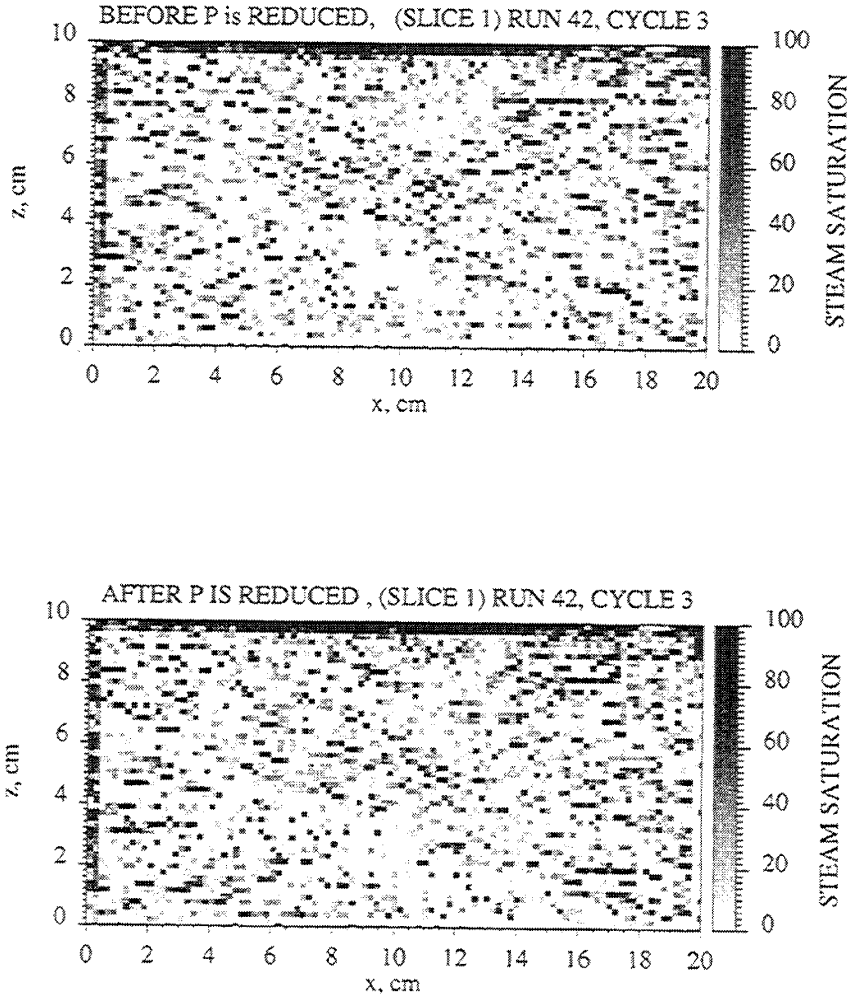

Figure 9.4: Steam saturations before and after pressure is reduced (Cycle 3).

three-dimensional simulations, and the numerical difficulties encountered with sudden changes in pressure for the pressure cycling run, justified the use of two-dimensional simulations. Since the heat losses are the most important factors in the modeling process, they were the first to be matched. Figure 9.5 shows the heat losses calculated from the simulator compared with the experiments for the initial constant back pressure period. The agreement is quite good.

Then the same three pressure cycles used in the experiment were used in the simulation run. Figure 9.6 shows the calculated steam saturations. The maps correspond to the times just before the buildup period after pressure was lowered. The results are similar to the experiment and to each other. No steam saturation developed in the matrix.

We know that heat losses are present and have a significant effect on steam saturation development. They are inevitable in this experimental model. However in the field, external heat losses from individual matrix blocks are not as significant. Therefore, the same pressure cycling scheme was used in a simulation run with no heat loss.

9.1.2 Pressure Cycling with No Heat Losses

In the previous chapter, a steam injection simulation run with no external heat losses was discussed. The results were found to be similar to the experiments and to the simulations with heat losses. This calculation was made at constant back pressure.

Now, pressure cycling simulations were repeated using zero external heat losses. The rest of the physical properties and operating parameters were unchanged.

Figure 9.7 shows the steam saturations calculated in the matrix, before the buildup period, for the same three cycles used in the simulations with heat losses. There is a significant steam saturation development of 40 to 50% in the matrix due to pressure cycling. The steam saturation slowly increases with every cycle. It averages 43% after the first cycle, 48% after the second, and 50% after the third cycle. These saturations correspond to a range of 2.1-1.6 psi on the matrix capillary pressure curve used in the simulation run which are different than the threshold value (Fig. 9.8).

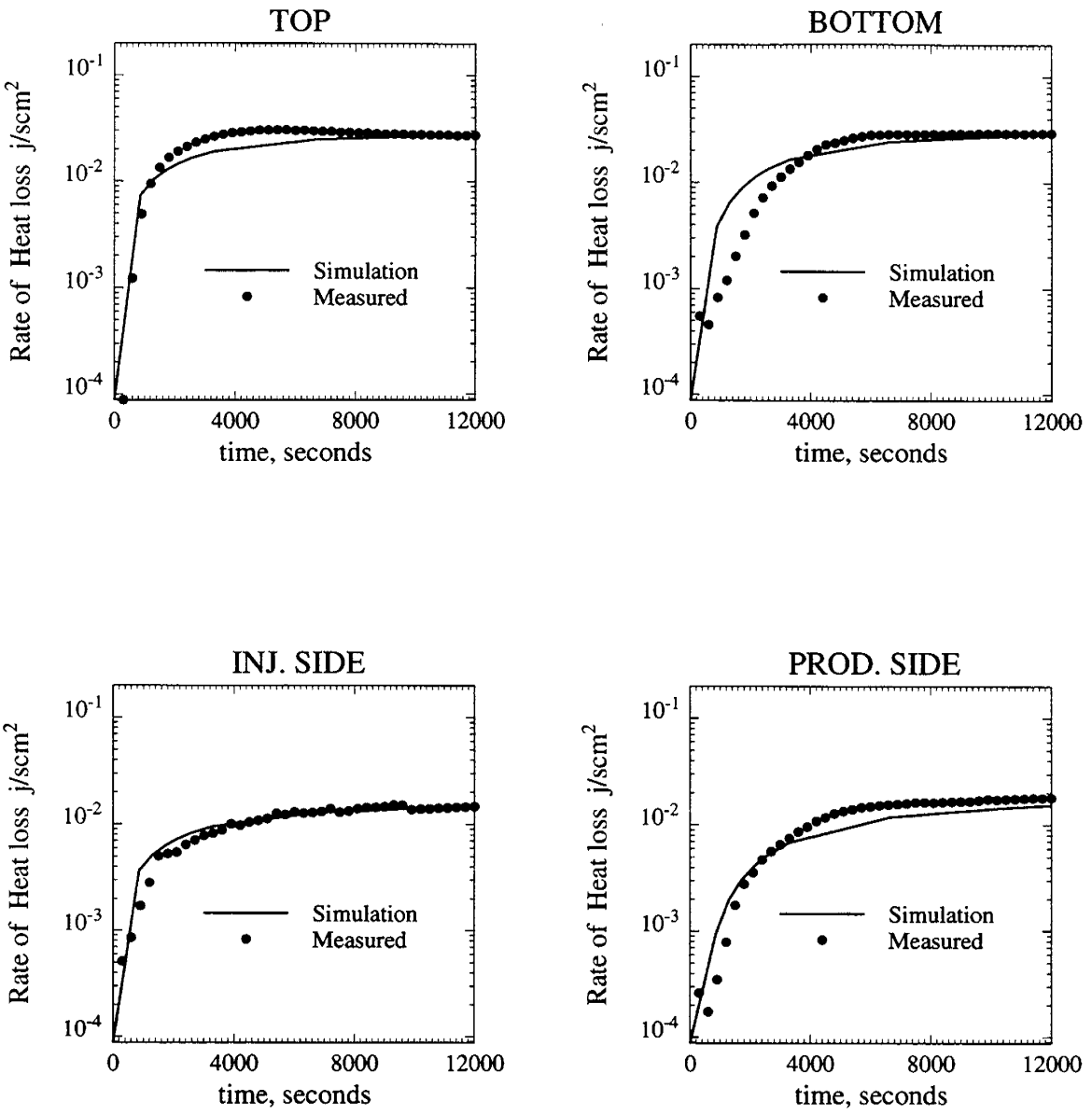

Figure 9.5: Comparison of experimental and the simulation heat losses (Run 42).

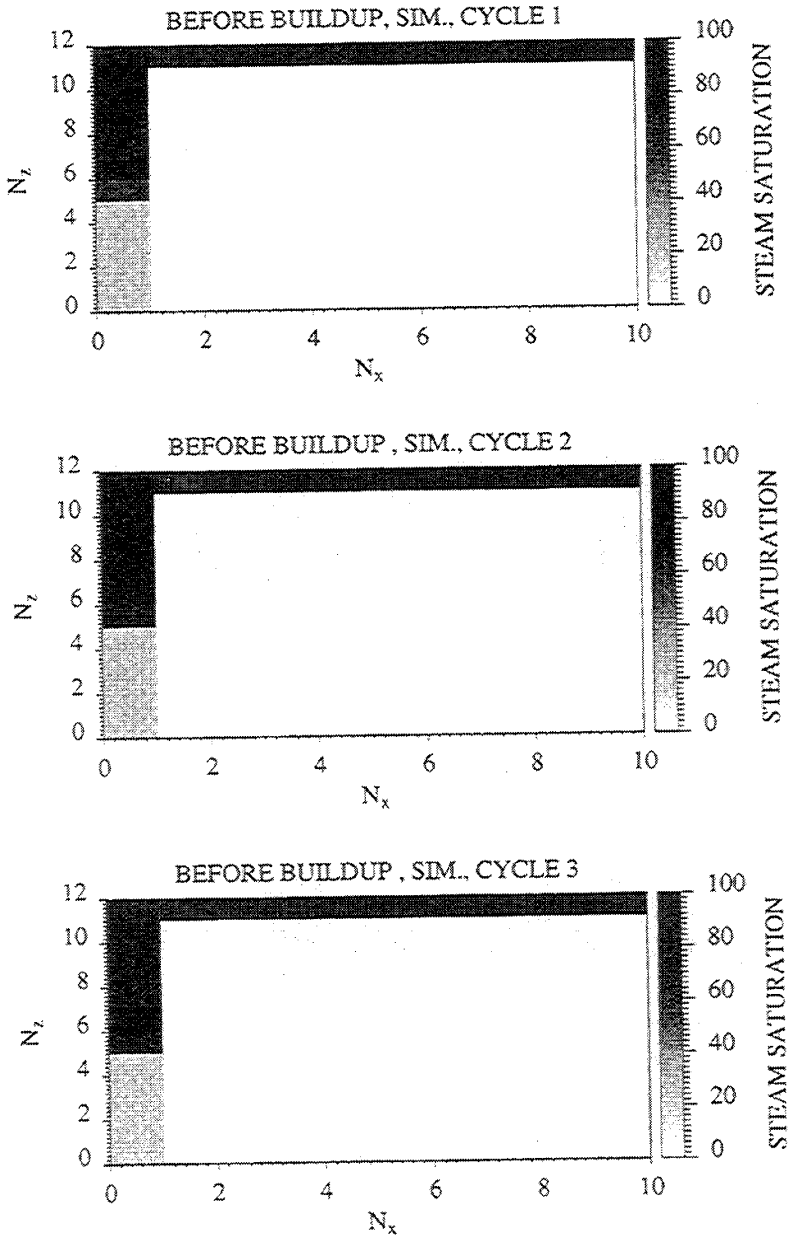

Figure 9.6: Steam saturations before the buildup periods (Pressure Cycling Simulation, Run 42).

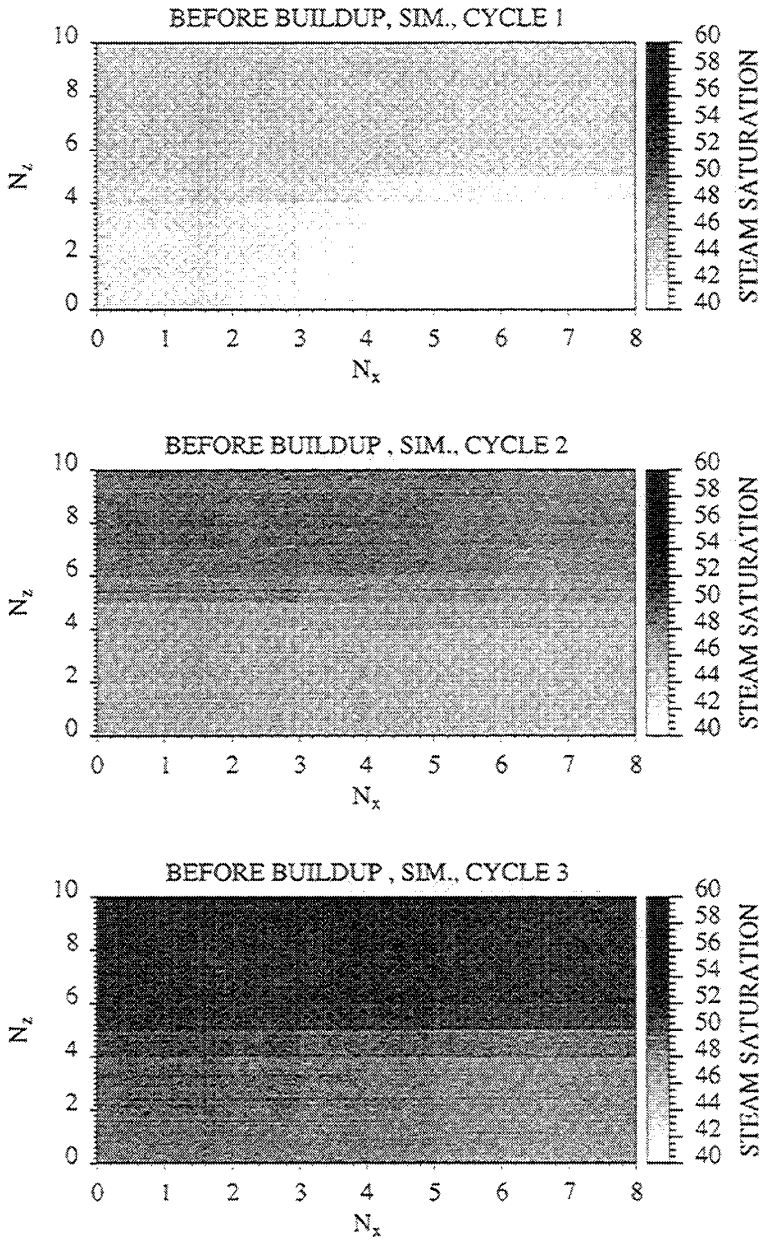

Figure 9.7: Steam saturations in the matrix before the buildup periods with no external heat losses (Pressure Cycling Simulation).

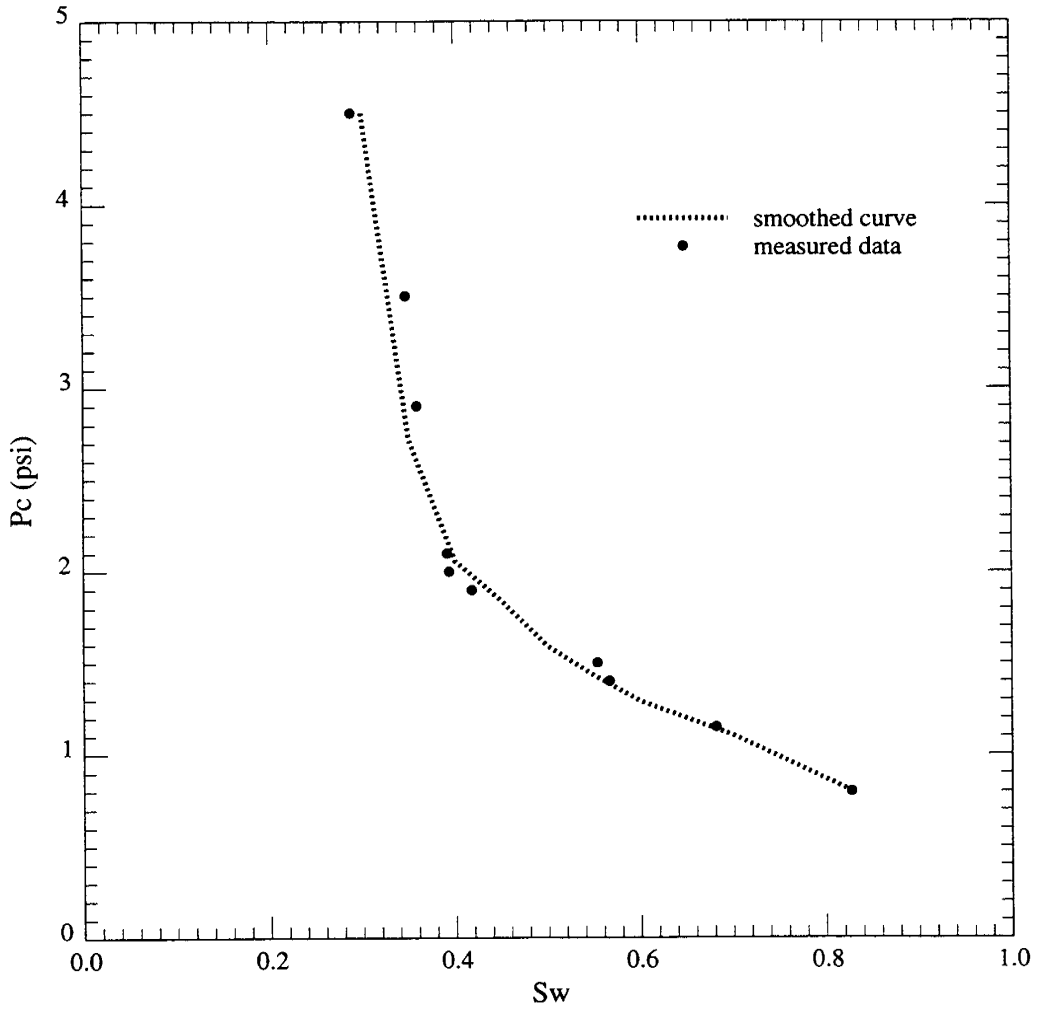

Figure 9.8: Matrix water-steam capillary pressures used in the simulations (Handy, 1960).

Saturation maps show that the steam tends to enter to a greater extent from the top of the matrix block. This is due to gravity override. Note that the scales of these maps are between 40-60% instead of 0-100%, so that saturation changes can be more clearly seen.

This is a very important finding since it shows the value of pressure cycling, instead of continuous steam injection, in a fractured reservoir when external heat losses are not very significant. The heat losses significantly affect steam saturation development in the matrix.

The analyses presented so far were for steam/water flow in fractured reservoirs. Both the experimental and simulation results showed the dominance of conduction as a fracture/matrix heat transfer mechanism, since steam only flows in the fracture. Conduction was found to be quite effective in heating the matrix, considering the heat losses in the experiments. However, when heat losses are not significant, steam can develop in the matrix with pressure cycling. Thus, in the field, convective heat transfer can also become important, if pressure cycling is used.

This analysis helped to isolate the heat transfer mechanisms for differing steam injection techniques, and also allowed the calibration of the heat loss models in the simulator. The next chapter discusses how we would expect fractured systems to behave when steam is injected into a system containing heavy oil.

Chapter 10

Steam Injection with Oil Present

In this chapter, the results of simulations for steam injection are described for a system filled with oil at irreducible water saturation. The system is the same as the experimental fractured model described earlier.

First, sensitivity studies on the effects of capillary pressures will be presented. These runs were performed to identify the important recovery mechanisms, and are all at constant back pressure. Then a simulation run with no heat losses will be described. Finally, the calculated effect of pressure cycling will be described for this system.

10.1 Simulations at Constant back Pressure

The simulations are exact replicas of the previously discussed simulations for modeling the steam/water experiments, in the sense that porosity, absolute permeabilities, thermal properties and heat losses are the same. Water-oil and liquid-gas relative permeability curves are from Oballa et al. [61] as shown in Fig. 3.19 in Chapter 3.

The grid system is again a two-dimensional cross-section with adjacent blocks simulating the core holder. These are assigned zero porosity and zero permeability, as described previously.

The simulations are different from the fine grid simulations described in Chapter 3, for the heat loss model and the conductivity are modified to match the experiments.

The purpose was to predict the behavior of this experimental system in the presence of oil, water and steam for future modeling of experiments with these fluids in the system.

Sensitivity studies were made on the water-oil and gas-oil capillary pressures of both matrix and fracture, since capillary pressure was found to be the most important parameter affecting the recovery as discussed in Chapter 3.

10.1.1 Capillary Pressure in Matrix

Water-oil and liquid-gas capillary pressures were taken from Oballa et. al [61] and were shown earlier in Fig. 3.4. Gas-oil capillary pressure of the matrix was found to not be an important parameter, so only the effect of water-oil capillary pressure of the matrix will be shown here.

The recovery has increased considerably with a nonzero water-oil capillary pressure (Fig. 10.1). This is due to the imbibition of condensed steam into the matrix. Hot water from condensed steam heats the oil, lowers its viscosity and displaces it. The movement of water into the matrix can be seen from the water saturation maps at 202 minutes of steam injection (Fig. 10.2a and 10.2b). When capillary pressure is zero, water saturation in the matrix is almost at its initial value of 20%. However, when capillary pressure is greater than zero, we see an increase in the water saturation to almost 50% due to water imbibition. The corresponding decrease in oil saturation in the matrix can be seen in Fig. 10.3b. When capillary pressure is zero, oil saturation remains at its initial value of 80% except very close to the fracture, on the injection side, where it is lowered due to stripping with steam (Fig. 10.3a).

The steam saturation map is very similar to the results from the steam/water experiments and simulations (Fig. 10.4). Steam does not develop in the matrix; it flows in the fracture. However, since hot water imbibition causes viscosity reduction in the oil, recovery is quite good. With about 1 PV of steam injection, 27% of the oil is recovered.

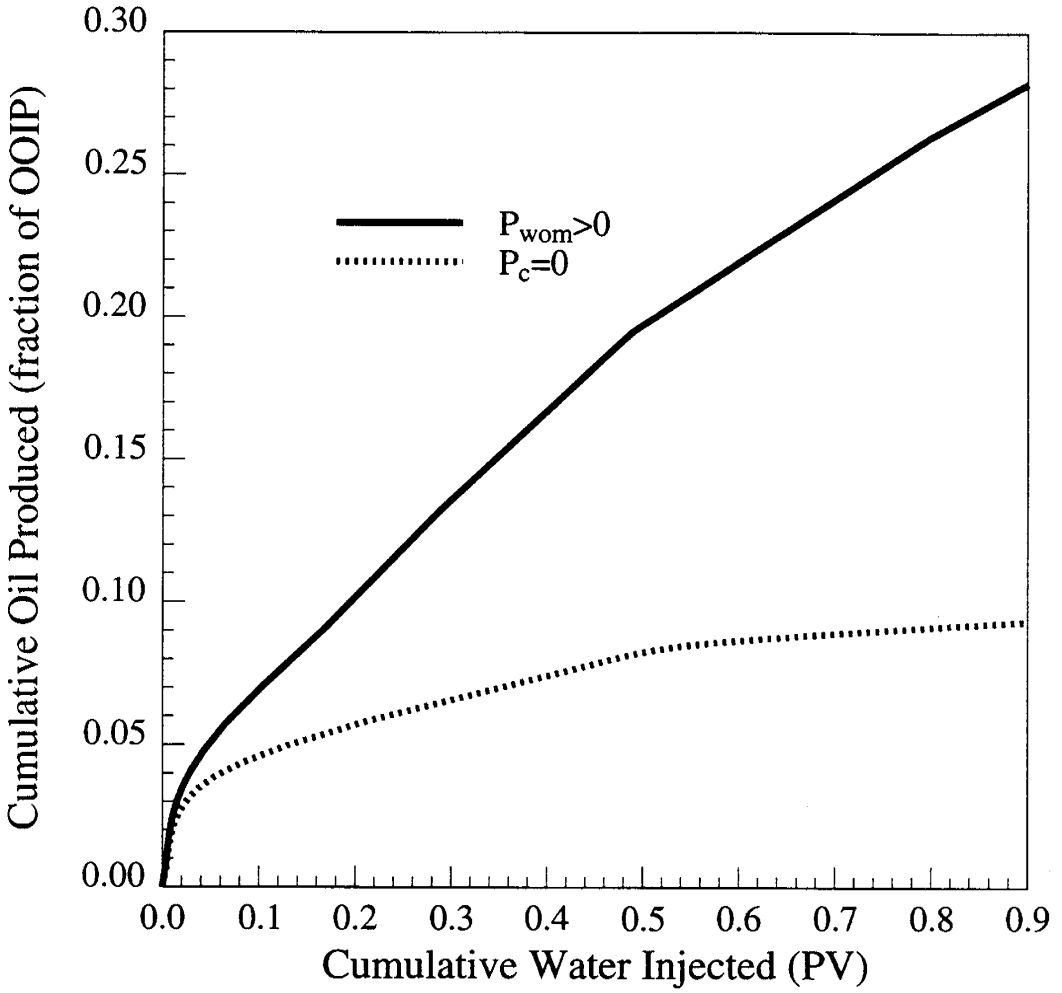

Figure 10.1: Effect of water-oil capillary pressure of matrix on recovery.

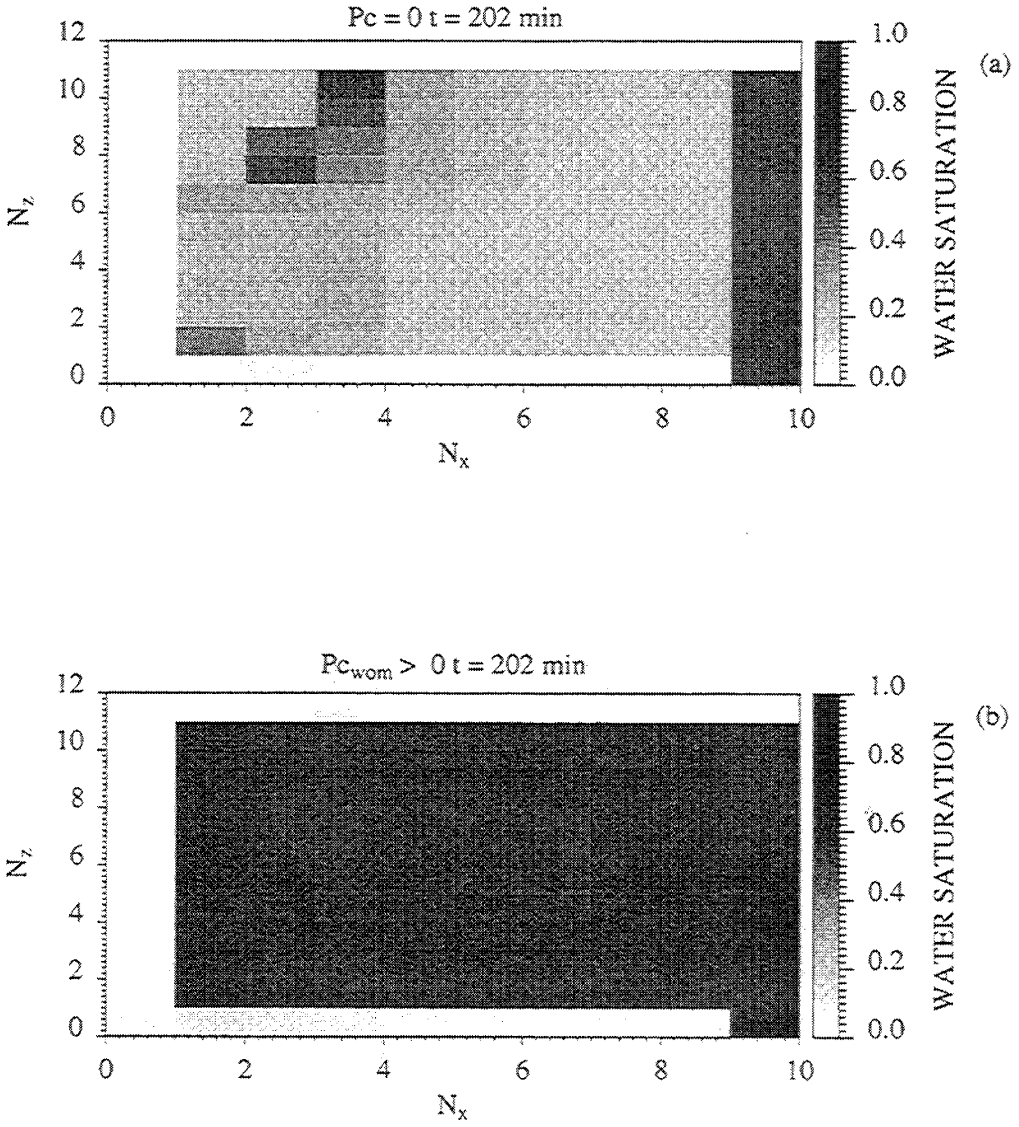

Figure 10.2: Water saturation maps at 202 minutes of steam injection (a) Zero capillary pressure. (b) Nonzero water-oil capillary pressure in matrix.

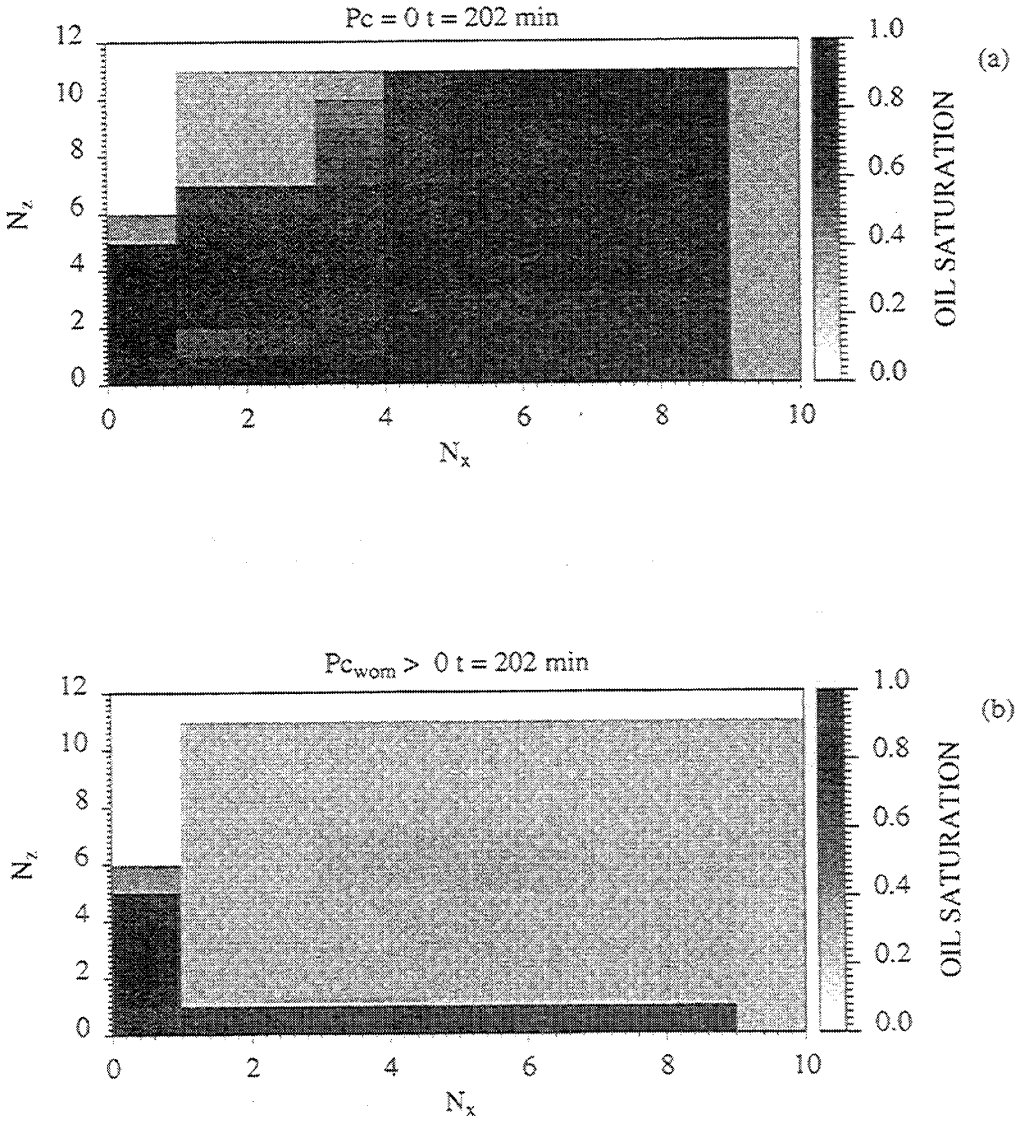

Figure 10.3: Oil saturation maps at 202 minutes of steam injection (a) Zero capillary pressure. (b) Nonzero water-oil capillary pressure in matrix.

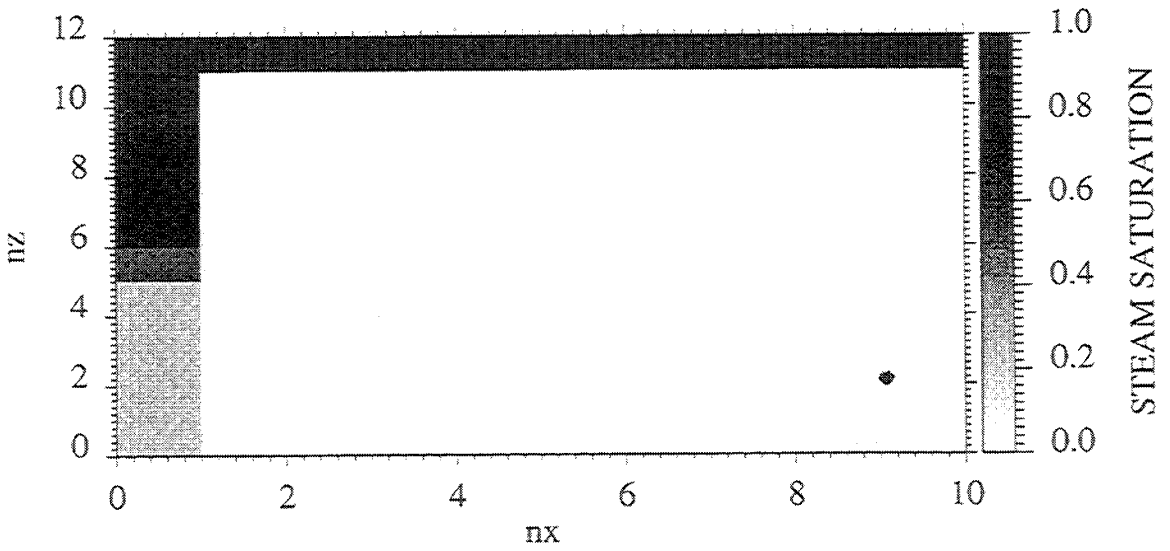

Figure 10.4: Steam saturation map at 202 minutes of steam injection.

10.1.2 Capillary Pressure in Fracture

Fracture capillary pressures used in the simulations were shown in Fig. 3.12 in Chapter 3. Gas-oil capillary pressure in the fracture caused steam to enter the matrix and increase oil recovery (Fig. 10.5). Fracture water-oil capillary pressure produced only a minor negative effect on recovery, and thus will not be shown here.

The advantage of steam injection over water flooding for a fractured system can be demonstrated better when we perform a simulation run for the same system by injecting cold water instead of steam. Figure 10.6 shows the comparison of the two simulation runs. An additional 20% increase in the oil recovery was obtained with steam injection compared to cold water injection. This proves that even though steam prefers to flow in the fractures, steam injection can be a feasible recovery technique for fractured reservoirs since the matrix can still be heated by conduction and by convective heating from imbibed water. Water imbibition is the main displacement mechanism for the oil in the matrix.

For the oil-water-steam simulations discussed so far, heat losses were present and were the same as for the steam-water experiments. To discover the effect of heat losses, a simulation was run with no external heat losses. Nonzero capillary pressures were used for the matrix since imbibition had been found to be the dominant mechanism. Fracture capillary pressure was taken to be zero.

The results were found to be similar to the run with heat losses. No steam was observed in the matrix (Fig. 10.7). The recoveries were very similar to the case with heat loss (Fig. 10.8).

10.2 Pressure Cycling for Systems with Oil

Pressure cycling was shown to cause steam saturation development in the matrix for the steam-water simulations with no heat losses, as discussed in the previous chapter. In fact, once steam saturation had developed, it increased with each cycle.

The same type of pressure cycling was applied to the system saturated with oil and connate water, assuming no external heat losses. Three cycles were simulated,

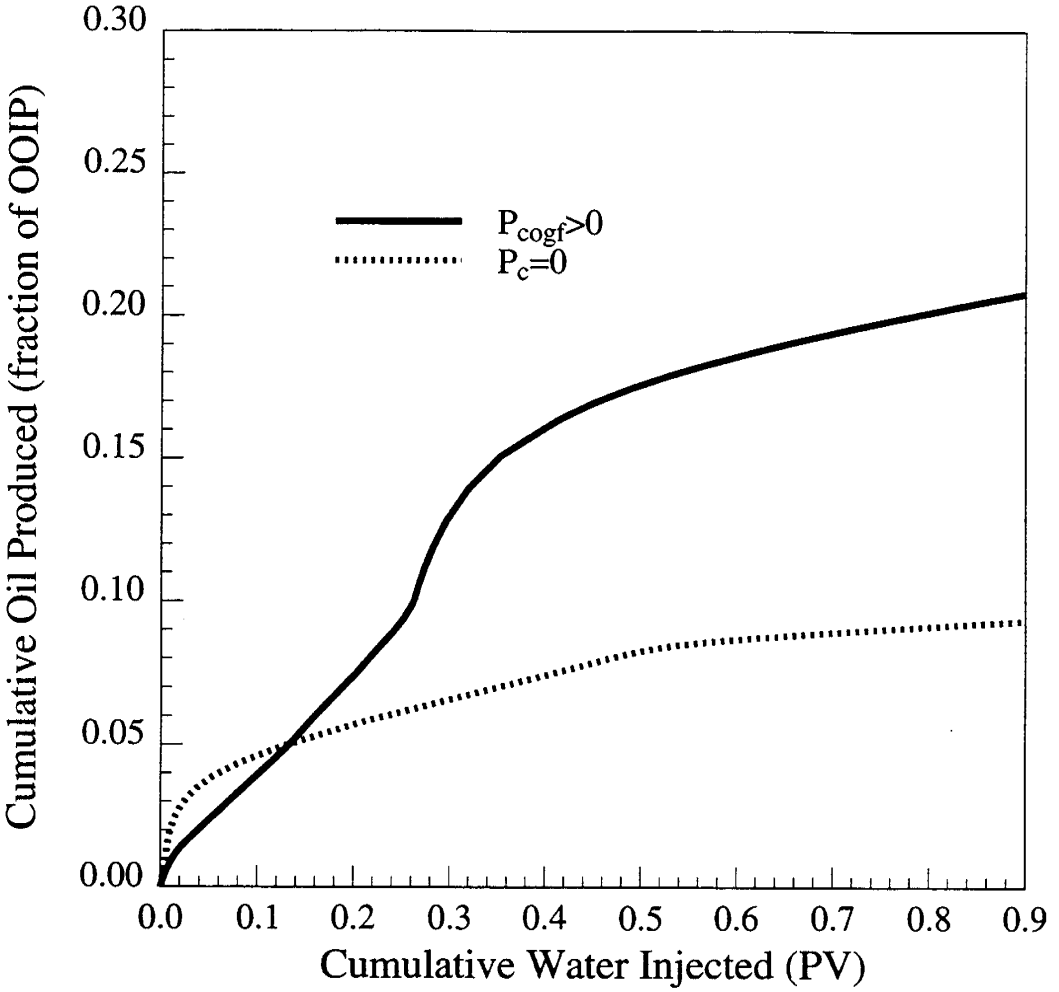

Figure 10.5: Effect of gas-oil capillary pressure of fracture on recovery.

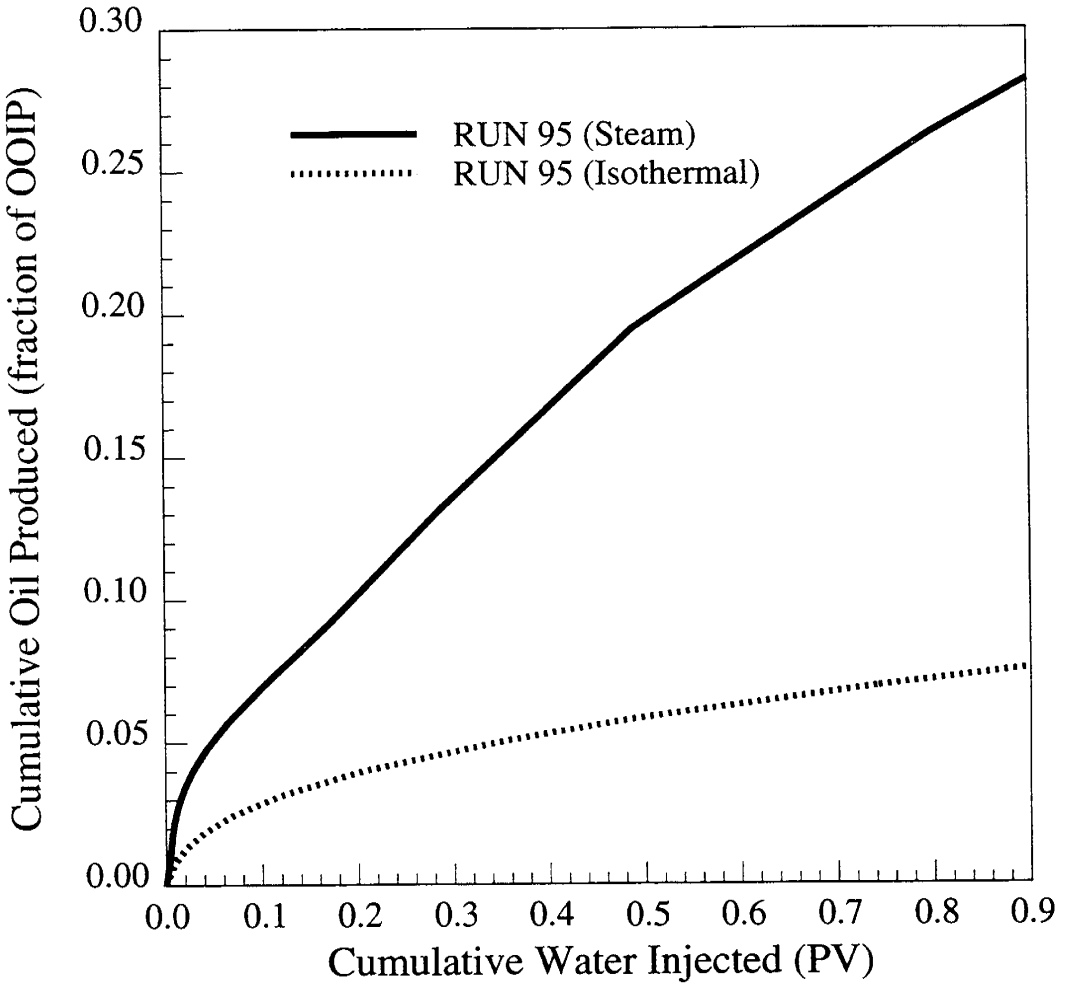

Figure 10.6: Comparison between cold water injection and steam injection.

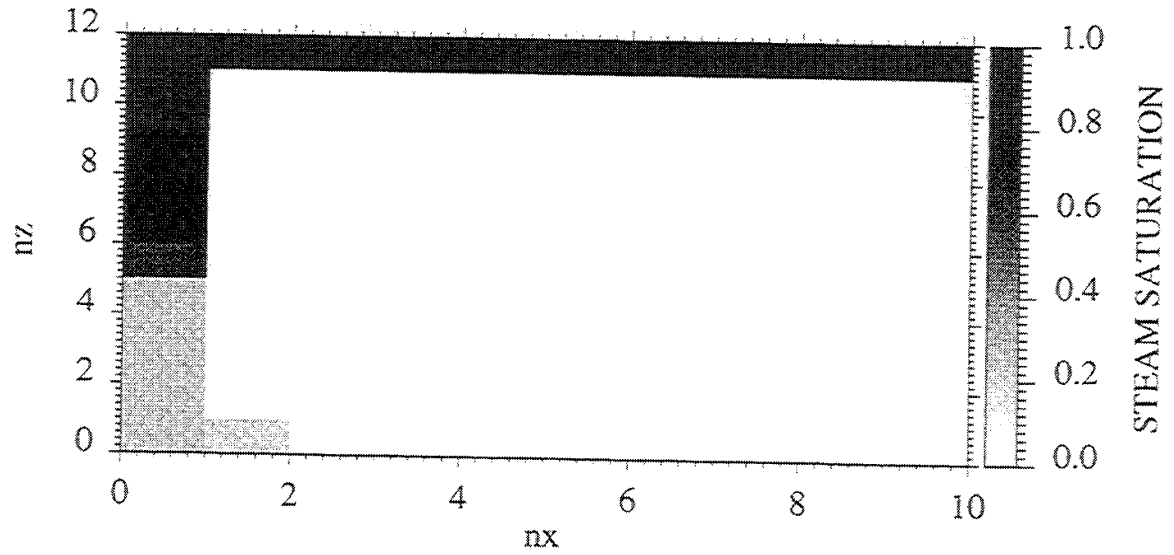

Figure 10.7: Steam saturation map at 202 minutes of steam injection (No heat losses).

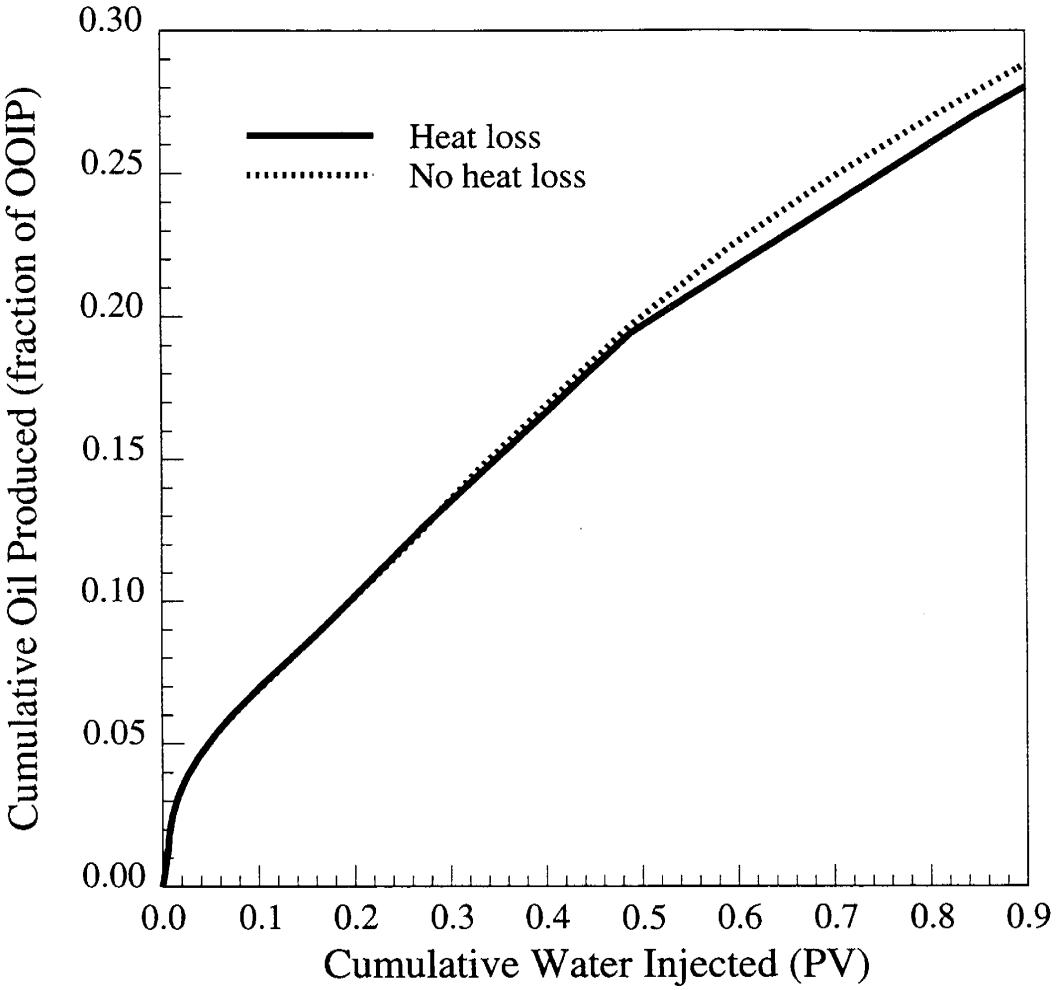

Figure 10.8: Comparison between the cases with and without heat loss.

consisting of pressure lowering periods followed by buildup periods. Steam saturations calculated before buildup for each of the three cycles are shown in Fig. 10.9. The pressure cycling caused steam saturation to develop in the matrix just as it had in the steam-water case. At the decreased pressure level steam phase formed in the matrix utilizing the excess heat at the lower saturation temperatures. This phase change caused the matrix to cool. However, in-situ emerging steam preferred to displace the remaining water within the pores instead of the remaining oil in place. This is because the oil mobility is lower than water. Therefore, when two cases are compared (with/without cycling), we observe that the two cases yield essentially the same recovery, (Fig. 10.10) due to the reasons mentioned before, the dominance of imbibition on oil recovery is evident. Even though steam developed in the matrix, it did not contribute to any additional recovery apart from the recovery caused by imbibition.

The oil saturation with respect to distance at the center of the core shows the effect of pressure cycling on the oil saturation remaining in the matrix (Fig. 10.11). It is slightly higher for the cycling case especially near the production side fracture. The emerging steam phase just replaces the pores occupied by water rather than the remaining oil. Also oil in the matrix becomes less mobile when the rock temperature drops due to pressure cycling.

Hysteresis of relative permeabilities and capillary pressures might be important during cycling. This may require further investigation.

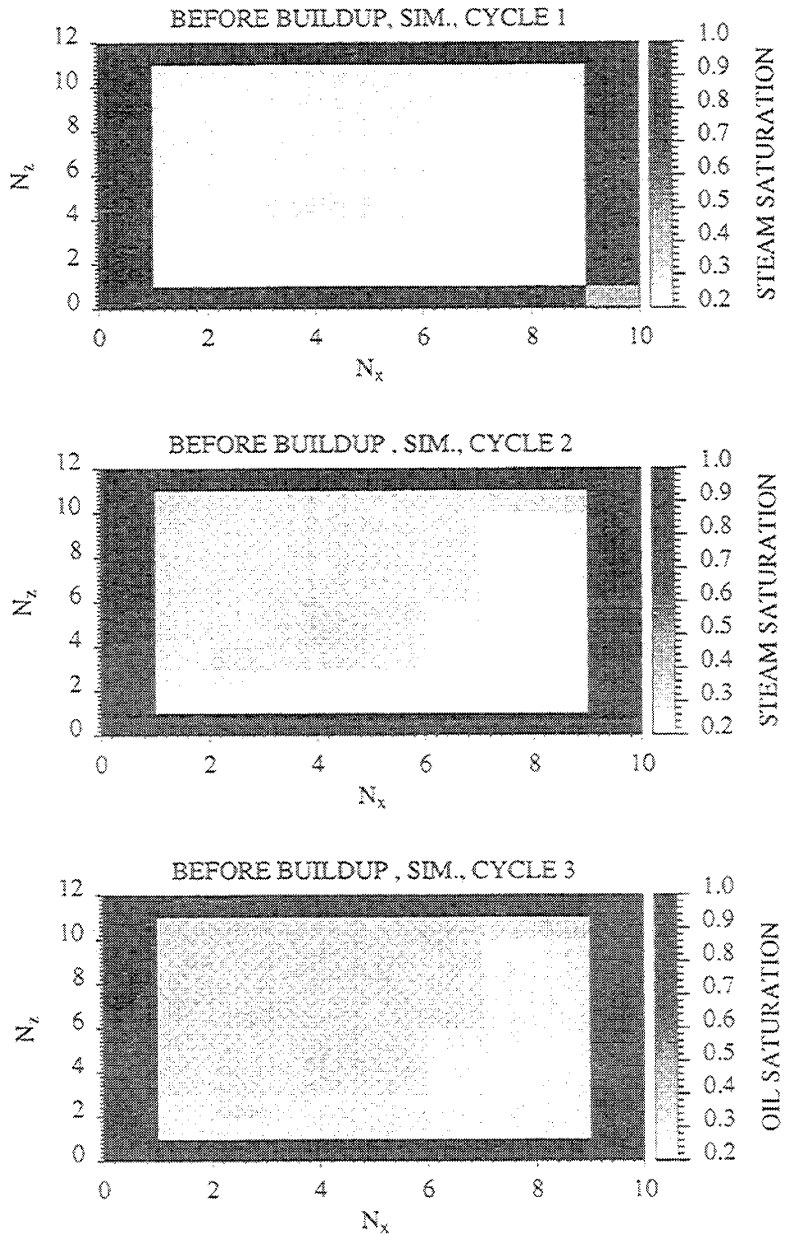

Figure 10.9: Steam saturations before the buildup periods (Pressure Cycling Simulation).

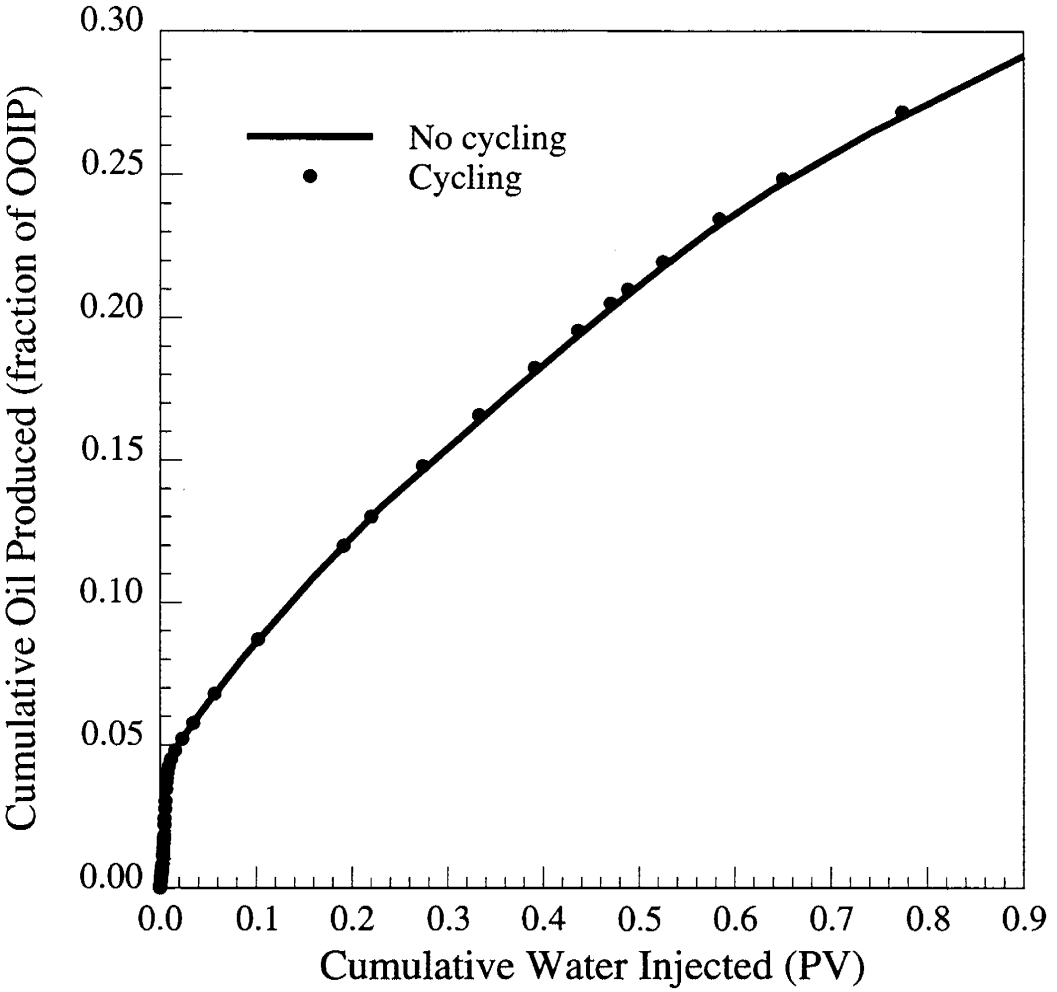

Figure 10.10: Effect of cycling on recovery.

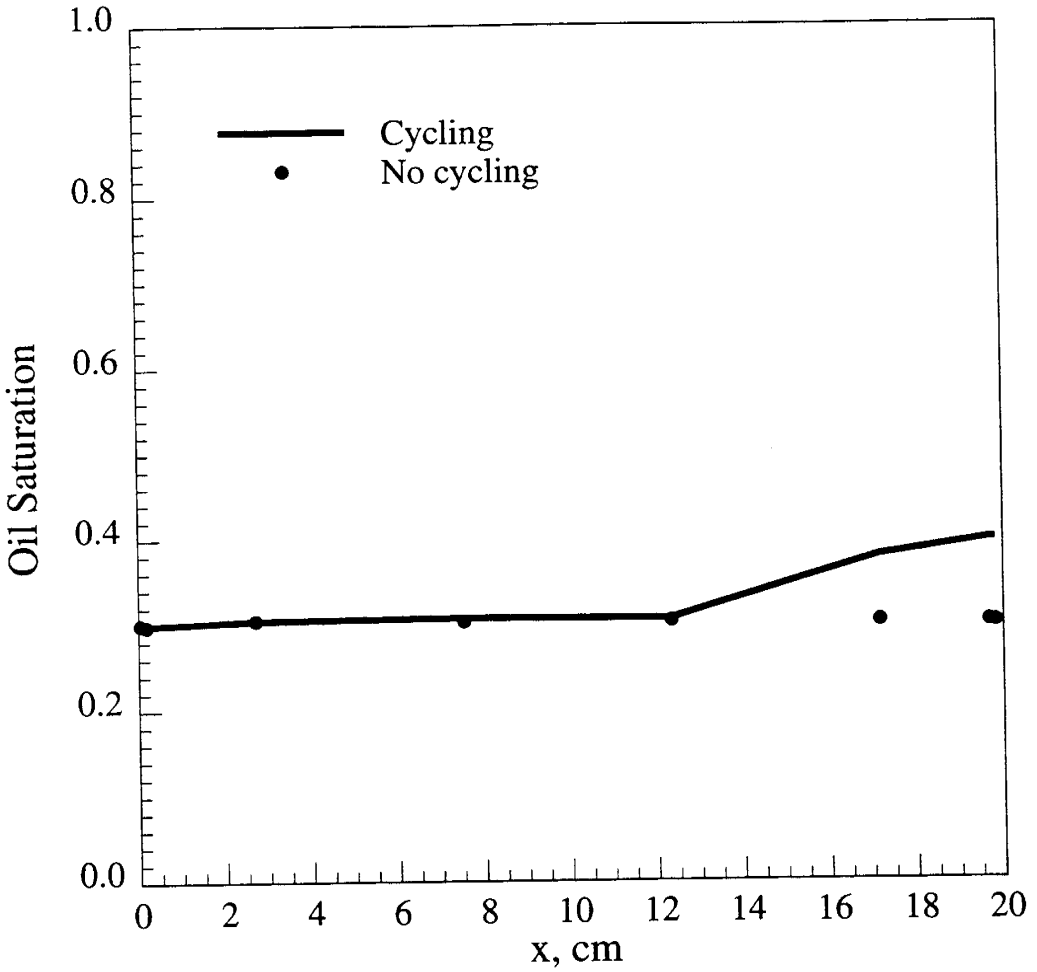

Figure 10.11: Effect of cycling on the oil saturation left in the system.

Chapter 11

Conclusions and Recommendations

The purpose of this study was to investigate the steam injection process in fractured systems, both experimentally and theoretically, and to understand the physical mechanisms in oil recovery from such systems. The lack of data on steam injection in fractured systems, prompted the design and building of an experimental model that would allow accurate measurements of the temperatures in both the fracture and the matrix. Measurement of steam saturations in-situ in the fracture was also accomplished for the first time in this study.

A numerical simulator was calibrated and was used to model the experiments and to analyze different aspects of steam injection, such as cyclic steam injection and steam injection for a case with no external heat losses, in order to mimic the processes in the field. The following sections summarize conclusions obtained from this study and recommendations for future studies.

11.1 Conclusions

1. Fine grid simulations and analytical calculations were used successfully in the design of a fractured laboratory model for steam injection. Several simulators were used; black oil, pseudo-compositional and thermal, in various stages of the design. The expected heat losses from the model were predicted from both steady state and transient heat transfer models. Simulations also helped in

the selection of the core holder material by determining the maximum pressure expected in the system.

2. A unique fracture laboratory model was built from a high temperature plastic that allowed the use of a CT-scanner for saturation measurements. Temperatures, pressures and heat losses from the model were measured. A thorough set of experimental measurements, for a fractured system undergoing steam injection, was done for the first time in this study.

3. Continuous steam injection experiments were performed to investigate the effects of various parameters; rate, injection temperature and back pressure. The effect of injection rate was not as significant as the injection temperature and the back pressure on the system. A higher injection temperature enabled the matrix to heat faster. A low back pressure caused the steam saturation to develop faster and thus, the matrix was heated faster.

4. Steam saturations were measured in the fracture by a CT scanner for the first time. The results showed that steam only flowed in the fracture. However, the matrix was still effectively heated by conduction.

5. Numerical simulations were used to model the experimental results. A procedure was developed to accurately model the heat losses by incorporating analytical heat transfer coefficients to the heat transfer models in the simulator.

6. Numerical simulations successfully matched the experiments. For the first time, there was a complete match of heat losses, temperatures measured at various locations both in the fracture and the matrix, and steam saturations.

7. Pressure cycling experiments were performed both in the laboratory and with simulations. Contrary to expectations, steam saturation did not develop in the matrix due to pressure cycling. Both the simulator and the experiment showed the same results.

8. Steam saturation development in the matrix was found to be greatly affected by the heat losses from the system. When heat losses from the system were set

to zero in the simulations, there was a considerable amount of steam saturation developed, due to pressure cycling.

9. Simulations were used to study the behavior of a system saturated with oil and connate water. Oil-water capillary pressure of the matrix and gas-oil capillary pressure of the fracture were both found to affect the oil recovery. Even though steam saturation did not develop in the matrix, oil was recovered due to water imbibition. Steam only flowed into the matrix with a nonzero gas-oil capillary pressure of the fracture.

10. Cyclic steam injection with no external heat losses caused steam saturation to develop in the matrix for simulations with oil present. However oil recovery was similar to the run with no cycling. Temperature decreases observed in the matrix due to vaporization caused the oil viscosity to decrease less than for the no cycling case. Overall oil viscosity in the system was much higher during cycling. The similarities in oil recoveries indicated that water imbibition was the dominant recovery mechanism.

11. If pressure cycling is not used, conduction heat transfer is the dominant fracture-matrix transfer mechanism, since steam prefers to flow in the fracture. Conduction heating reduces the viscosity of oil, and thus makes it mobile. Water imbibition into the matrix and the countercurrent displacement of oil is an important recovery mechanism, especially for water-wet reservoirs.

11.2 Recommendations

This work helped in understanding of the physical processes that take place during steam injection in fractured systems. The experimental results showed that, for continuous steam injection processes, steam does not enter the matrix and only flows in the fracture. However, the pressure cycling process causes steam saturation to develop in the matrix when no external heat losses are present.

Accurate experimental data were obtained for modeling the transfer mechanisms,

especially the conduction heat transfer. The experimental results were used successfully to calibrate the simulator for further modeling studies. Based on the results of this work, there are still important issues to investigate and more work to be done. Some issues that need to be investigated are:

1. By numerical simulations, we have investigated the recovery processes taking place for steam injection in fractured systems with oil present, and showed that cyclic steam injection helps to develop steam saturation in the matrix. However, the positive effect of steam saturation development is offset by the sudden temperature decrease in the system when the pressure is lowered. This result should be confirmed by laboratory experiments.

2. Numerical and experimental results indicated efficient heating of the matrix by conduction. Ways to scale this conduction heating to field size blocks should be investigated. It is expected that it will be a function of the matrix block size and a square root function of time.

3. Accurate measurement of three-phase saturations by the CT-scanner will be needed in these experiments. Higher scan speeds are needed to capture the steam flashing due to pressure cycling. Further, a revision to the design of the laboratory model is needed, to reduce the effects of external heat losses. One possibility is to heat the core holder externally.

4. Since water imbibition is the major recovery mechanism, capillary pressures should be accurately determined as a function of temperature. Fracture gas-oil capillary pressure affects steam entry into the matrix, thus more work is also needed on fracture capillary pressures.

5. Simulation results indicated that water imbibition is the main recovery mechanism for water wet systems with or without pressure cycling. Further studies are needed for oil wet systems and systems with intermediate wettability to isolate the recovery mechanisms. Furthermore the simulations should be repeated with a live oil to study the effects of gases released from the oil.

6. Steam relative permeabilities are crucial in modeling. Therefore more work should be done to measure relative permeabilities, especially for consolidated cores.

7. The effect of steam-water capillary pressure on the results was not investigated due to lack of data. An air-water capillary pressure curve was used in the simulations. More work is definitely needed on the effect of steam-water capillary pressures.

8. The importance of relative permeability and capillary pressure hysteresis during pressure cycling should be investigated.

9. Since heat transfer is mainly conductive, a matrix-fracture transfer function incorporating conductive heat transfer and convective heat transfer from imbibed hot water should be sufficient to model heat transfer to the matrix. This idea should be tested in a dual porosity simulator, and the experimental results obtained in this study should be used to validate the model results.

Nomenclature

a	=	width of the parallelepiped shell
A	=	area
b	=	length of the paralelepiped shell
b'	=	total thickness of the insulation
CT	=	CT number measured by the CT scanner
c	=	height of the parallepiped shell
d	=	diffusion length
G_o	=	geometric factor
h	=	width
h_{conv}	=	overall convective heat transfer coefficient
h_f	=	convective heat transfer coefficient
h_{f_1}	=	convective heat transfer coefficient from the system to the insulation
h_{f_2}	=	convective heat transfer coefficient from the insulation to the surroundings
k	=	absolute permeability
k_r	=	relative permeability
$(k_{ro})_g$	=	relative permeability to oil in the presence of gas
$(k_{ro})_w$	=	relative permeability to oil in the presence of water
L	=	length
N	=	number of grid blocks
p	=	pressure
P_s	=	saturation pressure

q	=	heat loss rate per unit area
S	=	saturation
S_1	=	total inner surface area of the parallelepiped shell
t	=	time
T	=	temperature
T_s	=	saturation temperature
V	=	volume
x	=	distance
W	=	weight
α	=	thermal diffusivity
δ	=	thickness of the parallelepiped shell
Θ	=	temperature difference between the reservoir and the adjacent formation
κ	=	thermal conductance
λ	=	thermal conductivity
μ	=	viscosity
ρ	=	density
ϕ	=	porosity

Subscript-Superscript

app	:	apparent
a	:	ambient
b	:	back
bu	:	bulk
c	:	capillary
dc	:	dry core
f	:	fracture
g	:	gas

m	:	matrix
o	:	oil
s	:	steam
w	:	water
wc	:	water saturated core
∞	:	free stream

Bibliography

[1] Abad, B.P. and Hensley, C.A.: "The Effect of Stratification, Fractures, and Dip on Steam Sweep Efficiency and Heat Requirements of Steamflood Operations," paper SPE 12748 presented at the 1984 California Regional Meeting, Long Beach, CA, April 11-13.

[2] Abdus Satter: "A Prediction Method for Conduction Heating of Reservoirs by Steam Injection," paper SPE 1950 presented at the 1967 SPE Annual Fall Meeting, Houston, TX, Oct. 1-4.

[3] Amyx, J.W., Bass, D.M., Jr. and Whiting, R.L.: *Petroleum Reservoir Engineering, Physical Properties*, McGraw-Hill, New York (1960).

[4] Anand, J., Somerton, W.H. and Gomaa, E.: "Predicting Thermal Conductivities of Formations from Other Known Properties," *Soc. of Pet. Eng. J.* (October 1973) 267–273.

[5] Bergosh, J.L., Marks, T.R. and Mitkus, A.F.: "New Core Analysis Techniques for Naturally Fractured Reservoirs," paper SPE 13653 presented at the 1985 SPE California Regional Meeting, Bakersfield, CA, March 27-29.

[6] Briggs, P.J.: "A Simulator for the Recovery of Heavy Oil from Naturally Fractured Reservoirs Using Cyclic Steam Injection," paper SPE 17954 presented at the 1989 SPE Middle East Oil Technical Conference and Exhibition, Manama, Bahrain, March 11-14.

[7] Briggs, P.J., Beck, D.L., Black, C.J.J. and Bissell, R.: "Heavy Oil from Fractured Carbonate Reservoirs," *SPE Reservoir Engineering* (May 1992) 173–179.

[8] Brigham, W.E. and Castanier, L.M.: "Supri Heavy Oil Research Program, Seventeenth Annual Report," No. Supri TR 98, Stanford University (February 1994).

[9] Brigham, W.E. and Castanier, L.M.: "Supri Heavy Oil Research Program, Eighteenth Annual Report," No. Supri TR 100, Stanford University (February 1995).

[10] Britton, M.W., Martin, W.L., Leibrecht, R.J. and Harmon, R.A.: "The Street Ranch Pilot Test of Fracture-Assisted Steamflood Technology," paper SPE 10707 presented at the 1982 SPE California Regional Meeting, San Francisco, CA, March 24-26.

[11] Chatzis, I., Kantzas, A. and Dullien, F.A.L.: "On the Investigation of Gravity-Assisted Inert Gas Injection Using Micromodels, Long Berea Sandstone Cores, and Computer-Assisted Tomography," paper SPE 18284 presented at the 1988 SPE Annual Technical Conference and Exhibition, Houston, TX, Oct. 2-5.

[12] Chen, J., Miller, M.A. and Sepehrnoori, K.: "Comparisons of Counter-Current Imbibition Transfer Functions in Dual Porosity Models of Naturally Fractured Reservoirs," *Insitu* (1991) 115–147.

[13] Chen, W.H., Wasserman, M.L. and Fitzmorris, R.E.: "A Thermal Simulator for Naturally Fractured Reservoirs," paper SPE 16008 presented at the 1987 SPE Symposium on Reservoir Simulation, San Antonio, TX, February 1-4.

[14] Chierici, G.L., Delle Canne, A. and Properzi, O.: "Steam Drive in a Fractured Carbonate: The Vallecupa, Italy, Pilot Plant," presented at the 1985 European Meeting on Improved Oil Recovery, Rome, Italy, April.

[15] Closmann, P.J. and Smith, R.A.: "Temperature Observations and Steam-Zone Rise in the Vicinity of a Steam-Heated Fracture," *Soc. of Pet. Eng. J.* (August 1983) 575–586.

[16] Computer Modeling Group: *Imex User's Manual, Version 4.3.0* (1991).

[17] Computer Modelling Group: *Stars User's Manual, Version 4.0* (1990).

[18] Computer Modelling Group: *Stars User's Guide, Version 95.00* (1995).

[19] Corporation, R. I.: *Instruction Manual for Operation and Maintenance of Ruska Liquid Permeameter, Model 1013-801* (1981).

[20] Couderc, B.M., Verpeaux, J.F., Monfrin, D. and Quettier, L.H.: "Emeraude Vapeur: A Steam Pilot in an Offshore Environment," *SPE Reservoir Engineering* (November 1990) 508–516.

[21] Cromwell, V., Kortum, D.J. and Bradley, D.J.: "The Use of a Medical Computer Tomography (CT) System to Observe Multiphase Flow in Porous Media," paper SPE 13098 presented at the 1984 SPE Annual Technical Conference and Exhibition, Houston, TX, September 16-19.

[22] Daltaban, T.S., Lewis, J.J.M. and Archer, J.S.: "Field Minipermeameter Measurements - Their Collection and Interpretation," presented at the 1989 European Symposium on Improved Oil Recovery, Budapest, Hungary.

[23] Demiral, B.M.R., Castanier, L.M. and Brigham, W.E.: "CT Imaging of Steam and Steam Foam Laboratory Experiments," paper SPE 22644 presented at the 1991 SPE Annual Technical Conference and Exhibition, Dallas, TX, October 6-9.

[24] Demiral, B.M.R., Pettit, P.A., Castanier, L.M. and Brigham, W.E.: "A Three-Dimensional Laboratory Steam Injection Model Allowing In Situ Saturation Measurements," No. Supri TR 83, U.S. Department of Energy, Fossil Energy (August 1992).

[25] Dillabough, J.A. and Prats, M.: "Recovering Bitumen from Peace River Deposits," *The Oil and Gas Journal* (November 1974) 186–196.

[26] Dindoruk, B.: *Personal communication* (April, 1995).

[27] Dreher, K.D., and Kenyon, D.E.: "Heat Flow During Steam Injection Into a Fractured Carbonate Reservoir," paper SPE 14902 presented at the 1986 SPE/DOE Symposium on Enhanced Oil Recovery, Tulsa, OK, April 20-23.

[28] Duerksen, J.H., Cruikshank, G.W. and Wasserman, M.L.: "Performance and Simulation of a Cold Lake Tar Sand Steam-Injection Pilot," *Journal of Petroleum Technology* (October 1984) 1781–1790.

[29] Eijpe, R. and Weber, K.J.: "Mini-Permeameters for Consolidated and Unconsolidated Sand," *The American Association of Petroleum Geologists Bulletin* (February 1971) 307–309.

[30] Exploration Consultants Limited: *Eclipse Reference Manual, Version 09/88* (1988).

[31] Farouq Ali, S.M.: *Oil Recovery by Steam Injection*, Producers Publishing Co. Inc., Bradford, PA (1970).

[32] Firoozabadi, A. and Hauge, J.: "Capillary Pressure in Fractured Porous Media," *Journal of Petroleum Technology* (June 1990) 784–791.

[33] Firoozabadi, A. and Thomas, L. K.: "Sixth SPE Comparative Solution Project: Dual-Porosity Simulators," *Journal of Petroleum Technology* (June 1990) 710–763.

[34] Geshelin, B.M., Grabowski, J.W. and Pease, E.C.: "Numerical Study of Transport of Injected and Reservoir Water in Fractured Reservoirs During Steam Stimulation," paper SPE 10322 presented at the 1981 SPE Annual Fall Technical Conference and Exhibition, San Antonio, TX, October 5-7.

[35] Goggin, D.J., Thrasher, R.L. and Lake, L.W.: "A Theoretical and Experimental Analysis of Minipermeameter Response Including Gas Slippage and High Velocity Flow Effects," *In situ* (1988) 79–110.

[36] Guzman, R.: "Design and Construction of an Experiment for Two-Phase Flow in Fractured Porous Media," Master's thesis, Stanford University, Stanford, California (December 1991).

[37] Handy, L.L.: "Determination of Effective Capillary Pressures for Porous Media from Imbibition Data," *Petroleum Transactions, AIME* (1960) 75–80.

[38] Hartemink, M., Escovedo, B.M., Hoppe, J.E. and Macaulay, R.: "Quarn Alam: Application of Simulation for Steam Pilot Design in a Fractured Reservoir," presented at the 1995 European IOR Symposium, Vienna, Austria, May.

[39] Holman, J.P.: *Heat Transfer*, McGraw-Hill Publishing Company (1990).

[40] Honarpour, M.M., Cromwell, V., Hatton, D. and Satchwell, R.: "Reservoir Rock Descriptions Using Computed Tomography (CT)," paper SPE 14272 presented at the 1985 SPE Annual Technical Conference and Exhibition, Las Vegas, NV, September 22-25.

[41] Horie, T., Firoozabadi, A. and Ishimoto, K.: "Laboratory Studies of Capillary Interaction in Fracture/Matrix Systems," paper SPE 18282 presented at the 1988 SPE Annual Technical Conference and Exhibition, Houston, TX, October 2-5.

[42] Horne, R.N. and Ramey, H.J., Jr.: "Steam/Water Relative Permeabilities from Production Data," presented at the 1978 Geothermal Resources Council Annual Meeting, Hilo, July 25-27.

[43] Hove, A., Ringen, J.K. and Read, P.A.: "Visualization of Laboratory Corefloods with the Aid of Computerized Tomography of X-Rays," paper SPE 13654 presented at the 1985 SPE California Regional Meeting, Bakersfield, CA, March 27-29.

[44] Hunt, P.K. and Engler, P.: "Computed Tomography as a Core Analysis Tool: Applications and Artifact Reduction Techniques," paper SPE 16952 presented at the 1987 SPE Annual Technical Conference and Exhibition, Dallas, TX, September 27-30.

[45] Jensen, T.B.: *Steam Flooding of Fractured Reservoirs: Experimental and Numerical Studies*, PhD dissertation, University of Wyoming (August 1991).

[46] Jensen, T.B., Sharma, M.P., Harris, H.G. and Whitman, D.L.: "Numerical Investigations of Steam and Hot-Water Flooding in Fractured Porous Media," paper SPE 24172 presented at the 1992 SPE/DOE Symposium on Enhanced Oil Recovery, Tulsa, OK, April 22-24.

[47] Johns, R. A.: *Diffusion and Dispersion of Solute in a Variable Aperture Fracture*, PhD dissertation, Stanford University (September 1991).

[48] Joshi, S.: "Computer Modeling of a Three-Dimensional Steam Injection Experiment," Master's thesis, Stanford University, Stanford, California (1993).

[49] Kantzas, A., Marentette, D.F. and Jha, K.N.: "Computer Assisted Tomography: From Qualitative Visualization to Quantitative Core Analysis," (April 21-24 1991).

[50] Kazemi, H. and Merrill, L.S.: "Numerical Simulation of Water Imbibition in Fractured Cores," *Soc. of. Pet. Eng. J.* (June 1979) 175–182.

[51] Kazemi, H., Gilman, J.R. and Elsharkawy, A.M.: "Analytical and Numerical Solution of Oil recovery from Fractured Reservoirs with Empirical Transfer Functions," *SPE Reservoir Engineering* (May 1992) 219–227.

[52] Labastie, A.: "Capillary Continuity Between Blocks of a Fractured Reservoir," paper SPE 20515 presented at the 1990 SPE Annual Technical Conference and Exhibition, New Orleans, LA, September 23-26.

[53] Lee, B.Y.Q. and Tan, T.B.S.: "Application of a Multiple Porosity/Permeability Simulator in Fractured Reservoir Simulation," paper SPE 16009 presented at the 1987 SPE Symposium on Reservoir Simulation, San Antonio, TX, February 1-4.

[54] Lesser, H.A., Bruce, G.H. and Stone, H.L.: "Conduction Heating of Formations with Limited Permeability by Condensing Gases," *Soc. of Pet. Eng. J.* (December 1966) 372–382.

[55] Lewis, Rhys: *Practical Digital Image Processing*, Ellis Horwood, West Sussex, England (1990).

[56] Lin, C.Y.: "A New Approach for Simulation of Cyclic Steam Stimulation Above Fracture Pressure by Modifying a Thermal Simulator," paper SPE 18077 presented at the 1988 SPE Annual Technical Conference and Exhibition, Houston, TX, October 2-5.

[57] MacAllister, D.J., Miller, K.C. and Graham, S.K.: "Application of X-ray CT Scanning to Determine Gas/Water Relative Permeabilities," *SPE Formation Evaluation* (September 1993) 184–188.

[58] Mark, H.F. et al. eds.: *Encyclopedia of Polymer Science and Engineering, Vol. 13*, John Wiley and Sons, New York, N. Y. (1988).

[59] Mukhopadhyay, S. and Sahimi, M.: "Heat Transfer and Two-Phase Flow in Fractured Reservoirs," paper SPE 24043 presented at the 1992 SPE Western Regional Meeting, Bakersfield, CA, March 30-April 1.

[60] Nolan, J.B., Ehrlich, R. and Crookston, R.B.: "Applicability of Steamflooding for Carbonate Reservoirs," paper SPE 8821 presented at the 1980 SPE/DOE Symposium on Enhanced Oil Recovery, Tulsa, OK, April 20-23.

[61] Oballa, V., Coombe, D. and Buchanan, L.: "Factors Affecting the Thermal Response of Naturally Fractured Reservoirs," No. 90.05.T, Computer Modelling Group (March 1990).

[62] Oballa, V., Coombe, D.A. and Buchanan, W.L.: "Factors Affecting the Thermal Response of Naturally Fractured Reservoirs," *JCPT* (October 1993) 31–42.

[63] Peters, E.J. and Afzal, N.: "Characterization of Heterogeneities in Permeable Media with Computed Tomography Imaging," *Journal of Petroleum Science and Engineering* (1992) 283–296.

[64] Peters, E.J. and Gharbi, R.: "Numerical Modeling of Laboratory Corefloods," *Journal of Petroleum Science and Engineering* (1993) 207–221.

[65] Pooladi-Darvish, M., Tortike, W.S. and Ali, F.: "Steam Heating of Fractured Formations Containing Heavy Oil: Basic Premises and a Single-Block Analytical Model," paper SPE 28642 presented at the 1994 SPE Annual Technical Conference and Exhibition, New Orleans, LA, September 25-28.

[66] Pruess, K. and Narasimhan, T. N.: "A Practical Method for Modeling Fluid and Heat Flow in Fractured Porous Media," *Soc. of Pet. Eng. J.* (February 1985) 14–26.

[67] Pruess, K. and Wu, Y.: "A New Semianalytical Method for Numerical Simulation of Fluid and Heat Flow in Fractured Reservoirs," paper SPE 18426 presented at the 1989 SPE Symposium on Reservoir Simulation, Houston, TX, February 6-8.

[68] Reis, J.C.: "Oil Recovery Mechanisms in Fractured Reservoirs During Steam Injection," paper SPE 20204 presented at the 1990 SPE/DOE Symposium on Enhanced Oil Recovery, Tulsa, OK, April 22-25.

[69] Reis, J.C.: "Studies of Fractures Induced During Cyclic Steam Injection," paper SPE 20033 presented at the 1990 California Regional Meeting, Ventura, CA, April 4-6.

[70] Rohsenow, W. M. and Hartnett, J.P.: *Handbook of Heat Transfer*, McGraw-Hill, New York, N. Y. (1973).

[71] Sahuquet, B.C. and Ferrier, J.J.: "Steam-Drive Pilot in a Fractured Carbonate Reservoir: Lacq Superieur Field," *J. Pet. Tech.* (April 1982) 873–880.

[72] Sanchez, J.M. and Schechter, R.S.: "A Comparison of the Two-Phase Flow of Steam/Water and Nitrogen/Water Through an Unconsolidated Permeable Medium," paper SPE 16967 presented at the 1987 SPE Annual Technical Conference and Exhibition, Dallas, TX, September 27-30.

[73] Sanyal, S.K.: *The Effect of Temperature on Electrical Resistivity and Capillary Pressure Behavior of Porous Media*, PhD dissertation, Stanford University (December 1971).

[74] Saraf, D. N.: *Measurement of Fluid Saturations by Nuclear Magnetic Resonance and Its Application to Three-Phase Relative Permeability Studies*, PhD dissertation, University of California, Berkeley (December 1966).

[75] Satman, A.: "Solutions of Heat- and Fluid-Flow Problems in Naturally Fractured Reservoirs: Part 1 - Heat Flow Problems," *SPE Production Engineering* (November 1988) 463–466.

[76] Sedgwick, G.E. and Miles-Dixon, E.M.: "Application of X-ray Imaging Techniques to Oil Sands Experiments," *Journal of Canadian Petroleum Technology* (March-April 1988) 104–110.

[77] Shallcross, D.C. and Wood, D.G.: "The Accurate Measurements of Heat Flux Using Thin Film Heat Flux Sensors with Application to Petroleum Engineering," No. Supri TR 74, U.S. Department of Energy, Fossil Energy (July 1990).

[78] Sharma, B.: "Displacement Studies Using a Three-Dimensional Laboratory Steam Injection Model," Engineer's report in progress.

[79] Somerton, W.H. and Boozer, G.D.: "Thermal Characteristics of Porous Rocks at Elevated Temperatures," *SPE Reprint Series, Thermal Recovery Processes*, 164–172.

[80] Stang, H.R. and Soni, Y.: "Saner Ranch Pilot Test of Fracture-Assisted Steamflood Technology," *J. Pet. Tech.* (June 1987) 684–696.

[81] Stehfest, H.: "Numerical Inversion of Laplace Transforms, Algorithm 368," *Communications of ACM* (January 1970) 47–49.

[82] Thomas, G.W.: "A Simplified Model of Conduction Heating in Systems of Limited Permeability," *Soc. of Pet. Eng. J.* (December 1964) 335–344.

[83] van Wunnik, J.N.M. and Wit, K.: "Improvement of Gravity Drainage by Steam Injection into a Fractured Reservoir: An Analytical Evaluation," *SPE Reservoir Engineering* (February 1992) 59–66.

[84] Vinegar, H.J. and Wellington, S.L.: "Tomographic Imaging of Three-Phase Flow Experiments," *Rev. Sci. Instrum.* (January 1987) 96–107.

[85] Vinsome, P.K.W. and Westerveld, J.: "A Simple Method for Predicting Cap and Base Rock Heat Losses in Thermal Reservoir Simulators," *Journal of Canadian Petroleum Technology* (July-September 1980) 87–90.

[86] Wang, S., Ayral, S. and Gryte, C.C.: "Computer-Assisted Tomography for the Observation of Oil Displacement in Porous Media," *Soc. of Pet. Eng. J.* (February 1984) 53–55.

[87] Warren, J.E. and Root, P.J.: "The Behavior of Naturally Fractured Reservoirs," *Soc. Pet. Eng. J.* (September 1963) 245–255.

[88] Wellington, S.L. and Vinegar, H.J.: "CT Studies of Surfactant-Induced CO_2 Mobility Control," paper SPE 14393 presented at the 1985 SPE Annual Technical Conference and Exhibition, Las Vegas, NV, September 22-25.

[89] Wheeler, J.A.: "Analytical Calculations for Heat Transfer from Fractures," No. SPE 2494 (1969).

[90] Withjack, E.M. and Akervoll, I.: "Computed Tomography Studies of 3-D Miscible Displacement Behavior in a Laboratory Five-Spot Model," paper SPE 18096 presented at the 1988 SPE Annual Technical Conference and Exhibition, Houston, TX, October 2-5.

Appendix A

List of Equipment

APPENDIX A. LIST OF EQUIPMENT

Equipment	Model #	Manufacturer
Chromatography Pump	Constametric Metering Pump III	Thermo Separation Products 3661 Interstate Park Rd. North, P. O. Box 10235, Riviera Beach, FL, 33419
Steam Generator	Hoskins Electric Furnace, FD303A	Hoskins, Mfg. Co. Detroit, MI
Inline Filter	Nupro, Compact Inline Filter, F series	Nupro Company 4800 East 345 th Street, Willoughby, OH 44094
Nylon Tubing	Nylon tubing, 1/8 " OD	Parker Hamilton Corporation P. O. Box 400004-1504, Huntsville, AL 35815-1504
Temperature Contr.	West 1440 Single Mode Temperature Controller	West, Gulton Industries Inc., Gulton Industrial Park, East Greenwich, RI 02818
Pressure Gauge	Valin, General Purpose Dry Gauges	Valin Corporation 209 Fair Oaks Av., Sunnyvale, CA 94086

APPENDIX A. LIST OF EQUIPMENT

Temperature Indicator	Omega, 2176 Digital Thermometer	Omega Eng. Inc. P. O. Box 2284, Stamford, CT 06906
Back Pressure Regulator	Grove, Mity Mite 90	Grove, Valve & Regulator Company 6529, Hollis Street, Oakland, CA 94608
Data Logger	HP 3497A Data Acq./control unit	Hewlett-Packard 1507, Page Mill Rd., Palo Alto, CA 94304
Plug-in Cards	HP 44421 A 20 Channel Relay Multiplexer	Hewlett-Packard 1507, Page Mill Rd., Palo Alto, CA 94304
	HP 44422 A Relay Multiplexer with T/C Compensation	
Heat Flux Sensors	RDF Micro-Foil Heat Sensor, 20457-2	RDF Corporation 23 Elm Av., P. O. Box 490, Hudson, NH 03051-0490
Fittings (PEEK)	Alltech Knurl-lok III M-F, Short Knurl-lok III Hex Head	Alltech Associates Inc. 2051 Waukegan Road, Deerfield, IL 60015-1899
Tubing (PEEK)	Alltech, 1/16" OD, 0.020" ID tubing	
Fittings (SS)	Swagelok Tube Fittings	Crawford Fitting Company 29500 Solon Road, Solon, OH 44139
Valves (SS & Brass)	Whitey, 40 Series Ball Valves, 2-way & 3-way	Whitey Company 318 Bishop Road, Highland Heights, OH 44143

APPENDIX A. LIST OF EQUIPMENT

High temperature valve (SS)	Whitey, 83 series 3-way ball valve	Whitey Company 318 Bishop Road, Highland Heights, OH 44143
CT -scanner	EMI 5000	EMI Medical 3605 Woodhead Drive, Northbrook, IL 60062
Precision Gauges	Heise Precision Gauge	International Quarters, Dresser Industries, 250 East Main Street, Stratford, CT 06497
Pressure Relief Valve	Nupro, N-787 "RL3 " Series, externally adjustable valve	Nupro Company 4800 East 345 th Street, Willoughby, OH 44094
Pressure transducers	DP 31, Differential Pressure	Celesco Transducer Prod., Inc. 7800 Deering Av., P. O. Box 1457 Canoga Park, CA 91304
Demodulators	CD10 DC Output Carrier-demodulator	Celesco Transducer Prod., Inc. 7800 Deering Av., P. O. Box 1457 Canoga Park, CA 91304
Thermocouples (Model)	Omega, Type J 1/16 " SS	Omega Eng. Inc. P. O. Box 2284 Stamford, CT 06906
Oven Thermocouple	Omega Dual Element Assembly, 1/8 " J	
Injection line T/C	Omega ICSS -116G-12-DUAL	
Thermocouple Wire	Omega Duplex Insulated Type J and T AWG No. 20	

Appendix B

Data Acquisition Software

This appendix gives a brief description of the data acquisition software and includes also a listing.

B.1 Description

Microsoft Quickbasic 4.0 interfaced with the HPIB Command library was used for the data acquisition software. The computer code consists of a main program and several subroutines. The descriptions of the main program and the subroutines are given below.

In the main program (deniznew.bas) first the setup program for the HPIB interface is included. Then the constants used in the program are initialized and output files are defined. The software generates eight output files. They are listed in Table B.1.

The keyboard keys are defined next. If F1 is pressed, program stops. If F2 is pressed, the subroutine to prepare the screen to display the temperature measurements is called (subroutine "pencere"), and if F3 is pressed the subroutine to prepare the screen to display the pressure measurements is called (subroutine "pencere1").

After screen setup is completed, the subroutine "datalog" is called which calls the subroutines for individual measurements. The description of those subroutines is given next.

Subroutine temp

Table B.1: Output files generated by the software.

file name	data
tc.out	system thermocouples
thflux.out	heat flux sensor thermocouples
hsensor.out	heat flux sensors
pressure.out	pressure transducers
pt1.out, pt2.out, pt3.out, pt4.out	output files for individual pressure measurements

It records the temperatures measured from 13 thermocouples located in the core holder, together with the injection line, production line and oven thermocouples. The heat flux sensor thermocouple measurements are recorded by this subroutine also. First the voltages generated by the thermocouples are recorded, then they are converted into temperatures by using thermocouple constants and polynomials.

Subroutine pres

Pressure transducer voltages are measured and they are converted into pressures in psi by using the pressure transducer diaphragm constants.

Subroutine flux

It records the voltages measured by the heat flux sensors.

B.2 Software Listing

To run the software, the command "deniznew.exe" should be executed.

```
DECLARE SUB pencere ()
DECLARE SUB pencere1 ()
DECLARE SUB temp ()
DECLARE SUB flux ()
```

```
DECLARE SUB pres ()
DECLARE SUB renk ()
' ' DATA LOGGING PROGRAM
' FOR STEAM INJECTION IN FRACTURED SYSTEM
' ' by DENIZ SUMNU
' june 1993
' modified in november 1993 for preliminary runs
' modified in June 1994 for water-steam runs in the scanner ' ' '
OPTION BASE 1
DEFINT A-Z
DIM rcold!(1)
DIM tctemp!(30)
DIM hflux!(20)
DIM htflux!(20)
DIM pt!(20)
DIM pressure!(20)
DIM dia!(20)
COMMON SHARED rcold!()
COMMON SHARED hflux!()
COMMON SHARED pressure!(), dia!()
COMMON SHARED htflux!()
COMMON SHARED iflag1 AS INTEGER, iflag2 AS INTEGER,
iflag3 AS INTEGER
COMMON SHARED a!, b!
COMMON SHARED dev AS LONG, ISC AS LONG
COMMON SHARED IM AS INTEGER, i AS INTEGER, K AS INTEGER
COMMON SHARED maxi AS INTEGER, actual AS INTEGER
COMMON SHARED tctemp!()
COMMON PCIB.BASERR, PCIB.ERR, PCIB.ERR$, PCIB.NAME$,
PCIB.GLBERR
COMMON FALSE AS INTEGER, TRUE AS INTEGER, NOERR
```

```
AS INTEGER
COMMON EUNKNOWN AS SINGLE, ESEL AS SINGLE,
ERANGE AS SINGLE
COMMON ETIME AS SINGLE, ECTRL AS SINGLE, EPASS AS SINGLE
COMMON ENUM AS SINGLE, EADDR AS SINGLE
' ESTABLISH ERROR VARIABLES "ON ERROR" BRANCHING
PCIB.ERR = 0
PCIB.ERR$ = STRING$(64, 32)
PCIB.NAME$ = STRING$(16, 32)
PCIB.GLBERR = 0
CALL DEFERR(PCIB.ERR, PCIB.ERR$, PCIB.NAME$, PCIB.GLBERR)
PCIB.BASERR = 255
ON ERROR GOTO 99
GOTO MNEMONICS
' ERROR HANDLING ROUTINE
ERRORHANDLER:
99 IF ERR = PCIB.BASERR THEN GOTO LIBERROR
PRINT "BASIC ERROR # "; ERR; "OCCURRED"
PRINT "ERROR: "; PCIB.ERR$
STOP
LIBERROR:
TMPERR = PCIB.ERR
IF TMPERR = 0 THEN TMPERR = PCIB.GLBERR
PRINT "HP-IB ERROR #"; TMPERR; "DETECTED"
PRINT "ERROR:"; PCIB.ERR$
STOP
MNEMONICS:
FALSE = 0
TRUE = NOT FALSE
NOERR = 0
EUNKNOWN = 100001!
```

```
ESEL = 100002!
ERANGE = 100003!
ETIME = 100004!
ECTRL = 100005!
EPASS = 100006!
ENUM = 100007!
EADDR = 100008!
'END PROGRAM SET-UP
' INITIALIZATION OF VALUES
ISC = 7
dev = 709
actual = 0
maxi = 1 iflag2 = 1
iflag3 = 0
'initialize transducer constants
dia!(1) = 5!
dia!(2) = 3!
dia!(3) = 3!
dia!(4) = 25!
OPEN "tc.out" FOR APPEND AS #1
OPEN "thflux.out" FOR APPEND AS #2
OPEN "hsensor.out" FOR APPEND AS #3
OPEN "pressure.out" FOR APPEND AS #4
OPEN "pt1.out" FOR APPEND AS #10
OPEN "pt2.out" FOR APPEND AS #11
OPEN "pt3.out" FOR APPEND AS #12
OPEN "pt4.out" FOR APPEND AS #13
PRINT #1, "TIME(SEC) TC#1 TC#2 TC#3 TC#4 TC#5
TC#6 TC#7 TC#8 TC#9 TC#10 TC#11 TC#12 TC#13 "
PRINT #3, "TIME(SEC) HFLUX#1 HFLUX#2 HFLUX#3 HFLUX#4 HFLUX#5
PRINT #4, "TIME (SEC) PT#1 PT#2 PT#3 PT#4"
```

```
' SYSTEM INITIALIZATION
TIME$ = "00:00:00"
CLS
CALL IORESET(ISC)
TIMEOUT = 5!
CALL IOTIMEOUT(ISC, TIMEOUT)
CALL IOCLEAR(ISC)
CALL IOREMOTE(ISC)
codes$ = "SISO1VA1VD5VF1VS0"
length = LEN(codes$)
CALL iooutputs(dev, codes$, length)
KEY OFF
' BEGIN KEY SETTING
KEY 1, ""
KEY 2, ""
KEY 3, ""
ON KEY(1) GOSUB progend
KEY(1) ON
ON KEY(2) GOSUB x2
KEY(2) ON
ON KEY(3) GOSUB x3
KEY(3) ON
' END OF KEY SETTING
ON TIMER(30) GOSUB datalog
TIMER ON
20 GOTO 20
END
x2:
CLS
iflag2 = 1
iflag3 = 0
```

```
RETURN
END
x3:
CLS
iflag3 = 1
iflag2 = 0
RETURN
END
'subroutine to call the datalogging subroutines
datalog:
CALL temp
CALL flux
CALL pres
IF iflag2 = 1 THEN
CALL pencere
END IF
IF iflag3 = 1 THEN
CALL pencere1
END IF
RETURN
END
'subroutine to stop the program
progend:
CLS
PRINT "program terminated"
END
' SUB flux
'read heat flux sensor readings from slot 2
'channels 44-51
DIM vflux!(1)
codes$ = "AF44AL51ASVR5VN1"
```

```
length = LEN(codes$)
FOR i = 1 TO 8
CALL iooutputs(dev, codes$, length)
CALL ioentera(dev, SEG vflux!(1), maxi, actual)
hflux!(i) = vflux!(1)
NEXT i
tm! = TIMER
PRINT #3, tm!, hflux!(1), hflux!(2), hflux!(3), hflux!(4), hflux!(5), hflux!(6),
hflux!(7), hflux!(8)
END SUB
' Subroutine to prepare the temperature screen
SUB pencere
CLS
COLOR 12, 0
LOCATE 24, 70
PRINT TIME$
COLOR 6, 0
LOCATE 1, 1
PRINT "INJECTION SIDE"
i = 3
CALL renk
LOCATE 19, 20
PRINT "TCM#3="
LOCATE 20, 20
PRINT USING "###.##"; tctemp!(3)
i = 4
CALL renk
LOCATE 22, 20
PRINT "TCF#4="
LOCATE 23, 20
PRINT USING "###.##"; tctemp!(4)
```

```
i = 9
CALL renk
LOCATE 4, 67
PRINT "TCF#9="
LOCATE 5, 67
PRINT USING "###.##"; tctemp!(9)
i = 10
CALL renk
LOCATE 1, 50
PRINT "TCF#10="
LOCATE 2, 50
PRINT USING "###.##"; tctemp!(10)
i = 12
CALL renk
LOCATE 4, 35
PRINT "TCM#12="
LOCATE 5, 35
PRINT USING "###.##"; tctemp!(12)
i = 13
CALL renk
LOCATE 1, 20
PRINT "TCF#13="
LOCATE 2, 20
PRINT USING "###.##"; tctemp!(13)
i = 1
CALL renk
LOCATE 4, 20
PRINT "TCM#1="
LOCATE 5, 20
PRINT USING "###.##"; tctemp!(1)
i = 2
```

```
CALL renk
LOCATE 11, 2
PRINT "TCF#2="
LOCATE 12, 2
PRINT USING "###.##"; tctemp!(2)
i = 11
CALL renk
LOCATE 11, 35
PRINT "TCM#11="
LOCATE 12, 35
PRINT USING "###.##"; tctemp!(11)
i = 5
CALL renk
LOCATE 19, 35
PRINT "TCM#5="
LOCATE 20, 35
PRINT USING "###.##"; tctemp!(5)
i = 8
CALL renk
LOCATE 11, 50
PRINT "TCM#8="
LOCATE 12, 50
PRINT USING "###.##"; tctemp!(8)
i = 6
CALL renk
LOCATE 22, 50
PRINT "TCF#6="
LOCATE 23, 50
PRINT USING "###.##"; tctemp!(6)
i = 7
CALL renk
```

```
LOCATE 19, 67
PRINT "TCF#7="
LOCATE 20, 67
PRINT USING "###.##"; tctemp!(7)
END SUB
' Subroutine to prepare the pressure screen SUB pencere1
CLS
CLS 1
'do the pressure screen and the balance screen
SCREEN 9
PALETTE 4, 13
'draw a box
LINE (150, 100)-(450, 250), 7, BF
LINE (50, 175)-(150, 175), 12
LINE (100, 175)-(100, 50), 12
LINE (450, 175)-(540, 175), 12
LINE (495, 175)-(495, 50), 12
LINE (100, 50)-(495, 50), 12
LINE (225, 100)-(225, 50), 12
LINE (375, 100)-(375, 50), 12
LOCATE 1, 3
PRINT "INJECTION SIDE"
LOCATE 23, 3
PRINT "top balance="; a!
LOCATE 23, 30
PRINT "bottom balance="; b!
LOCATE 14, 10
PRINT "PT#1="
LOCATE 15, 10
PRINT USING "###.####"; pressure!(1)
LOCATE 20, 10
```

```
PRINT "INJECTION LINE TC="
LOCATE 21, 10
PRINT USING "###.####"; tctemp!(15)
LOCATE 20, 55
PRINT "INJECTION LINE TC (CLOSE)="
LOCATE 21, 55
PRINT USING "###.####"; tctemp!(14)
LOCATE 3, 25
PRINT "PT#2="
LOCATE 3, 30
PRINT USING "###.####"; pressure!(2)
LOCATE 3, 45
PRINT "PT#3="
LOCATE 3, 51
PRINT USING "###.####"; pressure!(3)
LOCATE 1, 60
PRINT "PROD. TEMP.="
LOCATE 2, 60
PRINT USING "###.####"; tctemp!(16)
LOCATE 14, 60
PRINT "PT#4="
LOCATE 15, 60
PRINT USING "###.####"; pressure!(4)
LOCATE 23, 60
PRINT "TIME="; TIME$
END SUB
SUB pres
DIM vpt!(1)
DIM pt!(20)
'from slot 2 channels 40-43
'read the voltage from the pressure transducers
```

```
codes$ = "AF40AL43ASVR5VN1"
length = LEN(codes$)
FOR i = 1 TO 4
CALL iooutputs(dev, codes$, length)
CALL ioentera(dev, SEG vpt!(1), maxi, actual)
pt!(i) = vpt!(1)
timepp! = TIMER
PRINT #4, timepp!, vpt!(1), pt!(i)
'convert voltage reading into psi
pressure!(i) = dia!(i) * pt!(i) / 10!
NEXT i
timep! = TIMER
PRINT #4, timep!, pressure!(1), pressure!(2), pressure!(3), pressure!(4)
PRINT #10, timep!, pressure!(1) * 10! / dia!(1), pressure!(1)
PRINT #11, timep!, pressure!(2) * 10! / dia!(2), pressure!(2)
PRINT #12, timep!, pressure!(3) * 10! / dia!(3), pressure!(3)
PRINT #13, timep!, pressure!(4) * 10! / dia!(4), pressure!(4)
END SUB
DEFSNG A-Z 'Subroutine for color change in the temperature screen SUB renk
IF tctemp!(i) < 20! THEN COLOR 2, 0
IF tctemp!(i) > = 20! AND tctemp!(i) < 30! THEN COLOR 3, 0
IF tctemp!(i) > 30! AND tctemp!(i) <= 50! THEN COLOR 1, 0
IF tctemp!(i) > 50! AND tctemp!(i) <= 60! THEN COLOR 13, 0
IF tctemp!(i) > 60! AND tctemp!(i) <= 70! THEN COLOR 5, 0
IF tctemp!(i) > 70! AND tctemp!(i) <= 80! THEN COLOR 6, 0
IF tctemp!(i) > 80! AND tctemp!(i) <= 90! THEN COLOR 14, 0
IF tctemp!(i) > 90! AND tctemp!(i) <= 100! THEN COLOR 12, 0
IF tctemp!(i) > 100! AND tctemp!(i) <= 120! THEN COLOR 4, 0
IF tctemp!(i) > 120! THEN COLOR 4, 1
END SUB
SUB temp
```

```
DIM length AS INTEGER
DIM V2!(1) 'Thermocouple polynomial constants for Type J
R0# = -.00000075004344#
R1# = .0000505321995#
R2# = 2.348050017D-08
P0# = -.3595568424#
P1# = 19750.87948#
P2# = -175116.5425#
P3# = 18212965.58#
P4# = -2831128435#
P5# = 271508383300#
P6# = -13801412100000#
P7# = 379243843260000#
P8# = -5371925517000000#
P9# = 3.0840255439D+16
'READ COLD JUNCTION CHANNEL #19
'for type J thermocouple
'SLOT 0
codes$ = "AC19VR5VN1"
length = LEN(codes$)
CALL iooutputs(dev, codes$, length)
CALL ioentera(dev, SEG rcold!(1), maxi, actual)
TCOLD# = rcold!(1) * 10!
V1! = R0# + TCOLD# * (R1# + TCOLD# * R2#)
' 'FROM SLOT 0
'READ THERMOCOUPLE EMF AT CHANNELS 0 TO 14
' 13 system thermocouples, inj. line thermocouple and oven thermocouple
codes$ = "AF0AL14ASVR5VN1"
length = LEN(codes$)
FOR i = 1 TO 15
CALL iooutputs(dev, codes$, length)
```

```
CALL ioentera(dev, SEG V2!(1), maxi, actual)
V! = V1! + V2!(1)
P79# = P7# + V! * (P8# + V! * P9#)
P56# = P5# + V! * (P6# + V! * P79#)
P34# = P3# + V! * (P4# + V! * P56#)
P12# = P1# + V! * (P2# + V! * P34#)
T1# = P0# + V! * P12#
tctemp!(i) = INT(T1# * 100! + .5) / 100!
NEXT i
' from slot 1
'read cold junction for Type T thermocouple
'thermocouple polynomial constants for Type T
R0# = .000000525792984#
R1# = .00003860071243#
R2# = 4.186486602D-08
P0# = .1238117795#
P1# = 26861.17637#
P2# = -896494.2879999999#
P3# = -46489260.88#
P4# = 12441142450#
P5# = 2275304922000#
P6# = -639949686700000#
P7# = 5.435757807D+16
P8# = -2.02361537D+18
P9# = 2.830121167D+19
codes$ = "AC39VR5VN1"
length = LEN(codes$)
CALL iooutputs(dev, codes$, length)
CALL ioentera(dev, SEG rcold!(1), maxi, actual)
'PRINT "vcold="; rcold!(1)
TCOLD# = rcold!(1) * 10!
```

```
V1! = R0# + TCOLD# * (R1# + TCOLD# * R2#)
'from slot 1
'read type T heat flux thermocouples from channels 21-27
'channel 23 is empty
codes$ = "AF21AL22ASVR5VN1"
length = LEN(codes$)
FOR i = 1 TO 2
CALL iooutputs(dev, codes$, length)
CALL ioentera(dev, SEG V2!(1), maxi, actual)
V! = V1! + V2!(1)
P79# = P7# + V! * (P8# + V! * P9#)
P56# = P5# + V! * (P6# + V! * P79#)
P34# = P3# + V! * (P4# + V! * P56#)
P12# = P1# + V! * (P2# + V! * P34#)
T1# = P0# + V! * P12#
htflux!(i) = INT(T1# * 100! + .5) / 100!
NEXT i
codes$ = "AF24AL27ASVR5VN1"
length = LEN(codes$)
FOR i = 3 TO 6
CALL iooutputs(dev, codes$, length)
CALL ioentera(dev, SEG V2!(1), maxi, actual)
V! = V1! + V2!(1)
P79# = P7# + V! * (P8# + V! * P9#)
P56# = P5# + V! * (P6# + V! * P79#)
P34# = P3# + V! * (P4# + V! * P56#)
P12# = P1# + V! * (P2# + V! * P34#)
T1# = P0# + V! * P12#
htflux!(i) = INT(T1# * 100! + .5) / 100!
NEXT i
' read cold junction from channel 39 for type J T/C
```

```
R0# = -.00000075004344#
R1# = .0000505321995#
R2# = 2.348050017D-08
P0# = -.3595568424#
P1# = 19750.87948#
P2# = -175116.5425#
P3# = 18212965.58#
P4# = -2831128435#
P5# = 271508383300#
P6# = -13801412100000#
P7# = 379243843260000#
P8# = -5371925517000000#
P9# = 3.0840255439D+16
codes$ = "AC39VR5VN1"
length = LEN(codes$)
CALL iooutputs(dev, codes$, length)
CALL ioentera(dev, SEG rcold!(1), maxi, actual)
'PRINT "vcold="; rcold!(1)
TCOLD# = rcold!(1) * 10!
V1! = R0# + TCOLD# * (R1# + TCOLD# * R2#)
' 'read production line temperature from channel 28
codes$ = "AC28VR5VN1"
length = LEN(codes$)
CALL iooutputs(dev, codes$, length)
CALL ioentera(dev, SEG V2!(1), maxi, actual)
V! = V1! + V2!(1)
P79# = P7# + V! * (P8# + V! * P9#)
P56# = P5# + V! * (P6# + V! * P79#)
P34# = P3# + V! * (P4# + V! * P56#)
P12# = P1# + V! * (P2# + V! * P34#)
T1# = P0# + V! * P12#
```

```
tctemp!(16) = INT(T1# * 100! + .5) / 100!
tmt! = TIMER
PRINT #1, tmt!, tctemp!(14), tctemp!(15), tctemp!(16)
PRINT #1, tmt!, tctemp!(1), tctemp!(2), tctemp!(3), tctemp!(4), tctemp!(5),
tctemp!(6), tctemp!(7), tctemp!(8), tctemp!(9), tctemp!(10), tctemp!(11),
tctemp!(12), tctemp!(13)
PRINT #2, tmt!, htflux!(1), htflux!(2), htflux!(3), htflux!(4), htflux!(5), htflux!(6)
' END SUB
```

Appendix C

Problems with Stehfest Algorithm

The Stehfest Algorithm is the most widely used algorithm for the inversion of Laplace Transforms. When a variable temperature boundary condition was used for the solution of the heat conduction equation shown in Chapter 8, a polynomial was used for the temperature function. The calculated heat losses from the analytical solution are compared with the measured losses in Fig. C.1. The analytical solution becomes unstable and deviates from the measured values after about 2000 seconds, and never reaches steady state. The numerical problems were thought to come from the Laplace inversion algorithm. To test whether this was true, the same equation was solved numerically by an implicit finite difference scheme as shown in Fig. C.1.

The numerical solution agrees with the analytical solution up to the point where the analytical solution starts to increase rapidly. The numerical solution has the same shape as the measured heat loss curve. This shows that there was no error in posing the problem, and that the boundary conditions agree with the physics of the system. Thus, the heat losses calculated by the analytical solution are incorrect due to numerical instabilities in the inversion of the Laplace transformation.

To see how the results will be affected by changing the degree of polynomial used to fit the temperature measurements, polynomials with differing degrees of fit to the temperature data were used in the analytical solution. Figure C.2 compares those results. All the solutions with polynomials of degree higher than five became unstable at some point in the solution. When m = 5, the solution behaved nicely and

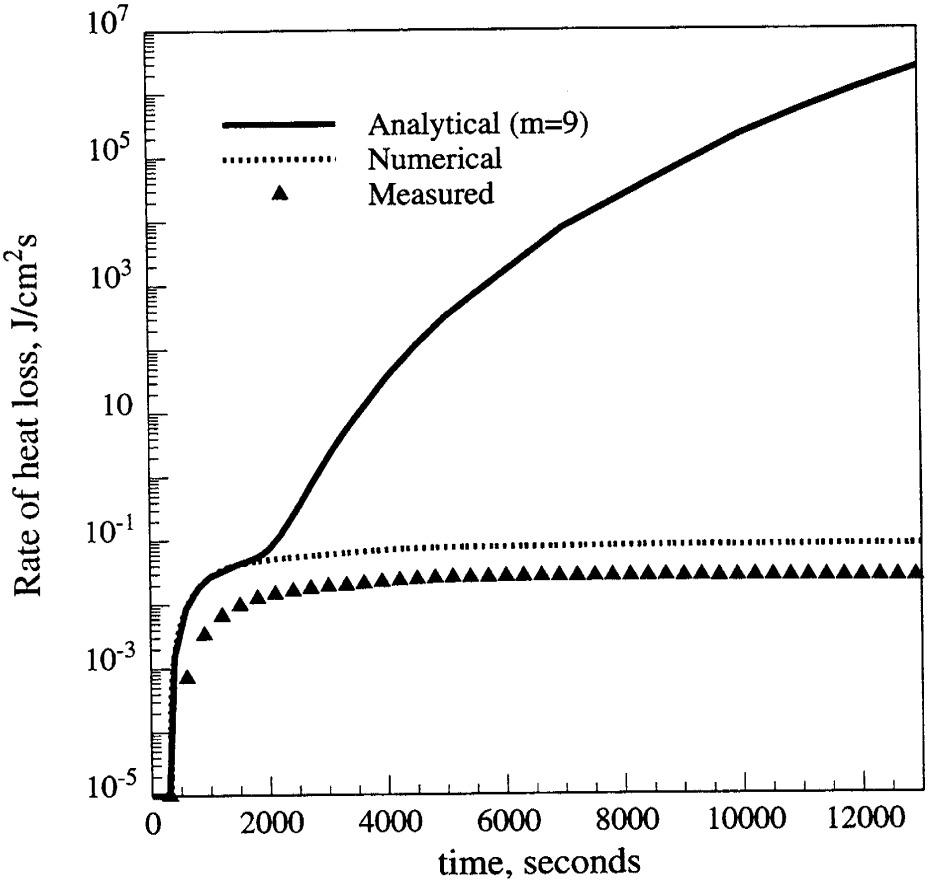

Figure C.1: Comparisons of measured heat losses with those calculated by variable temperature inner boundary condition (Numerical and analytical with m=9).

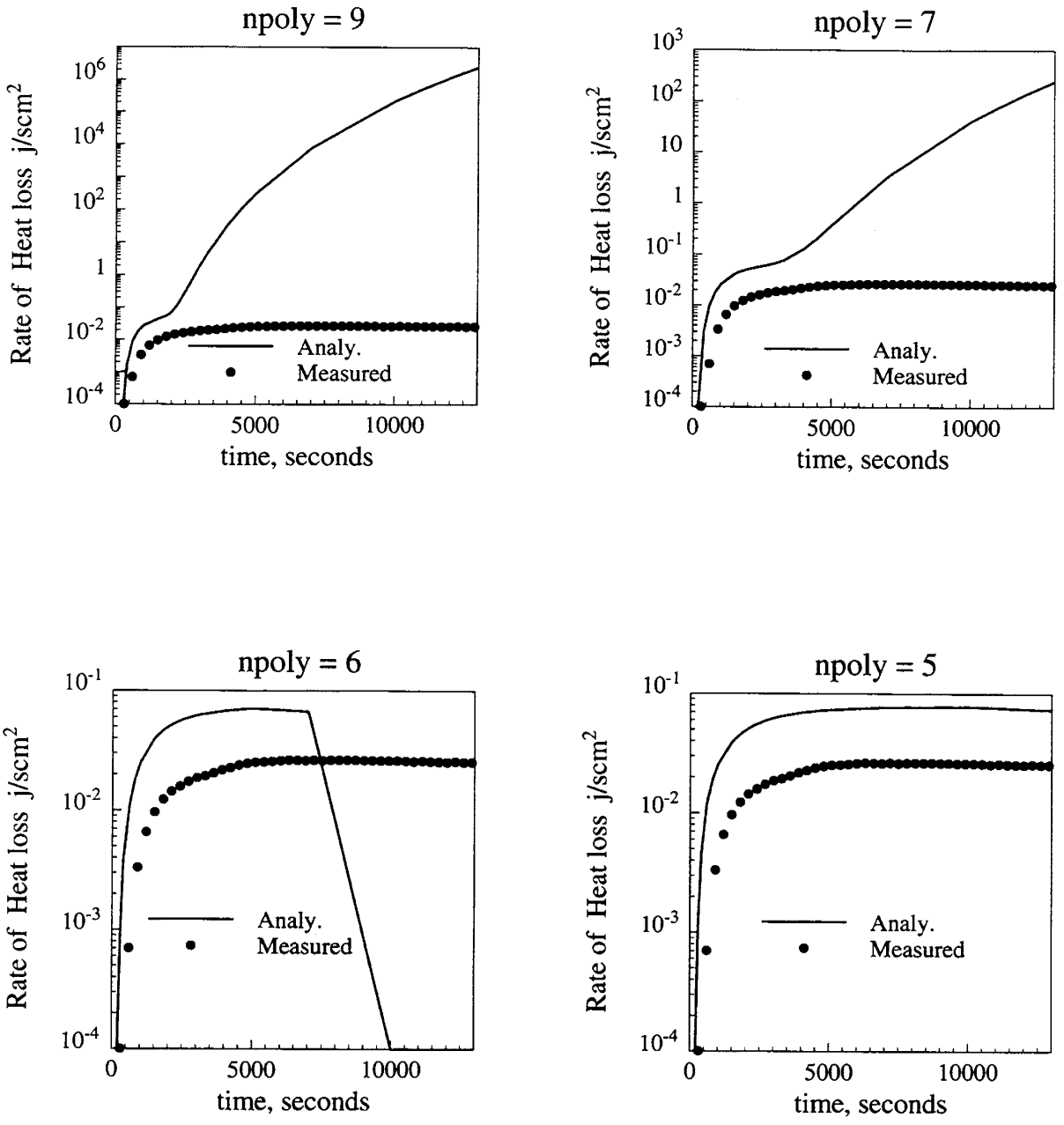

Figure C.2: Analytical solutions with different degrees of polynomial fits.

did not oscillate. This showed that the false solutions were due to the higher degree polynomials used. However, one drawback in using a lower degree of polynomial is that the temperature fit is not as good (Fig. C.3). An error in estimation of the temperature function may result in an inaccurate estimate of the heat loss.

The precision level used in the computer code can affect the results in numerical problems [26]. To test this idea, quadruple precision was used on the computer code for the ninth degree polynomial. Figure C.4 compares the solutions with double and quadruple precision. The quadruple precision solution was stable (dotted curve) and compared well with the numerical results of Fig. C.1 (dotted curve).

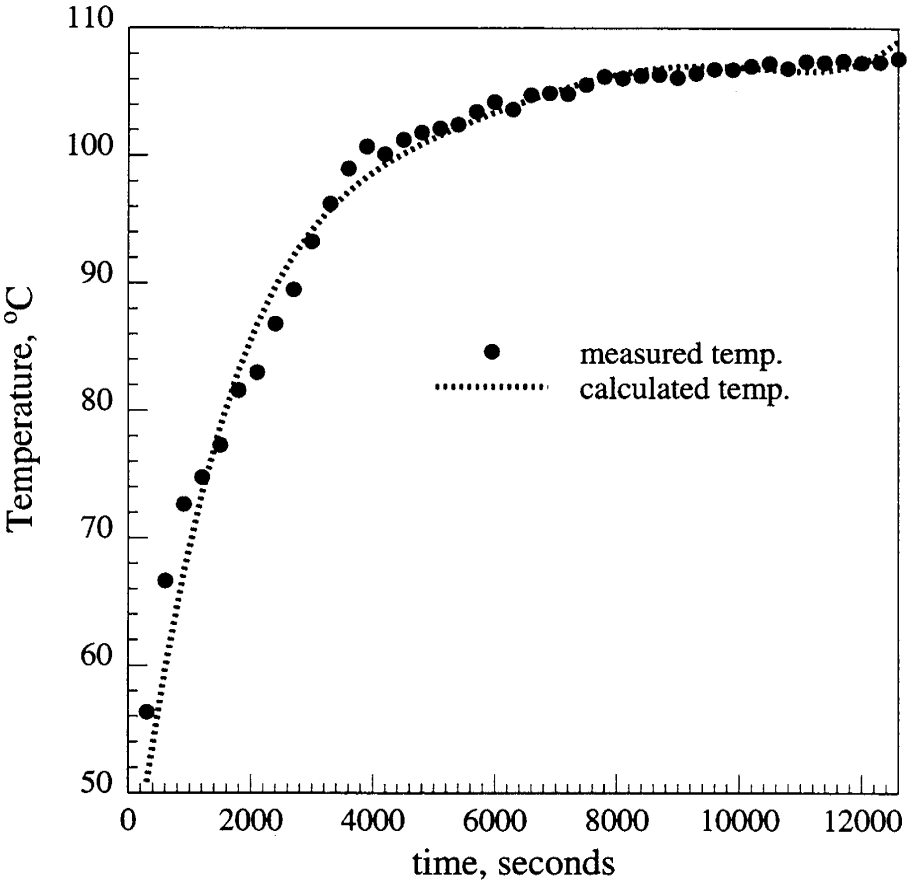

Figure C.3: Temperature calculated by a fifth degree polynomial.

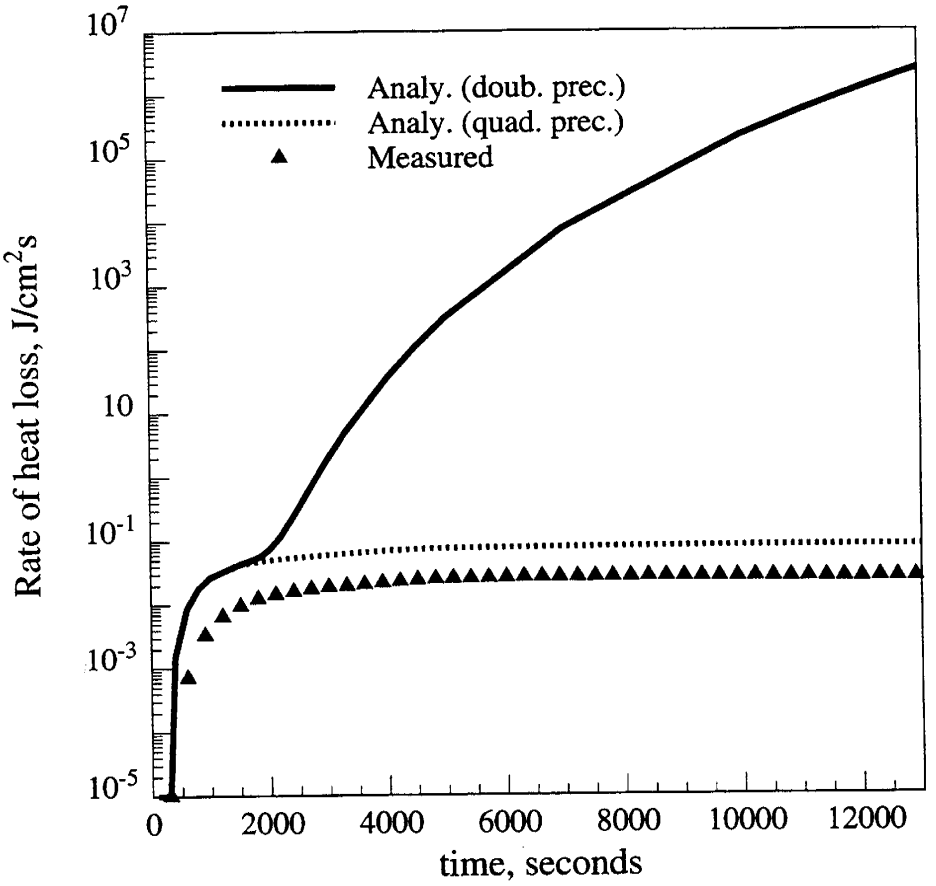

Figure C.4: Effect of precision in the code used for numerical inversion of Stehfest Algorithm.

☆U.S. GOVERNMENT PRINTING OFFICE: 1996 - 760-032/20077